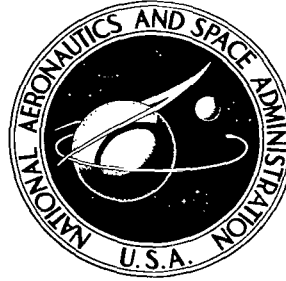


**NASA TECHNICAL
TRANSLATION**



NASA TT F-505

NASA TT F-505



TECH LIBRARY KAFB, NM

**LOAN COPY: RETURN
AFWL (WLIL-2)
KIRTLAND AFB, N MEX**

**STUDIES IN
PHYSICAL GAS DYNAMICS**

A. S. Predvoditelev, Editor

"Nauka" Press

Moscow, 1966



0068969

NASA TT F-505

STUDIES IN PHYSICAL GAS DYNAMICS

A. S. Predvoditelev, Editor

Translation of "Issledovaniya po fizicheskoy
gazodinamike." "Nauka"
Press, Moscow, 1966.

NATIONAL AERONAUTICS AND SPACE ADMINISTRATION

For sale by the Clearinghouse for Federal Scientific and Technical Information
Springfield, Virginia 22151 - CFSTI price \$3.00

TABLE OF CONTENTS

Abstract	iii
Rozhdestvenskiy, I. B., N. N. Tsitelauri, N. V. Voskresenskaya and Ye. V. Samuylov: Morse Potential Parameters for C-C, C-O, and C-N Interactions	1
Samuylov, Ye. V. and N. N. Tsitelauri: Collision Integrals, Effective Cross Sections, and Angles of Deviation for the Morse Potential . . .	13
Samuylov, Ye. V. and N. V. Voskresenskaya: Attractive Interaction Potentials Between Li-Li Atoms in Ground States	25
Zaytsev, S. G.: Thermodynamic Parameters of Cesium Behind Incident and Reflected Shock Waves	31
Nikolayev, V. M. and Yu. A. Plastinin: Calculation of Photoionization Cross Sections of Nitrogen and Oxygen Atoms and Their Ions in Excited States	35
Plastinin, Yu. A. and G. G. Baula: Absorption Cross Sections of Electronic Band Systems of Diatomic N_2 , O_2 , N_2^+ , NO, C_2 and CN Molecules at High Temperatures	42
Ambartsumyan, Ye. N., P. V. Ionov and A. A. Kon'kov: Investigation of the Spectral Characteristics of Gases Heated by Shock Waves	63
Ambartsumyan, Ye. A., P. V. Ionov and A. A. Kon'kov: An Experimental Determination of Oscillator Strength of the Violet System of the CN Radical	76
Makarov, Yu. V. and A. M. Maksimov: Investigation of the Structure of the Luminescence Front in an Electromagnetic Shock Tube	86
Bashilov, V. A.: Spectroscopic Investigation of an Ionized Gas in an Electromagnetic Shock Tube	94
Petrova, G. P.: Measurement of Temperature and Density of Charged Particles of an Argon Plasma Jet	103
Chekalin, E. K. and V. S. Shumanov: Jet Outflow of Metallic Plasma into a Vacuum	109
Chekalin, E. K. and V. S. Shumanov: Electrical Explosion of Wire in Air and in a Vacuum	116
Lobastov, Yu. S.: Experimental Determination of Electron Concentrations and Effective Frequencies of Electron Collision with Neutral Particles in Air, N_2 , O_2 , CO, Argon and CO_2 Behind Shock Waves	126
Bazhenova, T. V. and Yu. S. Lobastov: Secondary Phenomena During the Reflection of Shock Waves in Argon	138
Pleshanov, A. S.: Some General Inequalities of Chemical Thermodynamics for the Case of Partial Equilibrium	146

Pleshanov, A. S. and P. A. Kon'kov: Nonisentropic Nonequilibrium Flow of a Gas Through a Nozzle with Friction and Heat Exchange Taken into Account	148
Ionov, V. P. and G. N. Nikolayev: An Experimental Investigation of the Escape of Dissociated Gases Through Supersonic Nozzles	172
Nikolayev, G. N.: Calculation of the Recombination Rate Constants of Diatomic Gases According to the Mach Number of the Flow at the Exit of a Supersonic Nozzle	181
Zaytsev, S. G. and Ye. V. Lazareva: Measurement of Carbon Dioxide Density in the Flow Behind a Shock Front	186
Naboko, I. M.: An Investigation of the State of a Gas Behind a Shock Wave on the Basis of the Pattern of Flow Around an Obstacle Placed in a Shock Tube	189
Bazhenova, T. V.: Calculation of the Onset Time of Equilibrium Dissociation on the Basis of Experimental Data Concerning the Nonstationary Propagation of a Reflected Shock Wave	199
Gvozdeva, L. G. and O. A. Predvoditeleva: Peculiarities of Mach Reflection of Shock Waves Moving in Carbon Dioxide and Nitrogen at Velocities on the Order of 2,000 m/sec	203
Polyakov, Yu. A.: Nonstationary Heat Exchange in the Reflection of a Shock Wave	213
Predvoditeleva, O. A.: Heat Losses Associated with the Reflection of a Shock Wave from the End of a Tube	224
Salamandra, G. D.: Formation of a Gas Flow Before a Flame Front	227
Gusev, M. V. and O. I. Luneva: Piezoelectric Pressure Pickup.	234
Shatilov, A. P.: Mushroom-Shaped Transducer for Recording Pressure in a Shock Tube	244

STUDIES IN PHYSICAL GAS DYNAMICS

Edited by A. S. Predvoditelev

ABSTRACT. This book is a collection of articles devoted to basic research in physical gas dynamics with emphasis on molecular band spectra, shock tube studies, and interactions between diatomic molecules. Morse potential parameters, collision integrals, effective cross sections and angles of deviation are investigated for C-C, C-O, and C-N interactions in the ground and excited states. Attractive and repulsive interaction potentials between Li-Li atoms are considered. Thermodynamic parameters of substances behind incident and reflected shock waves are calculated and the spectral characteristics of gases heated by shock waves are given. Oscillator strength is determined experimentally in the violet system of the CN radical.

Several articles are concerned with various investigations employing electromagnetic shock tubes. Electrical wire explosions in air and in a vacuum are discussed. The results of experimental studies on the flow of dissociated gases through supersonic nozzles are presented and data from measurements of CO₂ density in the flow behind a shock front are tabulated. Several devices employed in the studies are described, including a piezoelectric pressure pickup and a transducer for recording pressure in a shock tube.

Each article in the collection is illustrated with graphs, figures, and diagrams; numerical data have been tabulated in many cases. Every article is followed by an extensive list of Soviet and foreign references.

N.B.: Commas should be interpreted as decimal points in all tabular material that has been reproduced directly from the original foreign document.

I. B. Rozhdestvenskiy, N. N. Tsitelauri, N. V.
Voskresenskaya, and Ye. V. Samuylov

Introduction

It is known that at high temperatures the interaction of atoms with a non-saturated electron shell in a number of cases is satisfactorily described by means of the Morse potential function. The second virial coefficient and its first two temperature derivatives for the Morse potential were calculated in [1, 2]. The collision integrals, effective cross sections, and collision angles were calculated for the Morse potential in [3]. The Morse potential parameters were determined for certain nonpolar molecules in [4] and the parameters of this potential were found in [5] for N-N, O-O, and N-O interactions on a potential curve with a minimum. The values of the Morse potential parameters are estimated in this article for interactions of atoms in diatomic molecules of C_2 , CO, and CN. The data provided in [6] and [7] were used to determine the parameters in the case of C_2 and CO, where potential curves are derived for the lower electronic states. Potential curves for the interaction of C and N atoms in the $X^2\Sigma^+$, $A^2\Pi_i$, and $B^2\Sigma^+$ states of a CN molecule are derived in this report.

Determination of Potential Parameters

A critical survey of various semi-empirical potentials from the standpoint of their applicability for describing the interaction of atoms in a diatomic molecule is given in [8]. An analysis of 27 molecules, which was conducted in this work, indicates that the Morse potential function at short distances lies somewhat above the potential curve obtained by means of spectroscopic data on the energy of vibrational and rotational levels with the Rydberg-Klein-Rees method, and that it lies somewhat below this curve and the Rydberg potential at long distances.

The Rydberg-Klein-Rees method makes it possible to determine the potential curve on the basis of experimentally known vibrational and rotational energy levels without resorting to any semi-empirical potential, *e.g.*, the Morse potential. The lower vibrational levels ($v \approx 10.20$) are usually examined most completely by the spectroscopic method. For higher levels, the vibrational energy may be obtained by extrapolation of the series $G(v)$. In this case, the conditions of $G(v_{max}) = D_e$ should be satisfied approximately:

$$\left. \frac{\partial G(v)}{\partial v} \right|_{v=v_{max}} = 0.$$

*Numbers in the margin indicate pagination in the foreign text.

Thus, the potential curve obtained by the Rydberg-Klein-Rees method can be considered in an experimental region as an experimental potential curve, and the parameters of the corresponding semi-empirical potential can be selected for it. 4

The Morse potential has the form

$$U(r) = D_e \left[1 - e^{-\beta \frac{r-r_e}{r_e}} \right]^2 \quad (1)$$

and depends on three parameters: D_e = the dissociation energy read from the minimum of the potential curve, r_e = the equilibrium distance between atoms, and the parameter

$$\beta = \frac{\omega_e}{2(B_e D_e)^{1/2}}, \quad (2)$$

where ω_e = the vibrational constant and B_e = the rotational constant of a diatomic molecule.

If the potential of the interaction of two atoms can be presented in the form of (1) with a sufficient degree of accuracy, the levels of vibrational energy, as it is known, will be expressed by a second-order step function

$$G(v) = \omega_e \left(v + \frac{1}{2} \right) - \omega_e x_e \left(v + \frac{1}{2} \right)^2. \quad (3)$$

The value of v_{max} in this case is found from the relationship

$$v_{max} = \frac{\omega_e}{2\omega_e x_e} - \frac{1}{2}, \quad (4)$$

which corresponds to the value

$$D_e = G(v_{max}) = \frac{\omega_e^2}{4\omega_e x_e}. \quad (5)$$

The use of (3)-(5) for finding v_{max} and D_e is equivalent to the Birge-Sponer graphic linear extrapolation. If the value of B_e is determined along with ω_e and D_e , the quantity β is calculated with formula (2). In many cases of the described segment of series (3), however, it is insufficient for finding the vibrational energy for all v . Series (3) is supplemented with higher order terms and constant anharmonicities are selected which satisfy the known experimental arrangement of the vibrational levels and the value of the dissociation energy.

Another method of determining the constant β in the Morse potential, which does not depend on the number of terms in series (3), is examined in [5] and consists in the following. From (1) we have

$$\beta^- = \frac{r_e \ln \left[1 + \left(\frac{U_v}{D_e} \right)^{1/2} \right]}{r_e - r_v^-}; \quad (6)$$

$$\beta^+ = \frac{r_e \ln \left[1 - \left(\frac{U_v}{D_e} \right)^{1/2} \right]}{r_e - r_v^+}. \quad (7)$$

Here β^- is the value of parameter β for part of the potential curve $r = r_v^- < r_e$ and β^+ is the value of β when $r = r_v^+ > r_e$. The values of r_v^- and r_v^+ correspond to the values of r_{min} and r_{max} determined by the Rydberg-Klein-Rees method. The subscript v to U and r indicates that the values of U and r are taken for $v = 0, 1, 2, \dots$. Thus, if the potential curve or part of it is known (to a certain value of v) (6) and (7) can be used to find the values of parameter β separately on each branch of this potential curve. The value of β is obtained for the entire curve as the average of β^- and β^+

$$\beta = \frac{1}{2} (\beta^- + \beta^+). \quad (8)$$

The value of β can be obtained from (1) in the form of an expression in which r_v^- and r_v^+ enter directly. In calculations, however, expression (8) is more preferable due to the loss of accuracy.

Expressions (6)-(8) are used to find the parameter β on the basis of the known potential curve. It is natural that the values of β in this determination will be dependent on the value of U_v , which is used in (6) and (7). A direct calculation indicates that the optimum mean representation of the potential curve for all v is provided by the values of β obtained for the values of U_v which are approximately half the value of the dissociation energy ($U_v \approx \frac{1}{2} D_e$). In those cases when the potential curve is unknown for values of energy near $\frac{1}{2} D_e$, the upper known value of U_v was used.

It might be suitable in various problems and at various temperatures to use β^- or β^+ as the parameter β . Tables 1-3 also list the quantities β^- and β^+ for this purpose.

The values of r_e for all excited states are calculated to zero accuracy in the calculation of β by means of linear extrapolation of the values of U_v as a

TABLE 1. MORSE POTENTIAL PARAMETERS FOR BOUND C₂ STATES*

Electronic state		Diss. ener.		$r_e, \text{\AA}$	β^-	β^+	β	$\beta,$ Based on [2]
C ₂	C + C	cm ⁻¹	eV					
X ¹ Σ_g^+	3P + 3P	51299,6	6,36	1,2420	2,999	3,091	3,045	3,037
a ³ Π_u	3P + 3P	50537,7	6,27	1,3117	2,828	2,958	2,893	2,856
b ³ Σ_g^-	3P + 3P	44846,8	5,56	1,3690	2,840	2,840	2,840	2,836
A ¹ Π_u	3P + 3P	42911,0	5,32	1,3179	3,012	3,162	3,087	3,055
d ³ Π_g	3P + 3P	31296,0	3,88	1,2644	3,594	3,900	3,747	3,818
D ¹ Π_g	3P + 3P	17019,2	2,11	1,2527	4,706	4,776	4,741	5,192
e ³ Π_g	3P + 1D	20648,9	2,56	1,5341	3,438	3,120	3,279	3,526
E ¹ Σ_u^+	1D + 1S	39845,9	4,94	1,2377	3,325	3,507	3,416	3,385
F ¹ Σ_g^+	1D + 1D	16615,9	2,06	—	4,684	5,073	4,879	4,842
	1D + 1S	28069,6	3,46	1,2520	3,802	3,269	3,536	3,725
	1S + 1S	39523,3	4,90	—	3,302	2,560	2,931	3,140

*The classification of electronic states of a C₂ molecule is taken from [9].

TABLE 2. MORSE POTENTIAL PARAMETERS FOR BOUND CO STATES

Electronic state		Diss. ener.		$r_e, \text{\AA}$	β^-	β^+	β	$\beta,$ Based on [2]
CO	C + O	cm ⁻¹	eV					
X ¹ Σ^+	3P + 3P	90676,7	11,24	1,1287	2,615	2,575	2,595	2,593
a ³ Π	3P + 3P	41989,1	5,206	1,2060	3,238	3,400	3,319	3,281
a ¹³ Σ^+	3P + 3P	34853,6	4,321	1,3549	2,899	3,031	2,965	2,842
d ³ Δ	3P + 3P	28376,3	3,518	1,3771	2,945	3,173	3,059	3,007
A ¹ Π	3P + 3P	25602,0	3,174	1,2344	3,506	5,172	4,339	3,673
e ³ Σ^-	3P + 3P	25336,6	3,141	1,3946	3,032	3,474	3,253	3,054
B ¹ Σ^+	—	29698,6	3,682	1,1199	4,193	4,665	4,429	4,477

function of $(r_v^- + r_v^+)/2$. This method of determining the values of r_e in the case of C₂, CO, and CN is sufficiently accurate since the anharmonicity near the potential minimum is small and the values of zero energy are not large. The dissociation energy in each case was selected independently of that available in the presence of the potential curve on the basis of the most reliable reference data. The values of β obtained by means of (2) are given in Tables 1-3 for a comparison.

TABLE 3. MORSE POTENTIAL PARAMETERS FOR BOUND CN STATES

Electronic state		Diss. ener.		r_e Å	β^-	β^+	β	β , Based on [2]
CN	C + N	cm^{-1}	eV					
$X^2\Sigma^+$	$3P + 4S$	69430,7	8,61	1,1719	2,768	3,129	2,948	2,849
$A^2\Pi_i$	$3P + 4S$	60184,6	7,46	1,2319	2,805	2,931	2,868	2,819
$B^2\Sigma^+$	$3P + 2D$	62901,5	7,18	1,1459	2,873	2,995	2,934	3,062

Interaction of C-C Atoms

Energy potential curves for the nine lower electronic states of a C_2 molecule for the $v'' \leftrightarrow v'$ transitions observed experimentally were determined in [6] by the Rydberg-Klein-Rees method.

TABLE 4. VALUES OF v FOR VARIOUS ELECTRONIC STATES

C_2		CO		CN	
State	v	State	v	State	v
$X^1\Sigma^+$	2	$X^1\Sigma^+$	23	$X^2\Sigma^+$	30
$a^3\Pi_u$	11	$a^3\Pi_r$	5	$A^2\Pi_i$	32
$b^3\Sigma_g^-$	3	$a^3\Sigma$	23	$B^2\Sigma^+$	30
$A^1\Pi_u$	5	$d^3\Delta$	20		
$d^3\Pi_g$	10	$A^1\Pi$	18		
$D^1\Pi_g$	6	$e^3\Sigma^-$	17		
$e^3\Pi_g$	4	$B^1\Sigma^+$	2		
$E^1\Sigma_u^+$	2				
$F^1\Sigma_g^+$	5				

The dissociation energy of C_2 was not precisely determined. Linear extrapolation of vibrational levels in the $1^1\Sigma_g^+$ state leads to the value of $D_0 = 7$ eV.

Extrapolation of the $d^3\Pi_g$ -state levels leads to the value of $D_0 = 5.3$ eV [9].

The value of $D_0 = 6.25$ eV [1] was adopted for C_2 in [9], which agrees well with the value of $D_e = 6.36$ eV used in [6]. The val-

ues of v for which the values of β^- , β^+ , and β were determined for various electronic states of C_2 are given in Table 4.

Interaction of C-O Atoms

Energy potential curves for the electronic states of a CO molecule were obtained in [7] by the Rydberg-Klein-Rees method for experimentally observed distributions of vibrational and rotational levels.

The calculation in [7] indicates that the six lower electronic states of the CO molecule converge at one dissociation limit (11.11 eV).

The $B^1\Sigma^+$ state dissociates into excited atoms. For this state, however, vibrational levels were not observed above $v = 2$. This does not make it possible to establish the dissociation products of CO in the $B^1\Sigma^+$ state. The vibrational levels for the $A^1\Pi$ state, as the calculations in [7] indicate, converge much more rapidly than this takes place for the other states. This makes it possible to assume that the potential curve of this state has a maximum. The values of v for which the values of β were determined for CO are given in Table 4.

Interaction of C-N Atoms

Of the possible electronic states of the CN molecule, the following three states have been examined most completely: $X^2\Sigma^+$, $A^2\Pi_z$, and $B^2\Sigma^+$. The maximum number of vibrational levels observed in these states is equal to 18, 19, and 19, respectively [10].

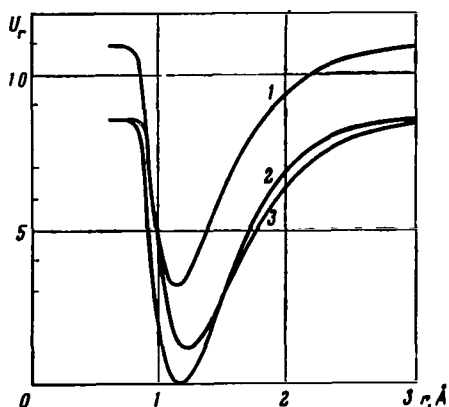


Figure 1. Dependence of Potential Energy U_r on Distance Between Atoms r for CN. (1) $B^2\Sigma^+$ state; (2) $X^2\Sigma^+$ state; (3) $A^2\Pi_z$ state.

The dissociation energy of a CN molecule has not been determined precisely. Two alternative values exist for D_0 CN, i.e., 7.50 eV and 8.48 eV. The first value, which was proposed by Gaydon, is being subjected to mass-spectrometric investigations of the equilibrium of carbon and nitrogen vapors at a temperature of 2200-2500°K [11]. The second value is based on the extrapolation of the vibrational levels X , A , and B of the CN states [10]. It is substantiated by the electron shock method and by experimentation in shock tubes. The value of $D_0 = 8.41$ eV was adopted in reference [9]. The potential curves for the $X^2\Sigma^+$, $A^2\Pi_z$, $B^2\Sigma^+$ states of CN were determined in this paper by the Rydberg-Klein-Rees method, following the procedure that was refined by Samuylov and Voskresenskiy (taking into account the term $\beta_e[(v + \frac{1}{2})^2 I(I + 1)]$

[12]. Tables 5-7 present potential data for the three states of a CN molecule obtained by this method (see appendix). The following values of the spectroscopic constants were used for these states (Table 8).

The constants $\omega_e z_e$ for the $X^2\Sigma^+$ and $A^2\Pi_z$ states and $\omega_e y_e$ for the $B^2\Sigma^+$ state were selected from the conditions of the convergence of levels at the dissociation limit when $v = v_{max}$; v_{max} was equal to 60, 63, and 60, respectively, for the indicated states. The remaining constants were taken from [9] and [10].

The $A^2\Pi_z$ state for CN dissociates into atoms in the ground states $C^3P + N^4S$.

TABLE 5. POTENTIAL ENERGY OF $X^2\Sigma^+$ STATE FOR CN

v	U_e, cm^{-1}	$r_{\min}, \text{\AA}$	$r_{\max}, \text{\AA}$	$U_e \text{eV}$
0	1031,0	1,1242	1,2249	0,1278
1	3073,3	1,0926	1,2680	0,3810
2	5089,4	1,0724	1,3000	0,6310
3	7079,0	1,0567	1,3274	0,8776
4	9042,2	1,0437	1,3524	1,121
5	10978	1,0326	1,3758	1,361
6	12888	1,0228	1,3980	1,598
7	14771	1,0139	1,4194	1,831
8	16628	1,0060	1,4402	2,061
9	18457	0,99868	1,4605	2,288
10	20259	0,99193	1,4804	2,512
11	22033	0,98566	1,5001	2,732
12	23781	0,97990	1,5196	2,948
13	25500	0,97431	1,5390	3,161
14	27191	0,96915	1,5582	3,371
15	28835	0,96427	1,5775	3,575
16	30490	0,95964	1,5967	3,780
17	32097	0,95525	1,6160	3,979
18	33675	0,95106	1,6353	4,175
19	35224	0,94706	1,6548	4,367
20	36743	0,94322	1,6744	4,555
21	38234	0,93955	1,6942	4,740
22	39694	0,93600	1,7141	4,921
23	41125	0,93259	1,7343	5,098
24	42525	0,92929	1,7548	5,272
25	43895	0,92608	1,7755	5,442
26	45234	0,92297	1,7966	5,608
27	46541	0,91993	1,8180	5,770
28	47817	0,91697	1,8398	5,928
29	49062	0,91406	1,8621	6,082
30	50273	0,91120	1,8848	6,233
31	51453	0,90837	1,9080	6,379
32	52599	0,90557	1,9318	6,521
33	53712	0,90279	1,9562	6,659
34	54791	0,90000	1,9813	6,793
35	55836	0,89721	2,0071	6,922
36	56847	0,89440	2,0337	7,048
37	57823	0,89155	2,0612	7,169
38	58763	0,88866	2,0897	7,285
39	59668	0,88569	2,1192	7,397
40	60536	0,88264	2,1499	7,505
41	61367	0,87948	2,1820	7,608
42	62162	0,87619	2,2155	7,707
43	62919	0,87275	2,2506	7,800
44	63637	0,86911	2,2877	7,890
45	64317	0,86525	2,3268	7,974
46	64958	0,86113	2,3683	8,053
47	65559	0,85668	2,4126	8,128
48	66119	0,85186	2,4601	8,197

TABLE 5. (Continued)

v	U_v, cm^{-1}	$r_{\min}, \text{\AA}$	$r_{\max}, \text{\AA}$	$U_v \text{eV}$
49	66639	0,84658	2,5114	8,262
50	67118	0,84074	2,5672	8,321
51	67555	0,83422	2,6285	8,375
52	67950	0,82685	2,6966	8,424
53	68301	0,81842	2,7732	8,468
54	68609	0,80859	2,8610	8,506
55	68872	0,79690	2,9639	8,538
56	69091	0,78258	3,0885	8,566
57	69265	0,76432	3,2467	8,587
58	69392	0,73941	3,4637	8,603
59	69473	0,70069	3,8112	8,613
60	69506	0,60898	4,7377	8,617

TABLE 6. POTENTIAL ENERGY OF $A^2\Pi_z$ STATE FOR CN

v	U_v, cm^{-1}	$r_{\min}, \text{\AA}$	$r_{\max}, \text{\AA}$	$U_v \text{eV}$
0	983,00	1,1819	1,2893	0,1219
1	2690,1	1,1484	1,3358	0,3335
2	4451,9	1,1270	1,3704	0,5519
3	6188,3	1,1106	1,4004	0,7672
4	7899,3	1,0970	1,4276	0,9793
5	9584,8	1,0854	1,4532	1,188
6	11244	1,0751	1,4775	1,394
7	12879	1,0660	1,5010	1,597
8	14487	1,0577	1,5239	1,796
9	16070	1,0501	1,5463	1,992
10	17626	1,0432	1,5693	2,185
11	19157	1,0367	1,5901	2,375
12	20661	1,0307	1,6118	2,561
13	22140	1,0251	1,6333	2,745
14	23592	1,0199	1,6548	2,925
15	25017	1,0149	1,6762	3,102
16	26416	1,0102	1,6978	3,275
17	27789	1,0058	1,7193	3,445
18	29135	1,0016	1,7410	3,612
19	30454	0,99763	1,7629	3,776
20	31746	0,99381	1,7849	3,936
21	33011	0,99017	1,8072	4,093
22	34249	0,98968	1,8297	4,246
23	35460	0,98334	1,8525	4,396
24	36643	0,98012	1,8756	4,543
25	37799	0,97703	1,8990	4,686
26	38928	0,97405	1,9229	4,826
27	40029	0,97117	1,9471	4,963
28	41101	0,96938	1,9718	5,096

TABLE 6. (Continued)

v	U_v, cm^{-1}	$r_{\min}, \text{\AA}$	$r_{\max}, \text{\AA}$	$U_v \text{eV}$
29	42147	0,96567	1,9969	5,225
30	43163	0,96304	2,0227	5,351
31	44152	0,96046	2,0489	5,474
32	45113	0,95795	2,0758	5,593
33	46045	0,95548	2,1034	5,708
34	46949	0,95305	2,1317	5,821
35	47824	0,95065	2,1607	5,929
36	48670	0,94827	2,1906	6,034
37	49487	0,94590	2,2215	6,135
38	50275	0,94353	2,2533	6,233
39	51034	0,94114	2,2863	6,327
40	51763	0,93873	2,3204	6,417
41	52464	0,93629	2,3559	6,504
42	53134	0,93379	2,3928	6,587
43	53775	0,93121	2,4313	6,667
44	54395	0,92855	2,4715	6,744
45	54966	0,92578	2,5137	6,814
46	55517	0,92286	2,5581	6,883
47	56037	0,91979	2,6050	6,947
48	56527	0,91650	2,6547	7,008
49	56985	0,91298	2,7076	7,065
50	57414	0,90916	2,7641	7,118
51	57811	0,90499	2,8250	7,167
52	58177	0,90038	2,8909	7,213
53	58512	0,89523	2,9628	7,254
54	58815	0,88943	3,0421	7,292
55	59087	0,88279	3,1305	7,325
56	59327	0,87507	3,2305	7,355
57	59534	0,86592	3,3458	7,381
58	59710	0,85481	3,4821	7,403
59	59854	0,84085	3,6492	7,420
60	59965	0,82242	3,8655	7,434
61	60044	0,79591	4,1737	7,444
62	60089	0,74997	4,7163	7,450
63	60102	0,60757	6,6576	7,451

TABLE 7. POTENTIAL ENERGY OF $B^2\Sigma^+$ STATE FOR CN

v	U_v, cm^{-1}	$r_{\min}, \text{\AA}$	$r_{\max}, \text{\AA}$	$U_v \text{eV}$
0	1076,9	1,1000	1,1986	0,1335
1	3209,4	1,0699	1,2419	0,3979
2	5283,9	1,0507	1,2746	0,6551
3	7327,3	1,0359	1,3030	0,9084
4	9330,9	1,0238	1,3291	1,157
5	11294	1,0133	1,3537	1,400

TABLE 7. (Continued)

ν	U_θ, cm^{-1}	$r_{\min}, \text{\AA}$	$r_{\max}, \text{\AA}$	U, eV
6	13219	1,0041	1,3773	1,639
7	15104	0,99596	1,4002	1,872
8	16950	0,98348	1,4226	2,101
9	18756	0,98163	1,4446	2,325
10	20524	0,97529	1,4655	2,544
11	22254	0,96939	1,4881	2,759
12	23944	0,96387	1,5097	2,968
13	25996	0,95867	1,5312	3,223
14	27210	0,95376	1,5529	3,373
15	28786	0,94909	1,5745	3,569
16	30324	0,94465	1,5964	3,759
17	31825	0,94040	1,6184	3,946
18	33288	0,93633	1,6406	4,127
19	34712	0,93242	1,6630	4,304
20	36100	0,92864	1,6857	4,476
21	37451	0,92499	1,7087	4,643
22	38765	0,92144	1,7321	4,806
23	40042	0,91799	1,7559	4,964
24	41283	0,91463	1,7801	5,118
25	42487	0,91134	1,8047	5,267
26	43654	0,90811	1,8298	5,412
27	44786	0,90494	1,8553	5,552
28	45881	0,90181	1,8818	5,688
29	46941	0,89871	1,9086	5,820
30	47965	0,89563	1,9362	5,947
31	48953	0,89257	1,9645	6,069
32	49907	0,88951	1,9936	6,187
33	50824	0,88644	2,0235	6,301
34	51707	0,88336	2,0544	6,410
35	52555	0,88023	2,0963	6,516
36	53369	0,87707	2,1193	6,617
37	54148	0,87385	2,1535	6,713
38	54892	0,87055	2,1890	6,805
39	55602	0,86717	2,2259	6,893
40	56278	0,86369	2,2644	6,977
41	56920	0,86007	2,3046	7,056
42	57529	0,85631	2,3468	7,132
43	58103	0,85238	2,3912	7,203
44	58645	0,84824	2,4379	7,271
45	59153	0,84386	2,4874	7,334
46	59628	0,83919	2,5400	7,392
47	60070	0,83420	2,5962	7,447
48	60479	0,82881	2,6564	7,498
49	60856	0,82296	2,7215	7,545
50	61200	0,81955	2,7923	7,587
51	61512	0,80946	2,8700	7,626
52	61792	0,80153	2,9562	7,661
53	62039	0,79255	3,0530	7,691
54	62255	0,78222	3,1636	7,718
55	62439	0,77009	3,2926	7,741

TABLE 7. (Continued)

v	U_v , cm $^{-1}$	r_{min} , Å	r_{max} , Å	U_e eV
56	62592	0,75546	3,4479	7,760
57	62713	0,73712	3,6432	7,775
58	62804	0,71266	3,9072	7,786
59	62863	0,67598	4,3175	7,794
60	62891	0,59743	5,2973	7,797

TABLE 8. VALUES OF SPECTROSCOPIC CONSTANTS

cm $^{-1}$	$X^2\Sigma^+$	$A^2\Pi_i$	$B^2\Sigma^+$
T_e	0	9246,04	25752,0
ω_e	2068,616	1812,316	2163,9
$\omega_e x_e$	13,111	12,588	20,2
$\omega_e y_e$	$-0,910 \cdot 10^{-2}$	$-0,120 \cdot 10^{-1}$	$0,267 \cdot 10^{-1}$
$\omega_e z_e$	$-0,421 \cdot 10^{-3}$	$-0,707 \cdot 10^{-4}$	—
B_e	1,8989	1,7166	1,985
α_e	$0,1717 \cdot 10^{-1}$	$0,1716 \cdot 10^{-1}$	$0,23 \cdot 10^{-1}$
β_e	$-0,473 \cdot 10^{-4}$	$-0,414 \cdot 10^{-4}$	—

The $B^2\Sigma^+$ state dissociates into excited atoms, whereas the following states of the dissociation products are possible (Table 9).

TABLE 9

C + N	Excitation Energy [9]	
	cm $^{-1}$	eV
$1D \rightarrow 4S$	40193,7	1,26
$1S \rightarrow 4S$	21648,4	2,7
$3P \rightarrow 2D$	19223	2,5

If the upper value of the dissociation energy of CN is adopted, the C and N atoms will be situated in the states with an excitation energy of 2.5 and 2.7 eV, which agrees well with the value of the excitation energy obtained by means of calculation in [13]. The values of r_e

for CN are found also by extrapolation of the values of U_v to zero. The values of v for which the Morse potential parameter β was calculated are shown in Table 4.

The potential curves of the $X^2\Sigma^+$, $A^2\Pi_i$, and $B^2\Sigma^+$ states for CN are given in Figure 1.

REFERENCES

/13

1. Samuylov, Ye. V. and I. B. Rozhdestvenskiy: The second virial coefficient for the Morse potential. In: *Fizicheskaya gazodinamika, teploobmen i*

termodinamika gazov vysokikh temperatur. (Physical Gas Dynamics, Heat Exchange, and Thermodynamics of High-Temperature Gases.) Izd-vo AN SSSR, 1962.

2. Konowalow, D. D., M. H. Taylor, and J. O. Hirschfelder: Second virial coefficient for the Morse potential. *Phys. Fluids*, Vol. 4, No. 5, 1961.
3. Samuylov, Ye. V. and N. N. Tsitelauri: Collision integrals, effective cross sections, and deflection angles for the Morse potential. In this collection, p. 13.
4. Konowalow, D. D. and J. O. Hirschfelder: Intermolecular potential functions for nonpolar molecules. *Phys. Fluids*, Vol. 4, No. 5, 1961.
5. Konowalow, D. D. and J. O. Hirschfelder: Morse potential parameters for O-O, N-N and N-O interactions. *Phys. Fluids*, Vol. 4, No. 5, 1961.
6. Reed, Sh. M. and J. T. Vanderslice: Potential energy curves for C₂. *J. Chem. Phys.*, Vol. 36, No. 9, 1962.
7. Tobias, J., R. J. Fallon and J. T. Vanderslice: Potential energy curves for CO. *J. Chem. Phys.*, Vol. 33, No. 6, 1960.
8. Varshni, Y. P.: Comparative study of potential energy functions for diatomic molecules. *Rev. Mod. Phys.*, Vol. 29, No. 4, 1957.
9. Gurvich, L. V., G. A. Khachkuruzov et al.: *Termodinamicheskiye svoystva individual'nykh veshchestv. (Thermodynamic Properties of Individual Substances.)* Vol. 1. Izd-vo AN SSSR, 1962.
10. Douglas, A. E. and P. M. Routly: The spectrum of the CN molecule. *Astrophys. J.*, Vol. 1, No. 9, Suppl., 1955.
11. Berkowitz, J.: Heat of formation of CN radical. *J. Chem. Phys.*, Vol. 36, No. 9, 1962.
12. Samuylov, Ye. V. and N. V. Voskresenskaya: Attractive interaction potentials between Li-Li atoms in ground states. In this collection.
13. Lippincott, E. R., D. Steele and P. Caldwell: General relation between potential energy and intermolecular distance for diatomic molecules. III. Excited states. *J. Chem. Phys.*, Vol. 35, No. 1, 1961.

COLLISION INTEGRALS, EFFECTIVE CROSS SECTIONS, AND ANGLES OF DEVIATION FOR THE MORSE POTENTIAL

Ye. V. Samuylov and N. N. Tsitelauri

It is known (see, for example, [1]) that in the calculation of the transport coefficients of gases (viscosity and thermal conductivity) information is required concerning the mean effective cross sections for the various interactions between the gas molecules, atoms, or ions. The mean effective cross sections of certain gases in a temperature range from 1,000–1,500°K have presently been obtained both experimentally and by calculation. At higher temperatures, the mean effective cross sections have not yet been investigated in sufficient detail experimentally or theoretically. Since molecules dissociate into atoms at high temperatures, of particular interest is the study of the mean effective cross sections of the interactions of atoms. We know that atoms with unsaturated electron shells can interact with various types of potential curves, depending on the mutual orientation of the orbital and spin moments of the electrons of the outer shell. /14

The total mean effective cross section can be calculated on the basis of known mean effective cross sections for each interaction curve [2]. Repulsive potential curves are satisfactorily described in many cases with the aid of a simple exponential function, the mean effective cross sections for which have been tabulated in dimensionless variables in [3]. Attractive potential curves are well described by the known Morse potential. In connection with this, the calculation of the mean effective cross sections for this potential is of interest. The mean effective cross sections in the expression for the viscosity, thermal conductivity, and diffusion coefficients of dissociating gases are expressed by collision integrals. The authors of [4] have briefly described the procedure for calculating the collision integrals for a corrected Morse potential. The same paper also presents the results of calculations of collision integrals for $\beta = 2, 2.5, 3, 3.5, 4, 4.5$, and 5. This paper gives the results of calculations of collision integrals for the Morse potential for $\beta = 1.5$ and also presents the results of calculations of the angles of deviation and the effective cross sections for the Morse potential which were not included in [4]. Some basic information is also given concerning the Morse potential and tabulated quantities.

The Morse Potential

The Morse potential, in which the energy of two atoms separated by an infinite distance is adopted as the zero energy, has the form

$$U(r) = D_e(e^{-2\beta r} - 2e^{-\beta r}), \quad (1)$$

where D_e is the dissociation energy of the electronic state of a diatomic mole- /15

cule being considered and is read off from the minimum of the energy potential curve:

$$\beta = \frac{\omega_e}{2(B_e D_e)^{1/2}} \quad (2)$$

(here ω_e and B_e are vibrational and rotational constants which are frequently determined on the basis of spectral laws);

$$\xi = \frac{r - r_e}{r_e} \quad (3)$$

In this relationship, r is the distance between the atomic nuclei and r_e is the equilibrium value of the internuclear distance in a diatomic molecule for the considered electronic state of the diatomic molecule. The function $U(r)$ will be used in dimensionless form

$$\Phi(r^*) = [e^{-2\beta(r^*-1)} - 2e^{-\beta(r^*-1)}], \quad (4)$$

where $\Phi(r^*) = U(r^*)/D_e$ and $r^* = r/r_e$. We shall designate the dimensionless relative kinetic energy of the two atoms when $r^* \rightarrow \infty$ by K

$$K = \frac{\mu g^2}{2D_e}, \quad (5)$$

where μ is the reduced mass and g is the relative velocity of the two atoms when $r^* \rightarrow \infty$. In the range of r^* values close to zero, function (4) does not satisfactorily describe the interaction between the atoms, since the approach of the atoms to $r^* = 0$ is possible at sufficiently large values of K which exceed the value of $\Phi(0)$, which is impossible under actual conditions. Therefore, the collision integrals $\Omega^{(L,g)*}$, the effective cross sections $Q^{(L)*}$, and the angles of deviation χ were tabulated for the corrected Morse potential, which differs from potential (4) by the fact that when $r^* < r_g^*$ the value of Φ is assumed to be equal to infinity. The quantity r_g^* is determined by the relationship

$$r_g^* = \alpha(1 - \ln 2/\beta), \quad (6)$$

where $\alpha < 1$, and $\Phi(1 - \ln 2/\beta) = 0$. It was assumed that $\alpha = 0.3$ in the calculations.

In addition to the dimensionless quantities Φ , r^* , K , which were determined above, we shall use the dimensionless impact parameter $b^* = b/r_e$ below, in which b is the impact parameter, and the dimensionless temperatures $T^* = kT/D_e$, where

T is the temperature in °K and k is the Boltzmann constant.

Collision Integrals, Effective Cross Sections, and Angles of Deviation

The following dimensionless quantities were tabulated: $\Omega^{(l,s)\star}(T^*, \beta) =$ collision integrals; $Q^{(l)\star}(K, \beta) =$ effective cross sections; $\chi(K, q, \beta) =$ angles of deviation in radians, where $1 \leq l \leq 3$ and $3 \geq s \geq l$;

$$\Omega^{(l,s)\star} = 2 [(s+1)!]^{-1} \int_0^\infty e^{-\gamma^2} \gamma^{2s+3} Q^{(l)\star} d\gamma; \quad (7)$$

$$Q^{(l)\star} = 2 \left[1 - \frac{1}{2} \frac{1 + (-1)^l}{1+l} \right]^{-1} \int_0^\infty (1 - \cos^l \chi) b^* db^*; \quad (8)$$

$$\chi(K, b^*, \beta) = \pi - 2b^* \int_{r_0^*}^\infty \frac{dr^*}{r^{*2}} \left\{ 1 - \left(\frac{b^*}{r^*} \right)^2 - \frac{\Phi}{K} \right\}^{-1/2}; \quad (9)$$

$r_0^* = r_0/r_e$; r_0 is the distance of closest approach of atoms in a collision. /16
The quantity b^* is related to the variable q in the following manner:

$$b^* = \left\{ \frac{r_0^{*2}}{K} [K - (e^{-2\beta}(r_0^{*-1}) - 2e^{-\beta}(r_0^{*-1}))] \right\}^{1/2}, \quad (10)$$

where

$$r_0^* = \frac{r_{00}}{q}, \quad (11)$$

r_{00}^* is the dimensionless distance of closest approach of atoms when $b^* = 0$ and is equal to

$$r_{00}^* = 1 - \frac{1}{\beta} \ln(1 + \sqrt{K+1}). \quad (12)$$

It is obvious that $b^* \rightarrow \infty$ when $q \rightarrow 0$ and $b^* \rightarrow 0$ when $q \rightarrow 1$.

The variable γ is related to K and T^* in the following manner:

$$\gamma^2 = \frac{K}{T^*}. \quad (13)$$

A transition was made from variable b^* to variable q when the effective cross sections were calculated. The value of r_0^* for each χ can be found with respect to q and on the basis of relationships (11) and (12). The distance of closest approach when $r_0^* \geq r_\sigma^*$ is determined as the maximum positive root of the equation

$$K = \Psi, \quad (14)$$

where

$$\Psi = \Phi + Kb^{*2}/r^{*2}. \quad (15)$$

For each K , depending on the values of b^* , the function Ψ can be either monotonically diminishing or may have a hump when $r_\sigma^* \leq r^* \leq \infty$. The region of monotonic variation of the function on the plane (Ψ, r^*) is separated from the region of nonmonotonic variation of Ψ by a curve which has a point of inflection. The value of b^* for this curve is designated by b_{inf}^* . The value of Ψ at the point of inflection is designated by Ψ_{inf} . If $\Psi_{inf} > K$, equation (14) can have three positive roots. If $\Psi_{inf} < K$, equation (14) has one positive root. The value of K , above which equation (14) always has only one positive root, is designated by K_{rt} . It is obvious that among the entire family of curves having a point of inflection, there is only one curve and only one point on this curve for which $\Psi_{inf} = K_{rt}$. The values of r_0^* and b_{inf}^* for this point are designated by r_{rt}^* and b_{rt}^* . The quantities K_{rt} , b_{rt}^* , and r_{rt}^* can be found from the system of equations

$$\Psi' = 0; \quad \Psi'' = 0; \quad K_{rt} = \Psi, \quad (16)$$

where Ψ' and Ψ'' are the first and second derivatives of Ψ with respect to r^* .

When $K < K_{rt}$, equation (14) has one positive root, if $\Psi_h < K$ (Ψ_h is the height of the hump in the curve for Ψ); it has two roots, if $\Psi_h = K$; it has three roots, if $\Psi_h > K$. The maximum root of equation (14) in the second case is designated by r_{1m}^* , and the second root by r_{2m}^* . There are two roots for the given K for a single value of b^* , which we will designate by b_m^* . The quantities b_m^* and r_{1m}^* are the solution to the system of equations

$$\Psi' = 0; \quad K = \Psi. \quad (17)$$

When the value of the corrected impact parameter is equal to b_m^* , the angle /24 of deviation is $\chi = -\infty$. The r_{1m}^* quantities can be obtained from the values of

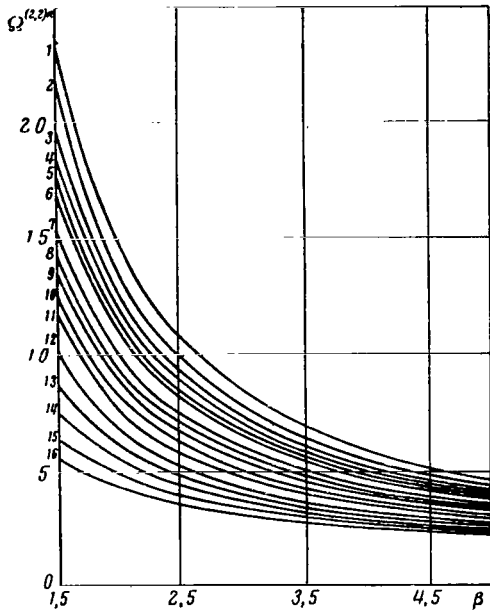


Figure 1. $\Omega^{(2,2)\star}$ as a Function of β . (1) $T^* = 0.010$; (2) 0.014; (3) 0.018; (4) 0.022; (5) 0.026; (6) 0.03; (7) 0.04; (8) 0.05; (9) 0.06; (10) 0.08; (11) 0.1; (12) 0.14; (13) 0.18; (14) 0.22; (15) 0.26; (16) 0.3.

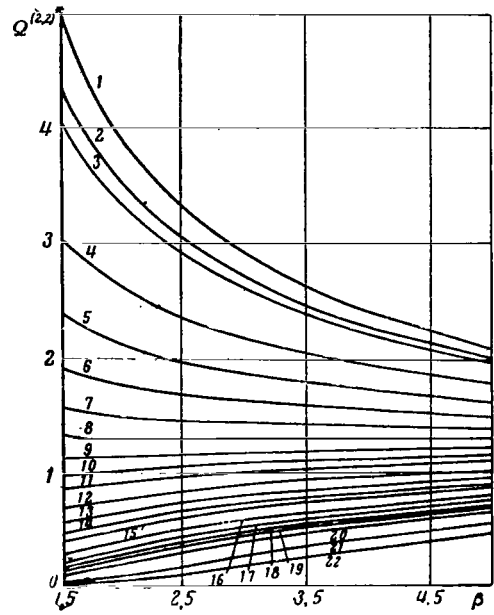


Figure 2. $\Omega^{(2,2)\star}$ as a Function of β . (1) $T^* = 0.34$; (2) 0.38; (3) 0.4; (4) 0.5; (5) 0.6; (6) 0.7; (7) 0.8; (8) 0.9; (9) 1.0; (10) 1.1; (11) 1.2; (12) 1.4; (13) 1.6; (14) 1.8; (15) 2.0; (16) 2.5; (17) 3.0; (18) 3.5; (19) 4; (20) 5; (21) 10; (22) 20.

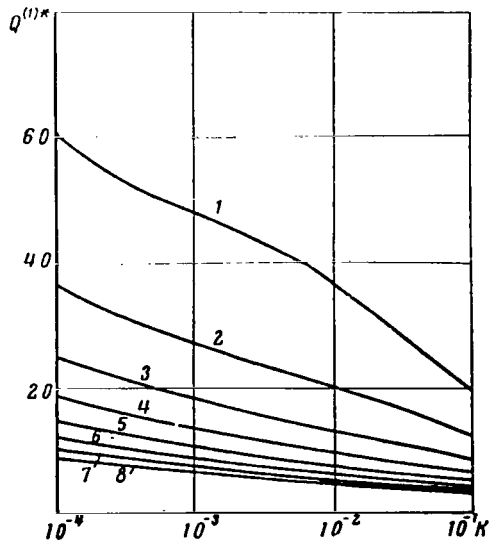


Figure 3. $Q^{(1)\star}$ as a Function of K . (1) $\beta = 1.5$; (2) 2.0; (3) 2.5; (4) 3.0; (5) 3.5; (6) 4.0; (7) 4.5; (8) 5.0.

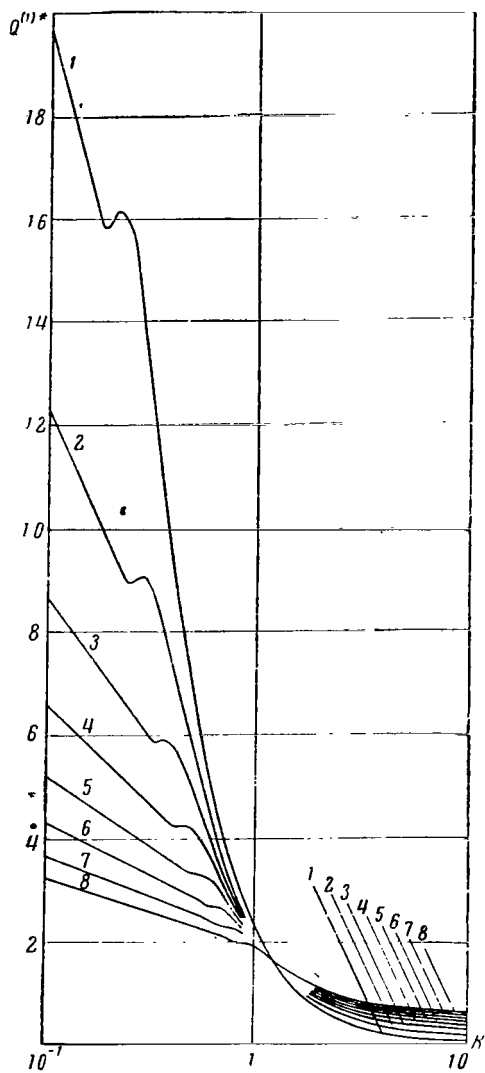


Figure 4. $Q^{(1)*}$ as a Function of K . (1) $\beta = 1.5$; (2) 2.0; (3) 2.5; (4) 3.0; (5) 3.5; (6) 4.0; (7) 4.5; (8) 5.0.

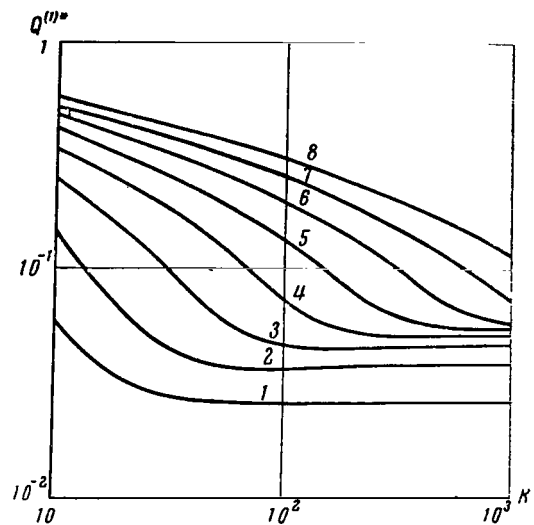


Figure 5. $Q^{(1)*}$ as a Function of K . (1) $\beta = 1.5$; (2) 2.0; (3) 2.5; (4) 3.0; (5) 3.5; (6) 4.0; (7) 4.5; (8) 5.0.

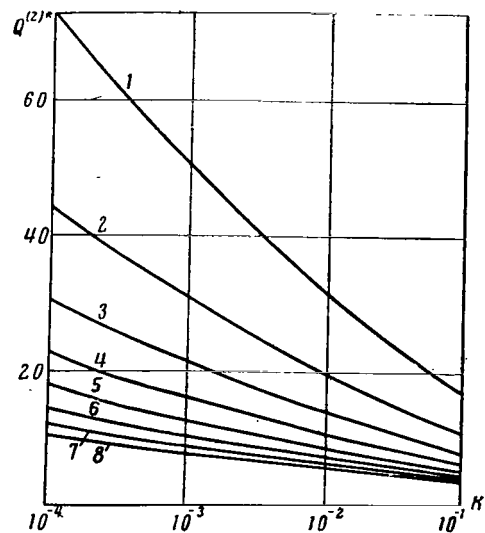


Figure 6. $Q^{(2)*}$ as a Function of K . (1) $\beta = 1.5$; (2) 2.0; (3) 2.5; (4) 3.0; (5) 3.5; (6) 4.0; (7) 4.5; (8) 5.0.

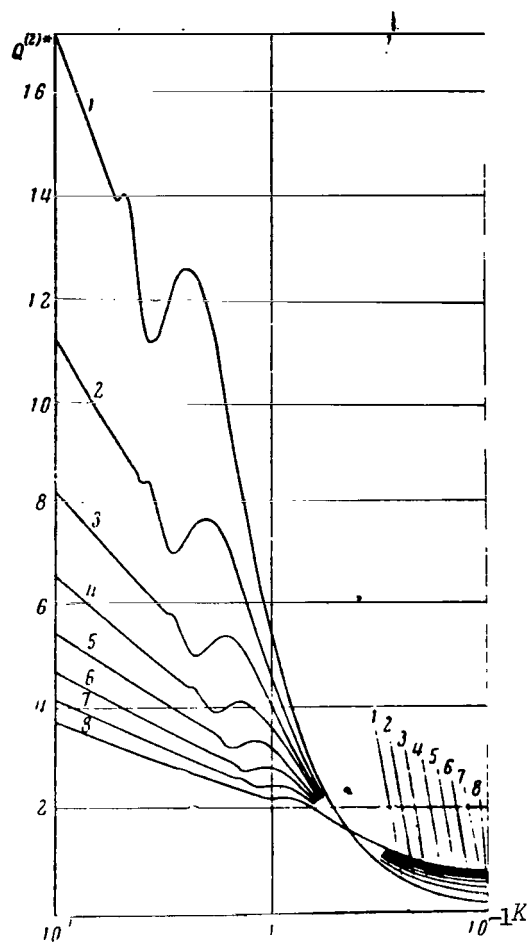


Figure 7. $Q^{(2)*}$ as a Function of K . (1) $\beta = 1.5$; (2) 2.0; (3) 2.5; (4) 3.0; (5) 3.5; (6) 4.0; (7) 4.5; (8) 5.0.

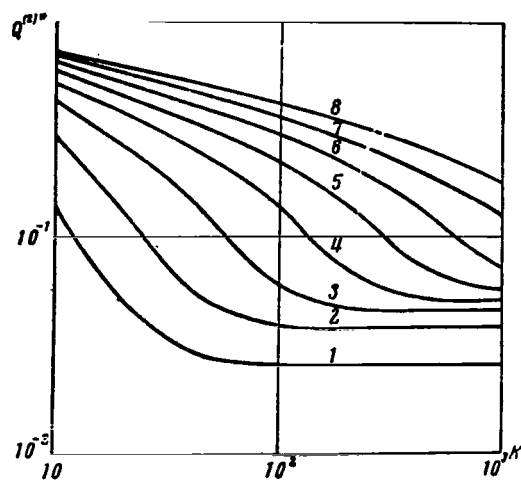


Figure 8. $Q^{(2)*}$ as a Function of K . (1) $\beta = 1.5$; (2) 2.0; (3) 2.5; (4) 3.0; (5) 3.5; (6) 4.0; (7) 4.5; (8) 5.0.

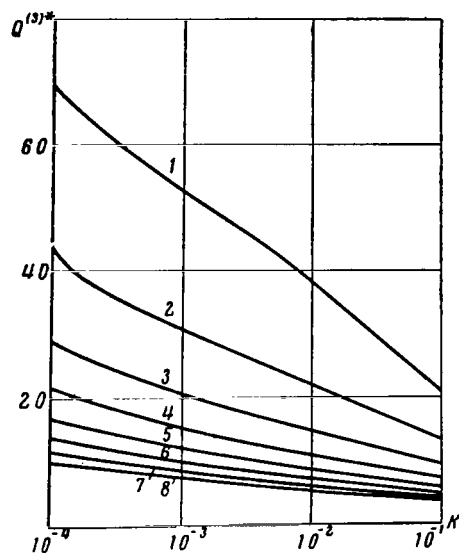


Figure 9. $Q^{(3)*}$ as a Function of K . (1) $\beta = 1.5$; (2) 2.0; (3) 2.5; (4) 3.0; (5) 3.5; (6) 4.0; (7) 4.5; (8) 5.0.

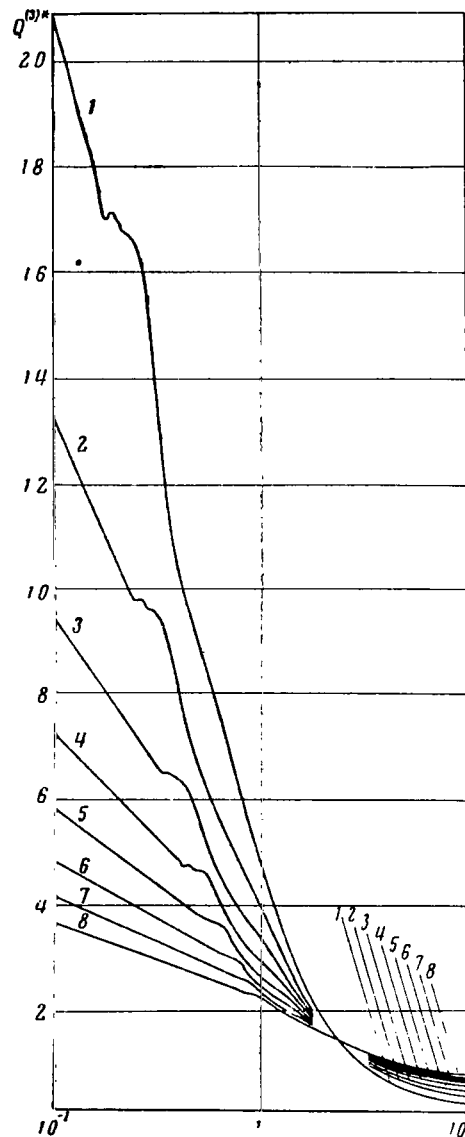


Figure 10. $Q(3)^*$ as a Function of K . (1) $\beta = 1.5$; (2) 2.0; (3) 2.5; (4) 3.0; (5) 3.5; (6) 4.0; (7) 4.5; (8) 5.0.

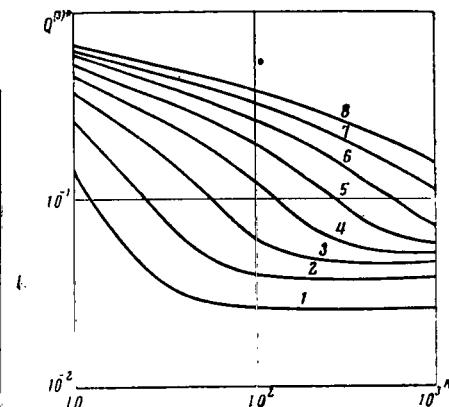


Figure 11. $Q(3)^*$ as a Function of K . (1) $\beta = 1.5$; (2) 2.0; (3) 2.5; (4) 3.0; (5) 3.5; (6) 4.0; (7) 4.5; (8) 5.0.

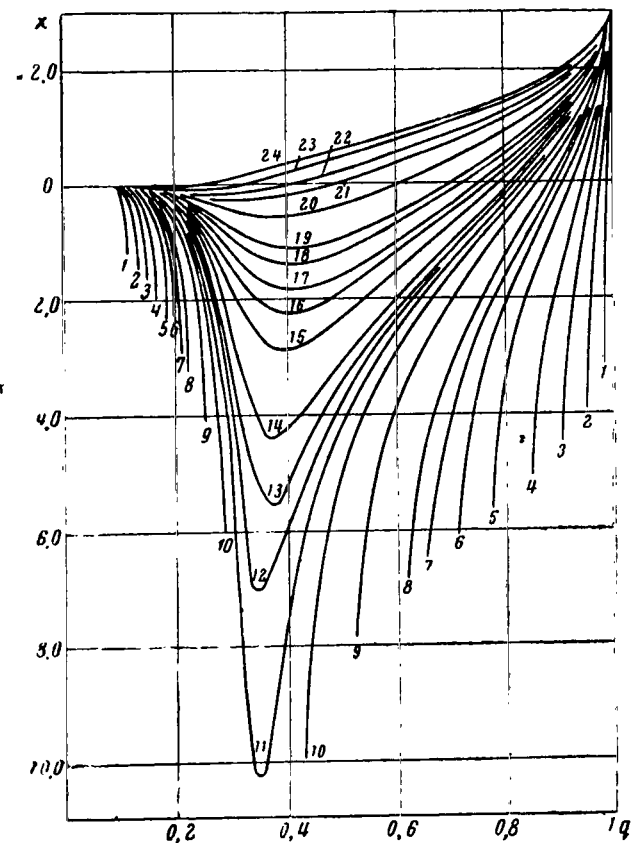


Figure 12. χ in Radians as a Function of q when $\beta = 2.0$. (1) $K = 0.001$; (2) 0.004; (3) 0.01; (4) 0.02; (5) 0.04; (6) 0.06; (7) 0.08; (8) 0.1; (9) 0.15; (10) 0.2; (11) 0.23; (12) 0.25; (13) 0.27; (14) 0.3; (15) 0.4; (16) 0.5; (17) 0.6; (18) 0.8; (19) 1.0; (20) 2; (21) 4; (22) 6; (23) 10; (24) 12.5.

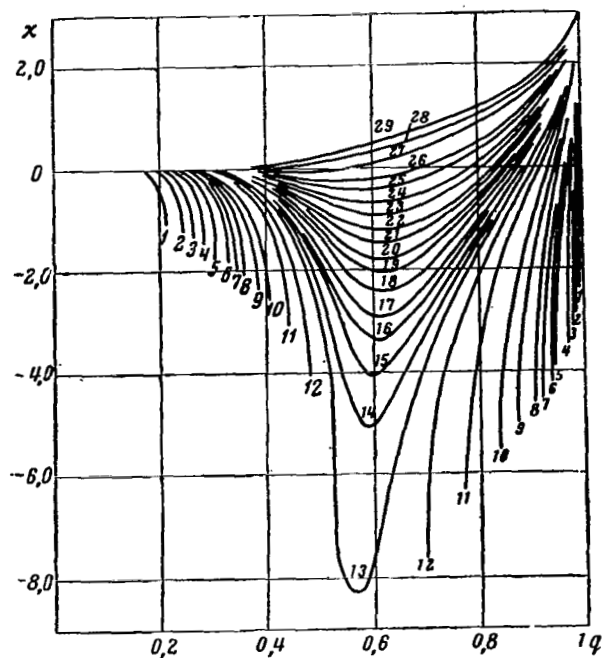


Figure 13. χ in Radians as a Function of q when $\beta = 3.5$. (1) $K = 0.001$; (2) 0.005; (3) 0.01; (4) 0.02; (5) 0.04; (6) 0.06; (7) 0.08; (8) 0.1; (9) 0.15; (10) 0.2; (11) 0.3; (12) 0.4; (13) 0.5; (14) 0.55; (15) 0.6; (16) 0.65; (17) 0.7; (18) 0.8; (19) 0.9; (20) 1.0; (21) 1.2; (22) 1.4; (23) 1.8; (24) 2.4; (25) 4.0; (26) 6.4; (27) 20; (28) 50; (29) 100.

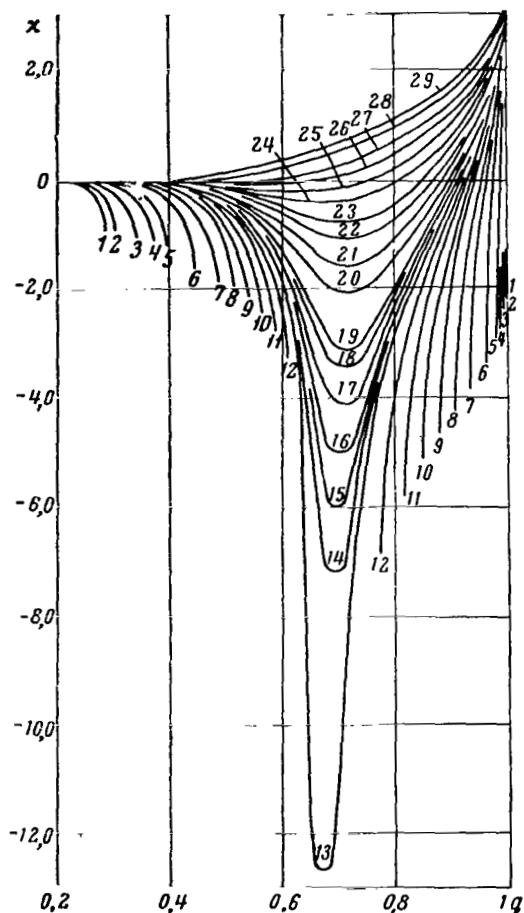


Figure 14. χ in Radians as a Function of q when $\beta = 5.0$. (1) $K = 0.001$; (2) 0.002; (3) 0.01; (4) 0.02; (5) 0.04; (6) 0.1; (7) 0.2; (8) 0.3; (9) 0.4; (10) 0.5; (11) 0.6; (12) 0.7; (13) 0.8; (14) 0.82; (15) 0.84; (16) 0.86; (17) 0.9; (18) 0.96; (19) 1; (20) 1.25; (21) 1.5; (22) 2; (23) 2.75; (24) 5; (25) 10; (26) 30; (27) 100; (28) 500; (29) 1,100.

TABLE

T^*	$g^{(1,1)} \star$	$g^{(1,2)} \star$	$g^{(1,3)} \star$	$g^{(2,2)} \star$	$g^{(2,3)} \star$	$g^{(3,3)} \star$
0,010	29,769	27,324	25,469	23,197	21,664	26,861
0,014	27,296	24,849	23,034	21,180	19,717	24,380
0,018	25,462	23,052	21,295	19,734	18,321	22,603
0,022	24,026	21,669	19,986	18,615	17,238	21,254
0,026	22,861	20,569	18,960	17,704	16,352	20,188
0,030	21,891	19,666	18,117	16,937	15,610	19,306
0,034	21,067	18,900	17,384	16,280	14,985	18,539
0,038	20,351	18,227	16,712	15,713	14,462	17,842
0,04	20,025	17,915	16,389	15,459	14,235	17,511
0,05	18,618	16,502	14,838	14,433	13,368	15,963
0,06	17,437	15,220	13,362	13,710	12,789	14,562
0,07	16,380	14,019	11,983	13,170	12,329	13,314
0,08	15,405	12,895	10,731	12,727	11,896	12,218
0,09	14,495	11,856	9,6155	12,327	11,452	11,264
0,1	13,644	10,904	8,6342	11,942	10,989	10,432
0,14	10,784	7,9142	5,8012	10,413	9,0793	7,9644
0,18	8,6614	5,9340	4,1250	8,9452	7,3811	6,3325
0,22	7,0867	4,5977	3,0801	7,6553	6,0253	5,1671
0,26	5,9013	3,6656	2,3918	6,5729	4,9759	4,2979
0,30	4,9920	2,9935	1,9161	5,6802	4,1653	3,6313
0,34	4,2813	2,4941	1,5740	4,9463	3,5334	3,1093
0,38	3,7159	2,1133	1,3196	4,3410	3,0345	2,6932
0,40	3,4757	1,9560	1,2161	4,0782	2,8241	2,5163
0,50	2,5733	1,3895	0,85122	3,0637	2,0453	1,8518
0,60	1,9923	1,0455	0,63540	2,3896	1,5569	1,4251
0,70	1,5952	0,82015	0,49613	1,9208	1,2305	1,1350
0,80	1,3110	0,66381	0,40043	1,5820	1,0012	0,92857
0,90	1,0999	0,55048	0,33150	1,3289	0,83339	0,77620
1	0,93860	0,46545	0,28002	1,1345	0,70655	0,66031
1,1	0,81219	0,39985	0,24047	0,98190	0,60807	0,56994
1,2	0,71110	0,34806	0,20938	0,85961	0,52989	0,49799
1,4	0,56101	0,27233	0,16420	0,67761	0,41473	0,39169
1,6	0,45628	0,22043	0,13351	0,55031	0,33507	0,31795
1,8	0,38004	0,18323	0,11174	0,45745	0,27752	0,26453
2,0	0,32264	0,15561	0,095744	0,38745	0,23451	0,22451
2,5	0,22841	0,11121	0,070468	0,27227	0,16471	0,15927
3,0	0,17292	0,085819	0,056375	0,20434	0,12437	0,12128
3,5	0,13738	0,069991	0,047786	0,16084	0,099027	0,097225
4,0	0,11321	0,059493	0,042203	0,13131	0,082115	0,081063
4,5	0,096034	0,052196	0,038390	0,11035	0,070298	0,069699
5,0	0,083381	0,046933	0,035683	0,094954	0,061736	0,061419
5,5	0,073791	0,043023	0,033701	0,083317	0,055346	0,055210
6	0,066350	0,040044	0,032212	0,074315	0,050460	0,050440
7	0,055746	0,035897	0,030174	0,061521	0,043615	0,043723
8	0,048706	0,033227	0,028893	0,053069	0,039172	0,039335
9	0,043803	0,031420	0,028044	0,047211	0,036139	0,036324
10	0,040259	0,030147	0,027459	0,042993	0,033984	0,034176
12	0,035603	0,028533	0,026741	0,037480	0,031215	0,031400
14	0,032789	0,027602	0,026344	0,034162	0,029583	0,029753
16	0,030971	0,027026	0,026112	0,032025	0,028551	0,028705
18	0,029736	0,026652	0,025969	0,030574	0,027863	0,028003
20	0,028863	0,026400	0,025879	0,029551	0,027385	0,027513

q for $\chi = -\infty$ by means of relationships (10), (11) and (12). The values of K_{rt} , r_{rt}^* and K_σ are given below for each β :

β	1.5	2.0	2.5	3.0	3.5	4.0	4.5	5.0
K_{rt}	0.15730	0.22112	0.29777	0.38514	0.48085	0.58285	0.689550	0.79974
r_{rt}^*	2.3550	1.8862	1.6278	1.4719	1.3713	1.3028	1.2539	1.2178
K_σ	5.3412	14.940	36.024	80.970	175.01	369.40	767.96	1,580.6

The values of b_{rt}^* can be found from (10).

The dimensionless collision integrals $\Omega^{(l,s)*}$ and the dimensionless effective cross section $Q^{(l)*}$ are related to the uncorrected quantities $\Omega^{(l,s)}$ and $Q^{(l)}$ in the following manner:

$$\Omega^{(l,s)*} = \frac{\Omega^{(l,s)} \sqrt{2\pi\mu/kT}}{\frac{1}{2}(s+1)! \left[1 - \frac{1}{2} \frac{1+(-1)^l}{1+l} \right] \pi r_e^2}; \quad (18)$$

$$Q^{(l)} = \pi r_e^2 Q^{(l)*}. \quad (19)$$

The values of $\Omega^{(l,s)*}$ for $\beta = 1.5$ are given in the table. Figures 1-14 are graphs of $Q^{(l)*}$ and χ .

Example

Calculate the viscosity coefficient η of a gas which consists of homogeneous structureless particles which interact with the Morse potential and have the following parameters for $T = 5,000^\circ\text{K}$: $D_e = 4$ eV; $r_e = 1.8$ Å; $\beta = 1.5$. The molecular weight of the gas is $M = 30$ g/g.mol. We then have

$$T^* = \frac{kT}{D_e} = \frac{1,38042 \cdot 10^{-16} \cdot 5 \cdot 10^3}{4 \cdot 1,60207 \cdot 10^{-12}} = 0,10771.$$

The obtained value of T^* does not coincide with the tabular values of T^* ; therefore, to find the value of $\Omega^{(2,2)*}$ for $T^* = 0.10771$, it is necessary to resort to interpolation. By selecting 0.14000 as the value of T^*_0 and using the Gaussian interpolation formula for equal intervals for backward interpolation [5], we obtain $\Omega^{(2,2)*}(0.10771) = 11.558$.

According to [1] (p. 420, formula 218),

$$\eta = 0,26693 \cdot 10^{-4} \frac{\sqrt{MT}}{r_e^2 Q^{(2,2)} \star} \text{ g/cm} \cdot \text{sec}, \quad (20)$$

where r_e is given in Å, T in °K, and M in g/g·mol. From (20) we obtain

$$\eta = 0,26693 \cdot 10^{-4} \frac{\sqrt{30 \cdot 5 \cdot 10^3}}{1,8^2 \cdot 11,558} = 0,27606 \cdot 10^{-3} \text{ g/cm} \cdot \text{sec}.$$

REFERENCES

1. Hirschfelder, J., C. Curtis and R. Berg: *Molekulyarnaya teoriya gazov i zhidkostey. (Molecular Theory of Gases and Liquids.)* Moscow, IL, 1961.
2. Mason, E. A. and J. T. Vanderslice: Transport properties of high-temperature multicomponent gas mixtures. *Phys. Fluids*, Vol. 2, No. 6, 1959.
3. Monchick, L.: Collision integrals for the exponential repulsive potential. *Phys. Fluids*, Vol. 2, No. 6, 1959.
4. Samuylov, Ye. V. and N. N. Tsitelauri: Collision integrals for the Morse potential. *Teplofizika Vysokikh Temperatur*, Vol. 2, No. 4, 1964.
5. Berezin, I. S. and N. P. Zhidkov: *Metody vychisleniy. (Calculation Methods.)* Vol. 1. Moscow, Fizmatgiz, 1962.

ATTRACTIVE INTERACTION POTENTIALS BETWEEN Li-Li ATOMS IN GROUND STATES

Ye. V. Samuylov and N. V. Voskresenskaya

Interaction potentials can be calculated, in principle, with the methods of /25 quantum mechanics. However, due to the awkwardness of the calculations by these methods, satisfactory results are obtained only for interactions between atoms with a small total amount of electrons.

Experiments on the scattering of atomic beams, experiments on the measurement of vibrational relaxation in gases, data on viscosity, thermal conductivity, and diffusion coefficients of gases at high temperatures, spectroscopic measurements, etc., are a source of experimental data on the interaction potentials between atoms. The transition from experimental data to interaction potentials is possible only in the presence of a sufficiently satisfactory theory of the investigated properties and involves awkward calculations in the majority of cases.

Atoms can interact with various types of potential curves in ground states, depending on the mutual orientation of the spin and orbital moments of the electrons of the outer shell, *i.e.*, with repulsive or attractive potential curves. The experimental data on spectroscopy of diatomic molecules make it possible to calculate attractive potential curves. The fundamentals of the method for calculating attractive potential curves on the basis of molecule band spectra were provided by R. Rydberg [1] and O. Klein [2]. A further development of the method is given by A. Rees [3], J. Vanderslice *et al.* [4], N. Singh and D. Jain [5]. In particular, reference [4] provides a method for calculating potential curves in which the vibrational energy of a diatomic molecule is expressed in the form of a power series $(v + \frac{1}{2})$ (v is the vibrational quantum number) which includes any powers of $(v + \frac{1}{2})$ above the second power. Reference [5] proposes a less awkward means of calculating f , which expresses the distances of minimum r_{min} and maximum r_{max} approach of atomic nuclei for the given value of total energy.

This paper gives a method for calculating attractive potential energy curves in a case when the rotational constant B_v is expressed in the form of a power series $(v + \frac{1}{2})$ which includes the second power of $(v + \frac{1}{2})$. The results of calculations of the attractive interaction potential between Li-Li atoms in the ground states also are given. Attractive curves were computed for the Li-Li interaction, with and without the second power of $(v + \frac{1}{2})$ taken into account in a series for B_v . r_{min} and r_{max} were obtained for all values of the vibrational quantum number from $v = 0$ to $v = v_{max}$ (v_{max} is the maximum value of the vibrational quantum number at which the molecule is stable).

Method for Calculating Potential Energy Curves
on the Basis of Spectroscopic Data

/26

According to [1, 2], the calculation of r_{\min} and r_{\max} for the given value of total energy U amounts to a calculation of f and g

$$r_{\min}^{\max}(U) = \left(\frac{f}{g} + f\right)^{1/2} \mp f, \quad (1)$$

where

$$f = \frac{\partial S}{\partial U}; \quad g = -\frac{\partial S}{\partial x}; \quad (2)$$

$$S(U, x) = \frac{1}{\pi(2\mu)^{1/2}} \int_0^{I'} [U - E(I, x)]^{1/2} dI; \quad (3)$$

$E(I, x)$ is the total energy of a molecule expressed in the form of a series with respect to I and x ;

$$I = h\left(v + \frac{1}{2}\right); \quad x = \frac{j(j+1)h^2}{8\pi^2\mu} = \frac{j(j+1)}{b};$$

j is the rotational quantum number of a molecule; $U = E(I', x)$; $\mu = m_1 m_2 / (m_1 + m_2)$; m_1 and m_2 are the masses of atoms 1 and 2; h is the Planck constant. The derivatives $\partial S / \partial U$ and $\partial S / \partial x$ are calculated in explicit form if $E(I, x)$ is a quadratic function of I [3]. If $E(I, x)$ includes higher powers of I , the integral of (3) can be broken down into $(v+1)$ segments in the calculation of f and g , and $E(I, x)$ can be approximated by a quadratic function with respect to I in each segment from I_{v-1} to I_v . As a result, we obtain

$$f_n = \frac{\partial S}{\partial U_n} = \frac{1}{2(2\pi^2\mu)^{1/2}} \sum_{v=0}^n \int_{I_{v-1}}^{I_v} \frac{dI}{(U_n - E_v)^{1/2}}; \quad (4)$$

$$g_n = -\frac{\partial S}{\partial x} = \frac{1}{2(2\pi^2\mu)^{1/2}} \sum_{v=0}^n \int_{I_{v-1}}^{I_v} \frac{\frac{\partial E_v}{\partial x}}{(U_n - E_v)^{1/2}} dI, \quad (5)$$

where $I_{v-1} = 0$. The quantity E_v has the following form in the variables v and j :

$$E_v = hc \left\{ \omega_v \left(v + \frac{1}{2}\right) - (\omega_v x_v) \left(v + \frac{1}{2}\right)^2 + \right. \\ \left. + \left[B_v - \alpha_v \left(v + \frac{1}{2}\right) - \beta_v \left(v + \frac{1}{2}\right)^2 \right] j(j+1) - D_v j^2 (j+1)^2 \right\}; \quad (6)$$

in variables I and x :

$$E_v = c[p_v I - m_v I^2 + hB_v b x + hD_v b^2 x^2], \quad (7)$$

where c is the velocity of light; B_v , α_v , and β_v are rotational spectroscopic constants in cm^{-1} . The quantities ω_{ev} and $(\omega_e x_e)_v$ in cm^{-1} are calculated on the basis of the values of the spectroscopic vibrational constants ω_e , $\omega_e x_e$, $\omega_e y_e$, and $\omega_e z_e$:

$$\omega_{ev} = \omega_e - \omega_e y_e \left(v^2 - \frac{1}{4}\right) - 2\omega_e z_e v \left(v^2 - \frac{1}{4}\right); \quad (8)$$

$$(\omega_e x_e)_v = \omega_e x_e - 2\omega_e y_e v - \omega_e z_e \left(3v^2 + \frac{1}{4}\right); \quad (9)$$

$$p_v = \omega_{ev} - \alpha_v b x; \quad m_v = \frac{(\omega_e x_e)_v}{h} + \frac{\beta_v b x}{h}. \quad (10)$$

The values of r_{min} and r_{max} will be calculated below for all possible vibrational states of an Li_2 molecule and the rotational energy equal to zero. This requires that f and g be determined when $x = 0$. As a result of integration of (4), we obtain

$$f_{n, x=0} = \frac{1}{(8\pi^2 \mu c)^{1/2}} \sum_{v=0}^n \frac{h^{1/2}}{(\omega_e x_e)_v} \ln W_v, \quad (11)$$

where

$$W_v = \frac{[\omega_{ev}^2 - 4(\omega_e x_e)_v U_v]^{1/2} - 2[(\omega_e x_e)_v (U_n - U_v)]^{1/2}}{[\omega_{ev}^2 - 4(\omega_e x_e)_v U_{v-1}]^{1/2} - 2[(\omega_e x_e)_v (U_n - U_{v-1})]^{1/2}}. \quad (12)$$

$U_{-1} = 0$ in expression (12); U_n , U_v and all spectroscopic constants are expressed in cm^{-1} . Expression (12) was derived in [4]. Consideration of the term proportional to $\beta_e(v + \frac{1}{2})j(j+1)$ in the expression for $f_{n, x=0}$ does not introduce any changes.

Integration of expression (5) results in

$$\begin{aligned} g_n = & \frac{c^{1/2} b}{2(2\pi^2 \mu)^{1/2}} \sum_{v=0}^n \left\{ \left[-\frac{\alpha_v}{m_v} - \frac{\beta_v}{h} \left(\frac{4p_v - \sqrt{p_v^2 - 4m_v A_v}}{4m_v^2} \right) \right] (hU_n - hU_v)^{1/2} - \right. \\ & \left. - \left[-\frac{\alpha_v}{m_v} - \frac{\beta_v}{h} \left(\frac{4p_v - \sqrt{p_v^2 - 4m_v A_{v-1}}}{4m_v^2} \right) \right] (hU_n - hU_{v-1})^{1/2} + \right. \\ & \left. + \left[-\frac{p_v \alpha_v}{2m_v} - \frac{\beta_v}{h} \left(\frac{3p_v^2}{8m_v^2} - \frac{A_v}{2m_v} \right) + hB_v + 2hD_v b x \right] \frac{1}{\sqrt{m_v}} \ln W_{x,v} \right\} \end{aligned} \quad (13)$$

where

$$W_{x,v} = \frac{2\sqrt{m_e(hU_n - hU_v)} - \sqrt{p_v^2 - 4m_e A_n}}{2\sqrt{m_e(hU_n - hU_{v-1})} - \sqrt{p_v^2 - 4m_e A_{v-1}}}; \quad (14)$$

$$A_v = h(U_v - B_e b x - D_e b^2 x^2). \quad (15)$$

All spectroscopic constants and the quantities U_n and U_v are expressed in cm^{-1} ; $U_{-1} = 0$. When $x = 0$, we obtain

$$\begin{aligned} g_{n,x=0} = & \left(\frac{2\pi^2\mu c}{h}\right)^{1/2} \sum_{e=0}^n \left[\left[\frac{2\alpha_e}{(\omega_e x_e)_v} + \frac{2\beta_e \omega_{ee}}{(\omega_e x_e)_v^2} \right] [(U_n - U_{v-1})^{1/2} - (U_n - U_v)^{1/2}] + \right. \\ & + \frac{\beta_e}{2(\omega_e x_e)_v^2} [(\omega_{ee}^2 - 4(\omega_e x_e)_v U_v)^{1/2} (U_n - U_v)^{1/2} - (\omega_{ee}^2 - 4(\omega_e x_e)_v U_{v-1})^{1/2} \times \\ & \times (U_n - U_{v-1})^{1/2}] + \left. \left[2B_e - \frac{\alpha_e \omega_{ee}}{(\omega_e x_e)_v} - \frac{3}{4} \frac{\beta_e \omega_{ee}^2}{(\omega_e x_e)_v^2} + \frac{\beta_e U_n}{(\omega_e x_e)_v} \right] \frac{1}{(\omega_e x_e)_v^{1/2}} \ln W_v \right\}. \quad (16) \end{aligned}$$

Only a small number of vibrational bands were examined for the majority of diatomic molecules, which makes it possible, strictly speaking, to calculate the potential curve in a small segment of values of total energy. To calculate the potential curve for the values of v which are greater than those observed, it is first necessary to evaluate the regularity of the arrangement of vibrational levels when $v > v_{obs}$ up to v_{max} (v_{obs} is the maximum value of the observed quantum number).

This can be done in the case of Li_2 after supplementing the expression for /28 the vibrational energy with an additional term equal to $\omega_e z_e (v + \frac{1}{2})^4$ and determining v_{max} and $\omega_e z_e$ from the combined solution of the following two equations:

$$G(v_m) = D_e; \quad \left. \frac{\partial G(v)}{\partial v} \right|_{v=v_m} = 0, \quad (17)$$

where

$$G(v) = \omega_e \left(v + \frac{1}{2}\right) - \omega_e x_e \left(v + \frac{1}{2}\right)^2 + \omega_e y_e \left(v + \frac{1}{2}\right)^3 + \omega_e z_e \left(v + \frac{1}{2}\right)^4;$$

D_e is the dissociation energy of an Li_2 molecule, read from the minimum of the /29 potential curve. Both equations (17) are approximate. This method of determining v_m and $\omega_e z_e$ was used, for example, in [6].

TABLE

v	$E_v, \text{ cm}^{-1}$	$\omega_e, \text{ cm}^{-1}$	$(\omega_e x_e)_v, \text{ cm}^{-1}$	$\beta_e = 0$		$\beta_e = 0.00008 \text{ cm}^{-1}$	
				$r_{\max}, \text{ \AA}$	$r_{\min}, \text{ \AA}$	$r_{\max}, \text{ \AA}$	$r_{\min}, \text{ \AA}$
0	175,07	351,43	2,5921	2,8480	2,5163	2,8480	2,5163
1	521,30	351,44	2,6049	2,9910	2,4129	2,9912	2,4130
2	862,28	351,46	2,6202	3,0976	2,3464	3,0981	2,3469
3	1198,0	351,51	2,6379	3,1897	2,2950	3,1907	2,2961
4	1528,3	351,58	2,6581	3,2736	2,2523	3,2754	2,2541
5	1853,1	351,68	2,6807	3,3524	2,2155	3,3551	2,2182
6	2172,5	351,82	2,7058	3,4276	2,1828	3,4313	2,1866
7	2486,2	352,00	2,7333	3,5002	2,1534	3,5053	2,1585
8	2794,2	352,22	2,7632	3,5711	2,1265	3,5777	2,1330
9	3096,4	352,50	2,7956	3,6408	2,1015	3,6461	2,1098
10	3392,6	352,83	2,8305	3,7097	2,0783	3,7199	2,0885
11	3682,8	353,22	2,8678	3,7781	2,0564	3,7904	2,0688
12	3966,6	353,68	2,9076	3,8463	2,0357	3,8611	2,0504
13	4244,2	354,20	2,9498	3,9147	2,0159	3,9320	2,0332
14	4515,1	354,81	2,9944	3,9834	1,9968	4,0037	2,0171
15	4779,4	355,49	3,0415	4,0527	1,9785	4,0762	2,0019
16	5036,7	356,26	3,0910	4,1229	1,9606	4,1498	1,9874
17	5287,0	357,12	3,1430	4,1943	1,9431	4,2248	1,9737
18	5529,9	358,07	3,1975	4,2670	1,9259	4,3016	1,9605
19	5765,4	359,12	3,2544	4,3414	1,9089	4,3802	1,9478
20	5993,1	360,28	3,3137	4,4177	1,8920	4,4612	1,9355
21	6212,9	361,54	3,3755	4,4964	1,8751	4,5449	1,9236
22	6424,5	362,93	3,4397	4,5777	1,8580	4,6315	1,9119
23	6627,6	364,43	3,5064	4,6622	1,8407	4,7217	1,9003
24	6822,0	366,05	3,5755	4,7503	1,8231	4,8160	1,8887
25	7007,5	367,80	3,6471	4,8427	1,8049	4,9149	1,8771
26	7183,7	369,69	3,7211	4,9400	1,7861	5,0192	1,8653
27	7350,3	371,72	3,7976	5,0432	1,7666	5,1298	1,8532
28	7507,1	373,89	3,8765	5,1533	1,7460	5,2479	1,8407
29	7653,8	376,21	3,9579	5,2716	1,7242	5,3747	1,8274
30	7789,9	378,68	4,0417	5,3998	1,7010	5,5121	1,8133
31	7915,3	381,31	4,1280	5,5403	1,6759	5,6624	1,7980
32	8029,5	384,10	4,2167	5,6959	1,6485	5,8285	1,7811
33	8132,3	387,07	4,3078	5,8709	1,6182	6,0147	1,7621
34	8223,2	390,20	4,4014	6,0712	1,5843	6,2273	1,7403
35	8301,9	393,52	4,4975	6,3061	1,5455	6,4753	1,7147
36	8368,0	397,01	4,5960	6,5904	1,5001	6,7739	1,6837
37	8421,1	400,70	4,6970	6,9507	1,4450	7,1501	1,6443
38	8460,9	404,58	4,8004	7,4427	1,3744	7,6595	1,5912
39	8486,8	408,65	4,9062	8,2149	1,2742	8,4514	1,5106
40	8498,6	412,93	5,0145	10,020	1,0837	10,278	1,3414

Preliminary Data and Calculation Results

The spectroscopic data used in the calculations were taken from the book by G. Herzberg [7]: $\omega_e = 351.435 \text{ cm}^{-1}$; $\omega_e x_e = 2.592 \text{ cm}^{-1}$; $\omega_e y_e = 0.0058 \text{ cm}^{-1}$; $B_e = 0.67272 \text{ cm}^{-1}$; $\alpha_e = 0.00704 \text{ cm}^{-1}$; $\beta_e = 0.00008 \text{ cm}^{-1}$; $D_0 = 1.04 \text{ eV}$ (D_0 is the dissociation energy of a molecule read from the zero vibrational level). As a result of solving equations (17), we have: $\omega_e z_e = -0.408 \cdot 10^{-3} \text{ cm}^{-1}$; $v_m = 40$.

The quantities r_{min} and r_{max} were calculated for two cases: when $\beta_e = 0$ and $\beta_e = 0.00008 \text{ cm}^{-1}$. The results of the calculation are given in the table.

The values of r_{min} and r_{max} do not reflect the actual behavior of the potential curve for large values of v (close to v_{max}). When the r values are large, the potential function should tend to a dispersion energy equal to $-a/r^6$, where a is constant.

REFERENCES

1. Rydberg, R.: The potential curve for HgH. *Z. Phys.*, Vol. 80, No. 3, 1932.
2. Klein, O.: The calculation of potential curves for diatomic molecules by means of spectroscopic measurements. *Z. Phys.*, Vol. 76, No. 2, 1932.
3. Rees, A.: The calculation of potential energy curves from band-spectroscopic data. *Proc. Phys. Soc.*, Vol. 59, No. 6, 1947.
4. Vanderslice, J. T., E. A. Mason, W. G. Maisch and E. R. Lippincott: Ground state of hydrogen by the Rydberg-Klein-Rees method. *J. Mol. Spectr.*, Vol. 3, No. 1, 1959.
5. Singh, N. L. and D. S. Jain: The Rydberg-Klein-Rees method of constructing the true potential energy curves of diatomic molecules. *Proc. Phys. Soc.*, Vol. 79, No. 2, 1962.
6. Gurvich, L. V., G. A. Khachkuruzov *et al.*: *Termodinamicheskiye svoystva individual'nykh veshchestv*. (Thermodynamic Properties of Individual Substances.) Vol. 1, Izd-vo AN SSSR, 1962.
7. Herzberg, G.: *Spectra of the Diatomic Molecules*. Toronto, N. Y., London, 1950.

THERMODYNAMIC PARAMETERS OF CESIUM BEHIND INCIDENT AND REFLECTED SHOCK WAVES

/30

S. G. Zaytsev

The experimental investigation of the specific properties of a dense low-temperature plasma may be conducted in a special shock tube which makes it possible to study the propagation of shock waves in the vapors of alkali metals. The selection of alkali metals was prompted by the fact that they possess an extremely low ionization potential and, consequently, make it possible to obtain a maximum degree of ionization, other conditions being equal.

To conduct these investigations, the wall temperature of the shock tube must be elevated to the dew point which corresponds to the required vapor pressure of the investigated substance in the low-pressure chamber. The values of the ionization potentials and the temperatures which correspond to the pressure of saturated vapors at 1, 10, and 100 mm Hg are listed in Table 1 [1].

TABLE 1.

Substance	Molecular weight	m.p. T° C	T° C p = 1	T° C p = 10	T° C p = 100	Ionization pot., eV
Li	6,947	186	723	881	1097	5,37
Na	22,997	97,5	439	549	701	5,12
K	39,096	62,3	341	443	586	4,32
Ru	85,48	38,5	297	389	514	4,16
Cs	132,91	28,5	279	375	509	3,87

As can be seen, the application of cesium for studying the properties of low-temperature plasma is more suitable since it possesses a minimum ionization potential and a minimum temperature at identical pressure of saturated vapors.

Let us consider the values of the thermodynamic parameters behind an incident and a reflected shock wave for two initial gas states: $T_0 = 600^\circ\text{K}$; $p_0 = 1$ mm Hg; $T_0 = 700^\circ\text{K}$; $p_0 = 10$ mm Hg (cesium vapors are close to saturation under these conditions).

The possible quantity of molecular cesium, Cs_2 , does not exceed $10^{-5}\%$ when $T_0 = 600^\circ$ and $p_0 = 1$ mm Hg. This estimate is made on the basis of the following constants of the Cs_2 molecule:

Ground state	ω_e	r_e	D_{diss} (eV)
Σ^+	41,99 [2]	$4.57 \cdot 10^{-3}$ [3]	0,453 [3].

The relative molar concentrations of cesium are determined from the relationship /31

$$\frac{X_{Cs}^2}{X_{Cs_2}} = \frac{1}{p} 0,4 T^{3/2} \frac{Q_{Cs}^2}{Q_{Cs_2}} e^{-\frac{D}{T}},$$

where Q_{Cs_2} and Q_{Cs} are the statistical sums of a cesium molecule and atom; X_{Cs} is the relative molar concentration of cesium; D is the dissociation energy of a cesium molecule in degrees; T is the temperature in degrees Kelvin; p is the pressure in atmospheres. By approximating a cesium molecule to a model of a rigid harmonic oscillator, we have

$$Q_{Cs_2} = \frac{1}{\frac{hc}{k} B_r} \frac{1}{1 - e^{-\frac{hc}{k} \omega_0}} \frac{1}{2},$$

where $B_r = 1.26 \text{ cm}^{-1}$ is the rotational constant of Cs_2 .

Thus, the influence of the molecular component on the thermodynamic parameters of cesium vapor in the initial state may be disregarded.

The thermodynamic properties of cesium vapors, which consist of atoms in the initial state, have the following values (Table 2).

TABLE 2.

Parameter	600°K (1 mm Hg)	700°K (10 mm Hg)
h_0 , cal/g	$0,22416 \cdot 10^2$	$0,2615 \cdot 10^2$
ρ_0 , g/cm ³	$0,355 \cdot 10^{-5}$	$0,304 \cdot 10^{-4}$
c , m/sec	250,7	270,1
μ	132,9	132,9

The parameters behind incident and reflected explosions were computed by means of the equations of the conservation of mass, momentum, and energy on a plane shock front. The calculation method is described in [4]. The process of the normal reflection of a shock wave from an absolutely rigid wall is assumed to be adiabatic. It is also assumed that the state of gas behind the shock front satisfies

the Clapeyron equation. The decrease in ionization potentials was not taken into account.

The results of the calculation are plotted on a graph [see Figure 1], where the 1S dots indicate the values of the pressure and temperature behind an incident shock wave which is propagating in cesium vapors ($T_0 = 600^\circ$, $p_0 = 1 \text{ mm Hg}$)

with the Mach number $M_s = i$. The 1R dots denote the values of the parameters behind a reflected wave. The 2S and 2R dots indicate the values of the temperature and pressure behind the incident and reflected waves, respectively, which are propagating in cesium vapors ($T_0 = 700^\circ$, $p_0 = 10$ mm Hg). The solid curves correspond to an identical degree of ionization determined from the relationship $\alpha = X_{Cs+} / (X_{Cs} + X_{Cs+})$.

The dashed curves correspond to the fixed values of the parameter β , which determine the ratio of the energy of the electrostatic interaction of charged particles to their thermal energy

$$\beta \simeq \frac{e^2}{r \frac{3}{2} kT}, \quad (1)$$

where r is the distance between charged particles, which can be determined from the relationship

$$r = \sqrt[3]{N(X_{Cs+} + X_e)}, \quad (2)$$

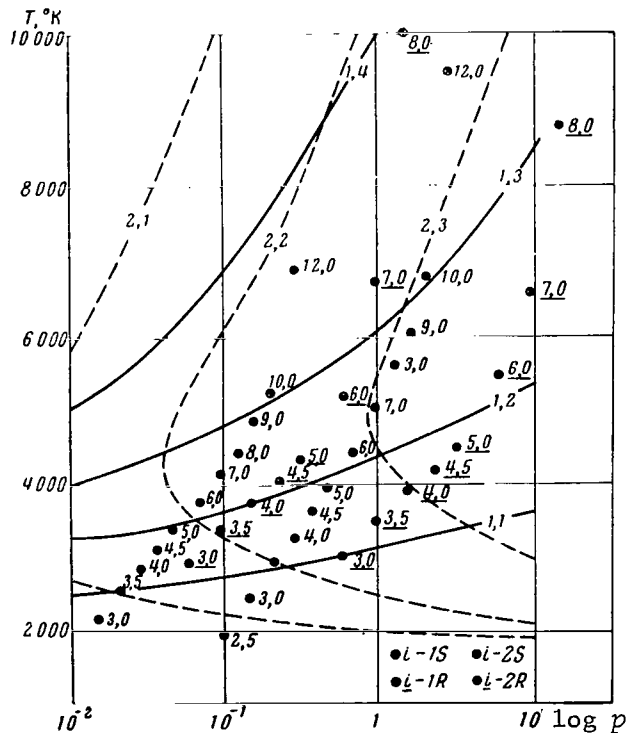
where N is the total number of particles in cm^3 . By substituting (2) into (1) /32 and using the relationship $p = NkT$, we have

$$\beta = 2,5 \cdot 10^4 (2X_{Cs+}p)^{1/3} T^{-4/3}$$

Here p is given in atmospheres and T in degrees.

The calculation was performed at temperatures to $10,000^\circ\text{K}$. Radiation losses were not taken into account. The graph indicates the values of temperature and pressure behind incident and reflected shock waves propagated at $M_s \leq 12$ and $M_s \leq 8$, respectively.

Figure 1. Values of Temperature and Pressure Behind Incident and Reflected Shock Waves Propagating in Cesium Vapors. (1.1) $\alpha = 0.01$; (1.2) $\alpha = 0.1$; (1.3) $\alpha = 0.5$; (1.4) $\alpha = 0.9$; (2.1) $\beta = 0.05$; (2.2) $\beta = 0.1$; (2.3) $\beta = 0.2$.



The substantial experience in working with shock tubes indicates that these conditions can be obtained by using a single-diaphragm tube and by employing mixtures of nitrogen and helium as the propelling gases.

As can be seen, the cesium plasma obtained behind the incident and reflected shock waves will have an ionization factor of approximately 80%, while the ratio of electrostatic energy to thermal energy, *i.e.*, the coefficient β , is approximately 20%.

This result indicates that in the given case one should expect to obtain a gas medium with properties which differ essentially from the properties of a perfect gas, since the percentage of energy of the electrostatic interaction of 33 particles is comparable with their thermal energy. The latter points out that the results of calculating the thermodynamic parameters may be considered only as tentative and indicative of the experimental feasibility of obtaining a low-temperature dense plasma.

REFERENCES

1. *Handbook of Chemistry and Physics*. 37th ed. Editor in Chief, Chemical Rubber Publishing Co., Cleveland, Ohio, 1955-1956.
2. Herzberg, G.: *Molecular Spectra and Molecular Structure*. I. *Spectra of Diatomic Molecules*. D. van Nostrand Co., Inc., Toronto, N. Y., London, 1951.
3. Somayajulu, G. R.: Dissociation energy of diatomic molecules. *J. Chem. Phys.*, Vol. 33, No. 5, 1960.
4. Zaytsev, S. G., A. P. Shatilov and Ye. V. Lazareva: An investigation of the density behind a reflected shock discontinuity in nitrogen. In: *Fizicheskaya gazodinamika i svoystva gazov pri vysokikh temperaturakh*. (Physical Gas Dynamics and Properties of Gases at High Temperatures.) Moscow, Izd-vo "Nauka", 1964.

CALCULATION OF PHOTOIONIZATION CROSS SECTIONS OF NITROGEN AND OXYGEN ATOMS AND THEIR IONS IN EXCITED STATES

V. M. Nikolayev and Yu. A. Plastinin

A general expression for a photoionization cross section can be presented /34
in the following form (without fine splitting taken into account):

$$\sigma(\lambda, T) = \sum_{n\bar{l}LS} w_{n\bar{l}LS}(T) \sigma_{n\bar{l}LS}(\lambda), \quad (1)$$

where $w_{n\bar{l}LS}(T)$ is the probability that an atom will be in the $n\bar{l}LS$ state;
 $\sigma_{n\bar{l}LS}(\lambda)$ is a photoionization cross section caused by emission with a wavelength
 λ of an atom in the $n\bar{l}LS$ state; $n\bar{l}$ is the principal quantum number and the orbital
moment of a photoionized electron; LS is the orbital and spin moment of the
atom.

In thermodynamic equilibrium, the state population is determined by the
Boltzmann law. In this case

$$w_{n\bar{l}LS}(T) = \frac{\omega_{n\bar{l}LS}}{B(T)} \exp \left\{ -\frac{\chi_{n\bar{l}LS}}{kT} \right\}, \quad (2)$$

where $\omega_{n\bar{l}LS}$ is the statistical weight of the $n\bar{l}LS$ state; $\chi_{n\bar{l}LS}$ is the excitation
energy of the $n\bar{l}LS$ state with respect to the ground state; $B(T)$ is the statisti-
cal sum.

The quantity $\sigma_{n\bar{l}LS}$ is determined in the wavelength range of $\lambda \leq \lambda_{n\bar{l}LS}$,
where $\lambda_{n\bar{l}LS}$ is the threshold wavelength for the $n\bar{l}LS$ state; $\sigma_{n\bar{l}LS} = 0$ in the
range of $\lambda > \lambda_{n\bar{l}LS}$.

Consequently, the dependence of the photoionization cross section on the
wavelength λ has a jump-like character, whereby due to the fact that $w(T)$ de-
pends exponentially on temperature, the jumps of the cross section in the
thresholds sharply increase as the temperature increases.

The total number of terms in an isolated atom is very great (although, of
course, it is related to radiation expansion of the upper excited terms which
are adjacent to the boundary of the continuous spectrum). Under the conditions
of actual plasma, due to the effect of microfields, the number of atomic terms
observed is significantly reduced, but nevertheless remains sufficiently large
(to several hundred levels). This imposes definite difficulties on numerical
calculations by means of formula (1) when employing such time-consuming methods
for calculating $\sigma_{n\bar{l}LS}$ cross sections as, for example, the Hartree-Fock self-

consistent field method with exchange, or the multiconfiguration approximation method. The semi-empirical quantum defect method developed by Seaton and Burgess [1, 2] has been used extensively at the present time.

This paper presents the results of calculating photoionization cross sections of nitrogen and oxygen atoms by the quantum defect method in the spectral range of $\lambda \geq 0.12 \mu\text{m}$, which corresponds to photoabsorption from excited states.

If we use the Seaton-Burgess expression for $\sigma_{n\ell LS}$ [2], formula (1) can be /35 presented in the following form (for excited $n\ell^q n'\ell'$ configurations):

$$\begin{aligned} \sigma(\lambda J) = & \frac{9.3924 \cdot 10^{-15}}{\lambda} \sum_{n\ell LS} \lambda_{n\ell LS}^2 (2\ell + 1) \frac{\omega_{n\ell LS}}{B(T)} \exp\left\{-\frac{\chi_{n\ell LS}}{kT}\right\} \times \\ & \times \sum_{l'=l\pm 1} \sum_{L'=L, L\pm 1} (2L' + 1) W^2(l'L'L'; 1L'') C_{ll'} \times \\ & \times \left| \frac{(-1)^{l+1} G_{ll'}(\nu) [1 + \epsilon'\nu^2]^{-\gamma_{ll'}(\nu)}}{\left[1 + \frac{2}{\nu^3} \frac{\partial \mu}{\partial \epsilon}\right]^{1/2}} \right|^2 \times \\ & \times \left| \cos \pi \left[\nu + \mu'(\epsilon') + \chi_{ll'} + \frac{\epsilon'\nu}{1 + \epsilon'\nu} \alpha_{ll'} + \frac{\epsilon'\nu^2}{1 + \epsilon'\nu^2} \beta_{ll'} \right] \right|^2, \end{aligned} \quad (3)$$

where L'' is the orbital moment of an ion obtained as a result of photoionization, *i.e.*, the so-called parent term.

• When calculating the sums of (3) with respect to $n\ell LS\ell'L'$, the quantum-mechanical selection rules with respect to S and L'' should be borne in mind: transitions are possible only between terms of identical multiplicity with identical parent terms.

The following designations are introduced in formula (3): λ is the wavelength in μm ; $\lambda_{n\ell LS}$ is the threshold wavelength of the $n\ell LS$ state in μm ; ν is the effective quantum number of the $n\ell LS$ state

$$\nu^2 = z^2 \frac{Ry}{I_{n\ell LS}}, \quad (4)$$

where $Ry = 109,737.309 \text{ cm}^{-1}$; $I_{n\ell LS}$ is the ionization potential of the $n\ell LS$ state in cm^{-1} ; z is the residual ion charge;

$$\epsilon = -\frac{1}{\nu^2} = -\frac{I_{n\ell LS}}{z^2 Ry}; \quad (5)$$

$$\epsilon' = \frac{0.09112671}{z^2} \left(\frac{1}{\lambda} - \frac{1}{\lambda_{n\ell LS}} \right); \quad (6)$$

μ is the quantum defect

$$\mu = n - \nu; \quad (7)$$

$\mu(\epsilon) = \mu(-1/\nu^2)$ is the analytical expression of the dependence of the quantum

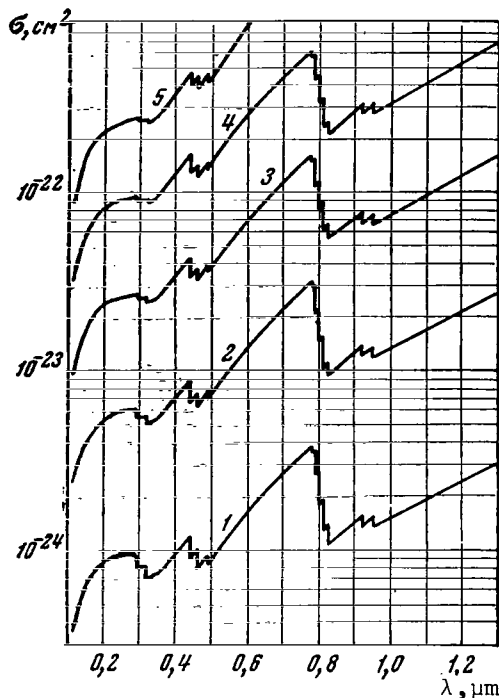


Figure 1. NI Cross Section.
(1) 8,000°K; (2) 9,000; (3)
10,000; (4) 11,000; (5)
12,000.

defect of the lLS series on $\epsilon = -1/\nu^2$;
 $\mu'(\epsilon')$ is the analytical expression of the
dependence of the quantum defect of the
 $l'L'S'$ series on ϵ' ;

$$C_{ll'} = \frac{l+1}{2l+1} \text{ when } l' = l+1; \quad (8)$$

$$C_{ll'} = \frac{l}{2l+1} \text{ when } l' = l-1; \quad (9)$$

$W^2(l'l'L'; lL'')$ is the square of the Racah
coefficient. The quantity W^2 is tabu-
lated in [3]; the analytical expression for
 W^2 can be found, for example, in [4]. The
functions $G_{ll'}$, $\gamma_{ll'}$, $\alpha_{ll'}$, $\chi_{ll'}$, and $\beta_{ll'}$
are tabulated in [2].

The quantities I_{nLLS} , χ_{nLLS} and ω_{nLLS}
for each $nLLS$ term, and also the analytical
expression of $\mu(\epsilon)$ for each lLS series are
determined from the data given in [5] with-
out taking into account splitting with re-
spect to J .

The selected calculation procedure [39]
has advantages as compared with those used
previously. Thus, it is indicated in [6, 7, 8, 9] that the application of the
Unsöld formula for calculating the photoionization cross sections of complex
atoms, which has been applied by many authors, can lead to large errors. An
expression is proposed in [6, 7, 8, 9] which differs from the Unsöld formula
by the correction factor $\xi(\lambda, T)$ [6]. It takes into account the deviations in
the photoionization cross sections from corresponding hydrogen cross sections
for terms which have an essential quantum defect. The analytical form of $\xi(\lambda, T)$
was obtained in [6-9] as a result of simplifications of the Seaton-Burgess ex-
pression for photoionization cross sections, whereby the function $\xi(\lambda, T)$ varies
the cross section in dependence on λ on the average, without taking into account
the structure of photoionization absorption in the thresholds. In addition, it
was proposed that the radial integrals are identical within the limits of each
set of terms s , p , d , etc.

Of interest in this connection are the calculations of the photoionization

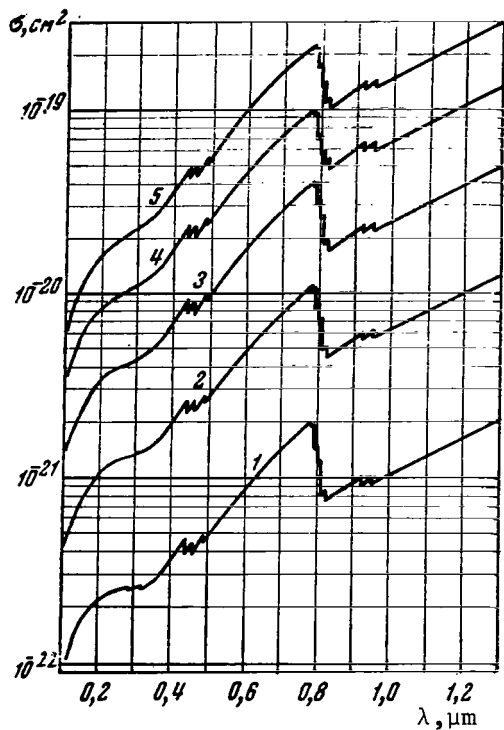


Figure 2. NI Cross Section. (1) 12,000°K; (2) 14,000; (3) 16,000; (4) 18,000; (5) 20,000.

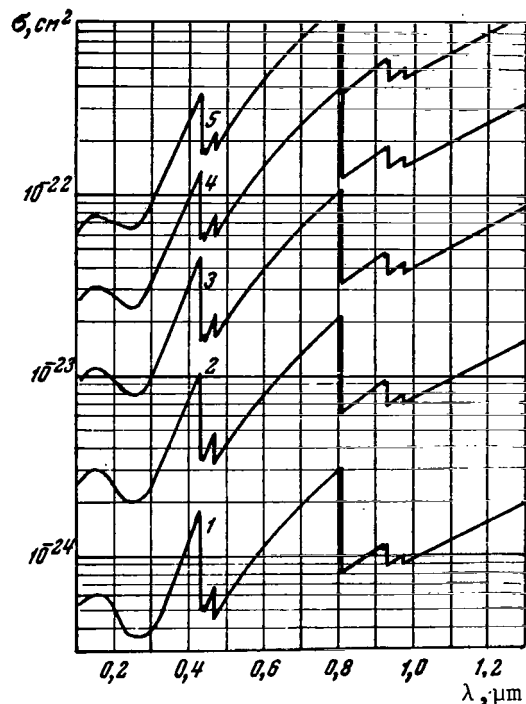


Figure 3. OI Cross Section. (1) 8,000°K; (2) 9,000; (3) 10,000; (4) 11,000; (5) 12,000.

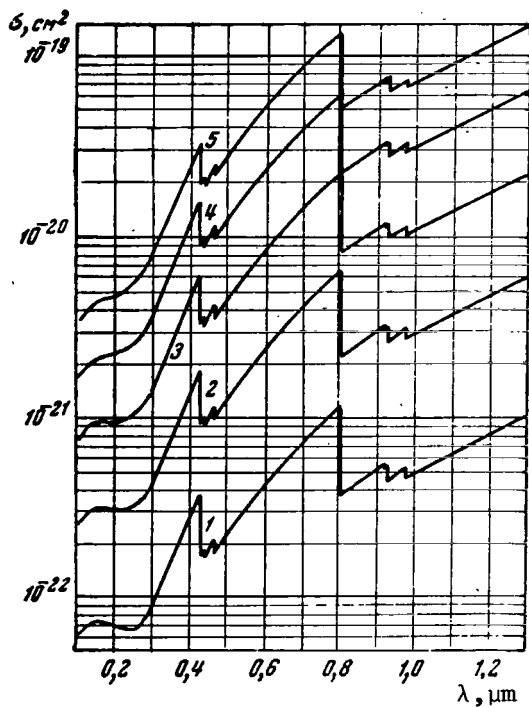


Figure 4. OI Cross Section. (1) 12,000°K; (2) 14,000; (3) 16,000; (4) 18,000; (5) 20,000.

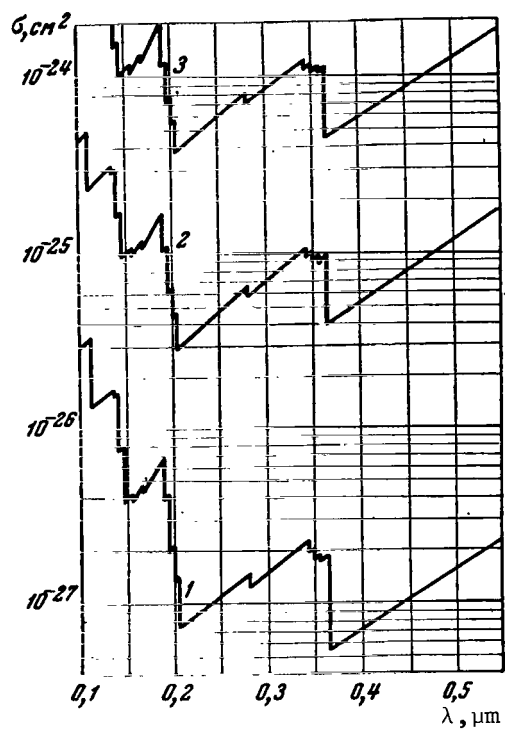


Figure 5. NII Cross Section. (1) 12,000°K; (2) 14,000; (3) 16,000.

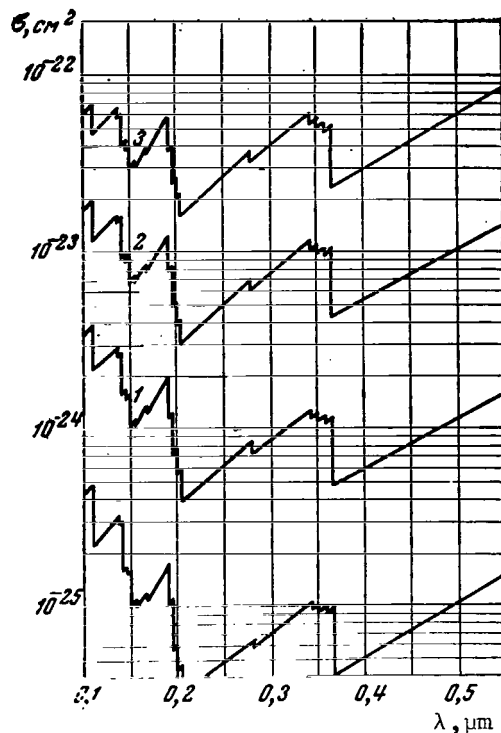


Figure 6. NII Cross Section. (1) 16,000°K; (2) 18,000; (3) 20,000.

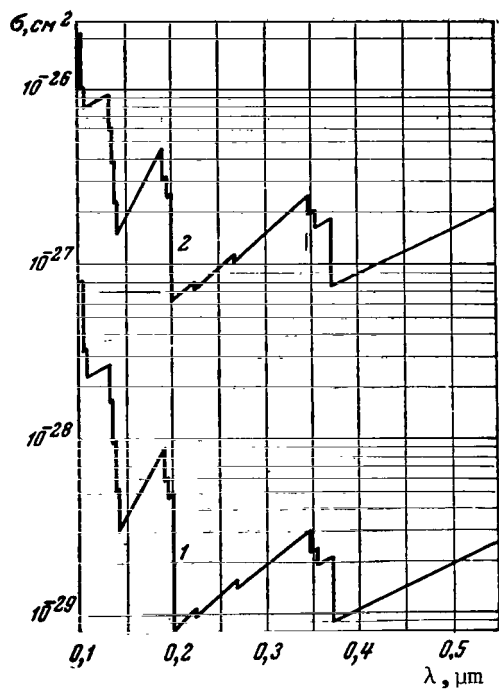


Figure 7. OII Cross Section. (1) 12,000°K; (2) 14,000.

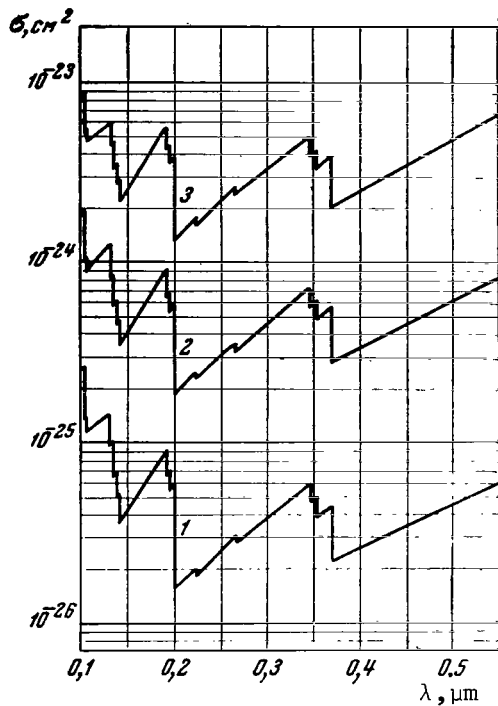


Figure 8. OII Cross Section. (1) 16,000°K; (2) 18,000; (3) 20,000.

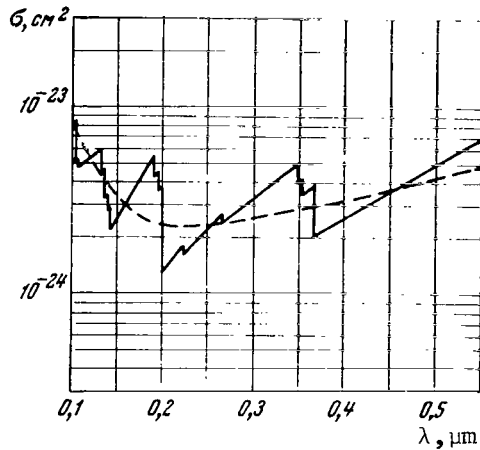


Figure 10. Comparison of the Results of Calculations of Cross Sections for an OII Ion at $T = 20,000^\circ\text{K}$. --- according to [8]; — according to formula (3).

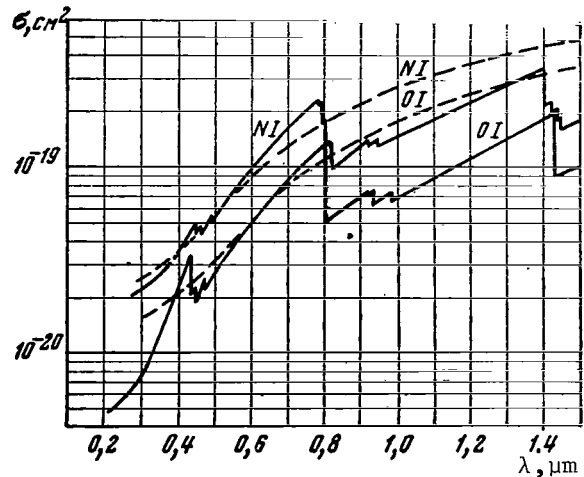


Figure 9. Comparison of the Results of Calculations of Cross Sections for NI and OI Atoms at $T = 20,000^\circ\text{K}$. --- according to [6-9]; — according to formula (3).

cross sections directly by means of the quantum defect formulas. These calculations were performed for NI and OI atoms and NII and OII ions, and are illustrated in Figures 1-8. The level energies given in [5] were used for the calculations. A comparison of the results with the data given in [6-9] is shown in Figures 9 and 10.

REFERENCES

1. Seaton, M.: The quantum defect method. *Monthly Notices of the Royal Astronomical Society*, Vol. 118, No. 5, p. 504, 1958.
2. Burgess, A. and M. Seaton: A general formula for the calculation of atomic photoionization cross sections. *Monthly Notices of the Royal Astronomical Society*, Vol. 120, No. 2, p. 121, 1960.
3. Baldin, A. M., V. M. Gol'danskiy and I. L. Rozental'; *Kinematika yadernykh reaktsiy*. (Kinematics of Nuclear Reactions.) Moscow, Fizmatgiz, 1959.
4. Sobel'man, I. I.: *Vvedeniye v teoriyu atomnykh spektrov*. (Introduction

- to the Theory of Atomic Spectra.) Moscow, Fizmatgiz, 1963.
5. Moore, C.: Atomic energy levels. *Circular NBS 467*, Washington, 1949.
 6. Biberman, L. M. and G. E. Norman: A calculation of photoionization absorption. *Optika i Spektroskopiya*, Vol. 8, No. 4, 1960.
 7. Biberman, L. M., G. E. Norman and K. N. Ul'yanov: A calculation of photoionization absorption in atomic gases. *Optika i Spektroskopiya*, Vol. 10, No. 5, 1961.
 8. Biberman, L. M., G. E. Norman and K. N. Ul'yanov: Photoionization of excited multielectron atoms and ions. *Astronomicheskiya Zhurnal*, Vol. 39, No. 1, 1962.
 9. Biberman, L. M. and G. E. Norman: Recombination emission and bremsstrahlung of plasma (free-bound and free-free transitions in a field of positive ions). *Journal of Quantitative Spectroscopy and Radiative Transfer*, Vol. 3, No. 3, 1963.

N_2 , O_2 , N_2^+ , NO, C_2 AND CN MOLECULES AT HIGH TEMPERATURES

Yu. A. Plastinin and G. G. Baula

The absorption cross sections of electronic band systems of diatomic N_2 , O_2 , N_2^+ , NO, C_2 and CN molecules are necessary for calculations of the radiation energy of heated gases [1, 2]. Therefore, the absorption cross sections of the enumerated molecules are calculated in this paper in a broad spectral range and in a large temperature interval of $T = 2,000-20,000^\circ K$.

Electronic band systems at high temperatures consist of a very large number of rotational lines. To simplify the calculation, the rotational lines in a band are considered to be completely overlapping and to form a continuum; summation with respect to a discrete series of lines is replaced by integration with respect to electron-vibrational bands. The integral exponent of the absorption of a rotational line is given by the expression [3].

$$\int_{\text{line}} k_\nu d\nu = \frac{8\pi^3 e^2}{3hc} \nu_{j',j''} \frac{N_{m''v''j''}}{2j''+1} S_{j',j''} \times \\ \times q_{v',v''} R_e^2(r_{e',e''}) \left[1 - \exp\left(-\frac{hc\nu_{j',j''}}{kT}\right) \right], \quad (1)$$

where $\nu_{j',j''}$ is the wave number of the line; $N_{m''v''j''}$ is the number of molecules situated on the lower energy level of a molecule, to which there correspond the quantum numbers m'' , v'' , and j'' ; $S_{j',j''}$ is the Hönl-London factor; $q_{v',v''}$ is the Franck-Condon factor; R_e^2 is the square of the electronic dipole matrix element; $r_{v',v''}$ is an r -centroid. The remaining designations are universal.

The integral exponent of the absorption of a group of rotational lines which have the same lower rotational level may be found by using the sum rule

$$\sum_{j'} S_{j',j''} = 2j'' + 1. \quad (2)$$

Since $\nu_{j',j''} \gg \Delta\nu_{j',j''}$ ($\Delta\nu_{j',j''}$ is the distance between lines of the given group), formula (2) can be used to derive the following from equation (1):

$$\sum_{j'} \int k_\nu d\nu = \frac{8\pi^3 e^2}{3hc} \bar{\nu}_{j''} N_{m''v''j''} q_{v',v''} R_e^2(r_{e',e''}) \left[1 - \exp\left(-\frac{hc\bar{\nu}_{j''}}{kT}\right) \right], \quad (3)$$

where $\bar{\nu}_{j''}$ is the mean wave number for the group of rotational lines. The summation in equation (3) corresponds to the addition of the integral absorption exponents of the lines of various band branches. If the distribution of molecules with respect to energy levels corresponds to the Boltzmann law, /42

$$N_{m''j''} = \frac{2j''+1}{Q_r^* Q_v^* Q_e} g_{m''} \exp \left[-\frac{B_v j''(j''+1)}{kT} \right] \exp \left(-\frac{T_e + G(v)}{kT} \right). \quad (4)$$

Here Q_r^* , Q_v^* , and Q_e are the rotational, vibrational and electronic statistical sums with respect to states, respectively; T_e and $G(v)$ are the electronic and vibrational terms of the molecules; $g_{m''}$ is the static [sic] weight of the lower electronic state; B_v is the rotational constant.

The mean absorption exponent for the selected interval of wave numbers $\Delta\nu$ can be obtained if expression (3) is integrated with respect to $\nu_{j''}$ and is divided by $\Delta\nu_{j''}$:

$$k_\nu = \frac{1}{\Delta\nu} \int_{\nu - \frac{\Delta\nu}{2}}^{\nu + \frac{\Delta\nu}{2}} \sum_{j'' \text{ line}} \frac{k_\omega d\omega}{\Delta\nu_{j''}} d\nu_{j''}. \quad (5)$$

Here $\Delta\nu_{j''}$ is the distance between adjacent groups of lines. The integrand function in equation (5) depends on the variable j'' , which is related to $\bar{\nu}_{j''}$ and $\Delta\nu_{j''}$. For high temperatures, at which large values of j'' correspond to maximum integral exponents, the approximate dependence of j'' on $\bar{\nu}_{j''}$ can be used for diatomic molecules [4]:

$$j'' \approx \sqrt{\left| \frac{\bar{\nu}_{j''} - \nu_{v',v''}}{B_{v'} - B_{v''}} \right|}. \quad (6)$$

Hence, we determine the distance between adjacent rotational lines

$$\Delta\nu_{j''} = 2 \sqrt{|\bar{\nu}_{j''} - \nu_{v',v''}| |B_{v'} - B_{v''}|}. \quad (7)$$

By substituting expressions (3), (4), (6), (7) into equation (5) and transferring /43
from the wave number to the wavelength, we obtain the following expression for the absorption cross section averaged in an interval of wavelengths $\Delta\lambda$:

$$\sigma_\lambda = \frac{k_\lambda}{N} = \frac{3,868 \cdot 10^{-14}}{T Q_e} \exp \left[-\frac{1,4388 \cdot 10^4}{\lambda_{00} T} \right] \times$$

$$\begin{aligned}
& \times \frac{g_k''}{\Delta\lambda} \exp\left(-\frac{hcT''_e}{kT}\right) \int_{\lambda - \frac{\Delta\lambda}{2}}^{\lambda + \frac{\Delta\lambda}{2}} \frac{1}{\lambda'} \left[\exp\left(\frac{1,4388 \cdot 10^4}{\lambda' T}\right) - 1 \right] \times \\
& \times \sum_{v', v''} \left\{ \frac{q_{v', v''} B_{v''}^* \cdot R_e^2(\lambda_{v', v''})}{|B_{v'} - B_{v''}| Q_v^*} \exp\left[-\frac{1,4388}{T} \left(\frac{B_{v'} \cdot 10^4}{(B_{v'} - B_{v''}) \lambda'} + \right. \right. \right. \\
& \left. \left. \left. + G'(v) - \frac{B_{v'} \cdot 10^4}{(B_{v'} - B_{v''}) \lambda_{v', v''}} \right) \right] \right\} d\lambda'.
\end{aligned} \tag{8}$$

Here

$$\lambda_{v', v''} = \frac{\lambda_{00} \cdot 10^4}{10^4 + \lambda_{00} [G'(v) - G''(v)]}; \tag{9}$$

$$G(v) = \omega_0 v - \omega_0 x_0 v^2 + \omega_0 y_0 v^3 + \omega_0 z_0 v^4; \tag{10}$$

$$B_v = B_e - \alpha_e \left(v + \frac{1}{2} \right); \tag{11}$$

$$Q_v^* = \sum_{v=0}^{v_{\max}} \exp\left\{-\frac{1,4388 [G^*(v) + G^*(0)]}{T}\right\}; \tag{12}$$

$$Q_e = \sum_k g_k \exp\left(-\frac{1,4388 T_k}{T}\right); \tag{13}$$

λ_{00} is the wavelength of the beginning of the (0, 0) band; g_k is the static [sic] weight of the electronic state; T_k is the energy of the electronic state; ω_0 , $\omega_0 x_0$, $\omega_0 y_0$, $\omega_0 z_0$, and α_e are molecular constants; N is the molecular concentration.

The quantities in formulas (8) and (12) denoted by a single prime refer /44 to the upper electronic state; those denoted by two primes refer to the lower electronic state; the ones denoted by the asterisk refer to the ground state. Summation in formula (8) is extended to all terms of the sum which satisfy the inequalities

$$\begin{aligned}
\lambda_{v', v''} &> \lambda', & \text{if } B_{v'} < B_{v''}; \\
\lambda_{v', v''} &< \lambda', & \text{if } B_{v'} > B_{v''}.
\end{aligned}$$

These conditions reflect the shading character of the vibrational bands.

In distinction from the equations for the mean absorption exponents given in [5, 6], the effects of the interaction of movements in a molecule, i.e.,

TABLE 1. SPECTROSCOPIC CONSTANTS

System	$\lambda, \mu\text{m}$	B'_e, cm^{-1}	B''_e, cm^{-1}	$\alpha'_e, \text{cm}^{-1}$	$\alpha''_e, \text{cm}^{-1}$	$\omega'_0, \text{cm}^{-1}$	$\omega''_0, \text{cm}^{-1}$
$\text{N}_2(1+)$	1,05095	1,6386	1,4550	0,0185	0,0183	1720,35	1446,248
$\text{N}_2(2+)$	0,33703	1,8259	1,6386	0,0195	0,0185	2016,307	1720,35
$\text{NO}(\beta)$	0,22029	1,126	1,7046	0,0152	0,0178	1030,15	1891,001
	0,21984						
$\text{NO}(\gamma)$	0,22687	1,9972	1,7046	0,09928	0,00178	2358,34	1891,001
	0,22625						
$\text{N}_2^+(1-)$	0,39114	—	1,9258	—	0,01743	—	2191,00
$\text{CN}(V)$	0,38762	1,985	1,8989	0,023	0,01717	2143,7	2055,50
$\text{CN}(R)$	1,0971	1,7166	1,8989	0,01716	0,01717	1799,728	2055,50
$\text{C}_2(Su)$	0,51603	1,7527	1,6326	0,01608	0,01683	1771,40	1629,68
$\text{O}_2(S-R)$	0,20258	0,819	1,445	0,011	0,01579	592,08	1568,33
$\text{N}_2(L)$	0,14501	1,6181	1,9983	0,0183	0,01709	1579,875	2344,52
$\text{N}_2^+(M)$	1,109	1,722	1,9258	0,018	0,01743	1888,42	2191,00

TABLE 1. (Continued)

System	$\omega'_0, \text{cm}^{-1}$	$\omega''_0, \text{cm}^{-1}$	$\omega'_0 \nu'_0, \text{cm}^{-1}$	$\omega''_0 \nu''_0, \text{cm}^{-1}$	$\omega'_0 z'_0, \text{cm}^{-1}$	$\omega''_0 z''_0, \text{cm}^{-1}$	$G^*(0), \text{cm}^{-1}$	ν_{max}
$\text{N}_2(1+)$	14,913	13,858	0,04842	$1,067 \cdot 10^{-3}$	$2,079 \cdot 10^{-3}$	$2,26 \cdot 10^{-3}$	1175,98	50
$\text{N}_2(2+)$	20,305	14,913	—2,15	$4,8423 \cdot 10^{-2}$	0	0	1175,98	50
$\text{NO}(\beta)$	7,458	14,76	0,0967	$6,7768 \cdot 10^{-2}$	0	0	949,844	47
$\text{NO}(\gamma)$	16,46	14,76	0	$6,7768 \cdot 10^{-2}$	0	$2,316 \cdot 10^{-3}$	949,844	47
$\text{N}_2^+(1-)$	—	16,190	—	$3,03 \cdot 10^{-2}$	—	$9,2 \cdot 10^{-4}$	1099,55	21
$\text{CN}(V)$	20,2	13,111	0	0,91	0	0	1031,02	20
$\text{CN}(R)$	12,188	13,111	—0,012	0,91	0	0	1031,02	20
$\text{C}_2(Su)$	17,2	11,670	—0,5067	$-2,98 \cdot 10^{-2}$	0	0	817,758	57
$\text{O}_2(S-R)$	8,565	11,993	—0,3753	0,0517	0	$1,43 \cdot 10^{-3}$	787,16	51
$\text{N}_2(L)$	13,825	14,872	0,0	0,04821	0	$1,46 \cdot 10^{-3}$	1175,98	50
$\text{N}_2^+(M)$	15,00	16,190	2,2	$-3,03 \cdot 10^{-2}$	$1,1 \cdot 10^{-4}$	$-9,2 \cdot 10^{-4}$	1099,55	21

vibrations with rotation, are taken into account in first approximation in formula (8). This is done by taking into account the dependence of the rotational constant on the vibrational quantum number ν and the interaction of the electronic motion with the vibrational motion, by means of the dependence of the square of the dipole matrix element on the mean internuclear distance. It should be noted that the use of the value of the vibrational sum with respect to states in formula (8) in the approximation of a harmonic oscillator, as this is done in [5, 6], can lead to an essential error in certain cases in calculations

with high temperature values. In our case, equation (12), which takes into account the anharmonicity of vibrations in the molecule, was used to determine Q_v .

Formula (8) was used to calculate the absorption exponents of N_2 , O_2 , NO , N_2^+ , CN and C_2 molecules in a calculation per particle. The spectroscopic constants required for the calculations were taken from [3, 7, 8] and are shown in Table 1. The sum with respect to electronic states was calculated with the use of the electronic level energies listed in Table 2.

TABLE 2. ENERGY OF ELECTRONIC STATES AND STATISTICAL WEIGHTS

State	T_u	g_k	State	T_u	g_k
N_2 [8]			C_2 [8]		
$x^1\Sigma$	0	1	$X^1\Sigma_g^+$	0	1
$A^3\Sigma^+$	50205,5	3	$a^3\Pi_u$	610	6
$B^3\Pi$	59583,4	6	$b^3\Sigma_g^-$	6243,5	3
$^3\Delta_u$	60500	6	$A^1\Pi_u$	8268,33	2
$Y^3\Sigma_u^-$	66270,9	3	$B^1\Delta_g$	10000	2
$a^1\Sigma_u$	68152,17	1	$C^1\Sigma_g^+$	14000	1
$a^1\Pi_g$	69285,6	2	$c^3\Sigma_u^+$	14300	3
$u^1\Delta_u$	72101,67	2	$d^3\Pi_g$	19916,26	6
$^5\Sigma_g^+$	79000	5			
$C^3\Pi_u$	89105	6			
N_2^+ [8]			CN [8]		
$X^2\Sigma_g^+$	0	2	$X^2\Sigma^+$	0	2
$A^2\Pi_u$	9168,4	4	$A^2\Pi$	9241,66	4
$B^2\Sigma_u^+$	25566,0	2	$B^2\Sigma^+$	25951,8	2
$C^2\Sigma_u^+$	64619,5	2			
NO [3, 7, 8]			O_2 [7, 8]		
$X^2\Pi_{1/2}$	0	2	$X^3\Sigma_g^-$	0	3
$X^2\Pi_{3/2}$	123	2	$a^1\Delta_g$	7917,46	2
$A^2\Sigma$	44199	2	$b^1\Sigma_g^+$	13196,38	1
$B^2\Pi$	45440	4	$A^3\Delta_u$	34660	6
$C^2\Pi$	52073	4	$B^3\Sigma_u^+$	35374,96	3
$D^2\Sigma^+$	53085	2	$c^1\Sigma_u^-$	36695,29	1
$B'^2\Delta_g$	60364,5	4	$C^3\Sigma_u^-$	49363,42	3
$E^2\Sigma^+$	60629	2			

For the upper electronic state of the first negative system of the N_2^+ molecule, the experimental data from [9] were used as G_v and B_v , since it was found that vibrational terms and rotational constants cannot express functions of v of the type (10) and (11) accurately enough (Table 3). The lower electronic state, β and γ , of the NO system has a significant amount of spin splitting, due

to which the vibrational bands are broken down into two systems of sub-bands. The absorption cross sections were calculated for each sub-band separately.

TABLE 3. VALUES OF G_v AND B_v FOR THE UPPER $B^2\Sigma_u^+$ STATE OF THE N_2^+ (1-) SYSTEM [9]

v	G_v, cm^{-1}	B_v, cm^{-1}		G_v, cm^{-1}	B_v, cm^{-1}
0	0	2,073	12	23275,1	1,595
1	2371,5	2,049	13	24551,4	1,545
2	4690,3	2,025	14	25747,7	1,494
3	6950,7	2,002	15	26874,3	1,452
4	9147,1	1,968	16	27941,4	1,404
5	11269,9	1,926	17	28956,9	1,367
6	13310,9	1,896	18	29922,9	1,328
7	15262,0	1,852	19	30844,9	1,293
8	17100,2	1,810	20	31726,9	1,256
9	18827,1	1,763	21	32571,9	1,220
10	20423,8	1,710	22	33381,9	1,188
11	21903,7	1,653	23	34156,9	1,152

The averaging interval of $\Delta\lambda$ for the spectral region $\lambda < 0.595 \mu\text{m}$ amounted to 50 \AA , and $\Delta\lambda = 100 \text{ \AA}$ for longer wavelengths. The factors $q_{v,v'}$ were calculated in a wide range of variation of the vibrational quantum number v for the systems N_2 (1+), N_2 (2+), N_2^+ (1-), N_2^+ (M) and N_2 (L) in reference [10], for the NO (β) and NO (γ) systems in [11], for the O_2 (S-R) system in [12], and for the C_2 (Sw) system in [13]. The values of $q_{v,v'}$ in these references were calculated for the Morse potential energy. The data from [14] were used for the CN (R) system and the data from [15] were used for the violet CN system.

The matrix elements of the electronic systems NO (γ), NO (β), N_2^+ (1-), N_2 (1+), N_2 (2+), and O_2 (S-R) are reviewed in [16, 17]. An essential shortcoming of [16] is its lack of results of the investigations of Soviet scientists [18-23]. A great deal of the data given in [17] is obsolete. Some brief notes on the matrix elements of the electronic band systems of N_2 , O_2 , N_2^+ , CN, C_2 and NO molecules will be given below.

O_2 (S-R) ($C^3\Sigma_u^- - X^3\Sigma_g^-$) System

The Schumann-Runge band system lies mainly in the $1,767\text{--}4,800 \text{ \AA}$ spectral region and the continuous photodissociation spectrum at room temperature is within $1,250\text{--}1,750 \text{ \AA}$. The data provided by Bethke [24] and Generalov [20] can /46

be utilized to determine R_e in the 1,767-2,245 Å spectral region.

The integral absorption exponents of bands belonging to the sequence $v'' = 0$ were used for the calculations of R_e with the aid of refined values of $q_{v',v''}$ for the Klein-Dunham potential curve [25]. The bands which lie near 2,245 Å correspond to transitions between vibrational levels $v' = 0$ and $v'' = 4.5$.

Generalov [20] found $R_e^2 = 0.5-0.75$ a.u. for them. Since the values of $q_{v',v''}$ from [12] for these combinations of v are sufficiently accurate [26], the corresponding values of R_e^2 are evidently reliable. Extensive measurements of the dependence of R_e^2 for bands lying in the 2,650-3,900 Å range and an analysis of other investigations are presented in [18]. The recommended dependence in the indicated spectral region is illustrated in Figure 1. In the spectral region

$\lambda > 3,900$ Å, Keck *et al.* [6, 27] measured the intensity of oxygen emission at $T \sim 4,000^\circ\text{K}$. These data were used for the calculations of R_e by means of formula (8). The results are shown in Figure 1.

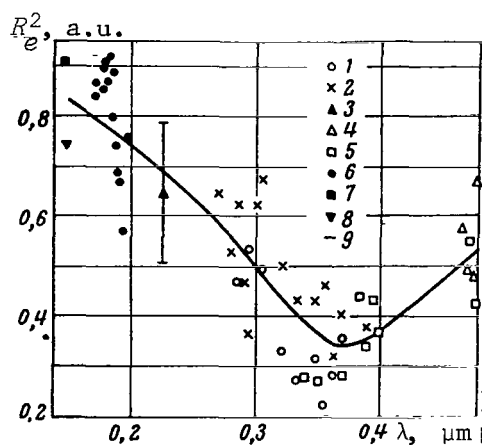


Figure 1. R_e^2 Systems of O_2 (S-R). (1) according to [18]; (2) [48]; (3) [20]; (4) [27]; (5) [6]; (6) [24]; (7) [47]; (8) [46]; (9) recommended curve.

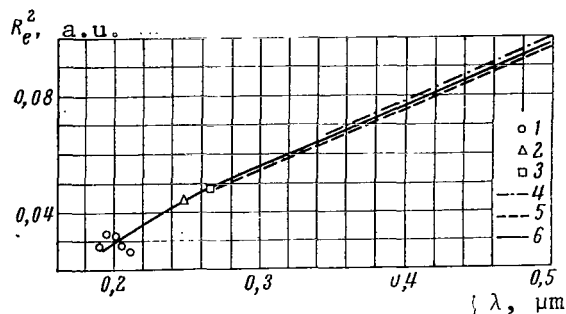


Figure 2. R_e^2 β Systems of NO. (1) according to [28]; (2) [19]; (3) [29]; (4) [6]; (5) [30]; (6) recommended curve.

β System of NO ($B^2\Pi-X^2\Pi$)

The major portion of the bands of the β system of the NO molecule lies in the spectral region from 1,900 to 5,000 Å. Measurements of the integral absorption exponents of the progression bands $v'' = 0$ were performed by Bethke at room temperature [28]. By using these data and the more accurate calculations of $q_{v',v''}$ for the Rydberg-Klein-Rees potential curve [16], we obtain the values of R_e^2 , which are presented in Figure 2 in the spectral region near $\lambda = 1,900$ Å.

In the spectral region of $\lambda > 2,480$ Å we can use the measurements performed by Sobolev, Antropov *et al.* [19], Daiber and Williams [29], Keck *et al.* [6], and also the relative measurements made by Robinson and Nicholls [30] for establishing the dependence of R_e on λ . All of these measurements provide agreeing values of R_e^2 , which are presented in Figure 2.

The bands of the γ system of the NO molecule lie mainly in the 1,700-3,170 Å spectral region.

Measurements of the integral absorption exponents of the progression bands $v'' = 0$ were performed by Bethke and Penner at room temperature [28, 31]. Measurements for heated NO were performed for the progression $v' = 0$ and $v'' = 0, 1, 2, 3, 4$ by Antropov, Sobolev, *et al.* [19], and also by Daiber and Williams [29]. These measurements give agreeing results and are illustrated in Figure 3. The relative dependence of Robinson and Nicholls [30], which is illustrated in the same figure, does not agree with the experimental data in [19, 29] and is obviously unreliable.

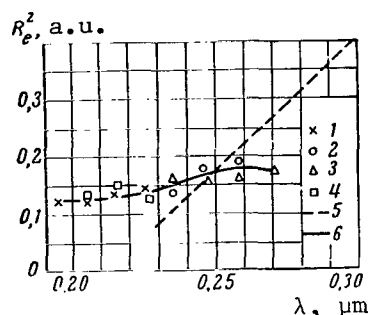


Figure 3. R_e^2 γ Systems of NO. (1) according to [28]; (2) [19]; (3) [29]; (4) [31]; (5) [30]; (6) recommended curve.

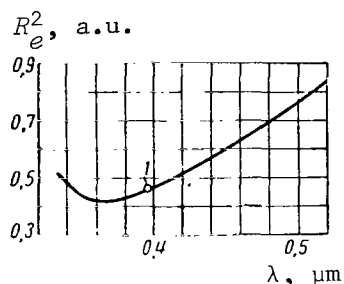


Figure 4. R_e^2 Systems of $N_2^+(1-)$. $R_e = 11.1$ ($1 + 0.679r - 1.62r$); $0.974 < r < 1.265$ Å. Point 1 according to [33].

First Negative System $N_2^+(1-)$ ($B^2\Sigma_u^+ - X^2\Sigma_g^+$)

The main portion of the bands of the first negative system of N_2^+ lies in the spectral region of 3,000-5,000 Å. The relative dependence of R_e^2 was investigated in [32]. The value of R_e^2 was determined for the (0,0) band from [32], in which the emission intensities of nitrogen behind an incident shock wave were measured. Formula (8) was used in this case. The oscillator strength corresponding to the found value of R_e^2 is equal to $3.6 \cdot 10^{-2}$, which agrees well with the oscillator strength found by means of the value of the lifetime of the $B^2\Sigma$ state of a N_2^+ molecule ($f_e = 0.0348$ [34]). If we use the values of the square of the matrix element determined above, the results of calculations of the absorption indices according to formula (8) also agree with the data in [23] on measurements of the emission intensity of nitrogen behind a reflected shock wave when $T = 6,000^\circ\text{K}$

and $p = 5$ atm. The dependence of R_e^2 on wavelength from [32], which was normalized by means of R_e^2 for the (0,0) band, is shown in Figure 4.

Violet System CN(V) ($B^2\Sigma^+ - X^2\Sigma$)

The bands of the violet system of the CN molecule lie in the spectral range of 3,000-4,600 Å. An analysis of reference data on the squares of the matrix

elements is given in [9, 21, 22]. Measurements in shock tubes [9, 21, 22] also of the lifetime of the upper state of the violet band system of $\text{CN } B^2\Sigma^+$ [35] give close values of f for the (0,0) band, i.e., $f = 0.027-0.03$. In accordance with [36], R_e depends slightly on the internuclear distance and is practically constant. We adopted $R_e^2 = 0.37$ a.u. in our calculations.

Red System $\text{CN}(R)$ ($A^2\Pi-X^2\Sigma^+$)

/48

The bands of the red system of the CN molecule lie in the spectral region of 5,500–20,000 Å. The relative dependence of R_e in the spectral region of 5,500–16,000 Å was investigated in [37]. It turned out that R_e for the $\text{CN}(R)$ system, as also in the case of $\text{CN}(V)$, is practically a constant. On the other hand, $R_e^2(V)/R_e^2(R) = 1.9$ was determined in [9, 21], which gives $R_e^2 = 0.20$ a.u. for the red system. This value was used in our calculations.

Second Positive System $\text{N}_2(2+)$ ($C^3\Pi_u-B^3\Pi_g$)

The main portion of the bands of the second positive system is located in the spectral region λ 2,650–5,000 Å. The relative dependence on the internuclear distance was determined in [32]. The results of determining R_e^2 from the data on the emission intensities of air, which are given in [6], are shown in Figure 5. The lifetime τ of the $C^3\Pi_u$ state was measured in [34]. The value of R_e^2

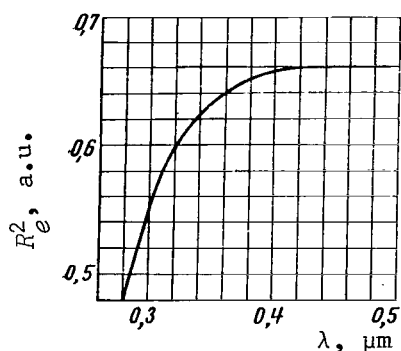


Figure 5. R_e^2 Systems of $\text{N}_2(2+)$. $R_e = 4.13 (1 - 2.32r + 1.102r^2)$; $1.014 < r < 1.351$ Å.

which corresponds to this τ for the (0,0) band is 2.5 times less than that shown in Figure 5. This value is unreliable, since τ is influenced by the cascade processes which took place in the experiments in [34]. The values of R_e^2 shown in Figure 5 were used to calculate the absorption cross sections in this paper.

First Positive System $\text{N}_2(1+)$ ($B^3\Pi_g-A^3\Sigma_u^+$)

The main portion of the bands of the $\text{N}_2(1+)$ system lies in the spectral region from 5,500 to 20,000 Å. The relative dependence of R_e on the internuclear distance was investigated by Turner and Nicholls [38]. Allen and his associates performed absolute measurements of the emission intensity behind an incident shock wave [33]. Wurster conducted analogous experiments behind a reflected wave [39]. Emission intensity of the air was measured by Keck *et al.* [6]. These data were used for normalizing the relative dependence of Turner and Nicholls with respect to formula (8). The results are shown in

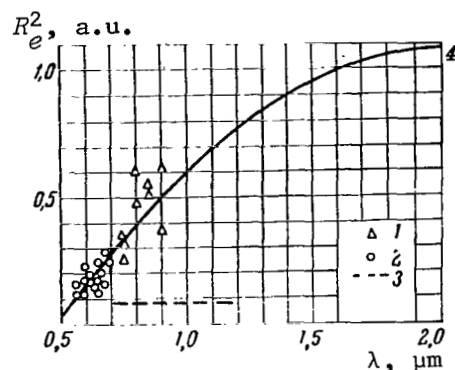


Figure 6. R_e^2 Systems of $N(1+)$.
(1) according to [6]; (2) [33];
(3) [39]; (4) [38].

Figure 6. It should be noted that the measurements of Keck [6] and Allen [33] give agreeing values of R_e . Several times smaller values of R_e , at the same time, are obtained from Wurster's measurements [39]. In addition, Wurster found that the matrix element in the spectral range of 0.74-1.2 μm does not depend on the wavelength, which contradicts the data in [6, 38]. It is possible that such a divergence was caused by the uncontrolled effect of the emission of the bands of the red system of the CN molecule contained in the investigated gas as an admixture [16]. In view of the noncorrespondence of the data in [6, 38] to the results given in [39], the question concerning a single-valued determination of R_e remains open. /59

Calculations of absorption cross sections were performed with the use of $R_e^2 = 0.0046$.

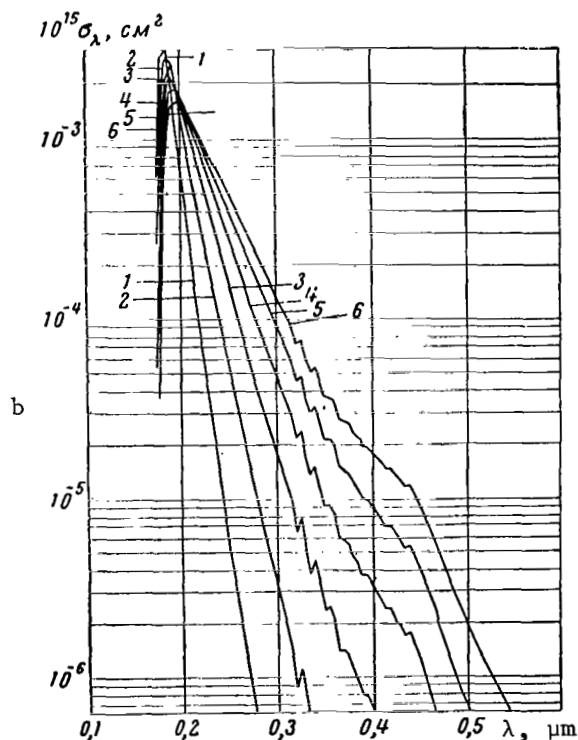
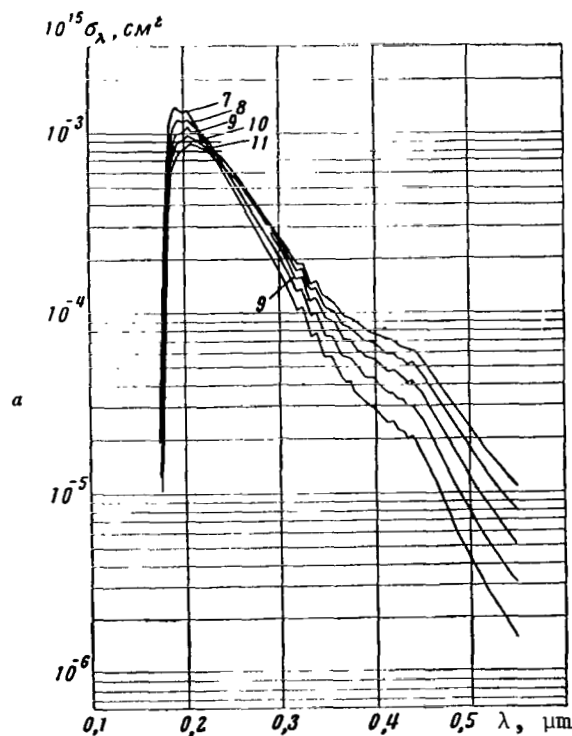


Figure 7a and b. σ Systems of $O_2(S-R)$. (1) $T = 2,000^\circ\text{K}$;
(2) 3,000; (3) 4,000; (4) 5,000; (5) 6,000; (6) 7,000; (7)
8,000; (8) 9,000; (9) 10,000; (10) 11,000; (11) 12,000.

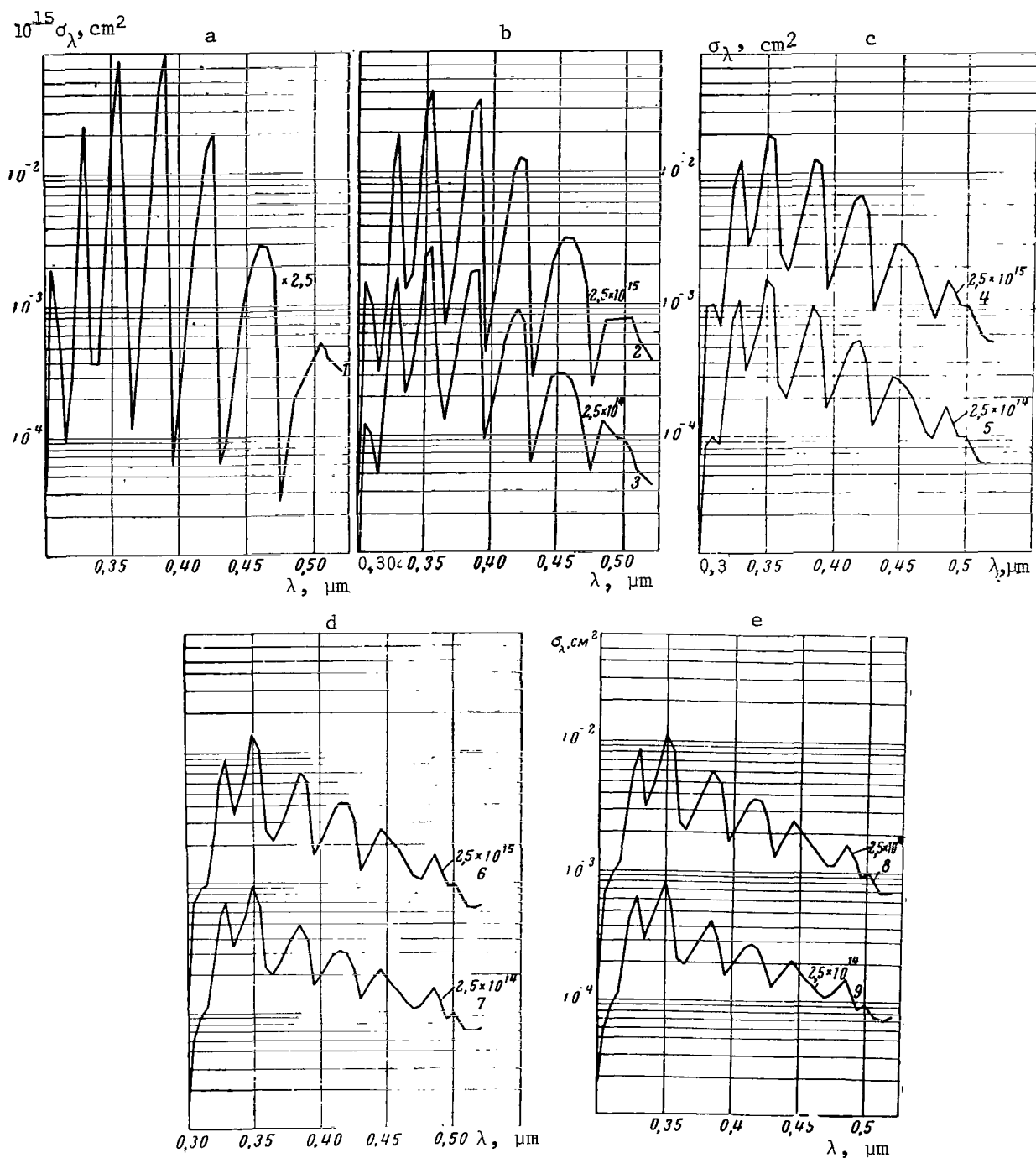


Figure 8a, b, c, d and e. σ Systems of $N_2^+(1-)$. (1) $T = 4,000^\circ\text{K}$; (2) 6,000; (3) 8,000; (4) 10,000; (5) 12,000; (6) 14,000; (7) 16,000; (8) 18,000; (9) 20,000.

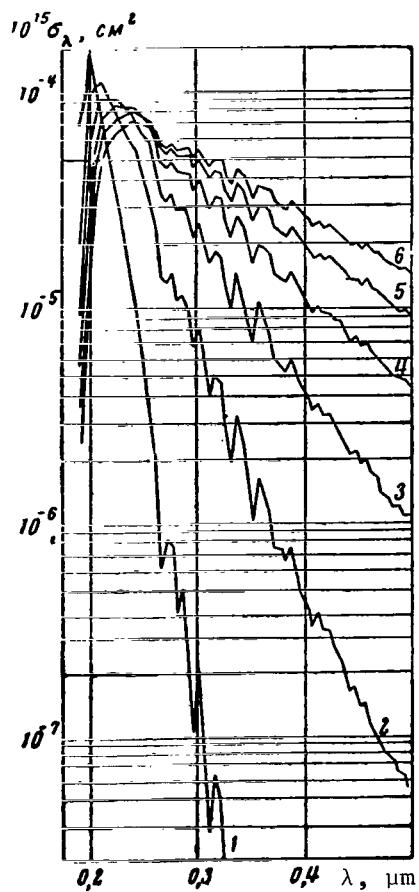


Figure 9. $\sigma\beta$ Systems of NO. (1) $T = 2,000^\circ\text{K}$; (2) 4,000; (3) 6,000; (4) 8,000; (5) 10,000; (6) 12,000.

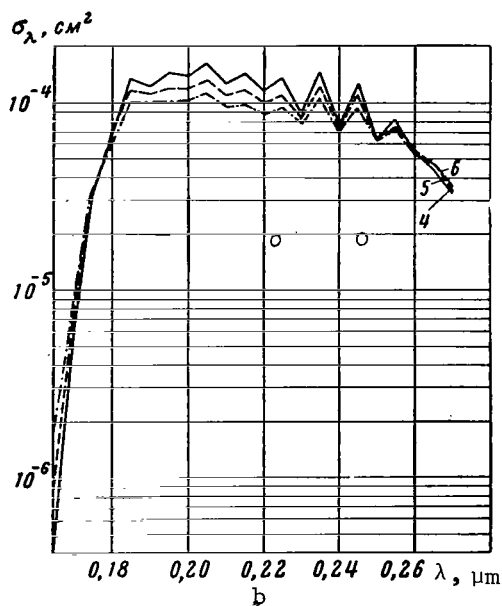
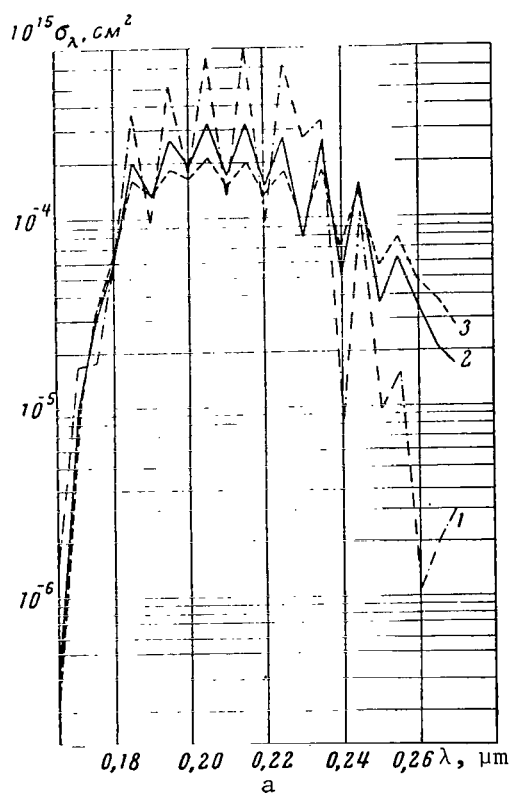
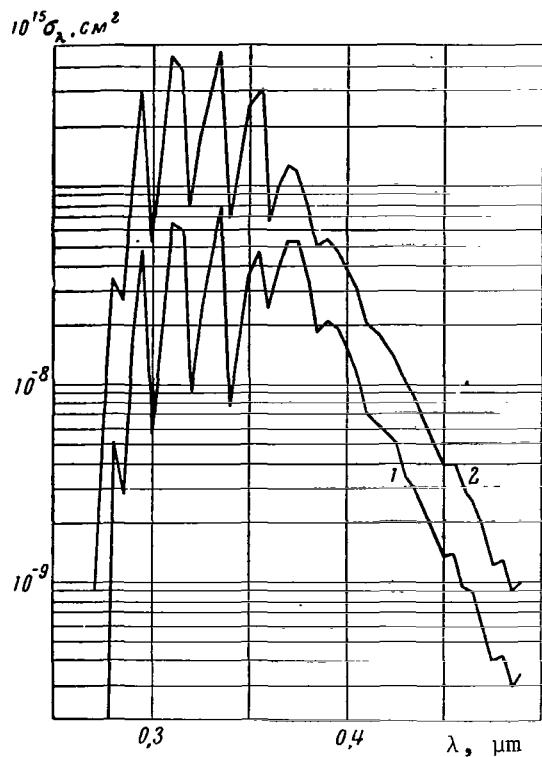
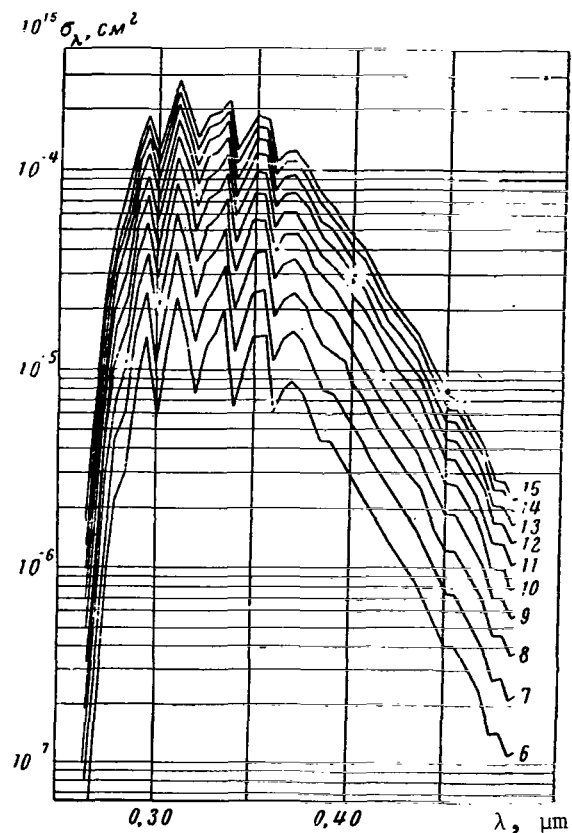


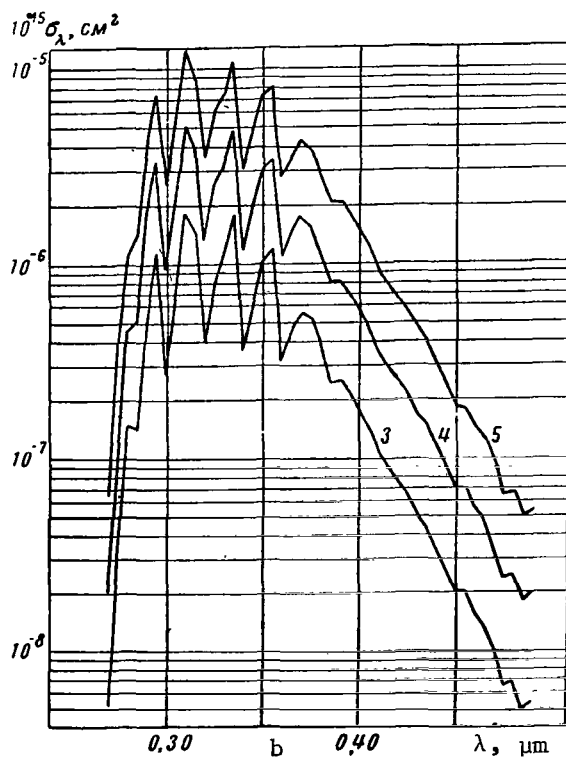
Figure 10a and b. $\sigma\gamma$ Systems of NO. (1) $T = 2,000^\circ\text{K}$; (2) 4,000; (3) 6,000; (4) 8,000; (5) 10,000; (6) 12,000.



a



c



b

Figure 11a, b and c. σ Systems of $N_2(2+)$. (1) $T = 6,000^\circ K$; (2) 7,000; (3) 8,000; (4) 9,000; (5) 10,000; (6) 11,000; (7) 12,000; (8) 13,000; (9) 14,000; (10) 15,000; (11) 16,000; (12) 17,000; (13) 18,000; (14) 19,000; (15) 20,000.

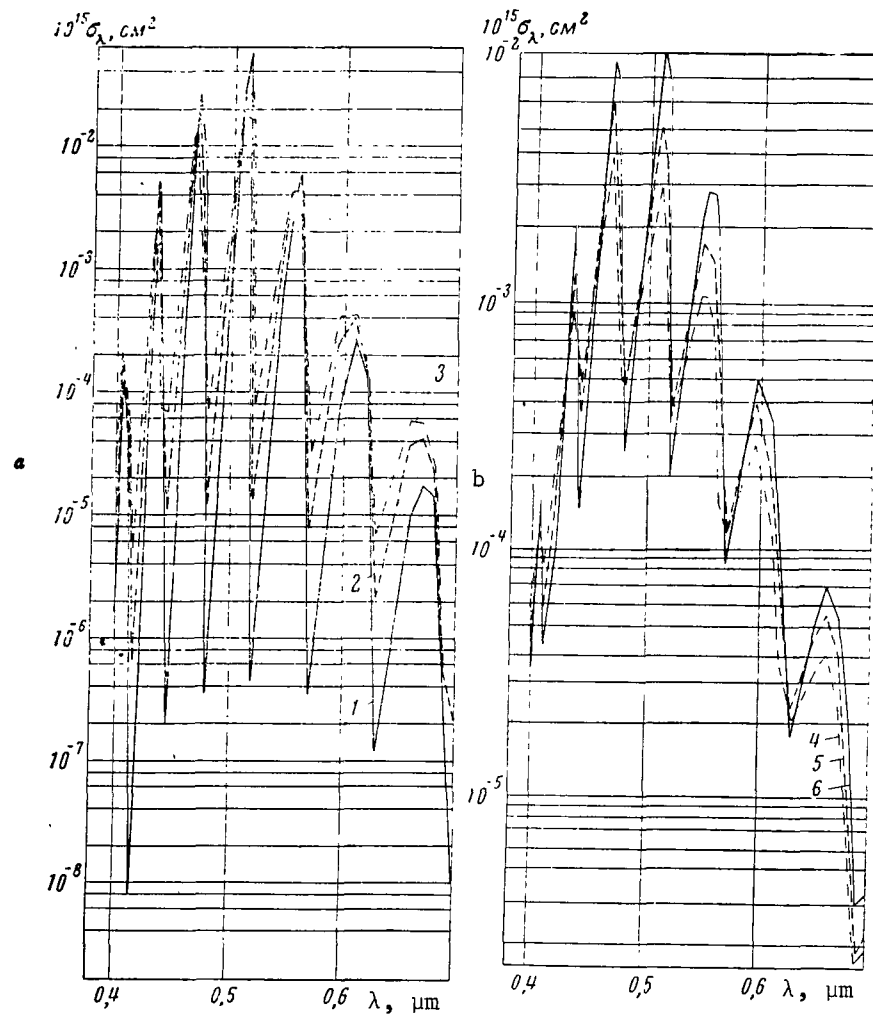


Figure 12a and b. σ Systems of $C_2(Sw)$. (1) $T = 2,000^\circ K$; (2) 3,000; (3) 4,000; (4) 6,000; (5) 9,000; (6) 12,000.

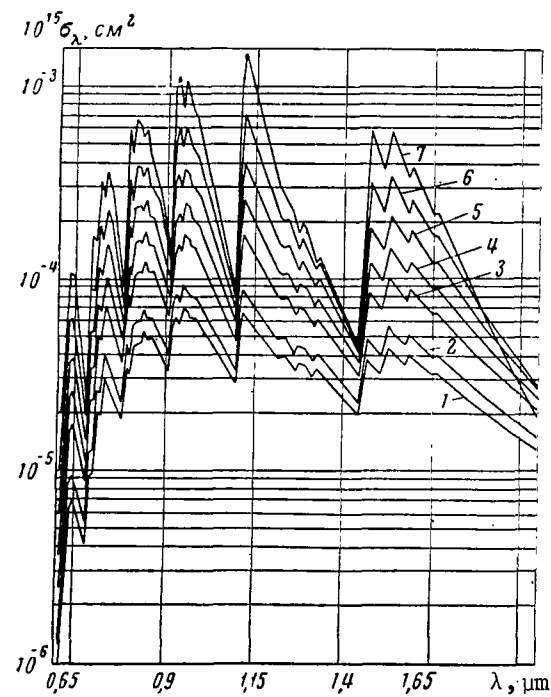


Figure 13. σ Systems of $N_2^+(M)$. (1) $T = 6,000^\circ K$; (2) 8,000; (3) 10,000; (4) 12,000; (5) 14,000; (6) 18,000; (7) 20,000.

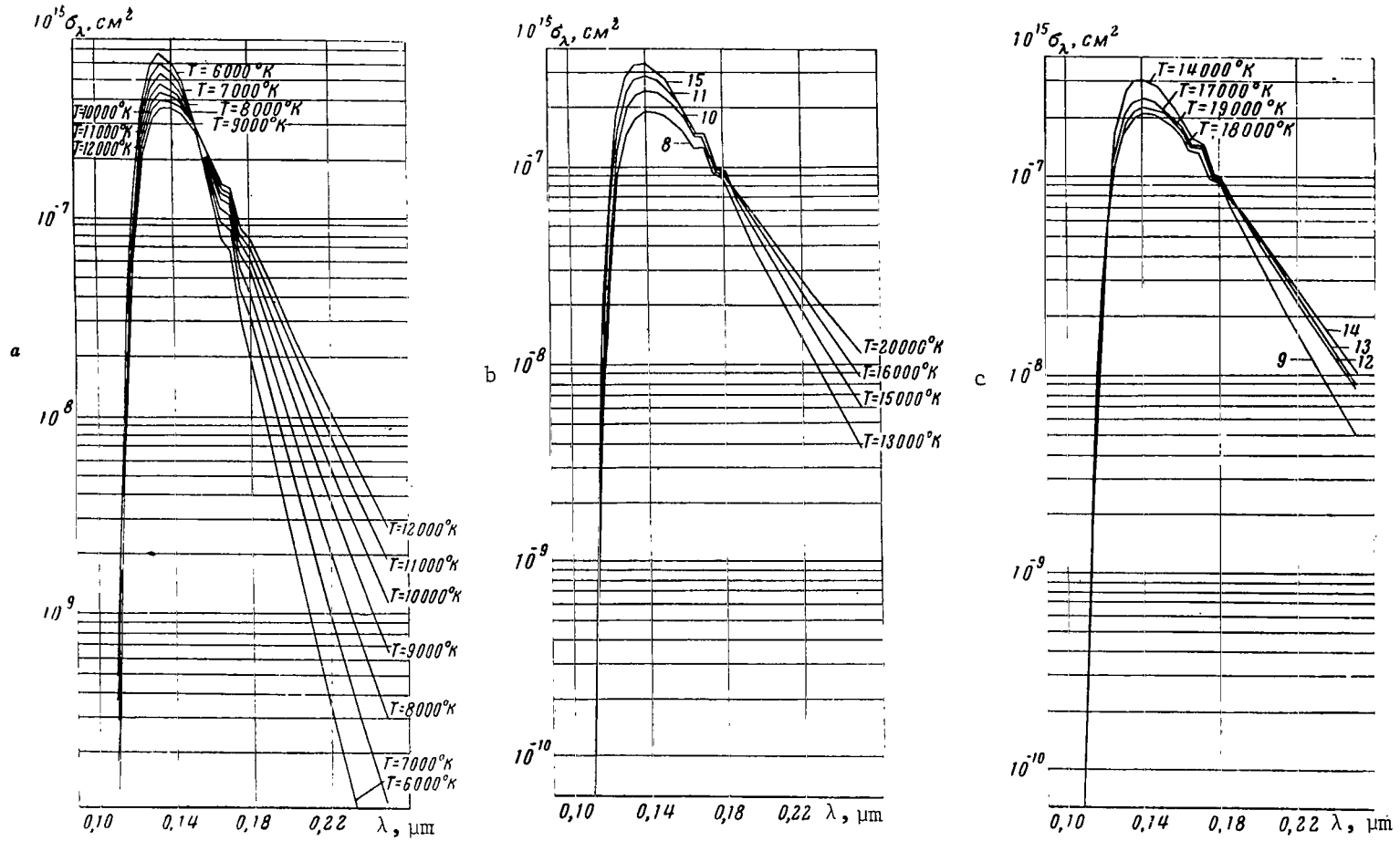
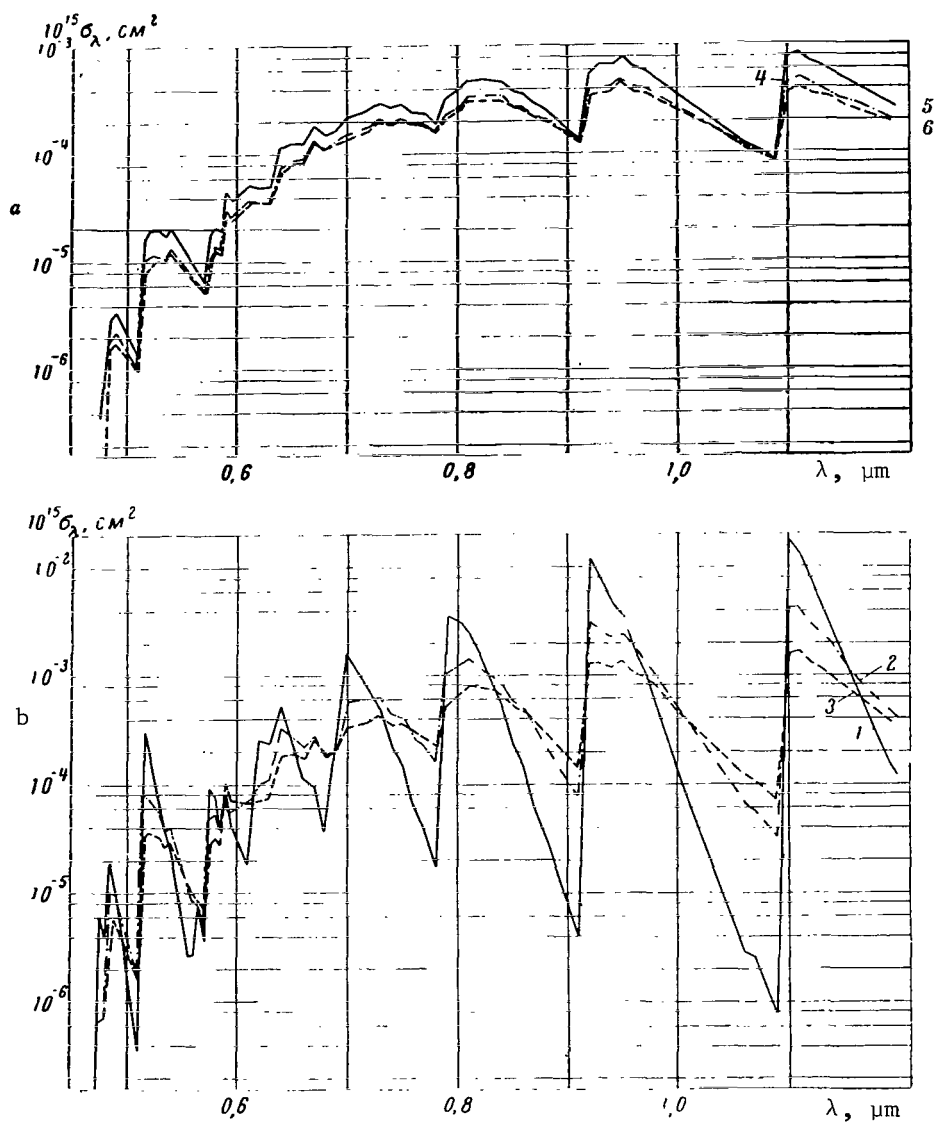


Figure 14a, b and c. σ Systems of $N_2(L)$. (1) $T = 6,000^\circ\text{K}$; (2) 7,000; (3) 8,000; (4) 9,000; (5) 10,000; (6) 11,000; (7) 12,000; (8) 13,000; (9) 14,000; (10) 15,000; (11) 16,000; (12) 17,000; (13) 18,000; (14) 19,000; (15) 20,000.



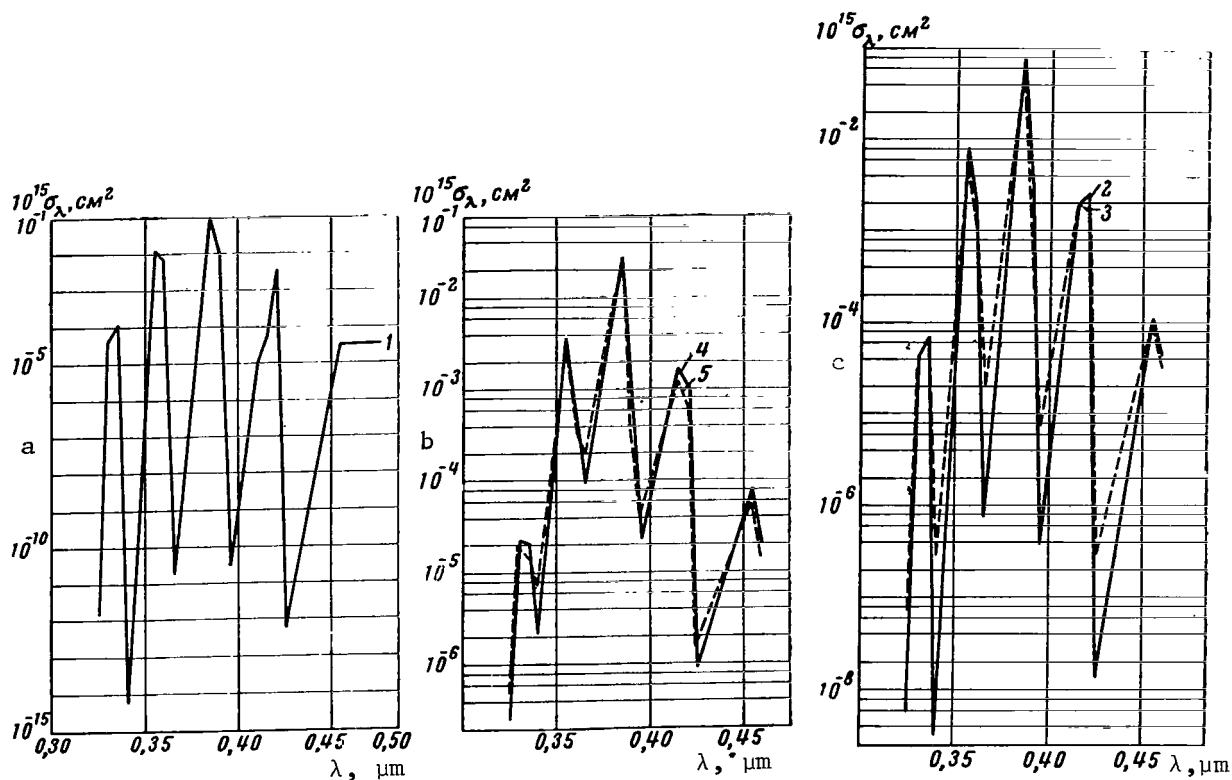


Figure 16a, b and c. σ Systems of $\text{CN}(V)$. (1) $T = 2,000^\circ\text{K}$; (2) 4,000; (3) 6,000; (4) 8,000; (5) 10,000.

Swan System $\text{C}_2(\text{Sw})$ ($d^3\Pi_g - a^3\Pi_u$)

The bands of the Swan system of the C_2 molecule lie in the spectral region of 4,000–7,000 Å. The value of R_e , according to relative measurements made in [40] in the spectral region of 4,365–6,191 Å, varies insignificantly with the internuclear distance, and R_e may be considered to be practically constant for the main portion of the bands. The results of absolute measurements of R_e are lacking in the literature. Therefore, we shall use the calculated value of the oscillator strength from [41] for our computations, $f = 0.024$, which corresponds to $R_e^2 = 0.42$ a.u. The value of f used is close to that given in [4] ($f = 0.02$).

Lyman-Berge-Hopfield System $\text{N}_2(L)$ ($a^1\Pi_g - x^1\Sigma_g^+$)

Absorption in the bands of the Lyman-Berge-Hopfield system occurs in the spectral region of 1,200–2,000 Å. The lifetime of the upper state $a^1\Pi_g$ was measured in [42], and has the value of $\tau = 6.23 \cdot 10^{-3}$ sec. To calculate the absorption cross sections, we used the constant value of R_e for all bands of the

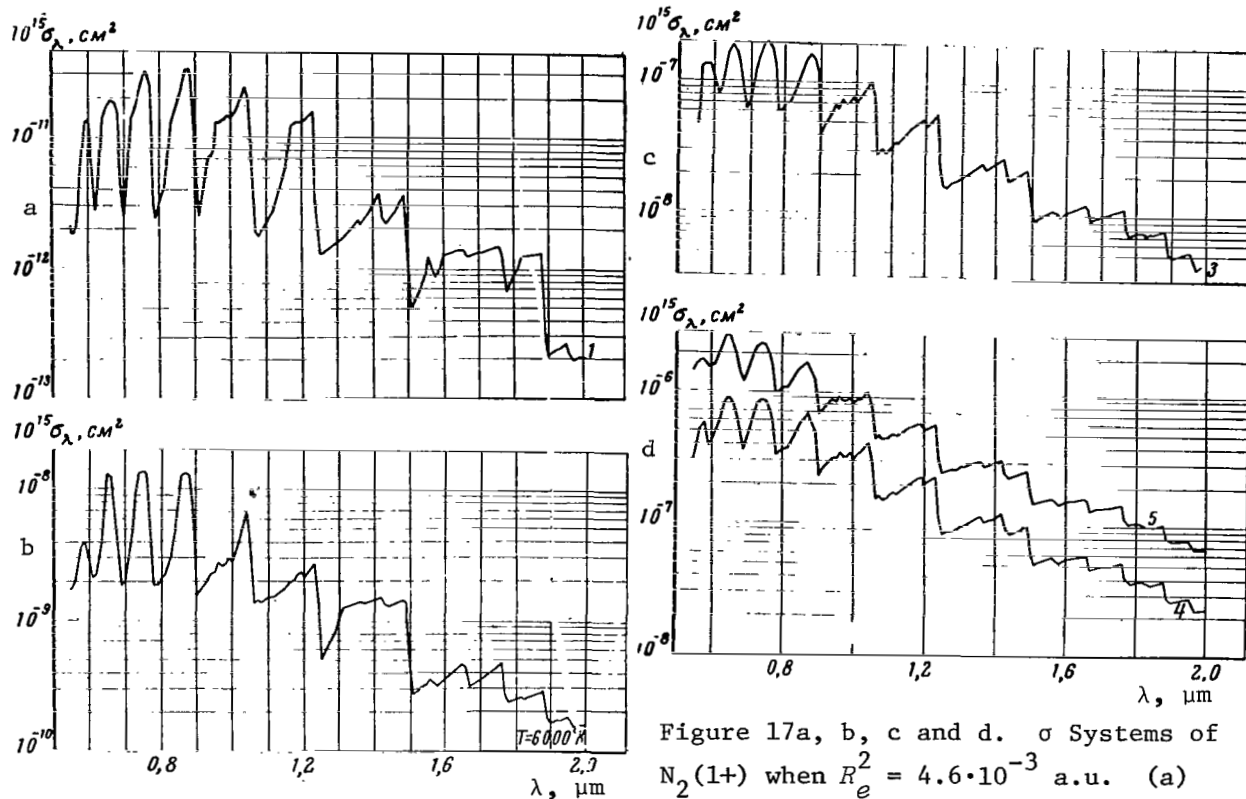
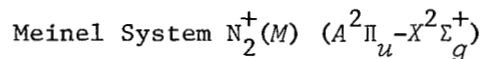


Figure 17a, b, c and d. σ Systems of $N_2(1+)$ when $R_e^2 = 4.6 \cdot 10^{-3}$ a.u. (a) $T = 4,000^\circ K$; (b) 6,000; (c) 8,000; (d) 4 = 10,000; 5 = 12,000.

system, which corresponds to the value of the lifetime from [42].



The bands of the Meinel system lie in the spectral region of 6,000–20,000 Å. The values of R_e can be determined on the basis of estimates of f from [40]. The value of R_e , which corresponds to the value of $f = 0.05$, is equal to 0.424 a.u. Relative measurements of R_e in the narrow spectral region were performed in [43]. In view of the absence of reference data on the dependence of R_e on λ in a broad spectral range, calculations of the absorption cross sections were performed for constant R_e .

In processing the data on the radiation of air and nitrogen [6, 33], with the aid of which R_e was determined, i.e., the dependence for the band systems of $N_2^+(1-)$, $N_2(1+)$, and $N_2(2+)$, we used the composition of air and nitrogen from [44, 45].

The results of calculations of the absorption cross sections at high temperatures for the band systems of $N_2(1+)$, $N_2(2+)$, $N_2(L)$, $N_2^+(1-)$, $N_2^+(M)$, $C_2(Sw)$, $O_2(S-R)$, $NO(\beta)$, $NO(\gamma)$, $CN(R)$, $CN(V)$ are shown in Figures 7-17.

REFERENCES

1. Meyerott, R.: Radiation heat transfer to hypersonic rockets. *Voprosy Rak-
etnoy Tekhniki*, No. 11, 1959.
2. Zel'dovich, Ya. B. and Yu. P. Rayzer: *Fizika udarnykh voln i vysokotemper-
aturnykh gidrodinamicheskikh yavleniy*. (Physics of Shock Waves and High-
Temperature Hydrodynamic Phenomena.) Fizmatgiz, Moscow, 1963.
3. Herzberg, G.: *Molecular Spectra and Molecular Structure. Spectra of Dia-
tomic Molecules*, Vol. 1, New York, 1951.
4. Penner, S. S.: *Kolichestvennaya molekulyarnaya spektroskopiya i izlucha-
tel'naya sposobnost' gazov*. (Quantitative Molecular Spectroscopy and
Emittance of Gases.) Moscow, IL, 1963.
5. Kivel, B., H. Mayer and H. Bethe: Radiation from hot air. 1. Theory of ni-
tric oxide absorption. *Ann. Phys.*, Vol. 2, 1957.
6. Keck, J. C., J. C. Camm, B. Kivel and J. Wentink: Radiation from hot air.
2. Shock tube study of absolute intensities. *Ann. Phys.*, Vol. 7, 1959.
7. Rosen, B.: *Constantes sélectionnées d'ondes spectroscopiques constant les* /60
molecules diatomiques. (Selection Criteria for Spectroscopic Constants
of Diatomic Molecules.) Paris, 1951.
8. *Termodinamicheskiye svoystva individual'nykh veshchestv*. (Thermodynamic
Properties of Individual Substances.) Handbook edited by V. P. Glushko,
Izd-vo AN SSSR, 1962.
9. Kudryavtsev, Ye. N., Ye. F. Gippius and A. M. Pechenov: Determination of
the matrix element of the dipole moment of an electronic transition of
the violet system of CN. *Teplofizika vysokikh temperatur*. (High-Temper-
ature Thermophysics.) Vol. 1, 1963.
10. Nicholls, R. W.: Franck-Condon factors to high vibrational quantum numbers.
I: N_2 and H_2 . *J. Res. Nat. Bureau of Standards*, Vol. 65 A, 1961.
11. Nicholls, R. W.: Franck-Condon factors to high vibrational quantum numbers.
II: SiO , MgO , SrO , AlO , VO , NO . *J. Res. Nat. Bureau of Standards*, Vol.
66 A, 1962.
12. Nicholls, R. W.: The Franck-Condon factor array to high vibrational quan-
tum numbers for the O_2 Schuman-Runge band system. *Canad. J. Phys.*, Vol.
38, 1960.
13. Orthenberg, F. S.: Calculation of Franck-Condon factors for the NO , C_2 ,
and CO band system. *Optika i Spektroskopiya*, Vol. 6, 1964.
14. Wyller, A. A.: Vibrational transition probabilities for the (8,8) matrix
of the $CN(A^2\Pi-X^2\Sigma)$ band system. *Astrophys. J.*, Vol. 127, 1958.
15. Nicholls, R. W.: Vibrational transition probabilities of diatomic mole-
cules, collected results, II: N_2 , CN , C_2 , O_2 , TiO . *Astrophys. J.*,
Vol. 119, 1954.
16. Keck, J. C., R. A. Allen and R. L. Taylor: Electronic transition moments
for air molecules. *Journal of Quantitative Spectroscopy and Radiant
Transfer*, Vol. 3, 1963.
17. Soshnikov, V. N.: Absolute intensities of electronic transitions in

- diatomic molecules. *Uspekhi Fiz. Nauk.*, Vol. 74, No. 2, 1961.
18. Krindach, N. N., N. N. Sobolev and L. N. Tunitskiy: Determination of electronic transition moments of Schuman-Runge bands of the oxygen molecule. *Optika i Spektroskopiya*, Vol. 5, p. 601, 1963.
 19. Antropov, Ye. T., A. P. Dronov, N. N. Sobolev and V. P. Cheremisinov: Experimental determination of the matrix element of the electronic transition and systems of NO molecules. *Doklady AN SSSR, Seriya Fizicheskaya*, Vol. 153, 1963.
 20. Generalov, N. A.: *Issledovaniye vzbuzhdeniya kolebaniy i raspada molekul kisloroda za frontom udarnoy volny. (Investigation of Vibrational Excitation and Decomposition of Oxygen Molecules Behind the Front of a Shock Wave.)* Candidate's Dissertation, MGU, 1963.
 21. Kudravytsev, Ye. M., Ye. F. Gippius, A. N. Pechenov and N. N. Sobolev: Determination of the matrix element of the dipole moment of the electronic transition of the cyanogen violet system II. *Teplofizika vysokikh temperatur. (High-Temperature Thermophysics.)* Vol. I, 1963.
 22. Ambartsumyan, Ye. N., P. V. Ionov, A. A. Kon'kov: Experimental determination of oscillator strength of the violet system of the CN radical. This collection, p. 76.
 23. Ambartsumyan, Ye. N., P. V. Ionov and A. A. Kon'kov: Investigation of the spectral characteristics of gases heated by shock waves. This collection, p. 63.
 24. Bethke, G. W.: Oscillator strengths in the far ultraviolet. II. Oxygen Schuman-Runge bands. *J. Chem. Phys.*, Vol. 31, 1959.
 25. Jarman, W. R.: Franck-Condon factor from Klein-Dunham potentials for the $V = 0$ progression of the Schuman-Runge system of O_2 . *Canad. J. Phys.*, Vol. 4, 1962.
 26. Sigh, N. L. and D. C. Jain: The potential energy curves of the $A'\Sigma^+$ state of LiH, $B^3\Sigma_u^+$ state of O_2 and $d^3\Pi_g$ state of C_2 . *Canad. J. Phys.*, Vol. 40, 1962.
 27. Keck, J., J. Camm and B. Kivel: Absolute emission intensity of Schuman-Runge radiation. *J. Chem. Phys.*, Vol. 28, 1958.
 28. Bethke: Oscillator strength in the ultraviolet. 1. Nitric oxide. *J. Chem.*, Vol. 31, 1959.
 29. Daiber, J. W. and M. J. Williams: Transition probabilities for nitric oxide in the ultraviolet. *Journal of Quantitative Spectroscopy and Radiant Transfer*, Vol. 1, 1961.
 30. Robinson, D. and R. W. Nicholls: Intensity measurements on the O_2 second negative, CO Angstrom and third positive, and NO β and γ molecular band system. *Proc. Phys. Soc.*, Vol. 71, 1958.
 31. Weber, D. and S. S. Penner: Absolute intensities for the ultraviolet bands of NO. *J. Chem. Phys.*, Vol. 26, 1957.
 32. Wallace, L. V. and R. W. Nicholls: The interpretation of intensity distribution in the N_2 second positive and N_2^+ first negative band system. *J. Atmos. and Terr. Phys.*, Vol. 7, 1959.
 33. Allen, R., J. Camm and J. Keck: Radiation from hot nitrogen. *Journal of Quantitative Spectroscopy and Radiant Transfer*, Vol. 2, 1962.
 34. Bennet, R. G. and F. W. Dalby. Experimental determination of the oscillator strength of the first negative bands of N_2^+ . *J. Chem. Phys.*, Vol. 31,

- 1951.
35. Bennet, R. G. and F. W. Dalby: Experimental oscillator strength of the violet system of CN. *J. Chem. Phys.*, Vol. 36, 1962.
 36. Prasad, S. S.: On the vibration of electronic transition moment R_e in the /61 CN violet band system. *Indian J. Phys.*, Vol. 34, 1960.
 37. Dixon, R. N. and R. W. Nicholls: An experimental study of the band intensities in the CN red system. *Canad. J. Phys.*, Vol. 36, 1958.
 38. Turner, R. G. and R. W. Nicholls: An experimental study of band intensities in the first positive system of N_2 . II. The transition moment. *Canad. J. Phys.*, Vol. 32, 1954.
 39. Wurster, W. H.: Measured transition probability of first positive band system of nitrogen. *J. Chem. Phys.*, Vol. 36, 1962.
 40. Nicholls, R. W.: The interpretation of intensity distribution in the CN violet, C_2 Swan, OH violet, and O_2 Schuman-Runge band systems by means of their r -centroids and Franck-Condon factors. *Proc. Phys. Soc., A*, Vol. 69, 1956.
 41. Lyddane, R. H., F. T. Rogers and I. Roach: The abundances of molecules in the solar reversing layer. *Phys. Rev.*, Vol. 60, 1941.
 42. Lichten, W.: Lifetime measurements of metastable states in molecular nitrogen. *J. Chem. Phys.*, Vol. 26, 1957.
 43. Nicholls, R. W.: Relative vibrational transition probabilities and r -centroids for the Meinel ($A^2\Pi_u - X^2\Sigma_g^+$) band system of N_2^+ . *J. Atmos. and Terr. Phys.*, Vol. 12, 1958.
 44. Predvoditelev, A. S. et al.: *Tablitsy termodinamicheskikh funktsiy vozdukh*. (Tables of Thermodynamic Functions of Air.) Izd-vo AN SSSR, 1957.
 45. Pleshanov, A. S.: Composition, thermodynamic and gas-dynamic properties of nitrogen. In: *Fizicheskaya gazodinamika, teploobmen i termodinamika gazov vysokikh temperatur*. (Physical Gas Dynamics, Heat Exchange, and Thermodynamics of High-Temperature Gases.) Izd-vo AN SSSR, 1962.
 46. Watanabe, K., F. Marmo and E. Inn: Formation of the D layer. *Phys. Rev.*, Vol. 90, 1953.
 47. Ditchburn, R. and D. Heddle: Absorption cross section in the vacuum ultraviolet. *Proc. Phys. Soc., A*, Vol. 226, 1954.
 48. Treanor, C. and W. Wurster: Measured transition probabilities for the Schuman-Runge system of oxygen. *J. Chem. Phys.*, Vol. 32, 1960.

INVESTIGATION OF THE SPECTRAL CHARACTERISTICS OF GASES HEATED BY SHOCK WAVES*

Ye. N. Ambartsumyan, P. V. Ionov and A. A. Kon'kov

Investigations of the spectral characteristics of gases at high temperatures and pressures are of interest from various points of view. In particular, calculation of radiant heat flows assumes the dependence of the medium's absorption coefficient on wavelength, temperature and pressure as known. However, even for air, a sufficiently large number of studies are devoted to calculating absorption coefficients whose calculation results present significant discrepancies. An experimental determination of absorption coefficients is all the more necessary for other gas systems. Data on the absorption capacity of gases permit us to determine the squares of the matrix elements of the dipole transition moments, or the oscillator strengths of electronic systems of molecules which are fundamental values in the theory of molecular structure. Furthermore, values of high-temperature gas absorption capacity are necessary for the solution of a number of astrophysical problems. /62

In connection with what has been stated, the spectral characteristics of nitrogen, argon, air, and mixtures of carbon dioxide and nitrogen have been studied within the following ranges: temperature -- 5,000-10,000°K; pressure -- 5-50 atm; and wavelength -- 6,000-3,000 Å.

Experimental Apparatus

A shock tube was used in the experiments which permitted us to record 2.0-10.0 km/sec shock wave velocities. The shock tube operates on the following principle: two gases are separated by a diaphragm; a pressure drop is created at their boundary after the diaphragm is shattered, and a compression wave shaped into a shock wave is propagated in the low-pressure gas. A rarefaction wave is simultaneously propagated in the high-pressure gas on the other side. The shock wave's velocity with an infinitely large pressure drop on the diaphragm is determined by the relationship

$$M = \frac{\gamma_1 + 1}{\gamma_2 - 1} \cdot \frac{a_2}{a_1} = \frac{\gamma_1 + 1}{\gamma_2 - 1} \cdot \frac{\sqrt{\gamma_2 \frac{R}{\mu_2} T_2}}{\sqrt{\gamma_1 \frac{R}{\mu_1} T_1}}, \quad (1)$$

where M is the Mach number of the shock wave; γ is the specific heat ratio; a is the speed of sound; μ is the molecular weight; and T is the temperature.

*The authors express their gratitude to I. K. Pechkin for his assistance.

Subscript 1 indicates that the quantity refers to the gas in the low-pressure chamber. Subscript 2 indicates that the quantity refers to the gas in the high-pressure chamber.

It follows from relationship (1) that it is necessary to have a gas with the lowest possible molecular weight at the highest possible temperature for the production of high-velocity shock waves in the high-pressure chamber. Nitrogen is usually employed as the propelling gas. It permits us to accelerate the shock wave up to 3.5 km/sec in air and gases similar in molecular weight. A detonating mixture is very effective from the point of view of increasing the shock wave's velocity since its combustion products have a relatively low molecular weight. Also, a very noticeable increase in the shock wave's Mach number results by virtue of the great temperature increase of the propelling gas. /63

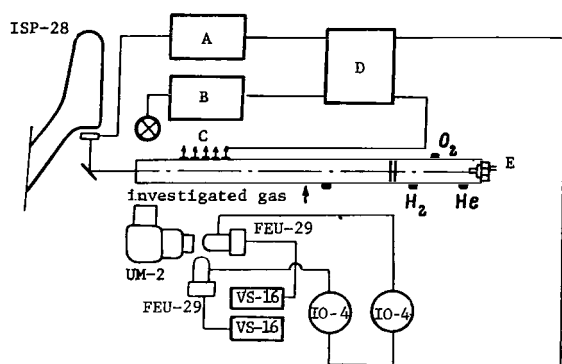


Figure 1. Overall Layout of the Experimental Apparatus. (A) shutter power; (B) DKSSh-1000 power; (C) ionization transducers; (D) synchronization unit; (E) system for initiating combustion of the mixture in the high-pressure chamber.

10^{-2} mm Hg pressure. Then it can be filled with hydrogen or OHHM, i.e., a mixture of oxygen (9%), hydrogen (18%) and helium (73%). Two electrodes are built into the end of the chamber. A discharge which initiates OHHM combustion takes place between the electrodes. When hydrogen was used, the pressure in the chamber before the experiment was 100-150 atm; when OHHM was used, the pressure was 25-35 atm. Monitoring was performed with a standard manometer.

The low-pressure chamber consists of two steel cylinders and a section equipped with observation windows. The overall length of the chamber is 350 cm. Its internal diameter is 3 cm, and its external diameter is 6 cm. The chamber is preliminarily evacuated (RVN-20 pump) to 10^{-2} mm Hg pressure. Then it is filled with the driver gas: a mixture of nitrogen and carbon dioxide in different percentage ratios, nitrogen and air. Pressure (monitored by a standard vacuum gage and an oil vacuum gage) was 5-10 mm Hg.

Using a gas mixture of helium (~80%) and a detonating mixture (~20%) in the high-pressure chamber is even more effective. This mixture's low molecular weight distinguishes it favorably from the detonating mixture; and it permits us to accelerate the shock wave up to 11 km/sec in air and gases similar in molecular weight. A precise expression of the elementary theory and operational principles of the shock tube can be found in [1].

The shock tube has high- and low-pressure chambers which are separated by either a copper or stainless steel diaphragm (Figure 1).

The high-pressure chamber is a steel cylinder 150 cm in length (internal diameter, 3 cm; external diameter, 6 cm). The chamber is first evacuated via a pipeline system (RVN-20 pump) to

The internal surfaces of the high- and low-pressure chambers are chrome-plated. In order to reduce the admixture effect, the inner chamber of the apparatus is thoroughly rubbed with flannel which has been soaked in an alcohol distillate before the experiment. After the experiment, the observation windows are treated with acid. /64

Ionization transducers measure the velocity of the incident shock wave. Signals are recorded on an IO-4 oscillograph. Measurement accuracy of the incident shock wave's velocity is $\pm 3\%$.

The temperature of the gas behind the reflected shock wave is calculated according to the velocity of the incident shock wave, assuming thermodynamic equilibrium and fulfillment of the laws of conservation. The validity of this calculation is corroborated in [2, 3] and by experimental data in [4].

Time Integral Emission Spectra of Gases Heated by Strong Shock Waves

A study of time integral emission spectra of gases is of interest from two points of view, *i.e.*, as an explanation of the basic emitting components and as a preliminary explanation of the emission intensity in the spectrum. Emission spectra were studied in the visible and ultraviolet regions. An ISP-28 quartz spectrograph was placed against the end observation window (Figure 1), so that the luminescence from the incident and reflected shock waves was fixed on a film without time resolution. As subsequent experiments indicated, the emission intensity from the gas behind the incident wave is at least one order lower in comparison to the emission intensity of the gas heated by the reflected wave. Therefore, it is impossible to take its effect into account. An ISP-51 glass spectrograph was placed against the side observation window (Figure 1). Then, depending on its position, it either recorded the luminescence spectrum of the gas behind the reflected shock wave or the luminescence spectrum of gas behind the incident wave. Furthermore, experiments were carried out where the ISP-28 spectrograph was placed against the side observation window. The spectra were recorded on *D* or *Panchromatic-X* film. Representative spectrograms are illustrated in Figures 2-6.

The following similarities exist in nitrogen, oxygen, carbon dioxide and air spectra:

- 1) the presence of continuous emission is characteristic in the spectra;
- 2) lines of an admixture of sodium, calcium, iron, copper, chromium, and bands of calcium oxide are clearly projected.

With the temperature and pressure increase behind the reflected shock wave (at velocities of the travelling wave 5-6 km/sec and higher), continuous emission begins to play a deciding role, and reversed lines of sodium, calcium, and copper (see Figure 3) appear on its background. The appearance of reversed lines of the admixture attest to the presence of large temperature gradients in the heated gas.

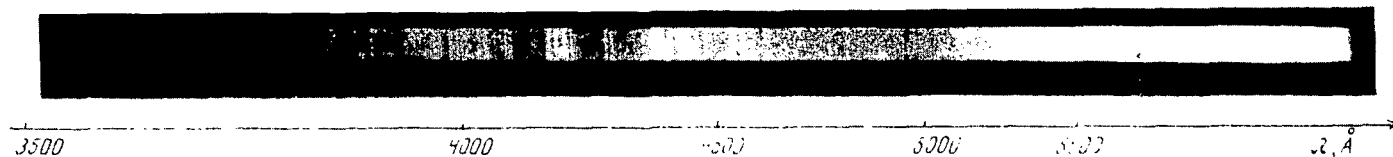


Figure 2. Integral Emission Spectrum of Air.

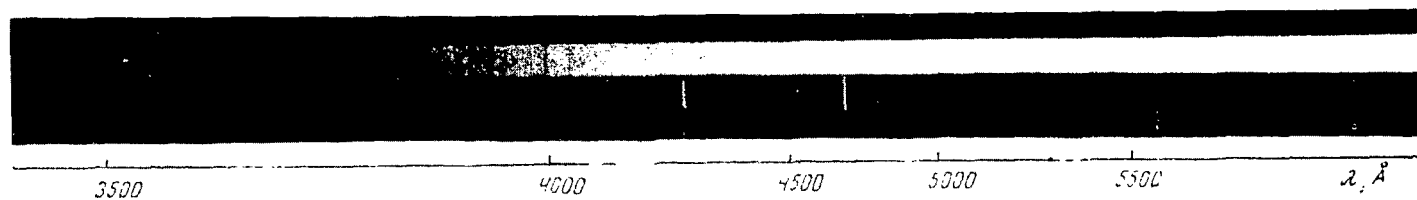


Figure 3. Integral Emission Spectrum of Nitrogen.

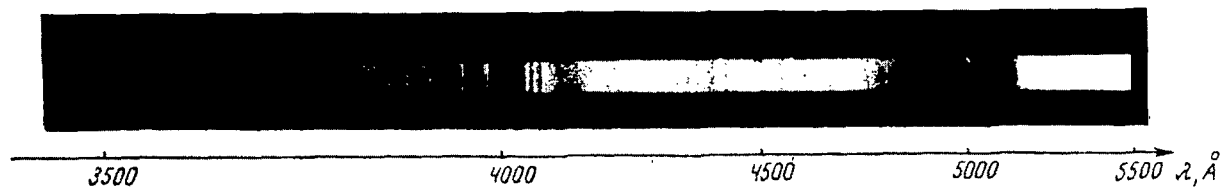


Figure 4. Integral Emission Spectrum of Gas Mixture: 75% CO₂ + 25% N₂.

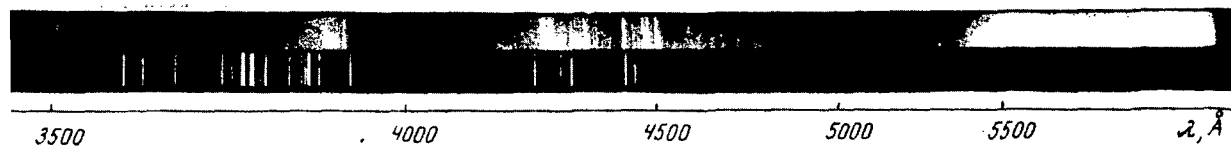


Figure 5. Integral Emission Spectrum of Gas Mixture: 30% CO₂ + 70% N₂.

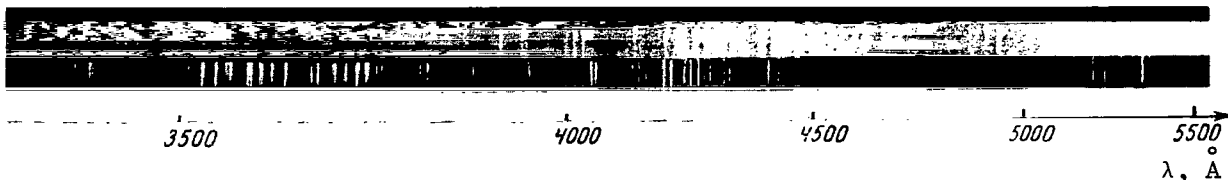


Figure 6. Integral Emission Spectrum
of Gas Mixture: 50% CO + 50% O₂.

In the air spectrum, we find the following bands which belong to the CN violet system: 4216, 4497.2, 4181.0, 4167.8, 3883.4, 3871.4, 3861.4 and 3854.7 Å. The authors of [5] established a similar fact during investigation of emission spectra of air heated by shock waves.

The emission spectra of CO₂ and N₂ mixtures are illustrated in Figures 4-5. It follows from the illustrated spectrograms that continuous emission and Na, Ca, Fe, etc. admixture lines are present in spectra of the mixtures indicated, just as in the cases described above.

The appearance of a CN violet system in the spectrum is characteristic for mixtures of carbon dioxide and nitrogen. The CN violet system in the mixtures indicated above is more intensive in comparison with the CN bands which are present in the emission spectrum of air. Thus, for example, the 4578 Å band in 65 the emission spectrum of air is barely visible and can only be identified hypothetically, whereas in the mixture spectra, it is clearly visible in its entirety.

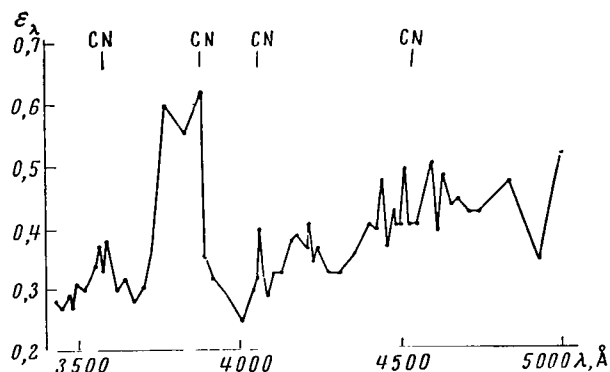


Figure 7. Dependence of ϵ_λ of Gas Mixture 75% CO₂ + 25% N₂ on λ . $T = 9,200^\circ\text{K}$; $p = 40 \text{ atm}$; $l = 3 \text{ cm}$.

In the emission spectrum of the mixture 50% CO + 50% O₂ behind the front of the detonation wave (see Figure 6), the velocity of the incident wave is $v = 7 \text{ km/sec}$; and in the wavelength region of 4200-3000 Å, nearly 100 bands of the Fox-Daffendack-Barker CO₂ molecular system are found, and about 10 bands are identified with emission bands of the OH radical. In addition, we find continuous emission and lines of the admixtures of iron, sodium, calcium and copper, and calcium oxide bands both in this mixture spectrum, as in the spectra described above.

Interpretation and identification of spectra recorded by the ISP-51 glass spectrograph indicated that there is no principal distinction between the latter 66 and those examined above. Iron, calcium, sodium, etc. lines were found in the visible region of the spectra of all of the gases mentioned above. Using a

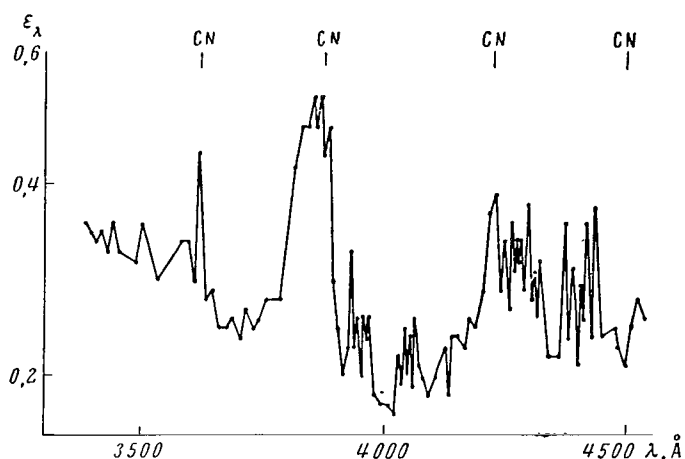


Figure 8. Dependence of Absorption Capacity of Gas Mixture 30% CO_2 + 70% N_2 on Wavelength. $T = 9,200^\circ\text{K}$; $p = 40 \text{ atm}$; $l = 3 \text{ cm}$.

illustrated above were recorded on an MF-4 microphotometer. A correction for film sensitivity was introduced into the distribution S obtained after photometry from wavelength λ . Inasmuch as the intensity in the continuous spectrum depends on spectrograph dispersion, a correction for spectrograph dispersion was introduced into the intensity distribution in the continuous spectrum. The lines of the Fe, Na, Ca, etc. admixtures were excluded from examination.

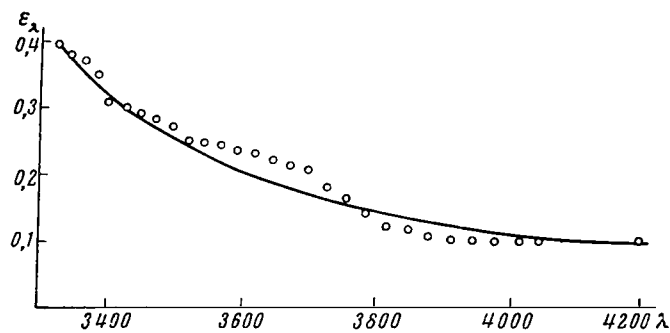


Figure 9. Dependence of ϵ_λ of Nitrogen on λ . $T = 12,000^\circ\text{K}$; $p = 50 \text{ atm}$; $l = 3 \text{ cm}$.

factor between intensity in the gas spectrum and the latter's values recorded after processing the spectrogram does not depend on wavelength, a comparison of photographic and photoelectric data for only one wavelength is sufficient for determination of the indicated normalizing factor. Having determined the normalizing factor, it is possible to calculate the intensity distribution in the emission spectrum of the gas in absolute units. Then the absorption capacity of the gas can be calculated using Kirchhoff's law (gas temperature was calculated according to the incident wave's velocity assuming the fulfillment of the

section with Duralumin observation panes led to the appearance of a highly intensive aluminum oxide band system. After replacing the above section with a steel one, aluminum oxide bands were not registered.

After identification of the bands and lines detected in the spectra of the indicated gases, it was of interest to compare their intensities. This enabled us to explain the role of separate band systems, and the role of the various gas components. With this in mind, the spectrograms described above were processed by heterochromatic photometry methods. Microphotograms of the spectrograms which are il-

Spectrograms processed in this way permitted us to obtain the dependence of emission intensity on wavelength in relative units.

In order to normalize the recorded dependence of emission intensity on wavelength, we used data from the photoelectric chamber of the apparatus (see Figure 1) through which absolute measurements of the emissivity of the (0-0) band of the CN violet system were carried out [4]. Insofar as the proportionality

conservation laws on the front of the shock wave).

Figures 7-9 illustrate the dependence of the absorption capacity ϵ_λ on wavelength for mixtures of 75% CO₂ + 25% N₂, 30% CO₂ + 70% N₂ and nitrogen, respectively. The following quantity is denoted by ϵ_λ , which is plotted along the /67 ordinate axis:

$$\epsilon_\lambda = (1 - e^{-\sigma_\lambda c N l}), \quad (2)$$

here σ_λ is the absorption cross section; c is the molecular concentration of the substance responsible for the emissive absorption of the given wavelength; N is the total number of particles per unit volume; l is the length of the path on which absorption proceeds, being equal to 3 cm.

An analysis of the data illustrated in Figures 7-8 permitted us to conclude that the CN violet system plays a vital role in the emission of carbon dioxide and nitrogen mixtures. In connection with this, we acquired extremely precise knowledge of the oscillator strength of the CN violet system.

Investigation of the Distribution of Emission and Absorption Capacities in the Visible and Ultraviolet Regions of the Spectrum.

A preliminary investigation of the integral spectra of the gases indicated above permitted us to explain the role of individual components and to obtain data on the absorption coefficients and the dependence of emission on time. In order to understand absorption coefficients precisely, it is necessary to examine time-evolved spectra instead of time-integral spectra since emission of the gas cooled after contact between the reflected shock wave and the contact region can make a substantial contribution to intensity distribution.

Drum cameras are usually used to record time-evolved spectra. They possess the shortcoming of having to modify the spectrograph plateholder. The latter, as a rule, impairs the spectrograph's quality and is not always convenient. The following method is proposed here for recording spectral scanings: at a certain angle to the spectrograph slit we place a second slit having a width of a few tenths of a mm. It will move relative to the spectrograph slit at a speed v .

The total time required to fix the spectral scanning is determined by the relationship

$$t = \frac{\bar{S} + l_0 \sin \alpha}{v}. \quad (3)$$

Time resolution is

$$\tau = \frac{\bar{S}}{\bar{S} + l_0 \sin \alpha} t. \quad (4)$$

The height of the line on the spectrogram is

$$h = k\tilde{S} \cot \alpha, \quad (5)$$

here $\tilde{S} = S_0 + S_{00} \cos \alpha$; $\tilde{S} = S_0 + S_{00}/\cos \alpha$; S_0 is the width of the spectrograph slit; S_{00} is the width of the inclined shutter slit; l_0 is the length of the inclined shutter slit; α is the angle of inclination; v is the speed of the inclined slit; k is the magnification factor of the spectrograph.

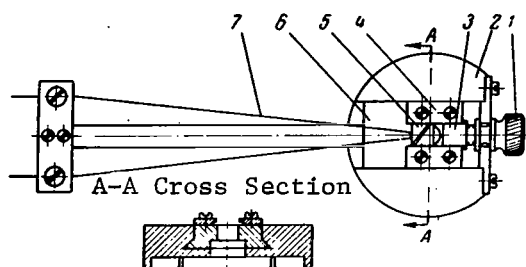


Figure 10. Design Diagram of Mechanical Portion of Shutter.

The shutter is designed on the basis of what has been stated. The schematic diagram of the shutter is illustrated in Figure 10. Here, 1 is the platform on which the parts of the shutter are fastened; 6 is the slider, in the guides of which the inclined slit 5 is fastened; 2 is a screw by which the slit is set in starting position; 3 is the inertial insert which prevents secondary opening of the spectrograph slit; 7 is a Nichrome wire which actuates the shutter slit.

The shutter operates on the following principle: a current pulse arriving /68 from the power supply heats the wire, which then expands. The free end of the wire begins to move and actuates the shutter. At each given moment, the spectrum (height h) is fixed on the spectrogram. Then, as the slit moves, the spectrum's position also moves. If the emission intensity changes in time, the blackening along the spectral line will also change correspondingly on the spectrogram. Thus, the time-evolved gas emission spectrum can be recorded with time resolution τ .

The shutter, which is constructed on the basis of the stated design diagram, permitted us to expand the spectrum with a time resolution of $\tau = 5 \mu\text{sec}$. The total time of spectral scanning was 30 μsec and more.

The electrical schematic of the shutter is illustrated in Figure 11. The circuit operates on the following principle: an impulse from the ionization transducer initiated by the shock wave triggers the synchronization block, which then opens the TGI 400/3.5 thyatron. Then the condenser C is discharged through the Nichrome wire. Voltage in the condenser casings was 800-1,400 V before the experiment.

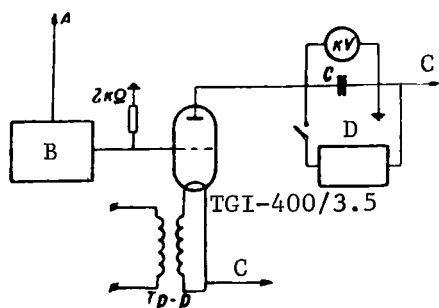


Figure 11. Schematic Diagram of Electrical Portion of Shutter. (A) cable to ionization transducer; (B) synchronization block; (C) cable to shutter; (D) charging unit.

The overall setup of the experiment was exactly as it was in the investigation of time-integral emission spectra.

Figures 12-13 illustrate time-evolved emission spectra of a mixture of carbon dioxide and nitrogen. The ISP-28 spectrograph was placed so that its optical axis coincided with the tube axis. The beginning of scanning coincides with the moment of the incident shock

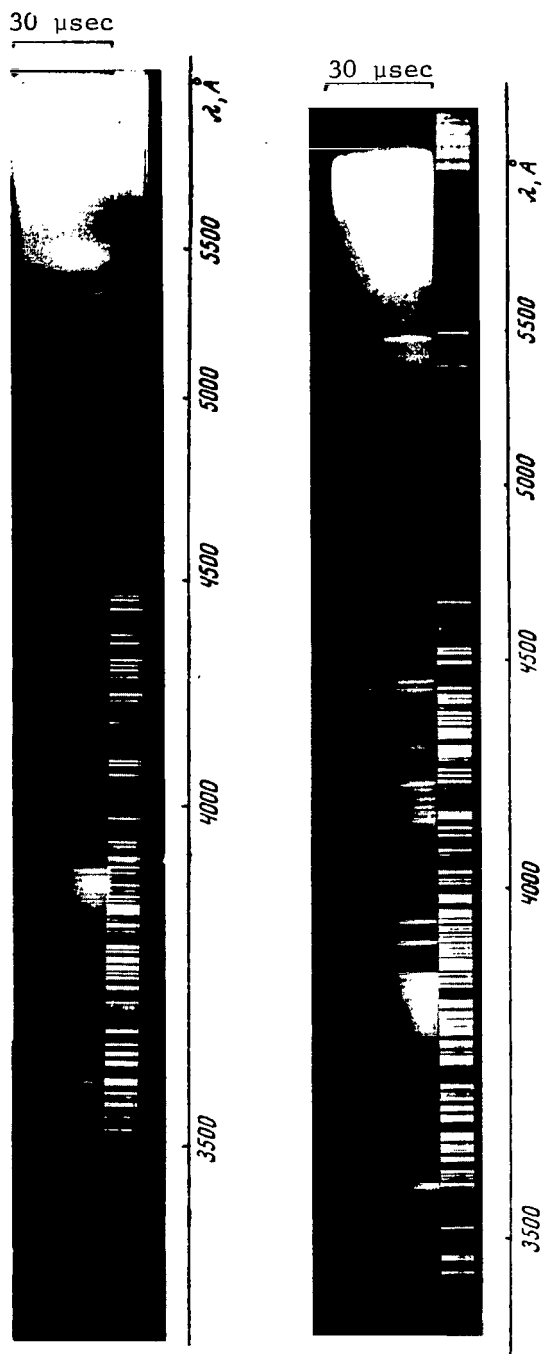


Figure 12 (left). Time-Evolved Emission Spectra of a Gas Mixture of 75% CO_2 + 25% N_2 .

Figure 13 (right). Time-Evolved Emission Spectra of a Gas Mixture of 30% CO_2 + 70% N_2 .

wave's reflection from the end window.

The spectrum of the CN radical's violet system was seen clearly and was unmistakably identified. Lines of the sodium, calcium and iron admixtures were seen. While photographing spectral scannings in a situation where the spectrograph was placed against the side window, a 5 μsec increase of emission related to the admixtures was seen.

"Secondary" emission, a continuum, on whose background reversed Na and Ca lines were seen, followed the first emission pulse of the gas heated by a reflected shock wave. Secondary emission is apparently related to the cooling gas; its beginning coincides approximately with the moment of contact of the reflected shock wave and the contact region. Since the entire action time of the shutter is limited to 30-50 μsec , it was impossible to trace the development of the secondary emission spectrum. However, emission oscillograms recorded by the photoelectric chamber indicate that it does not remain noticeable for more than 100 μsec [4]. Secondary emission intensity is most noticeable in the red-yellow region of the spectrum. Thus, if it is possible to disregard emission related to a gas behind the incident wave during quantitative evaluation of emissivity distribution in the gas spectrum by integral spectra, secondary emission can introduce a noticeable error. The latter is related to this: notwithstanding the fact that secondary intensity emission is a few times weaker than primary, it acts upon the film over a significantly long period. The error introduced into the distribution

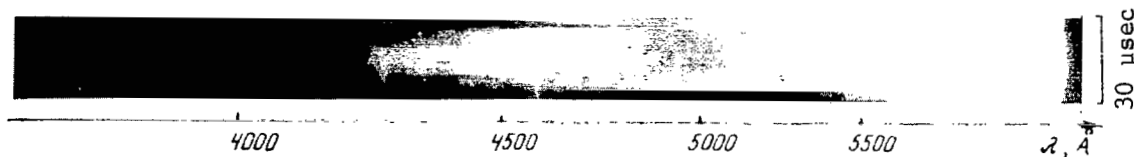


Figure 14. Time-Evolved Emission Spectrum of Nitrogen.

of emissivity during the processing of integral spectra plays the most essential role in the red-yellow region of the spectrum since secondary emission is most intensive here. In the violet and ultraviolet regions of the spectrum, the intensity of the latter is close to the threshold of film sensitivity and makes a relatively small contribution to the integral spectrum.

Figure 14 illustrates a time-evolved emission spectrum of nitrogen. Gas temperature behind the reflected shock wave is 6,000°K and pressure is 5 atm. The bands of the electronic system of nitrogen are not identified with certainty, since the temperature range up to 10,000°K in the given region of the band spectrum of the first and second positive N_2 systems and the first negative N_2^+ system overlap significantly.

As in the spectra of the carbon dioxide and nitrogen mixtures, an admixture of iron, sodium and calcium is present in the nitrogen spectrum. Secondary emission has the very same character as in the previous case.

Lines of the admixtures enumerated above are also present in the air and argon spectra (Figures 15-16). Furthermore, in the air spectrum, bands of the CN violet system are visible. They are present in the gas by virtue of the admixture of carbon dioxide in the air. Argon lines were not discovered; possibly this is related to the fact that argon and iron lines are next to each other in relative proximity ($\sim 1 \text{ Å}$) in the visual and ultraviolet regions of the spectrum.

The spectral scanings were processed by the heterochromatic photometry method. In order to take the variation in film sensitivity with wavelength into account, the spectrum of a standard light source (SI-8-200 tungsten lamp) was photographed next to the gas spectrum.

The following expression is valid for the distribution of blackness in the gas spectrum:

$$S_1(\lambda) = \gamma(\lambda) \log[kt_1^{p1} (d\lambda/de) \epsilon_1(\lambda, T_1) B(\lambda, T_1)] - \gamma(\lambda) j(\lambda). \quad (6)$$

For the standard light source:

$$S_2(\lambda) = \gamma(\lambda) \log[kt_2^{p2} (d\lambda/de) \epsilon_2(\lambda, T_2) B(\lambda, T_2)] - \gamma(\lambda) j(\lambda). \quad (7)$$

Thus, it follows that

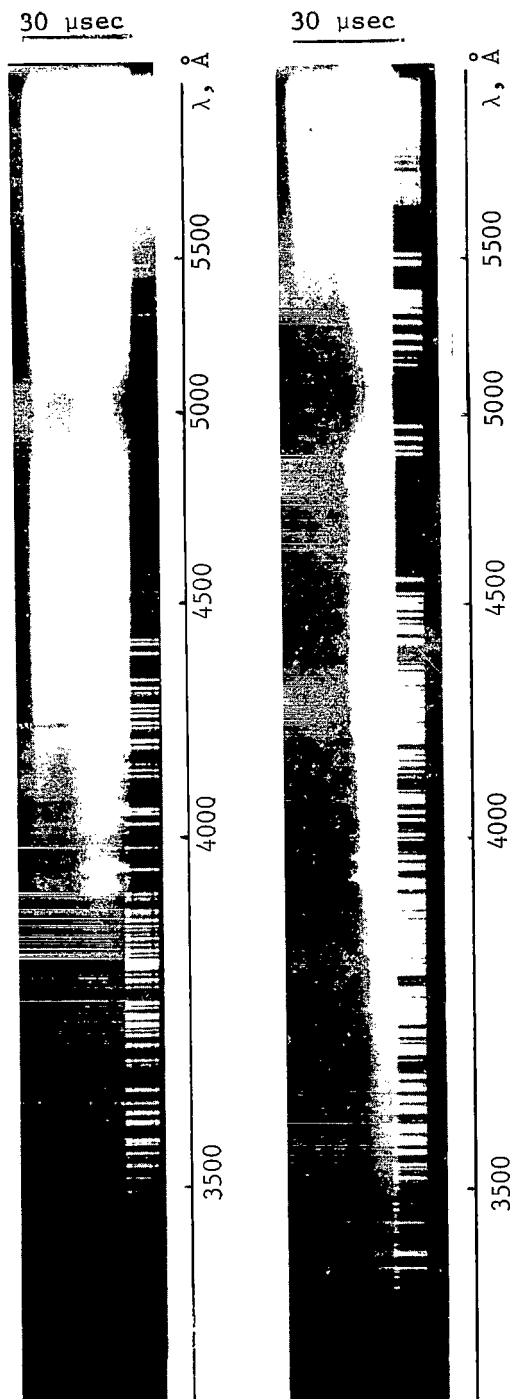


Figure 15 (left). Time-Evolved Emission Spectrum of Air.

Figure 16 (right). Time-Evolved Emission Spectrum of Argon.

$$\frac{S_1(\lambda) - S_2(\lambda)}{\gamma(\lambda)} = \log \left[\frac{\epsilon_1(\lambda, T_1)}{\epsilon_2(\lambda, T_2)} \frac{B(\lambda, T_1)}{B(\lambda, T_2)} \right] + \log \frac{[t_1]^{p_1}}{[t_2]^{p_2}} \quad (8)$$

Here, $\epsilon_1(\lambda, T_1)$ and $\epsilon_2(\lambda, T_2)$ are the degree of blackness of the gas and the standard source, respectively; $B(\lambda, T_1)$ and $B(\lambda, T_2)$ are the black body emissivity at gas temperature and at the temperature of the standard source; $\gamma(\lambda)$ is the film's contrast factor; $j(\lambda)$ is film sensitivity; p is Schwartzschild's constant; t_1 and t_2 are exposure times; and k is the proportionality factor.

If the temperature of the emitting gas is known, then, from relationship (8) /71

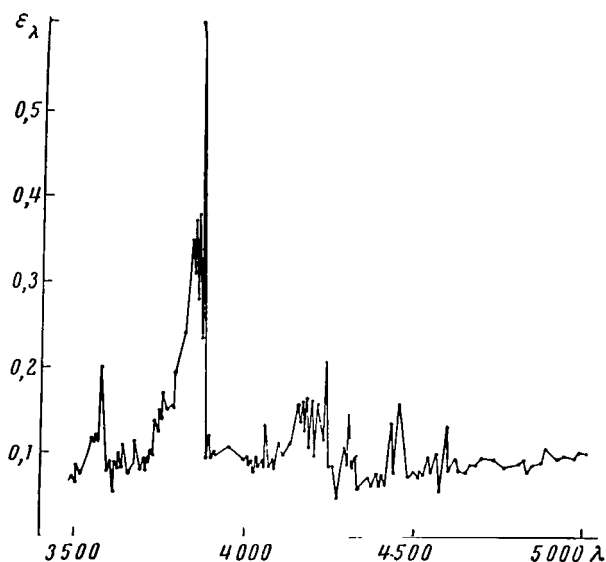


Figure 17. Dependence of ϵ_λ of a Gas Mixture of 75% CO_2 + 25% N_2 on λ . $T = 8,000^\circ\text{K}$; $p = 50 \text{ atm}$; $l = 1 \text{ cm}$.

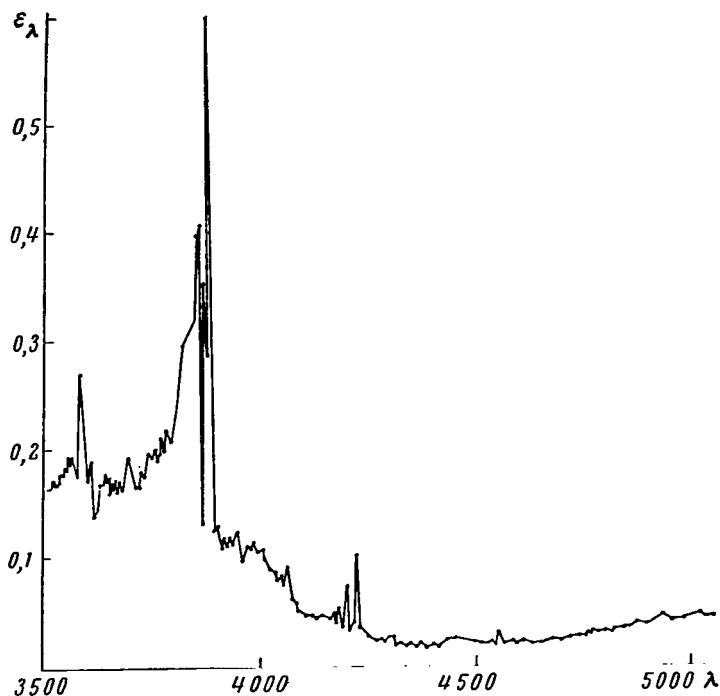


Figure 18. Dependence of ϵ_{λ} of a Gas Mixture of 30% CO_2 + 70% N_2 on λ . $T = 8,000^{\circ}\text{K}$; $p = 30$ atm; $l = 1$ cm.

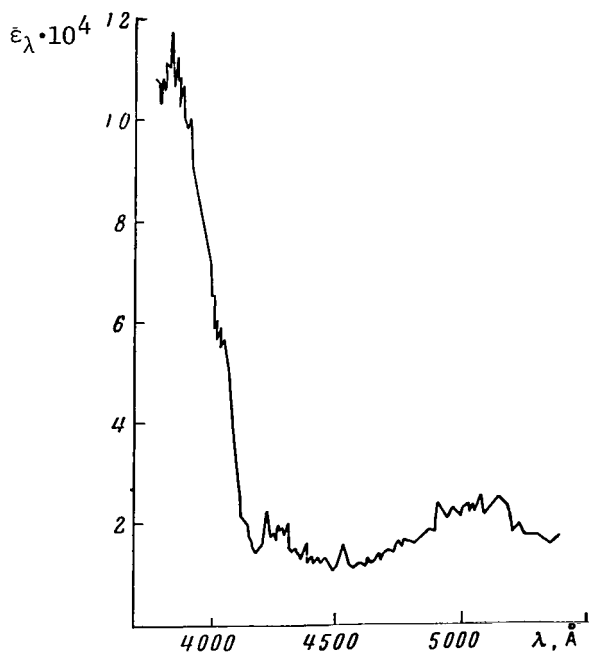


Figure 19. Dependence of ϵ_{λ} of Nitrogen on λ . $T = 6,000^{\circ}\text{K}$; $p = 5$ atm; $l = 1$ cm.

we can find the absorption capacity of the gas with an accuracy up to the constant factor which must be found. The normalizing factor k was determined by data recorded over the photoelectric channel.

Figures 17-19 illustrate the absorption ability distributions in the spectra of carbon dioxide and nitrogen, and nitrogen mixtures. They were recorded by the method indicated previously. Accuracy of the experimental results obtained is $\pm 40\%$. The absorption capacity measurement error is derived from the measurement error of the normalizing factor, $\pm 20\text{-}25\%$, and the error during measurement of intensity by the heterochromatic photometry method $\pm 15\%$.

Conclusion

1. The presence of the following are characteristic for the emission spectra of the gases enumerated in this report: (a) continuous emission; (b) lines of Fe, Cr, Cu, Ca, etc. admixtures; (c) bands of the CN violet system and presumably bands of the N_2 (1+), N_2 (2+), and NO (β) systems in the spectra of air, nitrogen, CO_2 and N_2 mixtures.

2. Time-evolved emission spectra of gases and gas mixtures were recorded.

Secondary emission was discovered in the time evolved spectra.

3. The spectra were quantitatively processed by heterochromatic

photometry methods. As a result, we recorded the distribution of spectral absorption capacity in reference to the unit length of the absorbent gas layer in dependence on wavelength for nitrogen and nitrogen and carbon dioxide mixtures. The CN violet system makes a noticeable contribution to the emission of carbon dioxide and nitrogen mixtures. The accuracy of the results was $\pm 40\%$

REFERENCES

1. Resler, E., S. C. Lin and A. Kantrowitz: The production of high-temperature gases in shock tubes. *Appl. Phys.*, Vol. 23, No. 12, p. 1390, 1952.
2. Fayzullov, F. S.: Pyrometric investigation of air, nitrogen and argon states behind a shock wave. *Tr. Fizicheskogo In-ta AN SSSR*, Vol. 8, 1962.
3. Kudryavtsev, Ye. M., I. N. Sobolev, L. N. Tunitskiy and F. S. Fayzullov: Pyrometric investigation of a gas behind a reflected shock wave. *Tr. Fizicheskogo In-ta*, Vol. 8, 1962.
4. Ambartsumyan, Ye. N., P. V. Ionov and A. A. Kon'kov: Experimental determination of oscillator strength of the violet system of the CN radical. *Supra*, p. 76.
5. Keck, J., B. Kivel and J. Wentink: Emissivity of air heated to a high temperature. In: *Udarnyye Truby. (Shock Tubes.)* Moscow, IL, 1962.

AN EXPERIMENTAL DETERMINATION OF OSCILLATOR STRENGTH
OF THE VIOLET SYSTEM OF THE CN RADICAL*

Ye. A. Ambartsumyan, P. V. Ionov and A. A. Kon'kov

Introduction

/72

Oscillator strength, or the square of the matrix element of the dipole moment of an electronic transition, is a fundamental quantity in the theory of molecular structure. The currently available methods for the theoretical calculation of oscillator strengths provide values which disagree essentially with those measured experimentally (sometimes by one order of magnitude). It is extremely important to determine the values of oscillator strengths from the standpoint of calculating radiant heat fluxes in various problems of heat exchange at high temperatures, and also for a number of astrophysical problems. Reference [1] investigates the absorption coefficients of gases in a wide range of wavelengths and indicates that the emission of the violet system of CN provides an essential contribution to radiant heat flux.

This article is concerned with the measurement of the radiation and absorption capacity of the (0,0) band of the violet system of CN in the temperature range of 5,000-10,000°K, which has made it possible to determine the size of the matrix element of the dipole transition moment of the given system.

The data on the oscillator strength of this system were extremely contradictory at the beginning of this investigation. The first data obtained by White [2], who measured absorption in the bands of the violet system of CN, excited by a discharge which was passed through C_2N_2 , provided the value of $f_e = 0.024$; however, he indicated in his subsequent work [3] that this value should be considered as the lower limit of the true value of oscillator strength, and gave the value of $f_e = 0.1$. Soshnikov's survey [4] gave the value of $f_e = 0.08$, which was obtained on the basis of White's subsequent work with a correction for reabsorption. Reference [5] gives an evaluation of oscillator strength of the violet system; and the obtained value of 0.013, in the opinion of the authors of that paper, is understated.

The value of $f_e = 0.027$ is obtained in [6] on the basis of the lifetime variation of the excited $B^2\Sigma^+$ state. The shortcoming of this work consists in the fact that the possible additional population of the $B^2\Sigma^+$ level due to cascade transitions from a lower-lying level is not taken into account. In [7], which was conducted simultaneously with this work, the value of $f_e = 0.03$ was obtained.

In connection with the data presented above, investigations were undertaken on the radiation and absorption capacity of the (0,0) band of the violet system of CN.

*The authors express their gratitude to I. K. Pechkin for his assistance.

Measurement of the Radiation Capacity of the (0,0) Band of the Violet System of CN

A shock tube was used in the experiments, which made it possible to obtain shock wave velocities to 10 km/sec. The design of the shock tube and the general arrangement of the experiment are outlined in [1]. The method consisted in the following: the gas, which was situated behind a reflected shock wave, was admitted into the input of a UM-2 monochromator and then recorded on an IO-4 oscillograph by means of a FEU-29 photoelectronic multiplier. A VS-16 stabilized rectifier supplied the power to the photomultiplier. The triggering of the oscillograph by means of a synchronization block was coordinated appropriately with the arrival of the reflected shock wave. /73

In order to improve the space resolution of the system, a slit approximately 0.15 cm in width was installed at a distance of 4 cm from the investigated gas layer and 0.5 cm from the end of the shock tube. The space resolution of the system in this case amounted to approximately 0.25 cm.

The system was graduated in absolute units by means of a SI-8-200 tungsten ribbon tube which was installed at the point of intersection of the axis of the shock tube and the optical axis of the system. This tube was used to monitor the decrease in the transmission coefficient of the glass and its variation from experiment to experiment after the appropriate cleaning. The transmission coefficient was monitored also by a DKSSh-1000 xenon tube. A clearly expressed dependence of the decrease in the transmission coefficient of the glass on the nature of the gas situated behind the front of the shock wave was not detected. It basically depends on the parameters of the incident gas flow. The transmission coefficient of the glass decreases during one experiment by approximately 1.3-1.5 times with a velocity of the incident wave at 3.0-3.5 km/sec, and up to 2 times at a velocity of the incident wave 5-6 km/sec.

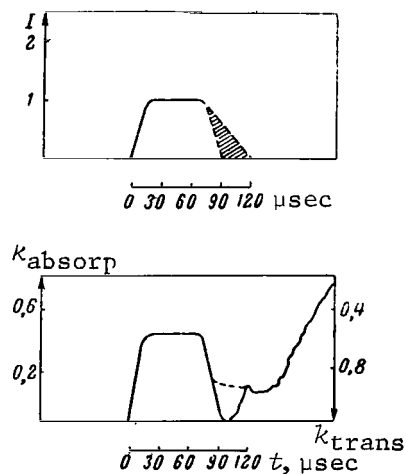


Figure 1. Dependence of I and k of a Gas Heated by a Reflected Shock Wave on t .

Figure 1 illustrates the characteristic time dependence of the radiation intensity of a gas ($\lambda = 3883 \text{ \AA}$) which has been heated by a reflected shock wave when hydrogen is in the high-pressure chamber.

Figure 2 illustrates an oscillogram of the radiation intensity of the (0,0) band of the violet system when an oxygen, hydrogen and helium mixture (OHHM) was employed in the high-pressure chamber. It can be seen in Figure 2 that the intensity behind the main pulse of radiation decreases to a certain relatively small value, which remains approximately constant for 100-150 μsec . /74

If the gas heated by the shock wave is in a state of thermodynamic equilibrium, after consulting Kirchhoff's law,

$$\frac{I(\lambda, T)}{\varepsilon(\lambda, T)} = B(\lambda, T), \quad (1)$$

where $I(\lambda, T)$ is the radiation capacity of the investigated gas layer; $\varepsilon(\lambda, T)$ is the absorption capacity of the investigated gas layer; and $B(\lambda, T)$ is Planck's function for the given temperature.



Figure 2. Oscillogram of the Radiation of a Gas that Has Been Heated by a Reflected Shock Wave.

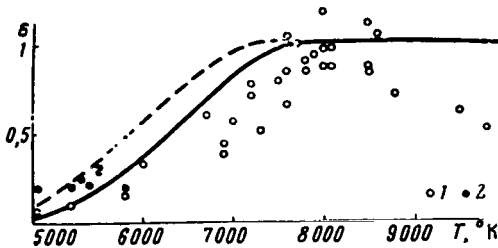


Figure 3. Dependence of Absorption Capacity of the (0,0) Band of the Violet System of CN on Temperature. (1) according to the radiation method; (2) according to the absorption method.

graph to $\pm 10\%$, the operational stability of the FEU-29 photoelectronic multiplier $\pm 5\%$, reproduction and recording accuracy by means of a standard light-flux oscillograph $\pm 10\%$, and amounts to $\pm 25\%$ on the whole.

Measurement of the Absorption Capacity of the (0,0) Band of the Violet System of CN

To increase the reliability of the results, the absorption coefficient of the (0,0) band of the violet system of CN was measured directly. On the one hand, the data obtained by this method were substantiated by the data obtained by the method described above; on the other hand, measurement of the radiation and absorption capacities made it possible to determine the gas temperature on the basis of Kirchhoff's law. The intensities of the incident and departed radiation in this case are related by the following expression:

Since the radiation capacity has been measured, and the temperature of the gas behind the reflected shock wave can be calculated according to the velocity of the shock wave, the absorption coefficient of the gas layer also can be determined for the given wavelength.

The absorption capacities $\varepsilon(\lambda, T)$ of the (0,0) band of the violet system of CN ($\lambda =$

$3,888 \text{ \AA}$, spectral region $\Delta\nu = 100 \text{ cm}^{-1}$) obtained by this procedure are illustrated in Figure 3 for the following gas mixture: 75% CO_2 + 25% N_2 . The data to $6,000^\circ\text{K}$ (velocity of incident wave to 3.5 km/sec) were obtained with the use of hydrogen in the high-pressure compartment, while OHHM was employed as the propelling gas for the others.

The accuracy of measurement by the described method is derived from the accuracy of measuring the potential difference by means of an IO-4 oscillo-

$$\frac{I_{\lambda}}{I_{\lambda 0}} = e^{-k_{\lambda} l}, \quad (2)$$

Here $I_{\lambda 0}$ is the intensity of incident radiation: I_{λ} is the intensity of departed radiation; k_{λ} is the absorption coefficient per unit length. /75

The absorption capacity is related to I_{λ} , $I_{\lambda 0}$, and k_{λ} by the following expression:

$$\epsilon_{\lambda} = \frac{I_{\lambda 0} - I_{\lambda}}{I_{\lambda 0}} = 1 - e^{-k_{\lambda} l} \quad (3)$$

A DKSSh-1000 xenon tube was employed as an auxiliary source: the tube was installed in the focal plane of the first lens. A parallel light beam, in passing the investigated gas layer, was focused on the entrance slit of the monochromator. A diaphragm was placed in the path of the light flux in such a way that this flux struck only the upper portion of the slit; therefore, only the radiation of the investigated gas struck the lower portion of the monochromator slit [1].

Radiation from both parts of the entrance slit proceeds correspondingly to two FEU-29 photoelectronic multipliers. The signals are then recorded on IO-4 oscillographs.

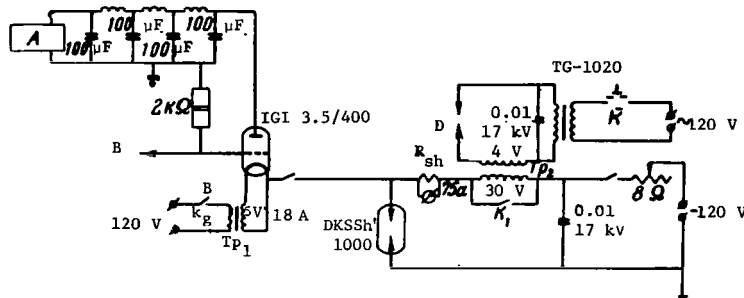


Figure 4. Schematic of DKSSh-1000 Xenon Tube Power Supply. (A) long-line charging rectifier; (B) to system which opens TGI-400/3.5 thyatron; (C) heating circuit of TGI-400/3.5 thyatron; (D) adjustable discharger.

Neutral light filters were installed between the second lens and the entrance slit of the monochromator, which made it possible to vary the sensing system within wide limits, leaving its other parameters unchanged. The relationship between the sensitivity of the system's channels on the whole was monitored by the following methods:

1) The section with the viewing windows was removed and the radiation pulse of the DKSSh-1000 tube was recorded on both channels;

2) An SI-8-200 tube was installed in place of the section with the viewing windows and its radiation was recorded on both channels.

3) The radiation of the investigated gas was recorded on both channels of the system. In this case the DKSSh-1000 tube was turned off and the sensitivity of the system was increased by selecting neutral light filters in such a way as to reliably fix the gas radiation.

The parameters of the system were selected in such a way that the magnitudes of the signals on both channels were approximately identical.

Figure 4 is a schematic of the power supply of the DKSSh-1000 xenon tube. After actuation of key K , the discharger breaks down, and then the discharge interval of the DKSSh-1000 tube also breaks down. The power supply circuit of the tube is closed in a continuous mode. The tube requires a current of 10-50 A in this mode.

In order to raise the brightness temperature of the tube and thereby expand the range of measurements of the absorption coefficients by means of the given method, additional pulsed feeding of the xenon tube was accomplished, which consisted in the fact that the long line which had been preliminarily charged to a voltage of 300-600 V was discharged through the tube after arrival of a triggering pulse from the synchronization block at the TGI-400/3.5 thyatron. The long line consisted of four IM-3-100 capacitors and four inductance coils. The inductances were selected in such a way that the additional radiation pulse of the xenon tube had a trapezoidal shape (Figure 5); the size of the portion where the radiation is constant is 200 μ sec. /76

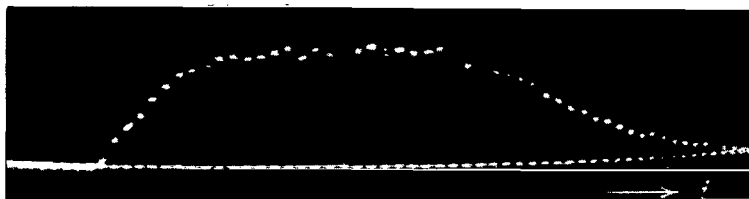


Figure 5. Oscillogram of Radiation Pulse of Xenon Tube.

The radiation pulse of the xenon tube was photographed prior to the beginning of the experiment, the low-pressure compartment of the shock tube was preliminarily flushed with the investigated gas, and then the compartment was filled to the required pressure (5-10 mm Hg). The moment of arrival of the shock wave was synchronized with the moment of the appearance of an additional illumination pulse from the xenon lamp in such a way that absorption of the tube's radiation by the investigated gas occurred on the portion of the pulse where the tube radiation remains constant. The quantity $I = I_0 - \epsilon I_0 + I'$ was thereby recorded on the first oscillograph and $\epsilon I'$ was recorded on the second oscillograph. Here I_0 is the intensity of the additional radiation pulse of the tube; I' is the intensity of radiation of the investigated gas layer; ϵ is

its absorption capacity, c is the channel sensitivity ratio. The sensitivity of the system was selected in such a way that there was no radiation pulse on the second oscillograph, *i.e.*, $cI' = 0$, and since $c \approx 1$, $I' = 0$. Consequently, the first oscillograph recorded $I = I_0 - \epsilon I_0$ in this case as a function of time. The absorption capacity was calculated with the following relationship:

$$\epsilon = \frac{I_0 - I}{I_0}. \quad (4)$$

The time variation of the absorption coefficient is given in Figure 1, and the same figure shows the variational behavior of radiation over time (in relative units). It follows from a consideration of Figure 1 that the absorption coefficient on the portion which corresponds to the time interval between the moment of reflection of the shock wave from the end of the shock tube and the moment of encounter of the first with the contact surface varies synchronously as the radiation varies. Then the radiation is not fixed, while the absorption coefficient again begins to increase from 0 (or from a certain value, as indicated by the dotted line) to unity. Control experiments indicated that the time in which the gas remains opaque is more than 500 μsec . The indicated "secondary absorption" cannot be explained by contamination of the glass, inasmuch as photographs of the radiation pulse of the xenon tube after the experiment indicated that the transparency of the glass was reduced during one experiment a maximum of two times. Since the radiation was not fixed simultaneously with the "secondary absorption", it should be considered that the gas located at a significantly higher temperature than the gas heated by the reflected shock wave is responsible for secondary absorption. It should be noted that the indicated "secondary absorption" was observed also at distances of 4, 7, 105 and 140 cm from the end window, *i.e.*, farther from the end of the shock tube than the place of encounter of the reflected shock wave and the contact region, even where primary absorption is not observed. The beginning of secondary absorption corresponds approximately to the moment of arrival of the reflected shock wave at the given cross section. /77

It follows from the facts that have been presented that "secondary absorption" is related to the state of the gas, which goes beyond the scope of the subject of the investigation and because of this has not been examined in detail.

The data on the absorption capacity obtained by this method for a mixture of 75% CO_2 + 25% N_2 are shown in Figure 3. The application of the method is limited by the relationship $I' \ll I_0$. The parameters of the DKSSh-1000 xenon tube (maximum brightness temperature approximately 10,000°K) made it possible to satisfy this relationship only to 6,000°K; therefore, the data obtained by this method are shown only to a temperature of 6,000°K.

The accuracy of the method is composed of the accuracy of measuring the potential difference by means of an IO-4 oscillograph to $\pm 10\%$; radiation stability of the DKSSh-1000 tube in a pulsed mode $\pm 5\%$, operational stability of the FEU-29 photoelectronic multiplier $\pm 5\%$, and amounts to $\pm 20\%$.

Discussion of Results

The relationship between the absorption capacity, the square of the matrix element of the electronic transition, and oscillator strength is determined by the following equations:

$$\varepsilon(\lambda, T) = \frac{1}{\Delta\nu} \int_{\Delta\nu} \{1 - \exp[-k(\nu, T)l]\} d\nu; \quad (5)$$

$$k(\nu, T) = \frac{8\pi^3 e^2}{3hc} \nu_m r' j' r'' j'' \frac{N}{z(T)} \exp\left(-\frac{E_m + E_{r'} + E_{j'}}{kT}\right) \times \\ \times |R_e^{mn}|^2 q_{e',e''} S_{j',j''} \delta(\nu, T, p); \quad (6)$$

$$f_e = \frac{8\pi^2 m}{3he^2} c \nu_{mn}^* |R_e^{mn}|^2. \quad (7)$$

Here $\delta(\nu, T, p)$ is the intensity distribution function in an individual rotational line, whereby $\int_{-\infty}^{+\infty} \delta(\nu, T, p) d\nu = 1$; ν_{mn}^* is the frequency of the (0,0) transition of the violet system of CN, and is equal to $26,271 \text{ cm}^{-1}$.

The graph in Figure 6 gives the intensity distribution in the (0,0) band of the violet system of CN, which was calculated with the aid of relationship (6). The distribution of the absorption coefficient in individual rotational lines (the left y -axis and the lower x -axis) and the total intensity distribution in the (0,0) band of the violet system of CN are shown here for $T = 8,000^\circ\text{K}$ and $p = 500 \text{ atm}$ to values of the rotational quantum number $j = 60$. The obtained dependence of the absorption coefficient of the (0,0) band of the violet system of CN was approximated by the function $k(\nu, T) = a(T)(1 - \frac{\nu}{\Delta\nu})$ (the dotted line /78 in Figure 6), where ν varies from 0 to $\Delta\nu$. Calculation of the absorption capacity by formula (5) gave

$$\frac{1}{\Delta\nu} \int_{\Delta\nu} (1 - e^{-k(\nu, T)l}) d\nu = 1 - \frac{1}{a(T)l} [1 - \exp(-a(T)l)]. \quad (8)$$

Hence, for extremely small k_ν and $a(T)$,

$$A = \int_{\Delta\nu} k_\nu d\nu = \frac{a(T)}{2} \Delta\nu. \quad (9)$$

Thus,

$$\epsilon(\nu, T) = 1 - \frac{1}{\frac{2l}{\Delta\nu} A} \left[1 - \exp\left(-\frac{2l}{\Delta\nu} A\right) \right]. \quad (10)$$

For complete absorption in the band $A \equiv \int_{\Delta\nu} k_\nu d\nu$, according to (6), we have

$$A = \frac{8\pi^3 e^2}{3\hbar c} \nu_{mn} \nu'' \frac{N}{z(T)} \exp\left(-\frac{E_m + E_{n''}}{kT}\right) |R_e^{mn}|^2 q_{e', e''}. \quad (11)$$

The relationship between $|R_e^{mn}|^2$ and f_e is given by expression (7).

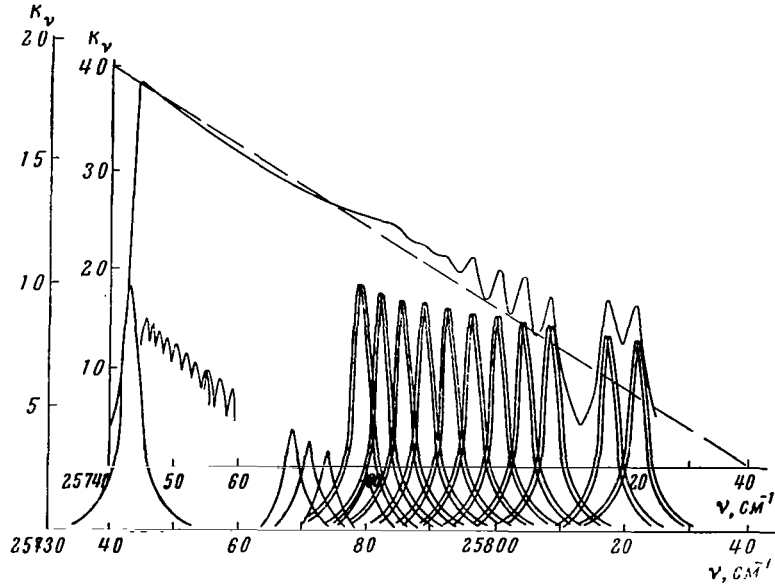


Figure 6. Dependence of k_ν on ν for the (0,0) Band of the Violet System of CN.

The results of the experiments described above are summarized in Figure 3. The absorption capacity of the investigated gas layer, $\epsilon(T) = \frac{1}{\Delta\nu} \int_{\Delta\nu} [1 - \exp(-k_\nu l)] d\nu$ is plotted on the ordinate axis for the (0,0) band of the violet system of CN ($\lambda = 3883 \text{ \AA}$, $\Delta\lambda = 12 \text{ \AA}$, and $l = 3 \text{ cm}$). The total number of particles in cm^3 and the density with the increase of temperature remain approximately constant, while the pressure varies from 26 atm at $T = 5,000^\circ\text{K}$ to 63 atm at $T = 9,000^\circ\text{K}$. Curves calculated with (10) and (11) are also given in the same figure; the continuous curve was calculated for the case of $R_e^{mn} = 0.35 \text{ a.u.}$, $f_e = 0.027$, $q_{e', e''} = 0.92$ according to (8); the CN concentration was calculated taking into account the analysis performed in (7), where it is indicated that $D_{\text{CN}} = 7.5 \text{ eV}$.

The dotted line shows the curve under the assumption that $D_{\text{CN}} = 8.1$ eV. Let us note that in the temperature range of 7,000–9,000°K, the experimental data lie somewhat below the calculated curve. This is evidently related to the fact that the action of the gas located behind the incident shock wave leads to a decrease in the transparency of the viewing windows right up to the arrival of the reflected shock wave. The decrease in transparency of the viewing windows during the experiments is 10–30% for the temperature range of 5,000–6,000°K. The same decrease in transparency of the windows should evidently be expected from the action of the gas situated behind the incident wave, since the temperature of the gas behind the incident wave is 5,000–6,000°K for the case under consideration. For temperatures of 9,000°K and higher, the experimental values lie significantly below the calculated curve, which is evidently related to the fact that the gas parameters, which were calculated according to elementary shock tube theory, are not realized.

Thus, it follows from the experimental data on the measurement of the absorption capacity of the (0,0) band of the violet system that $R_e = (0.35 \pm 0.08)$ a.u. and $f_e = (0.027 \pm 0.06)$.

The agreement of the experimental data (to 6,000°K) obtained by the two methods indicated above (see Figure 3) indicates that the gas temperature calculated according to the velocity of the incident wave and that which occurred in the experiment within the limits of accuracy coincides, which may be demonstrated in the following manner:

$$\epsilon_\lambda = \frac{I_\lambda}{B_\lambda(T_0)}; \quad (12)$$

$$\frac{I_\lambda}{\epsilon_\lambda} = B_\lambda(T_{00}); \quad (13)$$

$$\bar{\epsilon}_\lambda = \epsilon_\lambda. \quad (14)$$

Here the line denotes the quantities measured in the experiment, and T_0 is the gas temperature calculated according to the velocity of the shock wave; T_{00} is the gas temperature calculated on the basis of experimental data on the measurement of radiation capacity by means of Kirchhoff's law. Relationships (12) and (13) are written on the basis of Kirchhoff's law (14), proceeding from the agreement of experimental data obtained by the radiation and absorption method. By substituting I from (13) into (12) and taking into account (14), we obtain $B(T_0) = B(T_{00})$, which is equivalent to $T_0 = T_{00}$ in accordance with the conclusion made above.

The time of arrival of the system at equilibrium can be estimated on the basis of the leading front of the radiation pulse, since the radiation capacity is directly related to the concentration of particles in the excited state and to the gas temperature. The measurement of these quantities did not enter the problem on hand, and it may be a special subject of investigation; however, an estimation of the indicated time for a mixture of nitrogen and carbon dioxide

is of interest. It turned out that τ amounts to 20-10 μsec for $T = 5,000\text{--}6,000^\circ\text{K}$ and $p = 12\text{--}25\text{ atm}$; it approximately coincides with the time resolution of the system ($\sim 2\text{--}3\text{ }\mu\text{sec}$) for higher temperatures and pressures.

REFERENCES

1. Ambartsumyan, Ye. A., P. V. Ionov and A. A. Kon'kov: Investigation of the /80 spectral characteristics of gases heated by shock waves. In this collection.
2. White, I. U.: Spectroscopic measurements of gaseous CN. I. Dissociation in the electric discharge. *J. Chem. Phys.*, Vol. 8, No. 1, 1940.
3. White, I. U.: Spectroscopic measurements of gaseous CN. II. Thermal dissociation of cyanogen. *J. Chem. Phys.*, Vol. 8, No. 6, 1940.
4. Soshnikov, V. N.: Absolute intensities of electronic transitions in diatomic molecules. *Uspekhi Fizicheskikh Nauk.*, Vol. 74, No. 2, 1961.
5. Tsang, W., S. H. Bauer and M. Couperthuaite: Dissociation energy and rate of decomposition of C_2N_2 . *J. Chem. Phys.*, Vol. 36, No. 7, 1962.
6. Bennet, R. G. and R. W. Dalby: Experimental oscillator strength of the violet system of CN. *J. Chem. Phys.*, Vol. 36, No. 2, 1962.
7. Kudryavtsev, Ye. M.: Experimental determination of the matrix element of the dipole transition moment of the violet system of CN. *Kand. Dissert. Fizicheskiiy Institut AN SSSR. (Candidate's Dissertation. Physics Institute of the Soviet Academy of Sciences.)* 1965.
8. Nicholls, R. W.: The interpretation of intensity distributions in the CN violet, C_2 Swan, OH violet and O_2 Schumann-Runge band systems by use of their r -centroids and Franck-Condon factors. *Proc. Phys. Soc., A*, Vol. 69, 1956, part 10.

INVESTIGATION OF THE STRUCTURE OF THE LUMINESCENCE FRONT IN AN ELECTROMAGNETIC SHOCK TUBE

Yu. V. Makarov and A. M. Maksimov

The tasks of investigating the optical and kinetic properties of gases at /81 high temperatures and the problems of studying plasma gas dynamics required the creation of devices for generating high-temperature plasma moving at high velocities. The use of strong shock waves created in gases by the pulsed discharge of a condenser bank in a specially shaped chamber for this purpose led to the development of electromagnetic shock tubes. The obtainment of shock-wave velocities to 560 km/sec in devices at a low initial pressure in hydrogen has been reported [1]. There is presently very little information concerning the nature and structure of the luminescence front in these tubes, the duration of flow of the shock-heated gas, the thermodynamic state of the gas behind the shock front, the effect of a hot gas-discharge plasma on the gas parameters behind the shock wave, the relaxation phenomena in the front, etc.

This article reports the results of an investigation of the structure of the luminescence front in air at a large distance from the discharge chamber.

The installation, which is an electromagnetic shock tube with a conical discharge chamber, is described in [2], where the results of investigations of the dependence of the velocity of the luminescence front on various parameters are presented [3].

An investigation of the propagation of the luminescence front through a tube with the aid of an ultrahigh-speed SFR camera makes it possible to trace the changes in shape of the front along the tube and to compare separate phases of the process with the changes in the discharge current. The structure of the front has been investigated both near ($x \sim 20$ cm) the discharge chamber, and also at distances $x > 40$ cm from the annular electrode. A special device mounted in the SFR camera made it possible to phase in the survey process with the discharge current. The camera operated in a photoscanning and time-magnified mode. The survey field amounted to 13.5 cm. On the basis of experiments conducted at various initial pressures and voltages on the bank, the following picture of the evolution of the luminescence front can be given.

At an initial pressure of $p_1 = 0.5$ mm Hg and $U_b = 4$ kv at a distance to 25 cm from the annular electrode, the luminescence front is concave, with a brightly luminescent, partially asymmetrical region behind it (dimensions 2-3 cm). In the later phases, when the luminescence brightness is noticeably decreased, a string-like structure which expands in the direction toward the front is quite visible.

The front is flat or somewhat convex at the center at a distance of 40 cm

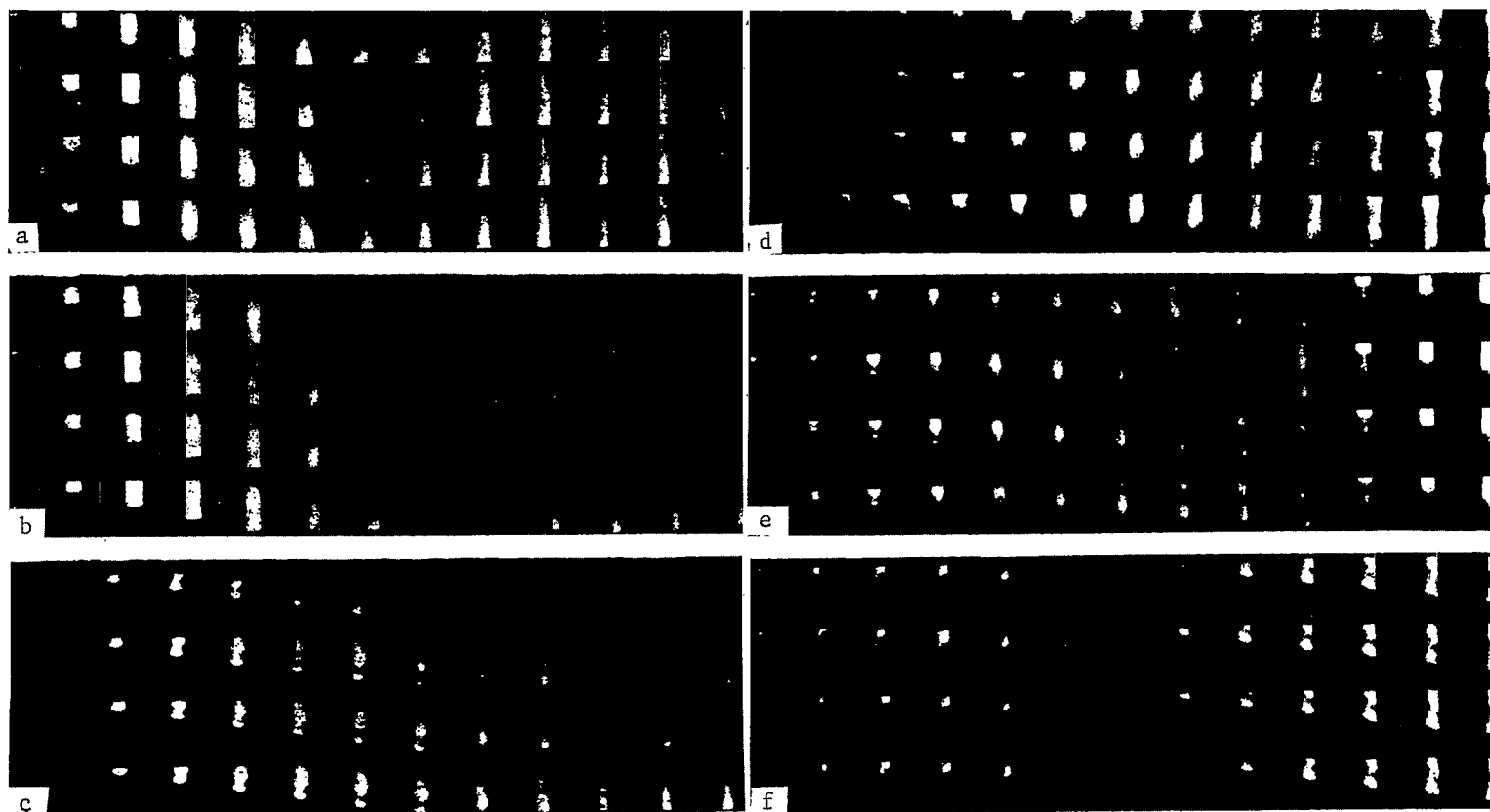


Figure 1. Frame-by-Frame Photography of Luminescence at Different Distances x from the Annular Electrode at $U_b = 4$ kv. (a) $x = 40$ cm, $p_1 = 0.5$ mm Hg; (b) $x = 40$, $p_1 = 2$; (c) $x = 57$, $p_1 = 2$; (d) $x = 65$, $p_1 = 2$; (e) $x = 90$, $p_1 = 1$; (f) $x = 90$, $p_1 = 1.5$. Exposure speed $1.5 \cdot 10^6$ frames/sec, after exposure of 13.5 cm. Frames are read from bottom to top, left to right.

(Figure 1a). Upon further movement of the front, its curvature increases, and a brightly luminescent region begins to separate behind the front, forming a "mushroom cap" structure (Figure 3a). At $p_1 = 0.5$ mm Hg the cap forms at a distance of $x > 75$ cm from the annular electrode. It should be noted that this stratification of the plasma behind the luminescence front occurs after the discharge current passes the maximum in the second half-period.

The luminescence of the plasma drops rapidly behind the front, and a second/83 dary front appears 30-40 μ sec after the first front (this time is comparable with the time between maxima of the discharge current in the first and second half-periods, *i.e.*, ~ 31 μ sec); this secondary front is rather extended in the center, diffuse, and relatively weakly luminescent.

It can be seen very well that the boundary becomes more distinct as the advancement of the curvature of the front decreases. The velocity of the secondary front is somewhat higher than the velocity of the primary front.

A series of experiments conducted at other values of p_1 indicated that an analogous mushroom-like structure occurs in all cases when the discharge current drops after the second half-period. Inasmuch as the velocity of the front decreases with the increase of p_1 , stratification of the front occurs closer to the discharge chamber. The velocity of the front at the moment of formation of the mushroom is approximately identical for different p_1 (~ 10 -11 km/sec). The luminescence front begins to decay as the front moves and as the discharge current decreases with the formation of various protuberances (see Figure 1d and e) and is completely obliterated, forming a weakly luminescent diffuse structure. Behind this weakly luminescent and obliterated zone there moves a brighter region of plasma behind the "pinch" which separates the mushroom-like structure from the plasma. A brightly luminescent, practically flat front appears 20-30 μ sec after the passage of the first front (shorter time corresponds to larger p_1), which is formed at large distances from the annular electrode and overtakes the primary front. The luminescence intensity of the plasma increases in the secondary front with the increase of p_1 .

The observed instability of the luminescence front, the fundamental stages of which proceed identically at various initial conditions and depend on the phase of the discharge current, makes it possible to conclude that the luminescence front is not a boundary of the shock wave which is stable at any M_s numbers.

For a qualitative investigation of the mutual arrangement of the shock wave and the luminescence front, the process of the reflection of plasma from an end plane inserted in a tube was investigated. Inasmuch as the gas is approximately doubled at this enthalpy and the relaxation time decreases several orders due to the increase in temperature, the front of the incident shock wave can be fixed by a single value on the basis of the moment of the appearance of luminescence at the end. To perform these experiments, a copper container was mounted in the tube at a distance of 105 cm from the annular electrode (the gas was evacuated through peripheral holes). Continuous photoscanning of the reflection

process was conducted through a slit parallel to the tube axis. Typical photographs are shown in Figure 2. At $p_1 = 0.5$ mm Hg (stage of mushroom-like structure of luminescence front) a brightly luminescent (approximately two orders brighter) reflected wave appears simultaneously with the approach of the incident luminescence front to the end (within the limits of the resolution time $0.445 \mu\text{sec/mm}$). The picture changes with the increase of p_1 . If reflection occurs simultaneously with the arrival of the luminescence front at the end when $p_1 = 0.7$ mm Hg, a certain lag of the bright luminescence front behind the weakly luminescent front is noticeable at $p_1 = 0.9$ mm Hg, which provides a reflected wave. The process of delaying the bright luminescence front with respect to the beginning of reflection is graphically visible at $p_1 > 1$ mm Hg (see Figure 2c and d). The front which provides the reflected wave grows very weakly. An analogous picture is observed in hydrogen, carbon dioxide, and nitrogen. Photographs were taken with a Yu-3 entrance objective (this front is not visible with a conventional SFR objective). With the increase of p_1 , a brightly luminescent region lags behind the weakly luminescent front, which leads to the formation of a ⁸⁴reflected shock wave. It is natural to identify this primary weakly luminescent front with the shock wave. The photographs show the arrival of the secondary front at the end, which also provides a reflected shock wave. At p_1 the flow behind the front of the incident shock wave is very nonuniform and contains regions which move at different velocities. The peculiarities of the reflection process are more graphically seen by means of frame-by-frame photography.

At $p_1 = 0.5$ mm Hg, the reflected wave appears simultaneously (within the limits of the time resolution of one frame $\sim 0.67 \mu\text{ sec}$) with the arrival of the peak of the "cap" at the end. It is characteristic that the luminescence of the reflected wave occurs on the entire surface of the wall, although the incident front is not flat. Even in the case when an extremely deformed or significantly obliterated incident front approaches the end, the reflected wave occurs immediately on the entire surface of the end. This indicates that the luminescence on the end is conditioned not by recombination of excited atoms in the plasma, but by the reflection of the shock wave. At higher pressures the reflected wave appears significantly earlier than the arrival of the diffusely obliterated luminescence front at the end (Figure 3c). This points out that the shock front significantly leads the luminescence front at high p_1 .

The detection of instability of the luminescence front is extremely essential in the results given above. Let us note that it develops when the shock front begins to leave the luminescence front. The shape of the luminescence front is similar to the contact surface observed in conventional shock tubes in photographs taken by means of an IAB-451 instrument. If we use this analogy as our point of departure, the conclusion concerning the fact that the luminescence front is the boundary of the gas-discharge plasma, which plays the role of a piston in the formation of the shock wave, is quite justified. This formation of instability may be caused by two factors. Due to the significant deceleration of the plasma at the distances at which the luminescence front begins to decay, Rayleigh-Taylor instability may develop [4]. It is sufficient for this that the



Figure 2. Photographic Survey of Plasma Reflection from End Plane 105 cm from Annular Electrode at $U_b = 4$ kv.

(a) $p_1 = 0.5$ mm Hg, $V_s = 11.5$ km/sec; (b) $p_1 = 0.9$, $V_s = 9.1$; (c) $p_1 = 1$, $V_s = 8.3$; (d) $p_1 = 2$, $V_s = 5.4$.

density in the gas-discharge plasma be higher than in the region of the shock-heated gas, which is extremely probable since the gas-discharge plasma contains a large quantity of heavy admixtures [3] and cools off after the discharge current ceases. Another possible cause may be the formation of significant density gradients in the initial stage of the formation of the plasma piston, which is brought about by the nonuniformity of breakdown at high p_1 .

Investigation of reflection from the end indicates that the reflected wave appears simultaneously with the approach of the luminescence front to the end when $p_1 < 0.7$ mm Hg ($V_s > 10$ km/sec).

When p_1 increases, the shock front is a weakly luminescent narrow zone, behind which, after the dark region that increases with the increase of p_1 , there follows a bright luminescence front. This luminescence distribution behind the shock front may be caused by relaxation phenomena or conditioned by the process of cooling off of the gas-discharge plasma described above. A single answer to this question can be given only after detailed investigations of the structure of the front are conducted by other methods; however, the formation of characteristic instabilities and plasma ejections, which almost reach the shock front (frame-by-frame photographs of reflection from the end), obviously indicates that the luminescence belongs to the gas-discharge plasma. We find in this case that with the increase in velocity of the front, the gas-discharge plasma follows the shock front so closely that it merges with it within the limits of the resolution time $0.445 \mu\text{sec/mm}$.

Frame-by-frame photography of the reflection pattern substantiates this conclusion very well (see Figure 3). The shape of the reflected wave at $p_1 = 0.5$ mm Hg has a peculiarity that resembles the λ -structure in the conventional shock tubes, which is caused by the interaction of the reflected shock wave with the boundary layer of the flow behind the incident wave [5]. This indicates the essentially gas-dynamic nature of the processes at large distances from the discharge chamber. /86

The following conclusions can be made on the basis of the experiments conducted:

1. At a certain distance from the annular electrode (depending on p_1 and U_b and the corresponding specific phase of attenuation of the discharge current) the luminescence front decays with the formation of various instability and, consequently, is not a shock wave.

2. The luminescence front is a gas-discharge plasma which plays the role of a "piston" in the formation of a shock wave. /87

3. The region of the shock-heated gas between the shock front and the gas-discharge plasma is significantly reduced when p_1 decreases and V_s increases, and becomes discernable ($p_1 < 0.7$ mm Hg, $V_s > 10$ km/sec).

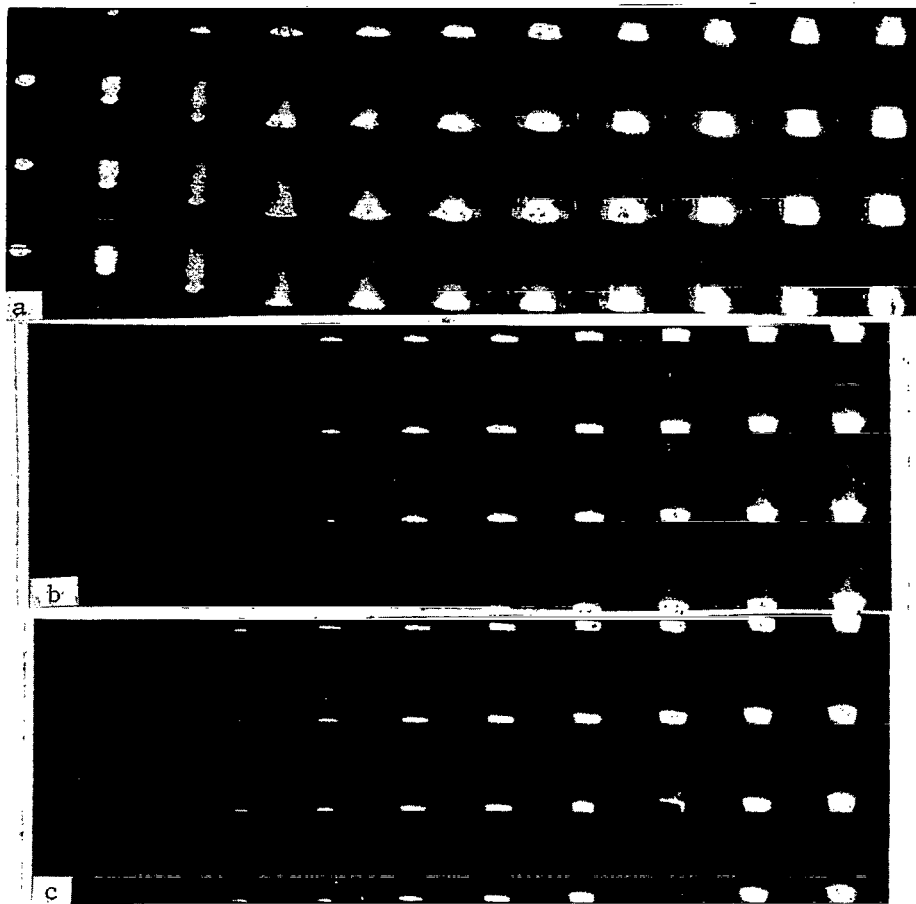


Figure 3. Frame-by-Frame Photographs of Shock Wave Reflection from End Plane 137 cm from Annular Electrode. (a) $p_1 = 0.5$ mm Hg, $U_b = 4$ kv; (b) $p_1 = 1$, $U_b = 4$; (c) $p_1 = 2$, $U_b = 4$.

4. Measurements in air, nitrogen, hydrogen, and carbon dioxide indicated that the peculiarity pointed out in 2 is characteristic for all the investigated gases. This indicates that the luminescence front observed in electromagnetic shock tubes by means of optical devices is the boundary of a gas-discharge plasma.

5. The decay of the boundary of the gas-discharge plasma may lead to a change in the state of the shock-heated gas due to the penetration of its "tongues" into the "plug" region.

REFERENCES

1. Kolb, A. C. and H. R. Griem: High-temperature shock waves. *Uspekhi Fizicheskikh Nauk*, Vol. 83, No. 1, 1964.

2. Makarov, Yu. V.: Some investigations of processes in a magnetohydrodynamic shock tube with a conical discharge chamber. In: *Fizicheskaya gazodinamika i svoystva gazov pri vysokikh temperaturakh*. (Physical Gas Dynamics and Properties of Gases at High Temperatures.) Moscow, Izd-vo "Nauka", 1964.
3. Makarov, Yu. V. and A. M. Maksimov: *Spektroskopicheskiye issledovaniya plazmy*. (Spectroscopic Investigations of Plasma.) Moscow, Izd-vo "Nauka", 1964.
4. Taylor, G. I.: The instability of liquid surfaces when accelerated in a direct perpendicular to their planes. *Proc. Roy. Soc., A*, Vol. 201, No. 1065, 1950.
5. Zaytsev, S. G., A. P. Shatilov, Ye. V. Lazareva and L. N. Trukhanova: Investigation of the process of the interaction of a reflected explosion with the boundary layer of a flow behind an incident shock wave. In: *Fizicheskaya gazodinamika i svoystva gazov pri vysokikh temperaturakh*. (Physical Gas Dynamics and Properties of Gases at High Temperatures.) Moscow, Izd-vo "Nauka", 1964.

SPECTROSCOPIC INVESTIGATION OF AN IONIZED GAS IN AN ELECTROMAGNETIC SHOCK TUBE

V. A. Bashilov

The questions associated with the structure of a luminescence front and the existence of a region of a shock-heated gas and contact surface having the nature of the substance which moves behind it in electromagnetic shock tubes have been insufficiently studied. This work was set up for this very purpose. /88

An experimental installation was prepared with the following characteristics.

The power portion of the installation consists of 38 IM5-150 condensers, the maximum energy of which is 71 kJ at a voltage of 5 kV.

To obtain minimum inductance of the loop, the condensers are connected by low-inductance leads as shown in Figure 1, which consist of two copper sheets, one of which is attached to the positive terminal of the condenser and the other is attached to the negative terminal. The copper sheets are isolated from one another by seven polyethylene sheets 0.5 mm in thickness. In the center of the bank, at the point of attachment of the lead buses, the leads are reinforced by a 10-mm bronze sheet. The inductance of the leads, condensers, and the feeder to the installation is approximately $3 \cdot 10^{-8}$ H.

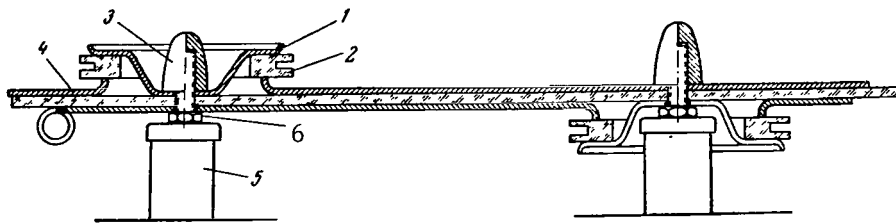


Figure 1. Design Diagram of Lead Attachment. (1) reinforcing plate (copper); (2) plexiglass insulation ring; (3) clamping cap; (4) copper sheets; (5) high-voltage condenser lead insulator; (6) support nut.

The experimental setup is a conical discharge chamber with annular and pin-type electrodes. The design of the discharge chamber may be seen in Figure 2.

The controlled discharger is depicted in the lower portion of the installation; it is screwed directly to the leads. The size of the discharge gap can be regulated by rotating the lower electrode. A channel is made in the lower electrode, through which an igniting electrode is attached in a teflon insulator. This ignition system is successful since upon breakdown of the gap

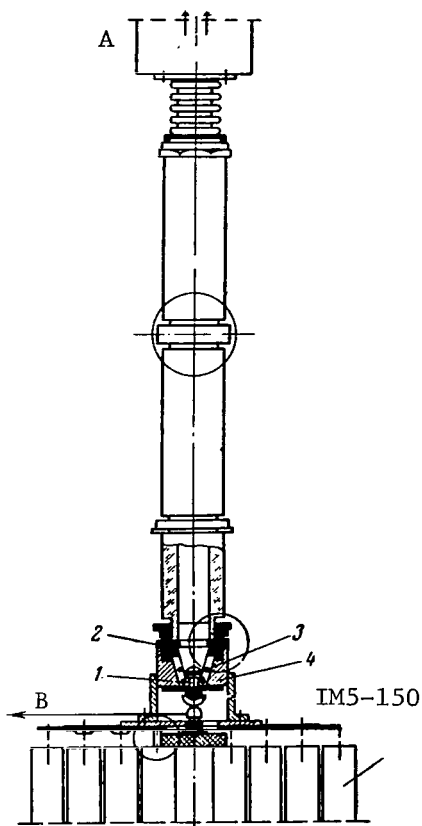


Figure 2. Design Diagram of Installation. (1) pin electrode (copper); (2) annular electrode; (3) conical chamber (plexiglass and teflon); (4) reverse conductor; (A) diffusion pump; (B) ignition.

experiments (see below). Optically transparent glass was inserted into the tube window to reduce absorption in the walls. The glass was washed with a solvent after each experiment. The tube was periodically washed with a solution of hydrofluoric or nitric acid. The intensity of the scanning lines was significantly increased by employing fresh "Panchromatic-13" film with a sensitivity of 2,000 GOST units manufactured by the Kazan' Chemical Plant.

The emission spectrum was recorded in two regions of the shock tube; at a distance of 30 and 150 cm from the annular electrode of the conical discharge chamber. To increase the luminosity of the instrument, a planar mirror was placed on the opposite side of the shock tube in some experiments to reflect light onto the entrance slit of the spectrograph.

In this case, the entrance slit of the spectrograph was illuminated by

by a high-voltage ignition pulse, the working volume of the conical chamber is simultaneously broken down. The initial ionization thus created in the chamber conditions stable operation of the installation.

A Rogowski integration loop, which measures ^{/89} the total discharge current, is installed in the chamber with the discharger.

The cone is fabricated from plexiglass or teflon. The electrodes are sealed with rubber. The central and annular electrodes are made from electrolytic copper. The cone is tightly inserted into the copper housing and is sealed by the annular electrode. The copper housing forms a reverse conductor. This design has complete axial symmetry.

The process of propagation of a shock wave is recorded in the tube, which is vacuum-coupled tightly to the conical chamber (see Figure 2).

Elongated tubes with a diameter of 70 mm, length 2 m, and a plexiglass tube with a square cross section 50 x 50 mm were employed in the experiments. One end of the tube is attached to the diffusion pump.

A spectrograph with mirror scanning was used to investigate the emission spectra of the ionized gas which forms in the shock tube [1].

As the first experiments indicated, the luminance intensities were not always sufficient for obtaining well-exposed films. Therefore, a reflecting mirror was employed in subsequent experiments.

means of a double-lens illumination system which was designed in such a way as to completely fill the aperture of the spectrograph and to simultaneously obtain the most effective illumination of the slit.

These conditions will be observed best of all if the collimating slit on the shock tube is reflected onto the spectrograph slit, and the rear mirror on to the collimator. The condenser system of the illuminator is described in [2].

The system makes it possible to double the amount of light, while retaining 90 good space resolution. The height of the slit was restricted by means of a diaphragm in such a way that the curvature of the spectral lines, which is caused by dispersion on the entrance slit, did not affect the quality of scanning. In the course of the preliminary preparation of the spectrograph, several control arc spectra were taken with iron electrodes and a dispersion curve was plotted on the basis of these spectra; several emission spectra of the discharge plasma were then obtained with a stationary mirror. Air was the working gas.

The reference spectrum from the arc with iron electrodes was imprinted on the same film with the aid of a Hartman diaphragm. The results of interpretation of the plasma spectrum in the case of filling the tube with air are given in the table.

Wave-length, Å	Element	Wave-length, Å	Element	Wave-length, Å	Element
4022,6	Cu II	5032,0	C II	4641,0	O I
4063,3	Cu I	5039,0	C I	4651,1	Cu I
4101,7	H _δ	5052,1	C I	4674,7	Cu I
4151,5	N I	5076,1	Cu I	4704,6	Cu I
4226,7	Ca I	4415,0	Cu I	4766,2	C I
4248,9	Cu I	4425,0	Ca I	4771,7	C I
4259,5	Cu I	5200,9	Cu I	5700,2	Cu I
4307,7	Ca I	5218,2	Cu I	5782,1	Cu I
4318,6	Ca I	5380,0	C I	5793,0	C I
4355,2	Ca I	6158,0	O I	5801,0	C I
4358,0	N I	4435,0	Ca I	5889,9	Na
4368	O I	4454,8	Ca I	5895,9	Na
4369,5	C I	4480,4	Cu I	6008,5	Ni
4378,2	Cu I	4509,4	Cu I	5105,5	Cu
4775,8	C I	4530,8	Cu I	5145,1	Cu II
4793,8	Cu I	4539,7	Cu I	5153,2	Cu I
4861,3	H _β	4554,0	Ba II	6439,0	Ca I
5016,4	Cu I	4587,0	Cu I	6462,5	Ca I
				6562,8	H _γ

As can be seen from the table, almost the entire spectrum consists of impurities in the gas-discharge plasma (the material of the discharger and the tube, contaminated air, etc.). Only a few lines were detected in the spectrum which correspond to hydrogen and oxygen. It should be noted that at high initial pressures in the tube (~ 5 -10 mm Hg) rather intense molecular bands (CN and C₂) appear in the spectrum. The emission spectrum did not change after fil-

ling the tube with hydrogen, *i.e.*, only more intense lines of the Balmer series appeared. The subsequent experiments were performed with hydrogen.

Scanning the Emission Spectrum Near the Discharge Chamber

A comparison of spectral scannings obtained at various distances from the discharge chamber is of considerable interest. The first part of the work was conducted with a spectrograph installation at a distance of 30 cm from the annular electrode. A large number of spectral scannings were obtained at various initial pressures in the tube (from 0.3 to 3 mm Hg) and various voltages in the ^{/91} discharge chamber. A typical spectrum is shown in Figure 3. Interpretation of

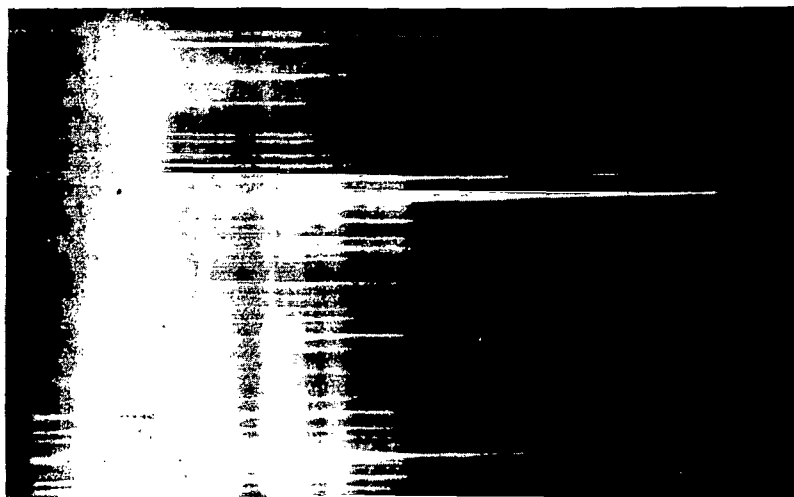


Figure 3. Spectral Scanning Near Discharge Chamber.

the spectra taken near the discharge chamber indicated that the emission belongs mainly to the lines of the Cu and Ca impurities (see table). The spectral scannings have a sharply expressed front, *i.e.*, the majority of lines which correspond to the impurities and the working gas begin to scintillate simultaneously. However, there are lines in the spectrum, the beginning of whose scintillation is several μsec behind the leading luminescence front. Spectral analysis indicated that these are the lines with the higher excitation potentials. As can be seen in Figure 3, the duration of luminescence of the lines also is extremely dissimilar. As a rule, lines with a high excitation potential glow for a shorter period of time. The most intense lines of copper continue to glow even after the luminescence of the hydrogen line ceases. A strong continuum is distinctly visible in the photographs of the spectral scannings near the discharge chamber; its "banded" structure indicates the presence of some pulsations of the plasma flow. The continuum appears in the spectrum ~ 10 μsec after the beginning of luminescence, and then, in ~ 40 μsec , there follows a number of bands which differ in duration and intensity. There is no periodicity in their appearance. It should be noted, however, that the spectral pic-

ture has good repetition from experiment to experiment (under identical initial discharge conditions). To explain the nature of the continuum "bands", emission spectra of an ionized gas were photographed at various initial pressures in the tube. It was established that these "bands" exist in the entire pressure interval, although their position changes. It can be seen from the photographs that the broadening of the lines increases simultaneously with the appearance of the continuum band. The bands of continuous emission are evidently fixed by the spectrograph at the moment of passage of a plasma cluster with a large concentration of charged particles (electrons and ions) in front of the slit. An increased concentration of electrons and ions leads to their intense interaction, and to an increase in the quantity of free-free transitions and intensity of ion-electron recombination. Frame-by-frame photography of the process of plasma motion in electromagnetic shock tubes [3] also indicates that the plasma flow /92 is not homogeneous, but consists of separate brightly luminescent clusters. Plasma spectral scannings indicate precisely this character of the process.

Measurement of the lag times of Cu lines with respect to hydrogen lines indicated that at a distance of 30 cm from the annular electrode the lines of copper and hydrogen scintillate simultaneously, *i.e.*, the gas-discharge plasma completely adheres to the front of the shock wave. An increase in the rate of spectral scanning to 2 km/sec provides the same result, *i.e.*, it was previously impossible to separate the gaseous region behind the shock wave from the gas-discharge plasma. An increase in the scanning rate above 2 km/sec led to significant attenuation of the spectrum.

Photographs of spectral scannings indicate that the H_{α} and H_{β} lines are significantly broadened, whereby their width changes periodically in time. As we already mentioned, broadening of the lines coincides with the pulsations of the continuum and indicates the non-homogeneous character of the plasma flow near the discharge chamber. The width of the lines decreases significantly in ~ 40 μ sec, and this moment coincides with the end of the first half-period of the discharge current simultaneously with the disappearance of the continuum.

Spectral scannings for the interval of initial pressures in the tube 0.3-3 mm Hg indicated that the luminescence intensity of the impurities practically does not change. This obviously points to the fact that the character of the discharge and the evaporation of the electrodes and the walls of the discharge chamber depend very little on pressure in the indicated range. The unchanged character of the current and voltage curves at various pressures in the discharge chamber also points to the same fact.

Spectral Scanning at a Large Distance from the Discharge Chamber

The second part of the experiments was conducted with the spectrograph set-up at a distance of 120 cm from the discharge chamber. A large number of spectral scannings were obtained under various initial conditions. As in the first case, interpretation of the spectrum indicated that it, to a significant extent, consists of lines which correspond to impurities whose luminescence intensity was somewhat decreased as compared with the spectra near the chamber. A typical

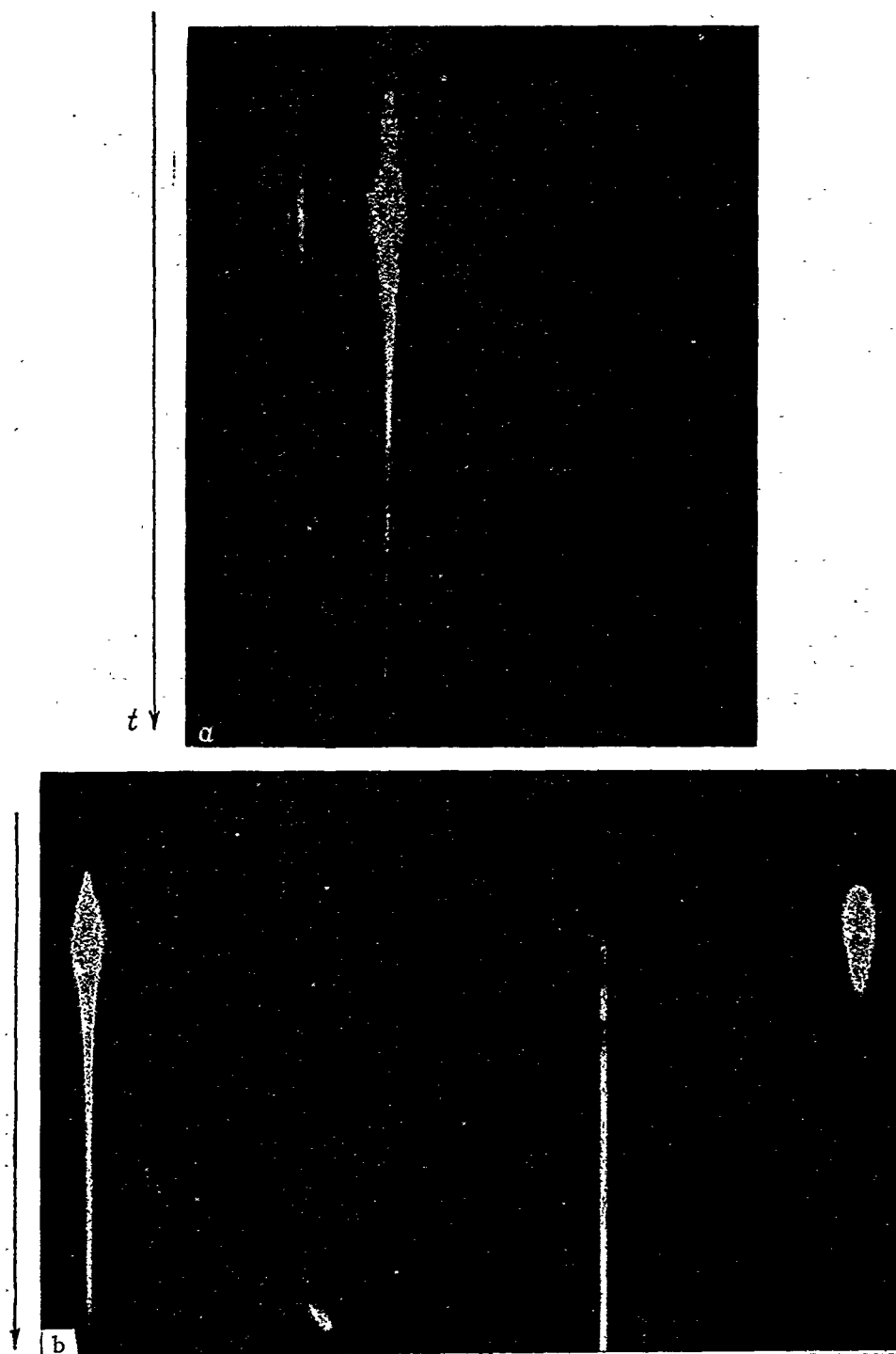


Figure 4. Spectral Scanning at a Distance of 120 cm from the Discharge Chamber. (a) H_{α} line visible; (b) H_{α} and H_{β} lines visible.

spectrum is shown in Figure 4.

As can be seen from the photographs, the most characteristic feature of the spectra is the fact that the hydrogen lines begin to scintillate somewhat earlier than the impurity lines. This lead is negligible at a pressure of 0.3 mm Hg ($\sim 0.5 \mu\text{sec}$), but it amounts to $\sim 5 \mu\text{sec}$ at a pressure of 5 mm Hg. The shape of the hydrogen lines is interesting. Let us examine, for example, the H_{α} line. At first only a weak luminescence of the line can be seen, whereby the line is very narrow. Then the luminescence intensity and the width of the line increase abruptly. A portion with a gradual decrease in width then follows, and with the appearance of lines in the spectrum which correspond to Cu and other impurities, the width of the line increases again, whereupon the width of the line becomes greater than at the beginning of the scanning. A well-defined continuum simultaneously appears with the appearance of the Cu lines in the spectrum. The width of the hydrogen lines gradually decreases in time, while the luminescence of the lines does not entirely cease in 40-50 μsec .

An analysis of time scanning of the plasma spectrum in comparison with the data of other research methods makes it possible to present the following picture of the process. When the gas-discharge plasma is ejected from the discharge volume, it is accelerated, whereby a shock wave is formed at the end of the gas-discharge "piston" which results in the obtainment of a boundary on the photographs of the spectral scannings near the chamber. As the piston moves along the tube, the shock wave begins to gradually drift from the piston, creating a region of shock-heated gas between the front of the shock wave and the gas-discharge plasma. /94

Emission from the front of the shock wave evidently creates a certain pre-ionization since slight illuminance of hydrogen is noted on the spectral scanning prior to the arrival of the shock front. The absence of a sharp boundary of the beginning of luminescence of the impurities indicates that a concise division of the region of the shock-heated gas and the gas-discharge plasma does not exist, while the impurities ejected from the discharge volume penetrate the "plug" to a significant extent, thereby creating a certain mixing zone.

In a qualitative comparison of the spectral scannings at distances of 30 and 120 cm from the discharge chamber, the following can be noted. The total spectral intensity is significantly weaker at a large distance. Because of this, the width of the entrance slit of the spectrograph was enlarged, which, of course, affected the quality of the spectrum.

It can be further noted that the spectra photographed near the discharge chamber were significantly more abundant in lines. This may be explained by the fact that some of the lines with high ionization potentials glow more weakly at a distance of 120 cm from the chamber due to a decrease in concentration of excited atoms, which in turn is explained by the decrease in temperature and the decrease in motion of the gas-discharge plasma through the tube; there occurs an intense mixing of various layers, whereby the inhomogeneities of the flow of the ionized gas are resorbed and decrease in size.

A comparison of the spectra in Figures 3 and 4 indicates that the lumines-

cence intensity of the continuum at a distance of 120 cm from the discharge chamber becomes significantly weak. At a low scanning rate, *i.e.*, 375 m/sec, the "banded" structure of continuous emission is already invisible, and only the first band is retained, which corresponds to the arrival of the gas-discharge plasma. This picture evidently points to the fact that there occurs an intense mixing of various layers as the gas-discharge plasma moves along the tube, whereupon some of the inhomogeneity is resorbed, while the others decrease in size. A powerful cluster, which evidently corresponds to ejection at the moment of the current maximum, goes only into the head of the gas-discharge plasma.

Determination of Plug Length Under Various Initial Discharge Conditions

Time scanings of plasma luminescence spectra have made it possible to determine the extent of the region of a shock-heated pure gas (plug length). As we have already mentioned, due to the absence of a sharp boundary of emission from the gas-discharge plasma, the plug length was estimated with an error to 30%. The plug length depends significantly on the initial pressure, which will be maximum at pressures of 5-8 mm Hg (Figure 5). The velocity of the leading front of luminescence decreases sharply at high initial pressures, whereby the region of the shock-heated gas is not recorded.

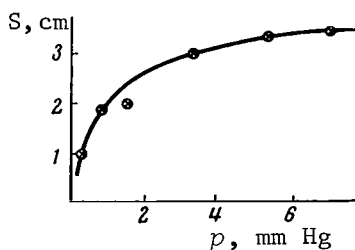


Figure 5. Dependence of "Plug" Width on Initial Hydrogen Pressure.

This may be explained by the decrease in gas temperature behind the shock front, which in turn leads to a decrease in the luminous emittance of the plug and it is not fixed on the scanning. The plug becomes smaller at low initial pressures, and its extent does not exceed several millimeters at a pressure of ~ 0.1 mm Hg.

A comparison of the data with measurements of ^{/95} the plug length by coloring the gas-discharge piston [4] indicates a coincidence (within the limits of the measurement errors) of the results.

From what has been stated above, we can present the picture (see Figure 5) of the processes which take place in electromagnetic shock tubes.

The current which flows in the discharge chamber causes intense evaporation of the electrodes and walls of the chamber, as well as heating and ionization of the investigated gas.

This gas-discharge plasma is accelerated during the action of electrodynamic forces, being a unique piston, in front of which a shock wave is formed. At sufficiently high initial gas pressures in the shock tube (1-7 mm Hg) at a distance of 1.5 m from the discharge chamber, a plug of shock-heated gas is formed, the maximum extent of which reaches 5 cm. The question concerning the applicability of the Rankine-Hugoniot relations for calculating the thermodynamic parameters in this region of plasma is complicated by the intense interaction on

it by the gas-discharge plasma.

REFERENCES

1. Bashilov, V. A.: A spectrograph with mirror scanning. *Prib. i Tekhn. Eksperim.*, No. 2, 1965.
2. *Uspekhi spektroskopii. (Advances in Spectroscopy.)* Edited by P. W. Thompson, Moscow, IL, 1963.
3. Makarov, Yu. V. and A. M. Maksimov: Investigation of the structure of the luminescence front in an electromagnetic shock tube. In this collection, p. 86.
4. Bashilov, V. A.: Some results of an investigation in an electromagnetic shock tube. *Prikladnaya mekhanika i tekhnicheskaya fizika* (in press).

MEASUREMENT OF TEMPERATURE AND DENSITY OF CHARGED PARTICLES OF AN ARGON PLASMA JET

G. P. Petrova

The installation with which the measurements were conducted is described in [1]. Two anode versions of the arc chamber were used in the experiments. One was made in the form of a conical water-cooled copper nozzle (Figure 1a). The same figure shows a diagram of the second diaphragm anode version (Figure 1b). The diameter of the diaphragm outlet is equal to the diameter of the nozzle critical cross section.

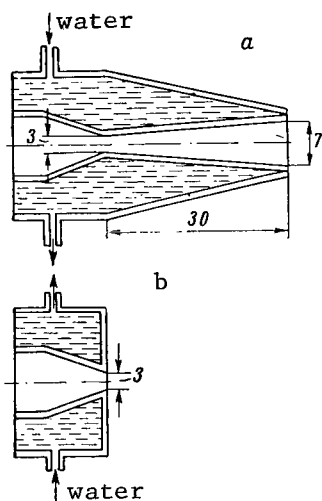


Figure 1. Two Anode Versions of Arc Chamber. (a) anode made in form of conical nozzle; (b) short anode, in form of diaphragm.

An arc jet of partially ionized argon was investigated. The conditions were as follows: pressure in arc chamber 3.7 atm (accuracy 1.7%); arc current 265 amp (accuracy 5%); voltage in discharge gap 37 V (accuracy 7%).

The density of electrons in the plasma of the argon jet was measured spectroscopically on the basis of the broadening of hydrogen lines. In order to obtain hydrogen lines in the jet spectrum, a mixture of argon and hydrogen was placed in a separate cylinder, which was then fed into the arc chamber in the form of a slight admixture. The arc discharge was preliminarily ignited in an atmosphere of pure argon.

The jet spectra were recorded with the aid of an ISP-51 spectrograph on *Agfa-Roth-Rapid* spectral plates. The dispersion of the ISP-51 spectrograph with an $f = 270$ mm camera amounted to 40 \AA/mm in the investigated range of wavelengths and the width of the instrumental function along the narrowest lines in the jet spectrum was approximately 0.2 \AA . The half-width of the H_β and H_δ lines, allowing for Doppler expansion, amounted to $\approx 0.25 \text{ \AA}$. The spectra of the argon plasma jet were recorded for the installation conditions indicated above.

The half-widths of the H_β lines, which were measured on the basis of jet spectra from various experiments within the limits of the conditions indicated above, differ from each other by no more than 4%. Figure 2 shows a typical outline of a H_β line plotted by means of heterochromatic photometry of spectrograms obtained in the case of an arc chamber with a conical nozzle. For a comparison, Figure 3 shows the outline of a H_β line for a spectrum photographed under the

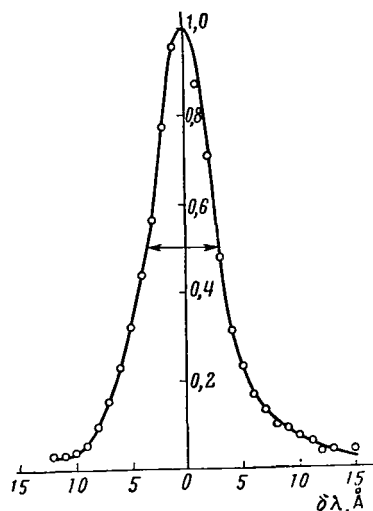


Figure 2. Shape of H_β Line. Spectrum Photographed on Installation with Nozzle. Half-Width of Line 3.62 \AA .

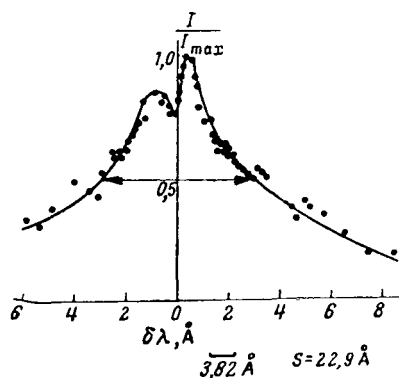


Figure 3. Contour of H_β Line. Spectrum Obtained with Installation with Anode Diaphragm. Half-Width of Line 22.9 \AA .

case the image of the jet is projected onto the slit of the spectrograph. The slit cuts off a portion of the image which corresponds to the cross section of the jet located at a distance of 1.5–2 mm from the nozzle exit. The hydrogen lines obtained in the spectrum, and the H_β lines in particular, have an intensity and width which are variable along the line, maximum in the center of the line, and decreasing toward the edges.

same conditions, but for the case when a diaphragm serves as the anode of the arc chamber, not a nozzle. As can be seen from a comparison of the graphs in Figures 2 and 3, the half-width of H_β in the case of the diaphragm anode is practically one order higher than in the case of the nozzle anode.

A comparison of the theoretical outlines of H_β and H_δ with experimental outlines, which was conducted in [2], indicated that it is not necessary to study their outlines in detail to determine the concentration of charged particles; it is sufficient to compare the experimentally found half-widths of H_β and H_δ with the theoretical ones.

The density of charged particles N_i was determined by the formula given in [3] with the effect of the electrons taken into account:

$$\delta\omega \simeq 23\bar{\alpha}N_i^{1/2}, \quad \text{sec}^{-1}.$$

Here $\delta\omega \sim \frac{\delta\lambda}{\lambda}$, where $\delta\lambda$ is the experimentally found half-width of a line; $N_i = N_e$, where N_e is the electron density; $\bar{\alpha}$ is a coefficient which equals 10.5 for H_β and 25 for H_δ . The values of N_e for the diaphragm anode with respect to the half-width of H_β are $2.1 \cdot 10^{16}, \text{ cm}^{-3}$, for the nozzle anode with respect to the half-width of H_β , $1.43 \cdot 10^{15}, \text{ cm}^{-3}$, and $1.24 \cdot 10^{15}, \text{ cm}^{-3}$ with respect to the half-width of H_δ . It should be noted that

these results were obtained with the aid of an optical system which provided average luminescence in the plane of the spectrograph slit.

It is of interest to estimate the density distribution of charged particles across the plasma jet in any of its cross sections. In this

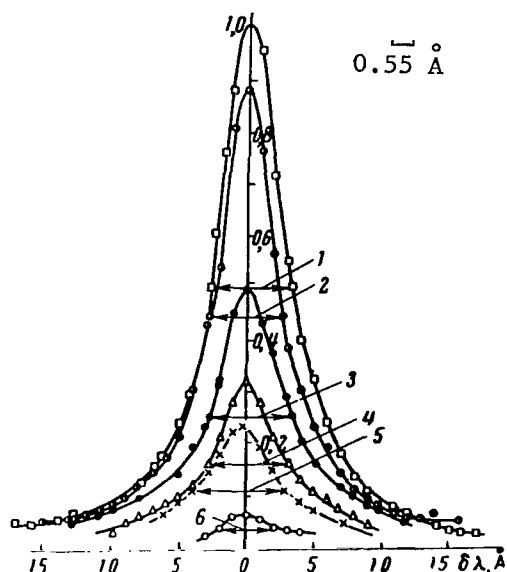


Figure 4. H_{β} Contours Plotted for Various Points Along the Line in a Direction from the Center to the Edge. Corresponding Half-Widths Are Equal to: (1) 3.42 Å; (2) 3.08; (3) 3.30; (4) 3.19; (5) 3.19; (6) 2.20.

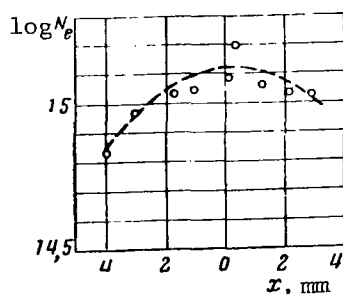


Figure 5. Distribution of Integral Electron Density with Respect to Cross-Sectional Diameter of Jet.

or

$$x_e(x_{H^+} + x_{Ar^+}) = 0.025 \frac{K_p(H^+)}{p} + \frac{K_p(Ar^+)}{p},$$

$$x_e^2 = 0.025 \frac{K_p(H^+)}{p} + \frac{K_p(Ar^+)}{p}. \quad (3)$$

Figure 4 illustrates the outlines of H_{β} constructed for half of the line in a direction from the center to the edge. Similar curves were derived for the other half of the line. On the basis of the half-widths of H_{β} determined from these

outlines, the distribution of the integral density of electrons is plotted in the given cross section of the plasma jet with respect to its diameter (Figure 5). The x -axis on this graph is directed along the spectrograph slit perpendicular to the axis of the optical system and the axis of symmetry of the arc jet. Inasmuch as a detailed examination of the investigated spectrum of the jet indicates that the argon and hydrogen lines are the most intense lines in the spectrum, the temperature of the arc jet may be considered as the temperature of a mixture of argon and hydrogen with respect to the electron density known in it. According to the conditions of the experiment, the final composition of the working gas in the arc after feeding the mixture of argon and hydrogen ^{/98} was the following: 98.5% Ar + 1.5% H_2 .

Taking into account that all H_2 molecules

dissociate at $T > 5,000^\circ K$, a system of equations of chemical equilibrium can be written, taking into account dissociation and ionization for the mixture indicated above:

$$\begin{cases} x_e x_{H^+} = 0.025 \frac{K_p(H^+)}{p}, \\ x_e x_{Ar^+} = \frac{K_p(Ar^+)}{p}; \end{cases} \quad \text{effective mass law} \quad (1)$$

$$x_{Ar^+} + x_{H^+} = x_e; \quad \text{charge conservation law} \quad (2)$$

We obtain the following equation for calculating temperature:

$$\frac{N_e k T}{p} = x_e = \left(0,025 \frac{K_p(H^+)}{p} + \frac{K_p(Ar^+)}{p} \right)^{1/2}, \quad (4)$$

where N_e are the experimental values of electron density; x_e , x_{H^+} , and x_{Ar^+} are the molar fractions of electrons, hydrogen ions, and argon ions. The calculation formulas for the equilibrium constants were taken from [4]:

$$K_p(H^+) = 6,57 \cdot 10^{-7} T^{3/2} e^{-140\,000/T}, \text{ atm};$$

$$K_p(Ar^+) = 6,57 \cdot 10^{-7} T^{3/2} e^{-182\,890/T}, \text{ atm}.$$

Inasmuch as the jet flowed into the atmosphere, the pressure was maintained equal to 1 atm.

The temperatures computed with equation (4) for the electron densities taken from the graph in Figure 5 make it possible, in turn, to estimate the character of the distribution of the integral temperature in the given cross section of the jet. The corresponding curve is shown in Figure 6 by the dotted line.

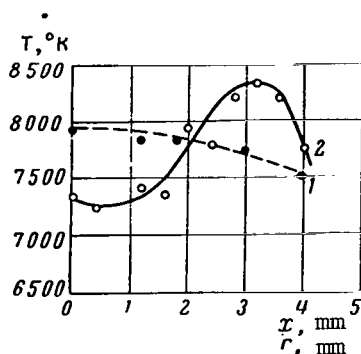


Figure 6. Temperature Distribution in Jet Cross Section. (1) integral temperature distribution; x = distance from axis of symmetry of source; (2) radial temperature distribution; r = radius.

It should be noted that the temperature determined with respect to N_e for the diaphragm anode case amounts to 10,850°K. In order to estimate the accuracy of this temperature determination, the results obtained were compared with the results of measuring the temperature by the method of relative intensities of spectral lines.

The temperature was determined with respect to the relative intensity of copper lines with wavelengths of 5105 Å, 5218 Å and 5782 Å under the condition that the selected lines are not reabsorbed. As was indicated by an experimental check with respect to lines with wavelengths 5153 Å and 5218 Å with identical excitation potentials, there is no reabsorption. The spectrograms were processed by the usual procedure of heterochromatic photometry. The radial temperature distribution in the same cross section of the jet and for the same operating conditions was found with the aid of Pierce coefficients [5], as in the method of broadening of spectral lines described above. The obtained radial temperature distribution in the jet cross section is shown in Figure 6 by the solid line. /99

As can be seen from this graph, a temperature drop appeared on the jet axis, which was not observed when determining the temperature with respect to broadening of the H_β line.

The results obtained by both methods, however, do not contradict each other. By plotting the H_β outlines at various points along the spectral line, we do not obtain its true outlines, which correspond to the specific temperature in the jet, but certain integral outlines. Since the jet is assumed to be axially symmetrical, these outlines are obtained by averaging with respect to various circular regions in the jet cross section, which has the shape of a disk. Densities are created at the ends of the line by the emission of the edge portions of the jet. In this case the line contour is practically undistorted, and here both methods provide an approximately identical temperature.

For the central sections of the spectral line, the half-widths of its integral outlines will be determined basically by the central regions of the jet with the highest temperature. It is obvious that the peripheral regions do not effect the width of the integral outlines upon summation of the emission from separate portions of the jet cross section; however, the intensity in their center increases somewhat. Due to this, the half-width of the outlines decreases, and consequently, the measured temperature also decreases.

Hence, it becomes clear why the distribution curve of integral temperature in the given jet cross section, determined by the broadening method, proceeds almost horizontally towards the x -axis and does not have a dip on the axis of symmetry of the source.

Thus, both methods of determining the temperature of the arc jet (the Ornstein method and the method of hydrogen line broadening) yield results which coincide within the limits of the experimental errors. The conclusion then follows that two such important parameters of a plasma jet, as temperature and electron density, can be determined with sufficient reliability. /100

A comparison of the results of measuring T and N_e for the two anode versions of the arc chamber, *i.e.*, the diaphragm anode and the nozzle anode, indicates that the arc jet which flows into the atmosphere from the conical nozzle has a lower temperature and electron density in it one order lower than for the jet which is formed in the short diaphragm anode.

REFERENCES

1. Petrova, G. P.: Investigation of some physical properties of an argon plasma jet. In: *Fizicheskaya gazodinamika i svoystva gazov pri vysokikh temperaturakh*. (Physical Gas Dynamics and Properties of Gases at High Temperatures.) Moscow, Izd-vo "Nauk", 1964.
2. Kitayeva, V. F., V. V. Obukhov-Denisov and N. N. Sobolev: Concentration of charged particles in a plasma jet heated in an argon and helium atmosphere. *Optika i Spektroskopiya*, Vol. 12, No. 2, 1962.
3. Kogan, V. I.: Broadening of spectral lines in a high-temperature plasma. In: *Fizika plazmy i problemy upravlyayemykh termoyadernykh reaktsiy*. (Plasma Physics and Problems of Controlled Thermonuclear Reactions.)

- Vol. 4, Izd-vo AN SSSR, 1958.
4. Stupochenko, Ye. V., I. P. Stakhanov, Ye. V. Samuylov, A. S. Pleshanov and I. B. Rozhdestvenskiy: *Termodinamicheskiye svoystva vozdukha v intervale temperatur ot 1,000 do 12,000°K i intervale davleniy ot 0.001 do 1000 atm. (Thermodynamic Properties of Air in a Temperature Range from 1000 to 12,000°K and a Pressure Range from 0.001 to 1,000 atm.)* Izd-vo AN SSSR, 1959.
 5. Pierce: Calculation of photon-emitter radial distribution in symmetrical sources. In: *Polucheniye i issledovaniye vysokotemperaturnoy plazmy. (Obtainment and Investigation of High Temperature Plasma.)* Moscow, IL, 1962.

JET OUTFLOW OF METALLIC PLASMA INTO A VACUUM

E. K. Chekalin and V. S. Shumanov

The necessity for the production and practical application of high-temperature hypersonic flows of metallic plasma having increased electrical conductivity arose in connection with the intensive development of contemporary engineering. At present, much interest is devoted to aerodynamic investigations in the flow of such plasma and the study of the interaction between metallic plasma and a solid. For detailed studies, it is desirable to use uniform and stable plasma flows with well monitored parameters: *e.g.*, temperature, density, pressure, composition, etc. For the purpose indicated, steady plasma jets in plasmatrons are widely used.

However, a number of difficulties arise in the investigation of such flows and during measurement of the plasma jet parameters.

In connection with this, the pulse method of producing metallic plasma flows in a vacuum acquires much interest. Evaporation of the electrode material in a precision pulse discharge with subsequent electrodynamic acceleration of the plasma which is formed is used to produce the flow of metallic plasma.

The average time parameters of a plasma flow of alkali metal in a vacuum have been determined in experiments.

A diagram of the experimental setup is illustrated in Figure 1. Metallic plasma was formed in a plasma gun placed in the lower section of the glass tube. The plasma gun consisted of a short alkali-metal central electrode 2 and a copper cylindrical electrode with an aperture at the top 3. Ebonite was used as an insulator between the gun's electrodes. The height of the exterior electrode was 250 mm, and its diameter was 90 mm. A vacuum of approximately $2 \cdot 10^{-5}$ mm Hg was created inside the glass tube which had a diameter of 10 cm and a length of 200 cm.

An electrical breakdown occurred inside the plasma gun along the insulator surface after initiation of the air spark gap 1 by the triggering pulse 12 from the panel of the UPR ultrahigh-speed photorecorder.

The plasma formed during the discharge in the process of evaporation and erosion of the central electrode was accelerated by electromagnetic forces, and moved upward toward the plasma gun, similar to the plasma in a coaxial accelerator [1].

Having reached the upper section of the gun, the plasma was injected into the vacuum chamber through aperture 3.

The initial voltage of the capacitor bank was 30 kV with a total capacitance of 45 μ F. The maximum discharge current, measured by a Rogowski loop, /102

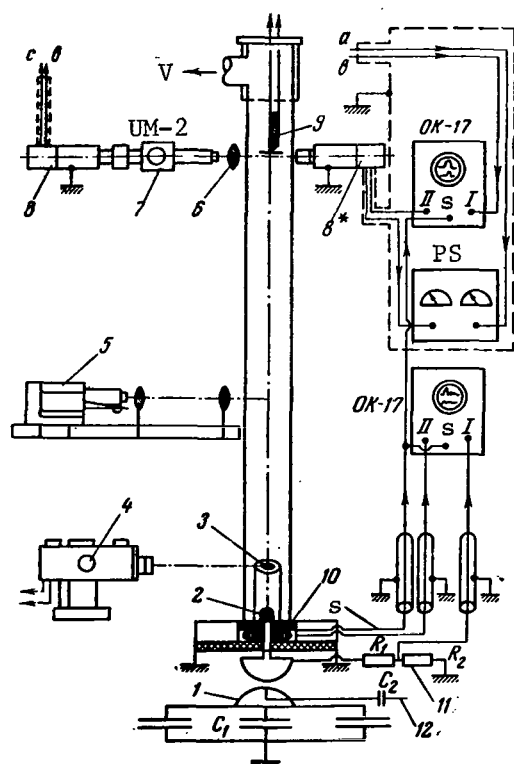


Figure 1. Diagram of Setup. (1) air spark gap; (2) electrode; (3) exterior electrode with aperture; (4) UPR; (5) ISP-51 spectrograph; (6) lens; (7) UM-2 monochromator with photomultiplier (FEU-17A); (8) FEU-19M integral (with respect to wavelengths) photomultiplier; (9) thermocouple transducer; (10) Rogowski loop; (11) pulse voltage divider; (12) start from UPR panel; (V) to vacuum pump; (PS) power supply; (S) starting signal sent to oscillograph.

see in Figure 3 that outflow in the first half-period of the discharge is characterized by disordered plasma ejections with a diffused leading edge of luminescence. The greatest outflow velocities correspond to the first plasma ejections. Plasma outflow is stable and the leading edge of plasma luminescence has a sharp boundary in subsequent discharge half-periods as a consequence of the plasma gun/103 being filled with gas.

For an explanation of the peculiarities of plasma formation in the initial stage of breakdown, the UPR camera was used to record ultrahigh-speed films of the electrical breakdown process. The filming was conducted from above along the axis of the plasma gun with the upper cover of the exterior electrode re-

reached 250 kA. The discharge frequency was 30 kHz. This matched the overall inductance of the discharge circuit of approximately $0.64 \cdot 10^{-6}$ H.

In experiments carried out with the UPR ultrahigh-speed camera, motion-picture frames of the plasma outflow into a vacuum were recorded from a gun aperture having a diameter of 30 mm (Figure 2).

The frames in Figure 2 should be viewed from top to bottom, and the columns from left to right. This will correspond to the direction of time [clockwise]. Figure 2 clearly depicts the periodic structure of plasma outflow corresponding to the vibrational character of the discharge. The presence of a bright region of luminescence close to the aperture and the rapid decrease of luminescence as the plasma flow expands is a peculiarity of the plasma outflow process. We clearly see that the plasma flow expands very quickly, and the plasma 100 mm from the aperture totally fills the cross section of the glass tube.

Figure 3 illustrates a photographic scanning recorded by the UPR camera. In the scanning, the velocity of the leading edge of plasma flow luminescence close to the plasma gun was measured. It was approximately 30 ± 2 km/sec.

It should be noted that the velocity of the leading edge of plasma flow luminescence within the limits of measurement errors did not depend on the diameter of the aperture in the exterior electrode. We

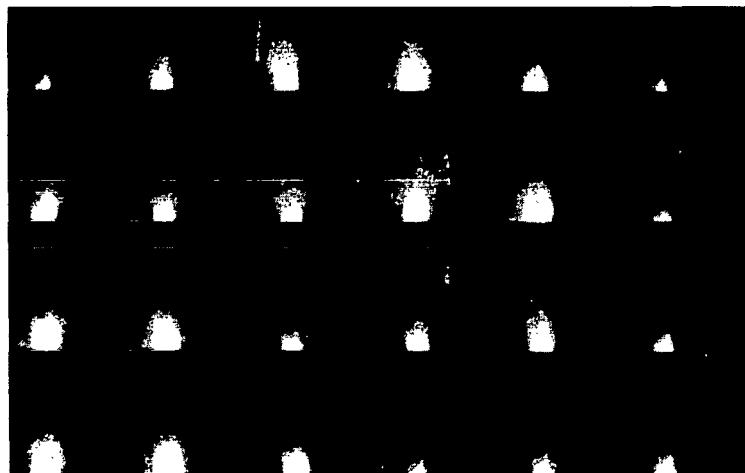


Figure 2. Ultrahigh-Speed Filming of Process of Plasma Outflow into a Vacuum. (2 μ sec time interval between adjacent frames).

moved. In Figure 4, the initial moment of breakdown is seen as a luminous plasma column that expands in time. Such a plasma column was not observed in subsequent periods. The bright halo around the edges of each frame in Figure 4 occurred as a consequence of light reflection from the inner surface of the glass tube. The presence of a plasma column in the initial stage apparently explains the strong nonuniformity of plasma flow in the first half-period of discharge.

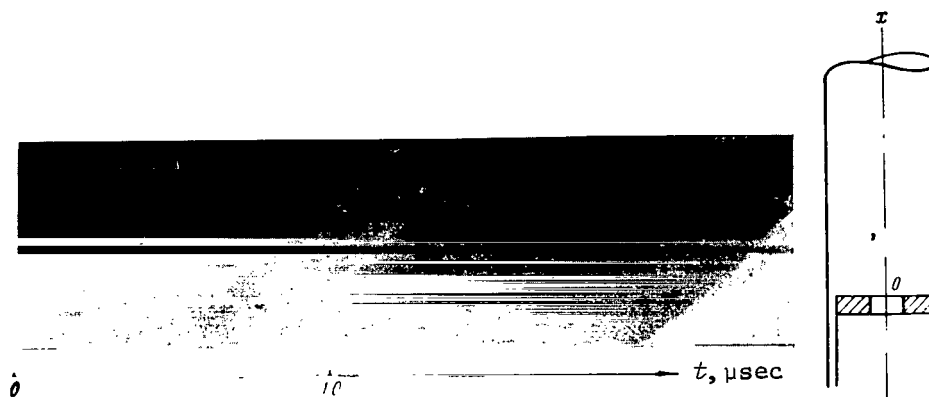


Figure 3. Photographic Scanning of Plasma Outflow into a Vacuum.

The parameters of the plasma flow were investigated in the upper part of the glass tube. Here, the plasma was more uniform, and the discharge current in the plasma was insignificant as a result of attenuation.

One of the important characteristics of plasma flow is the plasma's spectral composition. During an analysis of the plasma emission spectrum, we identified three lines of the alkali metal which we used, two lines of hydrogen (H_{α} /104 and H_{β}) and two lines of copper and sodium in the visible region. The hydrogen,

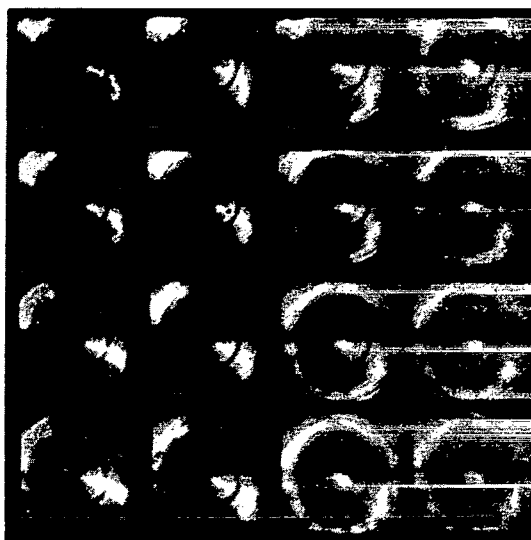


Figure 4. Ultrahigh-Speed Filming of Metallic Plasma Formation Process in Plasma Gun. (1 μ sec time interval between adjacent frames).

was thoroughly shielded by soft-magnetic iron.

From an analysis of the oscillograms (see Figures 5 and 6), we conclude that the plasma flow consists of separate clusters which correspond to periodic plasma ejections from the plasma gun. The overall duration of plasma flow was 100 μ sec.

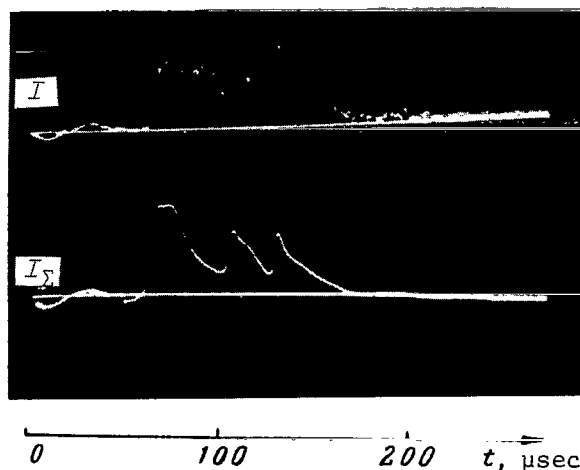


Figure 5. Oscillograms of the Emission of an Alkali Metal Line I and Integral (with Respect to Wavelengths) Emission of Plasma Flow I_Σ .

copper and sodium are admixtures of the insulator, electrode, and glass tube materials. Spectral investigations of plasma emission were carried out with a three-prism glass spectrograph (ISP-51) which was placed both in the center and upper region of the tube. In both cases, the spectral composition of the plasma proved to be identical.

Figures 5 and 6 illustrate oscillograms which show the luminescence intensity of individual spectral lines of plasma emission recorded by the UM-2 monochromator and FEU-17A photomultiplier (see Figure 1, 7 and 8). Figures 5 and 6 also illustrate oscillograms of integral (with respect to wavelengths) plasma luminescence recorded by a FEU-19M multiplier (see Figure 1, 8*). Signals from the FEU-17A and FEU-19M photomultipliers were simultaneously fed into the OK-17M double oscillograph. To avoid electromagnetic pickup, the photoelectric and electric recording apparatus

The average speed of the leading edge of plasma luminescence in a 180 cm section was calculated from the oscillograms (see Figures 5 and 6) with respect to time lags of the leading edge of plasma luminescence relative to the beginning of scanning, corresponding to the moment of electrical breakdown in the gun. The average speed was 25 ± 2 km/sec. This differs insignificantly from the corresponding speed of the luminous plasma front near the gun. Thus, we conclude that attenuation of the plasma velocity along the tube was not great.

To estimate some mean time parameters of the plasma, we used two copper-foil thermocouple transducers. They were flat square plates 60 μ

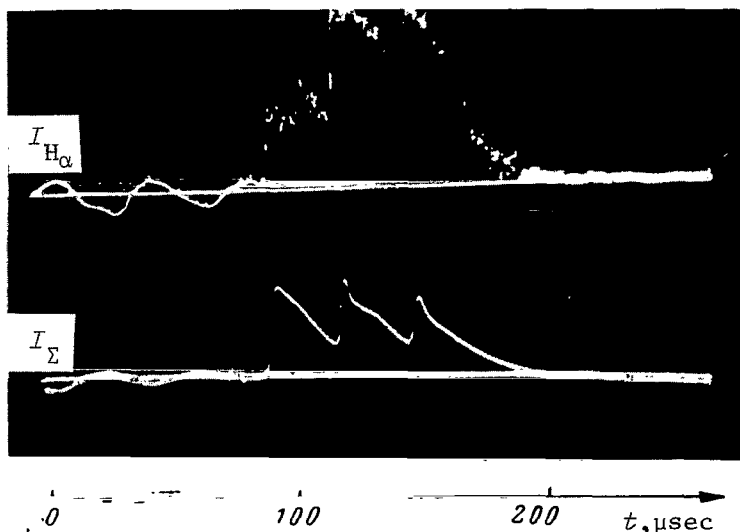


Figure 6. Oscillograms of Emission of a Hydrogen Line $I_{H\alpha}$ ($\lambda = 6562.8 \text{ \AA}$) and Integral (with Respect to Wavelengths) Emission of Plasma Flow I_{Σ} .

Let us examine a case in which the plasma consists of singly charged ions and electrons in thermodynamic equilibrium.

The amount of heat recorded by the transducer placed parallel to the plasma flow in this case can be written as

$$E_{\Sigma}'' = 2 \left(\frac{m_i w^2}{2} + 3kT_i + E_1 \right) N_i, \quad (1)$$

where k is the Boltzmann constant; T_i is the average temperature of the plasma flow in $^{\circ}\text{K}$, ($T_e = T_i$); E_1 is the amount of heat energy released during recombination in the singly ionized plasma, condensation, hardening and cooling of the metal on the cold thermocouple transducer surface, referred to one particle, in J; w is the velocity of plasma flow in cm/sec; m_i is the ion mass in g; N_i is the total number of ions which have struck the surface of the thermocouple transducer in the time τ ($N_e = N_i$).

From statistical physics, we know that

$$N_i = \frac{\bar{u}_i}{4} \bar{n}_i \tau, \quad (2)$$

where \bar{n}_i is the mean concentration of ions in the plasma flow in particles/cm³; τ is the duration of plasma flow in sec; \bar{u}_i is the arithmetic mean velocity of ions in the plasma flow, in cm/sec, which is expressed as follows:

thick and had an area of 1 cm². A thermocouple (copper-constantan junction) was soldered to each plate.

The plates of the thermocouple transducers were fastened to the thermocouple wires near the axis of the glass tube. In view of the small diameter of the wires ($\phi 0.1 \text{ mm}$), the heat losses of the transducer in the measurement process were rather small. One of the thermocouple transducers was placed perpendicular to the plasma flow, and the other was placed parallel to the flow (Figure 1, 9).

$$\bar{u}_i \simeq \sqrt{\frac{8kT_i}{\pi m_i}}. \quad (3)$$

Finally, we obtain

/106

$$E''_z = 2 \left(\frac{m_i w^2}{2} + 3kT_i + E_1 \right) \frac{\bar{n}_i \tau}{4} \sqrt{\frac{8kT_i}{\pi m_i}}. \quad (4)$$

The amount of heat recorded by the thermocouple transducer placed perpendicular to the plasma flow can thus be written;

$$E'_z = \left(\frac{m_i w^2}{2} + 3kT_i + E_1 \right) \bar{n}_i w \tau. \quad (5)$$

Solving equations (4) and (5) collectively, and using the experimental data $w = 19 \pm 2$ km/sec, $\tau = 100$ μ sec, $E'_\Sigma = 0.30$ J/cm² and $E'_\Sigma = 0.065$ J/cm², we estimated that \bar{n}_i was equal to $4.0 \cdot 10^{14}$ particles/cm³, and that the mean temperature of plasma flow was $T_i = (19 \pm 5) \cdot 10^3$ °K.

From the equation of state,

$$p = (\bar{n}_e + \bar{n}_i) kT_i, \quad \text{where} \quad \bar{n}_e = \bar{n}_i, \quad (6)$$

the average pressure in the plasma flow was determined to be 1.6 mm Hg.

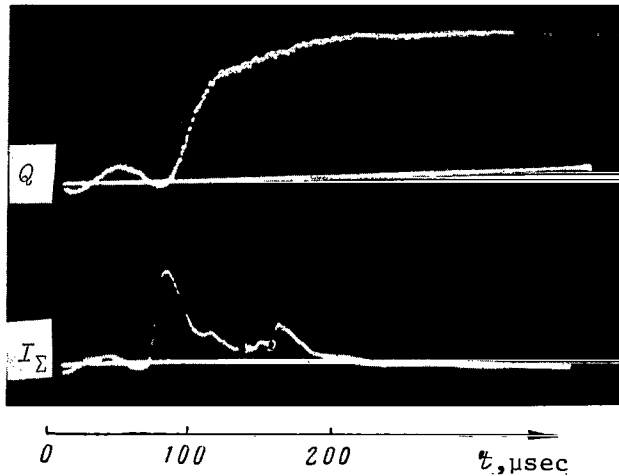


Figure 7. Oscillograms of Heat Transfer from Plasma to Incandescent Tantalum Foil Q and of Integral Emission of Plasma Flow I_Σ .

This method of estimating the plasma parameters is valid only under the condition of absolutely inelastic shock of the plasma particles against the surface of the thermocouple transducers. As it was shown in special experiments with a ballistic pendulum, a large part of the metallic plasma was condensed on the cold surface of the solid. Partial reflection of metallic plasma from the surface of the thermocouple transducers does not introduce serious errors into the estimation of the plasma parameters.

It was further necessary to demonstrate the validity of averaging the plasma parameters in an 100 μ sec interval.

For this, we recorded the time-resolved process of heat transfer from the plasma flow to the solid wall (Figure 7). We used a photoelectric method to re-



Figure 8. Ultrahigh-Speed Filming of a Plasma Flow Around a Flat Wedge. (4 μ sec time interval between adjacent frames. Direction of plasma flow from left to right).

cord intensity changes of the incandescent metallic foil's emission as a consequence of heat transfer to it from the flow [2]. An incandescent tantalum foil 10 μ thick at a temperature of approximately 1,300°K was placed perpendicular to the flow. Interpretation of the oscillograms (see Figure 7) permitted us to establish that the heat flow from the plasma lasts for 100 μ sec, which corresponds to the plasma luminescence recorded by the integral photomultiplier.

Thus, the averaging of plasma parameters in an 100 μ sec interval is completely validated. Experimentally, the measured mean quantities of the plasma flow's parameters must be close to true.

Figure 8 illustrates ultrahigh-speed photographs of the flow around a flat wedge by metallic plasma. This illustration can serve as an example of possible aerodynamic investigations in a pulsed plasma flow.

The results of investigations of the outflow of metallic plasma into a vacuum indicate that such plasma jets can be used to study heat transfer from a plasma flow to a solid wall, and for various aerodynamic investigations in plasma.

REFERENCES

1. Chekalin, E. K., V. I. Trukhin and A. I. Lozinskaya: An investigation of plasma movement in a gas-discharge tube with coaxial electrodes. In: *Fizicheskaya gasodinamika i svoystva gazov pri vysokikh temperaturakh.* (Physical Gas Dynamics and Properties of Gases at High Temperatures.) Moscow, Izd-vo "Nauka", 1964.
2. Prokhorov, Yu. G., V. F. Demichev and V. D. Matyukhin: Time measurement of plasma energy. In: *Diagnostika plazmy.* (Plasma Diagnostics.) Moscow, Gosatomizdat, 1963.

ELECTRICAL EXPLOSION OF WIRE IN AIR AND IN A VACUUM

E. K. Chekalin and V. S. Shumanov

Introduction

/109

The study of the properties of a moving plasma in a number of exceptionally important scientific problems has stimulated significant interest in physical investigations of the state of matter at high temperatures and the requirements of technology with regard to the production and practical use of high-temperature gases.

Research on the motion of a dense plasma is of particular interest in connection with this. An electrical explosion of thin metallic wires by a pulsed capacitor discharge is a convenient means of obtaining a dense high-temperature plasma. In addition, there is the possibility of investigating little-known properties of matter at high temperatures and pressures.

The phenomenon of wire explosion in various gaseous media has been studied rather well at the present time [3]. Meanwhile, the explosion of wire in a vacuum has prompted a great deal of interest. The results of such investigations may be useful when conducting aerodynamic experiments in a plasma flow. There is practically no detailed information on wire explosion in a vacuum in the current literature [1, 4].

This article presents the results of experiments with an electrical explosion of a copper wire in air and in a vacuum, which made it possible to detect essential distinctions between the explosion processes in a gaseous medium and in a vacuum. The work also presents spectroscopic investigations of time-resolved plasma emission and also the volt-ampere characteristics of the discharge at the initial stage of the explosion.

The article concludes with a presentation of the results of experiments concerned with a study of the process of expansion of a plasma cloud in a vacuum and the results of measuring certain plasma parameters.

Experimental Setup

Figure 1 shows a diagram of the experimental setup. The discharge loop consisted of a condenser bank, power buses, a discharger with an ignition system, a coaxial current-conductor, and the wire under investigation.

A bank of 45 μF condensers was used in the experiments; the bank was charged to a voltage of 22-30 kV so that the energy stored in the condenser bank amounted to 11-20 kJ. The maximum discharge current reached 150 kA. The discharge period was equal to 43 μsec .

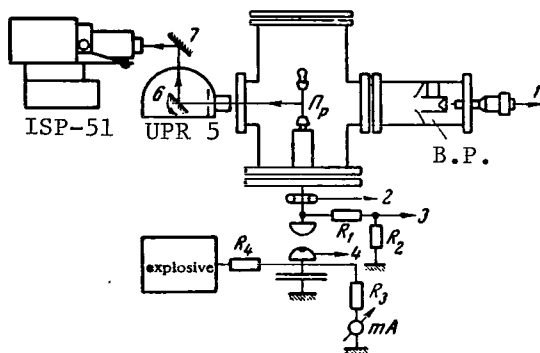


Figure 1. Installation Diagram. (1) system for measuring momentum and energy of plasma; B. P. = ballistic pendulum-calorimeter; (2) Rogowski loop; (3) pulse voltage divider; (4) air discharger; (5) entrance slit; (6) rotating mirror of UPR camera; (7) stationary mirror.

momentum of the plasma formed during the wire explosion was attached to one of the windows and the other window served for spectroscopic investigations and high-speed motion-picture photography of the process of wire explosion.

The vacuum system of the installation consisted of a VA-2-3 vacuum unit and a VN-1 fore pump which provided a vacuum of $3 \cdot 10^{-5}$ mm Hg inside the vacuum chamber.

Experimental Procedure and Equipment Used

The discharge current was measured with a Rogowski loop, while the pulsed voltage in the wire was measured with a voltage divider. Double pulsed oscillographs OK-17 M and OK-21 with slave sweep were used to record the wire explosion process. The oscillographs were triggered by a signal from the UPR panel. Ultrahigh-speed motion-picture photography of the process of electrical wire explosion was conducted by means of a UPR camera which operates in photorecorder and time-magnification modes.

An ISP-51 three-prism glass spectrograph with a camera that had a focal length of $f = 270$ mm was used for spectroscopic investigations.

The time-resolved emission spectrum of the plasma was investigated with a UPR camera combined with an ISP-51 spectrograph (see Figure 1). The light from the exploding wire entered the limiting horizontal slit 5 located in the focal plane of the optical system of the UPR camera. The image of this slit was reflected from the rotating mirror 6 of the UPR camera and mirror 7, and then entered the entrance slit of the ISP-51 spectrograph. The horizontal image of

The commutating device was an air-controlled discharger which was pulse-actuated from the control panel of an ultrahigh-speed photorecorder (UPR).

The wire to be investigated was /110 attached inside a vacuum chamber by means of two clamps, one of which was placed on a high-voltage electrode inserted into the vacuum chamber from below. The main experiments in the vacuum were conducted with a copper wire 0.31 mm in diameter and 85 mm in length.

The vacuum chamber was made from stainless steel in the shape of a cylinder with an internal diameter of 430 mm and a height of 700 mm. Vacuum-sealed windows were fabricated on the lateral surface. The chamber of a ballistic pendulum-calorimeter with a system for measuring the energy and

slit 5, which is bounded by the light flux from the plasma, shifted when mirror 6 was rotated with a given linear velocity along the vertical slit of the spectrograph. Time scanning of the spectrum, the geometric size of which with regard to height corresponded to the height of the entrance slit of the spectrograph, was obtained on the photographic plate of the spectrograph. Time resolution amounted to 2 μ sec.

The image of the central portion of the wire was focused on the spectrograph slit in the experiments.

To measure the momentum and energy of the plasma which forms during the wire explosion, a ballistic pendulum-calorimeter (B. P., Figure 1) was used. The calorimeter was made from copper foil 0.3 mm in thickness in the shape of a cylinder 50 mm in diameter and 100 mm in length. The bottom of the calorimeter had the shape of a conical surface with a 45° aperture angle (Figure 2). The calorimeter was suspended in a horizontal position inside the vacuum chamber by thin wires.

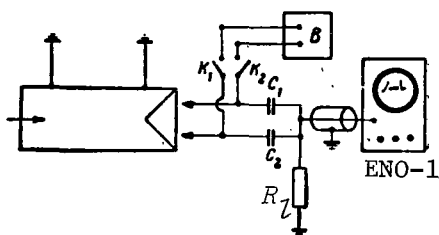


Figure 2. Electrical Circuit for Measuring Time Interval Between Moments of Contact of Calorimeter with Electrical Contacts.

This configuration of the ballistic pendulum-calorimeter provided minimum reflection of moving plasma from the calorimeter. Thus, the interaction of the moving plasma with the calorimeter could be considered as an absolutely inelastic shock. This made it possible to eliminate the errors in measuring the momentum and energy of the plasma which are caused by the partial reflection of plasma from the calorimeter. The momentum transmitted by the moving plasma to the calorimeter p_{pl} is equal to

$$p_{pl} = m_{pl} \bar{v}_{pl} \quad (1)$$

where m_{pl} is the mass of the plasma striking the calorimeter and \bar{v}_{pl} is the mean velocity of the plasma.

Knowing the mass of the calorimeter M_c and measuring its speed, the momentum of the plasma striking the calorimeter can be calculated. The speed of the calorimeter was measured with two miniature electrical contacts installed at strictly determined distances from the rear wall of the calorimeter. The contacts could be moved with the aid of micrometric screws with respect to the rear wall of the calorimeter to a distance of 0-15 mm. The distance was set by the micrometric screws with an accuracy of ± 0.02 mm.

In its movement, the calorimeter first touches one contact (the closer one), and then the other after a certain length of time. By measuring the time interval τ between moments of contact of both contacts and knowing the difference in distances from the contacts to the rear wall of the calorimeter ($\Delta l = l_1 - l_2$), the average speed of the calorimeter V_c was determined in this section.

The electrical circuit for measuring the time interval between moments of contact of the calorimeter with both contacts is shown in Figure 2. Each contact was connected in series to capacitances C_1 and C_2 , which had been charged to a voltage of 10 V from rectifier B before the experiment. The capacitances were connected to the ground across the electrical contacts during movement of the calorimeter after the wire explosion. Electrical pulses induced by a series discharge of capacitances C_1 and C_2 appeared on the common load R_L . A signal was sent from R_L through a cable to the input of the ENO-1 oscillograph with slave sweep. By measuring the time interval τ between pulses on an oscillogram and knowing the distance Δl , the average speed of the calorimeter V_c can be computed.

In order to exclude the effect of the moving plasma on the measuring system, a diaphragm with an aperture 47 mm in diameter was installed in front of the calorimeter (see Figure 1).

Application of the procedure described above for measuring the momentum of a plasma is possible only under the condition that the time interval between the closing of both contacts τ is much greater than the time of interaction of the moving plasma on the calorimeter. Under this condition, the calorimeter will move by inertia during the measurement.

To estimate the effect of the suspension system and calorimeter deceleration during its movement in section Δl as a result of compressing the spring of the front contact, the calorimeter was calibrated after installation in the vacuum chamber by means of a pendulum which imparted a mechanical impulse of a specific magnitude to the calorimeter. A plastiline sphere attached to a long string was used as the pendulum.

The results of calibration indicated that deceleration of the calorimeter during its motion in section Δl is small. A distance of $\Delta l = 0.5$ mm ($l_1 = 1.0$ mm; $l_2 = 0.5$ mm) was established in the experiments and during calibration.

By measuring the temperature difference on the calorimeter wall before and after the wire explosion, the energy transmitted from the plasma to the calorimeter could be calculated. Measurement of the heating of the calorimeter, into which the plasma fell, was conducted with the aid of a thermocouple which was soldered to the calorimeter (copper-constantan junction). Then

$$E = 4.17cM_c\Delta T, \quad (2)$$

where E is the total energy transmitted by the plasma to the calorimeter in J; M_c is the mass of the calorimeter in g; c is the thermal capacity of the calorimeter material in cal/g·deg; ΔT is the temperature difference on the calorimeter wall before and after the experiment in °C.

Experimental Results and Discussion

The first experiments were set up to investigate the electrical explosion of a copper wire 0.31 mm in diameter and 66 mm in length, at an initial voltage of 22 kV in the condenser bank, in air.

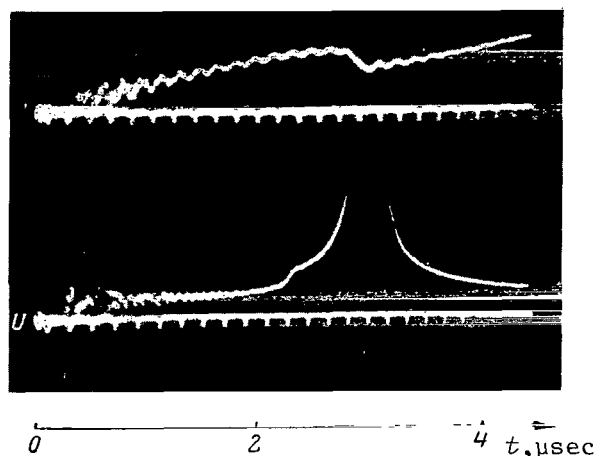


Figure 3. Oscillograms of Discharge Current I and Voltage U During the Explosion of a Copper Wire 0.31 mm in Diameter and 65 mm in Length in Air, $U_0 = 22$ kV. Time markers = 0.2 μ sec.

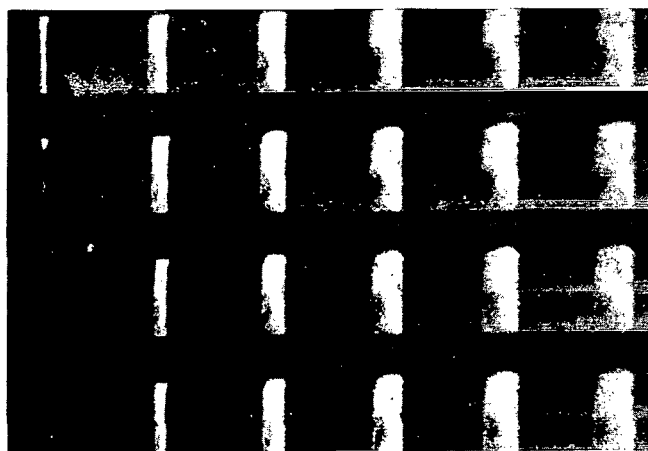


Figure 4. Ultrahigh-Speed Motion-Picture Photography of the Process of Explosion of a Copper Wire 0.31 mm in Diameter and 65 mm in Length, $U_0 = 22$ kV, in the Air. Time interval between frames = 0.4 μ sec.

Figure 3 shows oscillograms of the discharge current and voltage obtained in an electrical explosion of a wire in air. The current discontinuity and the corresponding voltage peak which occur at the moment of a sharp decrease in conductivity of the material of the exploding wire, caused by the conversion of the overheated liquid metal of the wire into vapors [1, 2], is quite visible on the oscillogram. The energy density in the wire, which reaches 6 J/mg at the moment of current discontinuity, was calculated on the basis of the oscillograms.

Figure 4 shows frames from ultrahigh-speed motion-picture photography of the process of wire explosion in air. The frames should be examined from bottom to top, and the columns from left to right. It can be seen very well in Figure 4 that the luminescence of the internal regions of the expanding plasma cloud has a transverse structure and a sharply outlined uniform luminescence front.

Figure 5 (left) shows a photographic scanning of the explosion of a wire 65 mm in length ($U_0 = 22$ kV) in air. It is distinctly seen that the luminescent plasma cloud expands. ^{/113} The velocity in this case at the initial moment, which amounted to $8 \cdot 10^5$ cm/sec, decreases significantly subsequently.

An analysis of the photographic scanning in Figure 5 (left) points to the fact that the wire explosion probably

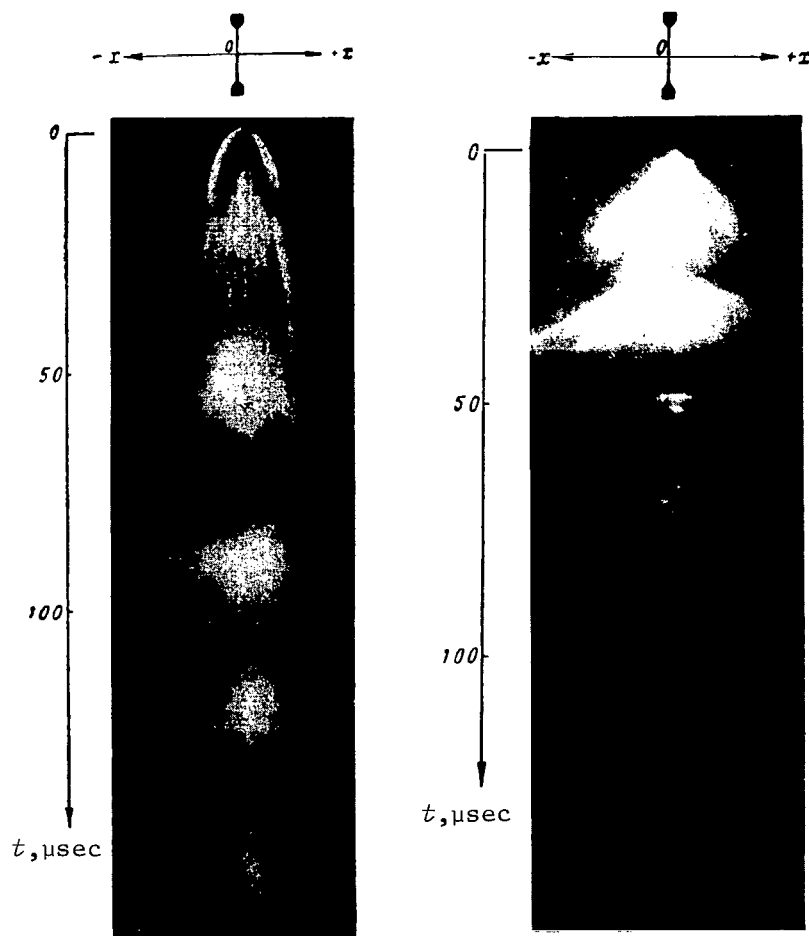


Figure 5. Photographic Scannings of the Processes of Explosion of a Copper Wire 0.31 mm in Diameter.

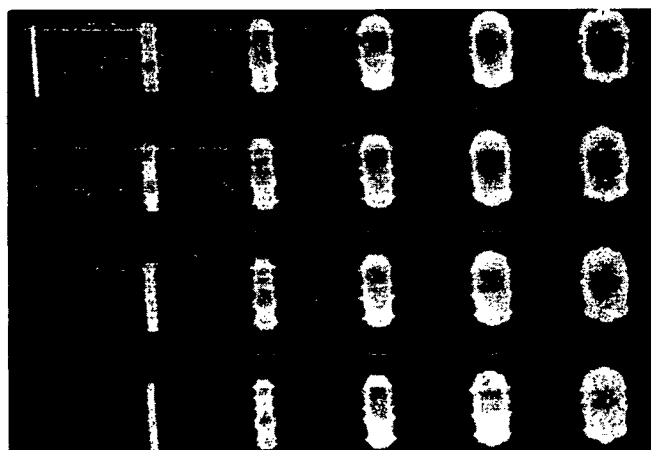


Figure 6. Ultrahigh-Speed Motion-Picture Photography of the Process of Explosion of a Copper Wire 0.31 mm in Diameter and 85 mm in Length, $U_0 = 30$ kV, in a Vacuum. Time interval between frames = 0.4 μ sec.

leads to the formation of a cylindrical shock wave in the air, the velocity of which is quickly attenuated [1].

Figure 6 illustrates the results of ultrahigh-speed motion-picture photography of the process of wire explosion in a vacuum. A characteristic feature of explosion in a vacuum is a distinctly expressed transverse structure of the expanding plasma cloud with sharp ejections of plasma on the luminescence front. The indicated structure has a periodic character. This peculiarity of the expanding cloud indicates the presence of significant instability of dense plasma /114 at the initial period in contrast to a wire explosion in the air (see Figure 4).

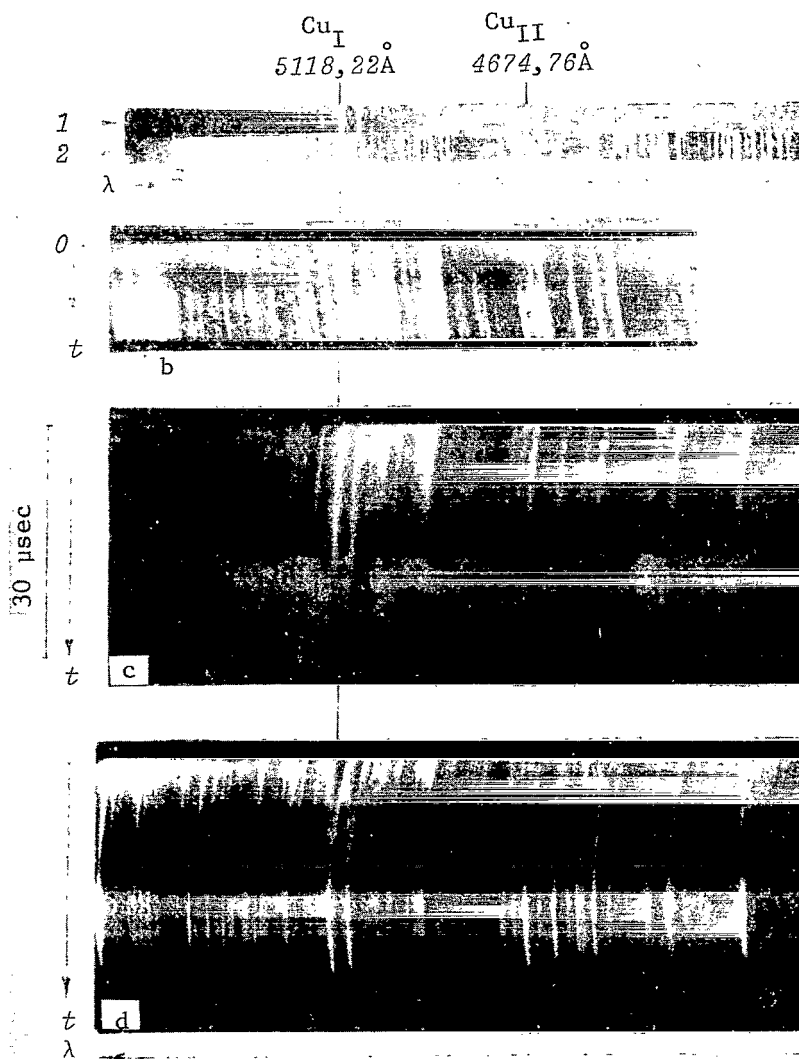


Figure 7. Emission Spectrum of Plasma Which Forms During the Explosion of a Copper Wire 0.31 mm in Diameter and 85 mm in Length, $U_0 = 30 \text{ kV}$, in a Vacuum. (a) integral (with respect to time) emission spectrum of exploding wire; (b,c,d) time scannings of emission spectrum of exploding wire.

Figure 5 (right) illustrates a photographic scanning of the process of explosion of a wire 85 mm in length, $U_0 = 30$ kV, in a vacuum, on which it can be seen that expansion of the plasma occurs at a constant rate, but the front itself does not have a concise boundary. The rate of expansion of the leading luminescence front of the plasma in a vacuum during a long period of time changes insignificantly ($3 \cdot 10^5 - 4 \cdot 10^5$ cm/sec) and exceeds the corresponding velocity of the luminescence front at later stages during an explosion in the air. The secondary electrical discharges in the plasma, which were formed in the process of wire explosion, are distinctly visible in the figure.

A comparison of the results obtained indicates that the processes of plasma expansion in a vacuum are less stable than in air.

Figure 7 shows the integral (with respect to time) spectrum and the time-resolved emission spectrum which accompanies the explosion of a copper wire in a vacuum.

Analysis of the integral spectrum indicated that significantly broadened /115 atomic lines and singly ionized ions of copper are mainly observed in the visible region of the spectrum.

Figure 7b, c and d illustrates typical time scanings of spectral lines which correspond to the various stages of explosion of the copper wire.

A continuous spectrum is distinctly seen in Figure 7b at the initial stage of the explosion for 3 μ sec, which evidently originates due to the emission of quickly evaporating solid and liquid particles of the wire that are suspended in the plasma.

The appearance of a continuous spectrum at the later stages of the explosion (see Figure 7c and d) was probably caused by recombination and retardation emission which develops in the process of secondary electrical discharges in the expanding plasma.

The appearance of an absorption spectrum and the reversal of the copper lines on the brighter background of the continuous spectrum points to the fact that secondary electrical discharges occur in the internal regions of the expanding plasma cloud (see Figure 5, right) and the temperature of the plasma then increases inside the cloud.

In the process of expansion in the later stages, the plasma becomes optically transparent and phenomena of reversal and absorption of spectral lines are not observed (see Figure 7d). In this case the atomic lines of the electrode material and copper atoms, the significant expansion of which indicates an increase in concentration of charged particles in the plasma, flare up simultaneously with the appearance of the continuous spectrum. The emission of the central portion of the plasma cloud is recorded directly in this case.

To measure some of the plasma parameters and to study the character of plasma expansion in a vacuum, experiments were conducted with a ballistic pendulum-calorimeter. The calorimeter was placed inside a vacuum chamber at two

fixed distances from the wire, equal to 190 and 330 mm, respectively. The results of measuring the plasma energy and momentum transmitted to the calorimeter are given below. These data were obtained by averaging the results of ten experiments. /116

l	p	E	U_0	d	L
190	175	33	30	0.31	85
330	94	20	30	0.31	85

Here, l is the distance from the wire to the calorimeter in mm; p is the momentum of the plasma measured by the calorimeter in dynes·sec; E is the total energy of the plasma measured by the calorimeter in J; U_0 is the initial voltage in the condenser bank in kV; d is the diameter of the wire in mm; L is the length of the wire in mm.

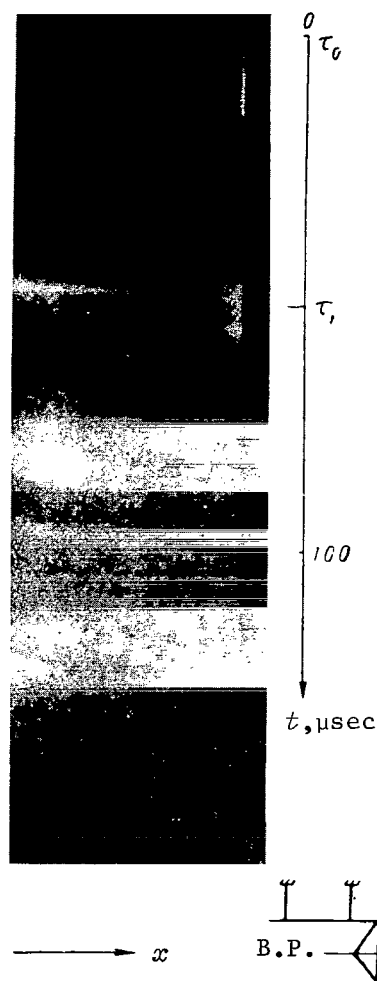


Figure 8. Photographic Scanning of Plasma Motion near Calorimeter. B. P. = ballistic pendulum-calorimeter.

A photographic scanning of the plasma motion near the calorimeter was then obtained (Figure 8). The plasma was photographed through the lateral window in the calorimeter chamber. The luminescence of the exploding wire, which is reflected from the forward portion of the calorimeter, is distinctly seen in Figure 8 in the time interval from τ_0 to τ_1 . The time τ_0 corresponds to the beginning of the wire explosion. At time τ_1 , the leading front of the luminescent plasma reaches the calorimeter. The average speed of the plasma in the section from the point of attachment of the wire to the calorimeter (330 mm) is equal to $6 \cdot 10^5$ cm/sec, and the speed of the plasma in direct proximity to it amounts to about $(7 \pm 1) \cdot 10^5$ cm/sec. /117

Thus, having data on the average speed of the plasma near the calorimeter, the mass of the material striking the ballistic pendulum-calorimeter can be estimated: $m_{pl} = p_{pl}/v_{pl} = 1.57 \cdot 10^{-4}$ g.

Hence, the plasma density n , averaged for the entire luminescence region (see Figure 8), is equal to $1.75 \cdot 10^{15}$ particles/cm³.

The kinetic energy W_k of the plasma striking the calorimeter can be estimated:

$$W_k = m_{pl} v_{pl}^2 / 2 = 2.8 \text{ J.} \quad (3)$$

The total energy of the plasma, recorded by the calorimeter located at a distance of 330 mm from the investigated wire, was equal to 20 J. This increase in the energy of the plasma striking the calorimeter, in comparison with W_k , may be explained either by the significant internal energy of the plasma, or by the heating of the calorimeter by intense luminous radiation from the expanding plasma cloud. The following experiment was conducted to estimate the heating of the calorimeter by radiation. A barrier made of organic glass 5 mm in thickness was installed in front of the calorimeter. Neither the movement of the calorimeter nor its heating was recorded in this case. Thus, heating of the calorimeter due to luminous radiation was insignificant, at least in the interval of wavelengths that can be passed by organic glass. Consequently, heating of the calorimeter is explained by the internal energy of the substance which strikes the calorimeter.

An increase in the speed of the plasma as compared to the speed measured by means of photographic scanning (Figure 5, right) at the initial stage of plasma expansion is probably a result of heating of the substance in the process of the secondary discharges and a consequence of the origination of cylindrical shock waves in the expanding plasma cloud.

Estimation of the mean temperature of the plasma requires investigations of the spectral composition of the plasma in the region of the ultraviolet range of wavelengths. This makes it possible to establish the probable existence of ions of a multiple degree of ionization, allowance for the recombination of which is necessary for calculations of mean plasma temperature in experiments with a ballistic pendulum. /118

Thus, the explosion of a wire in a vacuum, in spite of the significant complexity of the phenomenon on the whole, makes it possible to study a number of physical properties of a dense plasma expanding in a vacuum.

REFERENCES

1. *Vzryvayushchiyesya provolochki. (Exploding Wires.)* Collection of articles edited by A. A. Rukhadze, Candidate of Physical and Mathematical Sciences, Moscow, IL, 1963.
2. Keilhacker, M.: The mechanism of quasi-explosive vaporization of copper wires. *Z. Angew. Phys.*, Vol. 12, No. 2, 1960.
3. Nash, C. P. and W. McMillan: On the mechanism of exploding wires. *J. Phys. Fluids*, Vol. 4, No. 7, 1961.
4. Kvartskhava, I. F., V. V. Bondarenko, R. D. Meladze and K. V. Suladze: Electrical explosion of wires in a vacuum. *Zhurnal Eksperimental'noy i Teoreticheskoy Fiziki*, Vol. 34, No. 5(11), 1956.

EXPERIMENTAL DETERMINATION OF ELECTRON CONCENTRATIONS AND
EFFECTIVE FREQUENCIES OF ELECTRON COLLISION WITH
NEUTRAL PARTICLES IN AIR, N₂, O₂, CO,
ARGON AND CO₂ BEHIND SHOCK WAVES

Yu. S. Lobastov

The first experimental data on the effective cross sections of electron collisions with neutral particles were obtained by Ramsauer and Townsend [1]. However, at electron temperatures below 11,000°K, the methods of these authors are extremely inaccurate. In thermally ionized air, the effective collision cross sections were determined by the magnetic method at 3,500-6,200°K [2]. The electron concentrations in this case were taken from the calculation. /119

This article is devoted to an experimental determination of electron concentrations and effective frequencies of electron collisions with neutral particles in various gases behind reflected shock waves. The indicated parameters were determined by measuring the attenuation of radio waves simultaneously at two frequencies, i.e., 37,500 MHz and 18,750 MHz. The advantages of this method in comparison with those indicated above should also include the good space resolution of the radio equipment as well as the possibility of independent determination of electron concentrations and effective collision frequencies.

Theory of Method

The actual parts of high-frequency conductivity of an ionized gas σ and its dielectric permeability ϵ can be written in the following form [3]:

$$\sigma = K_{\sigma} \left(\frac{\omega}{\nu_{\text{eff}}} \right) \frac{e^2}{m} \frac{n_e \nu_{\text{eff}}}{\omega^2 + \nu_{\text{eff}}^2}, \quad (1)$$

$$\epsilon = 1 - K_{\epsilon} \left(\frac{\omega}{\nu_{\text{eff}}} \right) \frac{4\pi e^2}{m} \frac{n_e}{\omega^2 + \nu_{\text{eff}}^2}, \quad (2)$$

where $K_{\sigma}(\omega/\nu_{\text{eff}})$ and $K_{\epsilon}(\omega/\nu_{\text{eff}})$ are certain functions of the circular frequency ω of the sounding plasma of the radio signal; ν is the effective frequency of electron collisions with neutral gas particles; n_e is the electron concentration in cm³; e and m are the electron charge and mass. Graphs of the functions K_{σ} and K_{ϵ} are given in [3]. The absorption coefficient of the radio waves has the following form:

$$\delta = \frac{2\omega}{c} \chi, \quad (3)$$

where

$$\chi = \sqrt{-\frac{\epsilon}{2} + \sqrt{\left(\frac{\epsilon}{2}\right)^2 + \left(\frac{2\pi\sigma}{\omega}\right)^2}}. \quad (4)$$

If the degree of ionization of the gas is not very great, *i.e.*,

/120

$$\frac{4\pi\sigma}{\omega} \ll |\epsilon|, \quad (5)$$

then when $\epsilon > 0$

$$\delta \approx \frac{4\pi\sigma}{c\sqrt{\epsilon}}. \quad (6)$$

Criterion (5) denotes in our case that the conductivity for the lowest frequency of 18,750 MHz should not exceed the value of $|\epsilon| 0.9 \cdot 10^{10} \text{ sec}^{-1}$. The following parameters were maximum in this work: $n_e = 10^{12}$ and $v_{eff} = 5 \cdot 10^{11}$. Then $K_\sigma = 1$, $K_\epsilon = 1.4$, $\sigma = 5 \cdot 10^8$ and $\epsilon = 0.98$. Thus, inequality (5) is valid for all gas parameters that are not so high, and formula (6) can be used in the calculations.

The amount of apparent growth of absorption of the radio waves due to their reflection from the plasma layer should also be estimated. According to [3], the ratio of the energy flux in a reflected wave to the energy flux in an incident wave for a plane electromagnetic wave normally incident to a plasma layer with a sharp boundary is expressed by the following formula:

$$|R|^2 = \frac{(1-n)^2 + n^2\chi^2}{(1+n)^2 + n^2\chi^2}, \quad (7)$$

where n is the refractive index of the plasma. Then for the given values of $n_e = 10^{12}$ and $v_{eff} = 5 \cdot 10^{11}$, $|R|^2 = 2 \cdot 10^{-4}$, *i.e.*, the percentage of reflected energy amounts to approximately 0.02% of the incident energy.

Equation (6) is the dependence of δ on ω , n_e and v_{eff} ; therefore, the measurement of δ at two frequencies makes it possible to independently determine both n_e and v_{eff} :

$$v_{eff}^2 = \frac{\delta_1 \omega_1^2 \sqrt{\epsilon_1} - \delta_2 \omega_2^2 \sqrt{\epsilon_2}}{\delta_2 \sqrt{\epsilon_2} - \delta_1 \sqrt{\epsilon_1}}. \quad (8)$$

Since the frequencies differ from one another only by two times, the following can be stated, without introducing any notable error:

$$\sqrt{\varepsilon_1} \approx \sqrt{\varepsilon_2};$$

$$v_{eff}^2 = \frac{\delta_1 \omega_1^2 - \delta_2 \omega_2^2}{\delta_2 - \delta_1}; \quad (8a)$$

$$n_e = \frac{mc}{4\pi e^2} \frac{\sqrt{\varepsilon_1} \delta_1 (\omega_1^2 + v_{eff}^2)}{v_{eff}}. \quad (9)$$

It is usually assumed at the beginning of the calculation of n_e that $\sqrt{\varepsilon_1} = 1$ and, having obtained a zero approximation for n_e , it and v_{eff} are substituted into (2). Then the next approximation for n_e is found from the already complete formula (9).

The first independent determination of n_e and v_{eff} by means of measuring the absorption of radio waves simultaneously at two frequencies was undertaken in the USSR in flames [4], and then in a gas heated by a shock wave [5].

Experimental Procedure

The measurements were conducted in a shock tube with a channel of square cross section 7.2 x 7.2 cm (Figure 1). The high-pressure chamber was 125.0 cm long and the low-pressure chamber consisted of several measuring sections. The distance from the diaphragm to the plane in which the microwave antennas were placed amounted to 600 cm. The depth of the vacuum in the low-pressure chamber was monitored by a VT-2P thermocouple vacuum meter. The filling of the measuring sections with the investigated gas to the required pressure was monitored with the aid of an oil manometer.

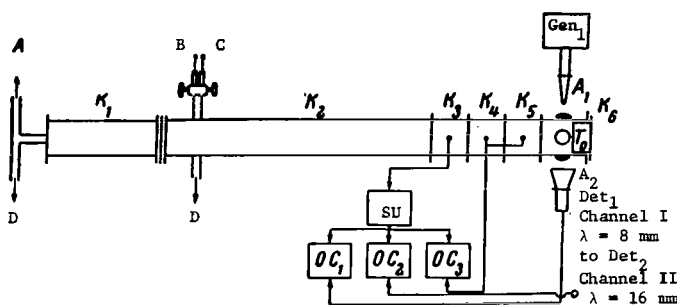


Figure 1. Block Diagram of Installation for Measuring the Absorption of Radio Waves. (A) to cylinder; (B) to manometer; (C) to filling system; (D) to evacuation system.

Three piezosensors were built into the measuring chambers (see Figure 1). The first sensor was used to start the electronic equipment, while the second and third, which were connected together and had opposing polarities, fixed the velocity of the departing shock wave. The chamber in which the absorption of radio waves was investigated was made from an intact piece of organic glass and was 250 mm in length. Radio-wave absorption was measured simultaneously on two wavelengths: 8 and 16 mm. One beam passed through the center of the chamber in a horizontal direction, while the other passed in a vertical direction, but both passed in one plane perpendicular

to the tube axis. The 8-mm measuring set consisted of a GS-701 generator, a polystyrene narrow-directional antenna, two polystyrene lenses, a horn antenna, a D5-8 measuring attenuator, an AVR 0812/20 decoupling attenuator, and a DS 0812 detector section. A D601A crystal was used as the detector. An IVL-634 measuring line was used to match the receiving track and to check the measuring attenuator by the short-line method. The 16-mm track similarly consisted of a GS-702 generator, antennas, lenses, D5-7 attenuators, an AVR 1218/20, a DS1218 detector section and a D601B crystal. An IVL-635 line was used for tuning.

Particular attention in tuning the radio tracks was devoted to the coaxiality of the transmitter and receiver systems, the parallel nature of the radio beam, and identical cross section of the radio beam at both the 8-mm and 16-mm wavelengths. In the opposite case, varying space resolution can lead to additional errors in measurements, especially in the gas behind a reflected shock wave. The width of the radio beam in a direction along the tube axis amounted to 20 mm on a level of 10 decibels [6]. The microwave generators, for measurements behind a reflected shock wave, operated in a modulation mode with square voltage from an external generator with a pulse duration of 20 μ sec.

A 630-ohm resistance served as the load of each crystal, and it was equal to the resistance of the microammeter with which the crystal characteristics were recorded. The 50- μ A current across the crystals provided a sufficient level of the measured signal above the noise, although the crystals also went beyond the quadratic range of operation. The characteristics of the crystals were checked also in a 50- μ A current after each series of experiments, since a certain change was observed in them over time. The power of the radio signal recorded by the receiver was maintained on one level, so that the initial current across the crystals always (except during the experiment) remained constant and the detector did not go beyond its characteristics.

The level of zero and total absorption of the radio signal was noted on each oscillogram during the course of the process. With respect to the amplitude of the signal fixed on the film to the distance between markers of zero and total absorption, we find the value of attenuation α in decibels with the aid of a graduated graph on the absorption path z in cm. The quantity in formulas (8) and (9) is related to α by the expression

$$\delta = \frac{\alpha}{4.34 \cdot z}. \quad (10)$$

Results of Experiments

The experiments were performed in the following gases: air, nitrogen, oxygen, and carbon monoxide and dioxide. The determination of v_{eff} in argon by measuring the absorption at two frequencies was extremely difficult, since reliable results can be obtained only if $v_{eff} \sim \omega$ [4]. According to the same data [1, 2, 7], the cross section of electron collisions with neutral argon atoms $Q \approx 2 \cdot 10^{-17} \text{ cm}^2$, which leads to a value of $v_{eff} \approx 0.45 \cdot 10^{28} (p_2/\sqrt{T_2}) Q = 10^9$ at

$T_2 = 4,000^\circ \text{ K}$ and $p_2 = 1 \text{ atm}$, where T_2 and p_2 are the gas temperature and pressure behind a reflected shock wave. It is obvious that the Q determination of argon requires the use of longer (centimeter) waves or the simultaneous measurement of absorption and reflection of radio waves.

Our investigations were conducted behind reflected shock waves, since this made it possible to obtain sufficiently high temperatures and pressures for small M_0 numbers of the incident shock waves, which in turn provided an extremely rapid arrival of the gas to the equilibrium state.

Air

The amplitude of the first "plateau" on absorption oscillograms was adopted as the radio-wave absorption level behind a reflected shock wave (Figure 2) since a comparison with pressure scannings and a Töpler reflection scanning indicated that the beginning of the increase in absorption coincides with the beginning of the intersection of the radio beam with the reflected wave. Having reached a certain level, absorption remains unchanged during a certain length of time. Hence, the conclusion can be made concerning the achievement and existence of equilibrium ionization during this period of time. In addition, the values of the electron concentrations are extremely close to equilibrium (Figure 3).

The equilibrium achievement times amount to 70-170 μsec . The presence of secondary processes caused by the interaction of the reflected shock wave with the contact surface can be estimated on the basis of the form of the absorption oscillograms. At initial pressures of approximately 1 mm Hg, the absorption, having reached values of approximately 20 μsec , then decreases to a level which can be called the secondary level or the absorption level behind a super-reflected wave (see Figure 2, top). At higher initial temperatures (above 2 mm Hg) the second maximum always becomes greater than the first (see Figure 2, bottom). The lower values of secondary conductivity at low pressures are explained by the shorter dimensions of the gas plug and by the fact that the axes of the radio /123 beams are at a distance of 20 mm from the end. Measurements of radio-wave absorption indicated that not only does the electron concentration increase in the second maximum, but also the frequency of electron collisions. For example, at $M_0 = 5.9$ of an incident shock wave and at an initial pressure of 3 mm Hg, the electron concentration and effective collision frequency behind a reflected shock wave are as follows: $n_e = 7.7 \cdot 10^{10}$ and $\nu_{eff} = 1.2 \cdot 10^{11}$. $n_e = 2.5 \cdot 10^{11}$ and $\nu_{eff} = 1.4 \cdot 10^{12}$ behind a super-reflected wave, which indicates a significant increase in temperature and pressure as a result of this process.

The very time of the existence of the equilibrium state behind a reflected shock wave increases as the initial pressure increases. If it amounted to approximately 60 μsec at $M_0 = 6.25$ and a pressure of 2 mm Hg in front of the incident shock wave, it would be 150 μsec at $M_0 = 6.45$ and a pressure of 10 mm Hg.

A super-reflected wave R_r , which arises at the moment of encounter of the re- /124

flected wave R with the contact surface K and moving in a direction to the end, is very visible in a Töpler scanning (Figure 4).

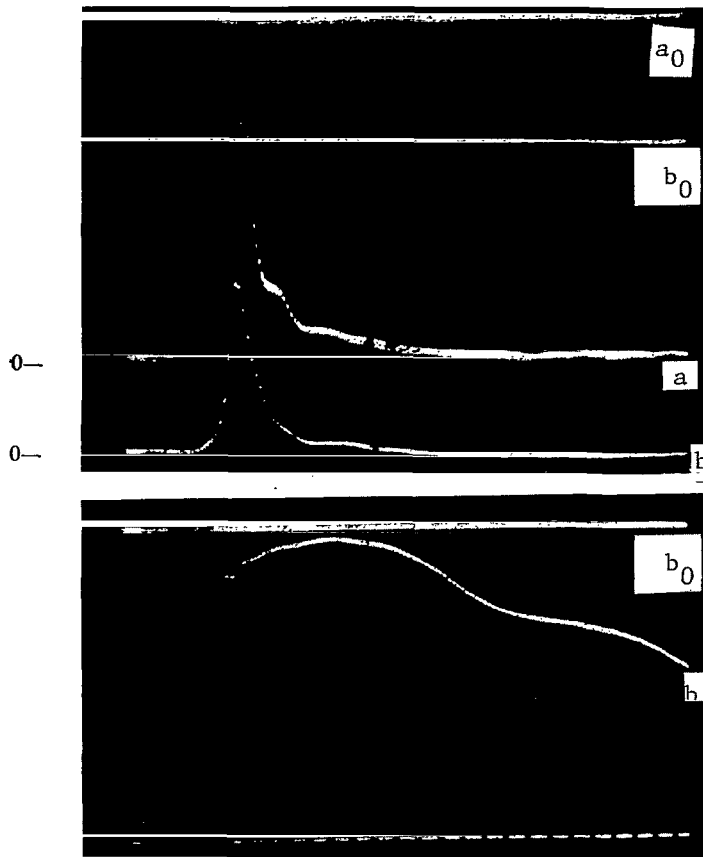


Figure 2. Radio-Wave Absorption Oscillograms in Air Behind Reflected Shock Waves at a Frequency of 18,750 MHz (a) and 37,500 MHz (b). Top: $p_0 = 1$ mm Hg and $M_0 = 6.45$; Bottom: $p_0 = 10$ mm Hg and $M_0 = 6.45$; 0 = complete absorption lines. 100- μ sec markers are given at the top.

Nitrogen

The form of the absorption oscillograms in nitrogen is similar to the absorption curves in air. The times of achievement of equilibrium ionization and the duration of existence of the equilibrium state also are close to the times in air. However, as can be seen from Figure 6, the values of the electron con-

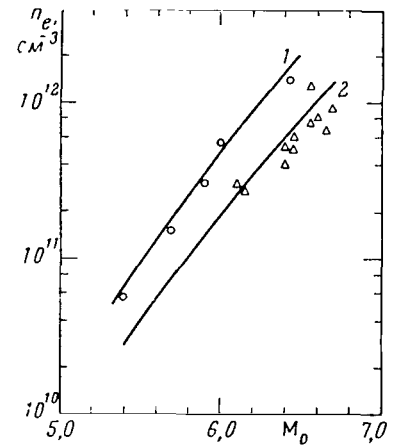


Figure 3. n_e Behind a Reflected Shock Wave in Air as a Function of M_0 . Curves 1 and 2: equilibrium calculation for $p_0 = 10$ and 5 mm Hg, respectively. Points: experiment for same pressures.

The values of v_{eff} which correspond to equilibrium ionization behind a reflected shock wave were converted into the values of effective cross sections (Figure 5). Curve 1 was calculated for $p_0 = 2$ mm Hg, while curve 2 was calculated for $p_0 = 10$ mm Hg with the aid of the data on cross sections [2] and composition [8]. The data on temperature and pressure were taken from [9].

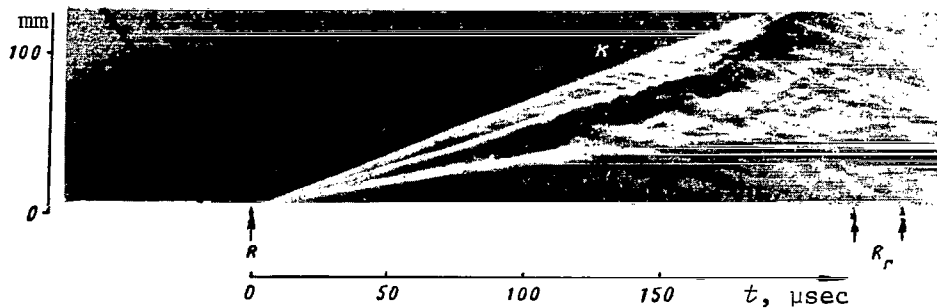


Figure 4. Töpler Scanning of the Reflection of a Shock Wave in Air at an Initial Pressure of 10 mm Hg and $M_0 = 6.6$.

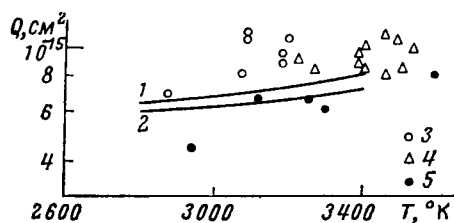


Figure 5. Q in Air as a Function of T_2 . (3) $p_0 = 2$ mm Hg; (4) 5; (5) 10.

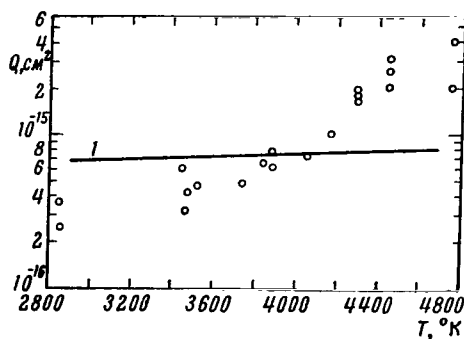


Figure 7. Q in Nitrogen as a Function of T_2 . (1) according to [2].

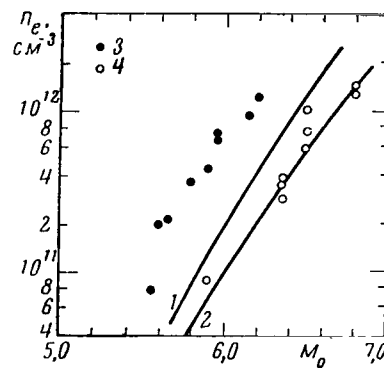


Figure 6. n_e Behind a Reflected Shock Wave in Nitrogen as a Function of M_0 . (1) equilibrium calculation for $p_0 = 10$ mm Hg; (2) 2. Points: experiment; (3) $p_0 = 10$ mm Hg; (4) 2.

centrations lie somewhat higher than the equilibrium values. Calculated data on equilibrium values of n_e , T_2 and p_2 behind a reflected shock wave were taken from [10].

The effective collision cross sections calculated on the basis of experimental effective collision frequencies are given in Figure 7. The same figure illustrates the effective cross sections obtained by Townsend's method [2]. The air impurity did not exceed 1% in the experiments.

Oxygen

Experiments were conducted in oxygen at three initial pressures: 5, 10 and 20 mm Hg and M_0 numbers from 5.6 to 7.5. The form of the absorption oscillograms is analogous to the oscillograms in air and nitrogen with the only difference being that approximately 1 millisecond from the beginning of scanning the absorption of radio waves does not decrease, but reaches a high value due to heating of the propelling gas (hydrogen) in the oxygen (Figure 8).

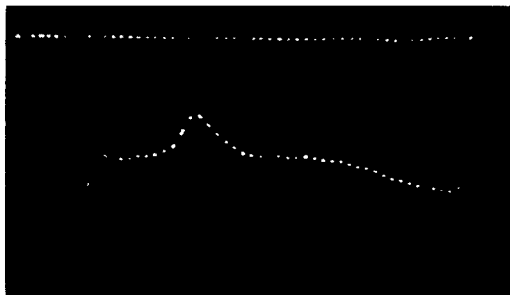


Figure 8. Radio-Wave Absorption Oscillogram in Oxygen Behind a Reflected Shock Wave at a Frequency of 18,750 MHz, $p_0 = 20$ mm Hg and $M_0 = 5.8$

As the reflected shock wave passes the antennas, absorption of the radio waves increases rapidly, reaching a horizontal section, *i.e.*, a "plateau".

The absorption growth time, which amounted to 60 μ sec in our experiments at an M_0 number of the incident shock wave 6.0, temperature 3,180°K and pressure 1.8 atm behind the reflected shock wave ($p_0 = 5$ mm Hg), exceeds the time of

arrival at equilibrium dissociation, which amounts to, according to Logan [11], 12 μ sec under these conditions. It is obvious that this long growth time in the experiments was caused by the resolution time of the equipment. The time of arrival to equilibrium will be even shorter at higher gas parameters behind shock waves.

Thus, it is quite natural to use the equilibrium values of the temperatures and pressures upon transition from effective collision frequencies to effective cross sections. The total values of effective cross sections Q_c were obtained in the course of the calculations, and they can be expressed by the cross section of molecular and atomic oxygen, Q_{O_2} and Q_O , and by their relative concentrations, x_{O_2} and x_O , in the following manner:

$$Q_c = x_{O_2} Q_{O_2} + x_O Q_O. \quad (11)$$

Knowing the composition and Q_c for one temperature, but for two different pressures, two equations (11) can be used to determine Q_{O_2} and Q_O independently.

This calculation was performed for two temperatures, 3,600 and 3,200°K, and for initial pressures of 5, 10 and 20 mm Hg. The third point -- approximately 2,600°K -- is the asymptote, to which the cross sections tend for these pressures, since here $x_O \rightarrow 0$, while $Q_c \rightarrow Q_{O_2}$ (Figure 9). The upper curve in this

figure corresponds to cross sections with atomic oxygen, while the lower curve corresponds to cross sections with molecular oxygen obtained in this work;

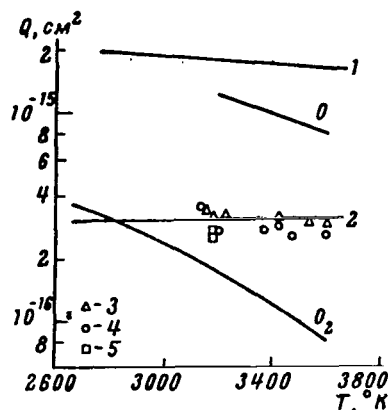


Figure 9. Q in Oxygen as a Function of T_2 . Q_c at Initial Temperatures Plotted by Points. (1) and (2): according to [10]. (3) $p_0 = 5$ mm Hg; (4) 10; (5) 20.

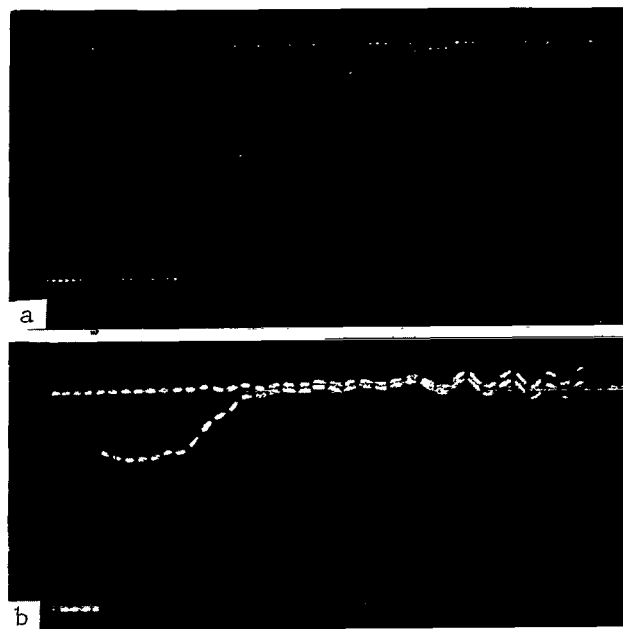


Figure 10. Oscillograms of Radio-Wave Absorption in CO Behind Reflected Shock Waves at a Frequency of 18,750 MHz. (a) $p_0 = 5$ mm Hg, $M_0 = 5.9$, 20- μ sec markers; (b) $p_0 = 10$ mm Hg, $M_0 = 5.3$, 100- μ sec markers.

curves 1 and 2 correspond to cross sections with atomic and molecular oxygen taken for the Chinitz comparison [12].

A comparison of the results obtained for cross sections in this work and in the Chinitz work indicates that the values of Q_0 are extremely close, whereas the values of Q_{O_2} have a sharply distinct temperature behavior.

Carbon Monoxide

Experiments were conducted in carbon monoxide at initial pressures of 5, 10 and 20 mm Hg and M_0 numbers from 4.8 to 6.4.

A very long (with respect to time) horizontal section (Figure 10) is characteristic for the oscillograms of radio-wave absorption in CO. Thus, when $M_0 = 5.3$ and the initial pressure is 10 mm Hg, the extent of the "plateau" amounts to 700 μ sec. The presence of this plateau makes it possible to use the equilibrium values for temperature and pressure. CO dissociation could have been neglected in the utilized temperature (2,380–4,330°K) and pressure (1.3–6.0 atm) ranges. It can be considered that the effective collision frequencies converted to the cross sections refer to pure CO. It is interesting to note the very good agreement between our data and the cross-sectional data of Chinitz [12] (Figure 11).

Carbon Dioxide

/128

Experiments were conducted in CO_2 at an initial pressure of 10 mm Hg and M_0 numbers of the incident shock wave from 6.3 to 7.4. A typical absorption oscillogram at a frequency of 37,500 MHz is shown in Figure 12. The

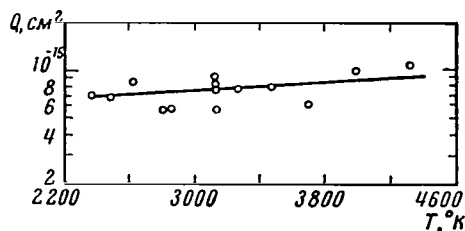


Figure 11. Q in CO as a Function of T_2 . Curve according to [12].

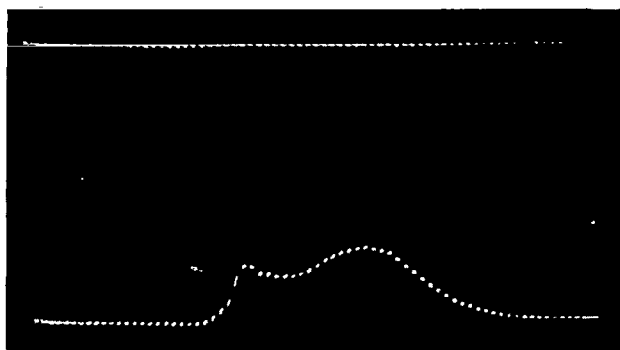


Figure 12. Oscillogram of Radio-Wave Absorption in CO_2 Behind a Reflected Shock Wave at a Frequency of 37,500 MHz. $p_0 = 10$ mm Hg and $M_0 = 7.4$.

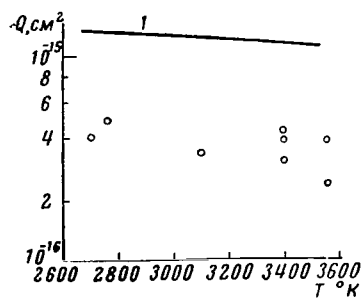


Figure 13. Q in CO_2 as a Function of T_2 . (1) according to [10].

absorption, as this curve indicates, having reached a certain maximum level in time τ_1 , does not remain on it during any notable period of time, but immediately begins to decrease, while the super-reflected wave that has departed does not increase the gas temperature and pressure. The absence of a horizontal section after achieving the maximum and the rather steep drop in the absorption curve evidently indicate that equilibrium is not achieved in the time τ_2 up to encounter

with the super-reflected wave in CO_2 . On the basis of data concerning the temperatures and pressures behind a reflected shock wave, under the assumption of equilibrium dissociation, taken from [13], and with the aid of data on the molecular percentages of electrons at these temperatures and pressures from [14], the equilibrium electron concentrations were calculated. It turned out that the experimental points lie significantly below the equilibrium concentrations. Evidently, such high experimental values of electron concentrations are caused by impurity ionization [15]. The time of achievement of the maximum in absorption coincides well with the time of passage of the

front of the reflected shock wave by the sounding beams. This points to the fact that conductivity reaches a maximum value almost immediately behind the shock front. According to the data in [11], the times of achievement of equilibrium dissociation of CO_2 at temperatures of 2,000–4,000°K amount to $1\text{--}3 \cdot 10^{-4}$ sec. Therefore, the effective frequencies can be converted into effective cross sections, based on the nonequilibrium values of the temperatures. Pressure depends practically very little on dissociation (Figure 13). These cross sections, consequently, may refer to pure CO_2 . The presence of dissociation ^{/129} could have led only to a decrease in the cross sections for CO_2 since the cross section in CO amounts to approximately 10^{-15} cm^2 .

The radio-wave reflection coefficient in air and argon was subjected to an experimental check in this work. The measurements were conducted at a frequency of 18,750 MHz, whereby the reflection coefficient as well as the absorption coefficient were measured simultaneously.

The reflection coefficient reached a measurable value ($|R|^2 = 0.02$) in air only when $M_0 = 7.9$ at an initial pressure of 2 mm Hg, while the transmission power was absorbed on the whole. The absorption coefficient in argon, however, was extremely large even with incomplete attenuation of the transmitted signal. Simultaneous measurement of both coefficients in argon made it possible to determine the effective frequency and cross section of the collisions (see below).

M	$T, ^\circ K$	p, atm	$\alpha, \delta\delta/\text{cm}$	R^2	$n_e \cdot 10^{-12}, \text{cm}^{-3}$	$\nu_{\text{eff}} \cdot 10^{-9}, \text{sec}^{-1}$	$Q \cdot 10^{-17}, \text{cm}$
4.4	4,400	0.79	0.25	0.025	2.0	2.7	5.0
4.9	5,900	2.05	0.66	0.084	3.0	3.6	3.0

These values are quite similar to the data in the Phelps discharge [7].

Conclusions

Measurement of radio-wave absorption simultaneously at two frequencies of 37,500 MHz and 18,750 MHz behind a reflected shock wave in a shock tube indicated that equilibrium ionization is achieved in air and nitrogen in 70-170 μsec at 2,800-4,800°K and pressures of 0.3-6.20 atm.

Comparison of the absorption curves with Töpler scanings of the process of reflection of a shock wave from the end of the tube made it possible to explain the significant increase in conductivity after its achievement of the equilibrium value as a result of additional heating of the gas of a shock wave that had been reflected from a contact surface.

The measured values of effective cross sections of electron collisions with neutral particles in air, nitrogen and CO are quite similar to those given in [1, 2]. However, the cross section in nitrogen at temperatures above 4,000°K has a tendency towards a steeper growth. The cross sections were significantly smaller in molecular oxygen and in CO_2 in our experiments than in those conducted in [12].

REFERENCES

1. Massey, G. and E. Barhop: *Elektronnyye i ionnyye soudareniya. (Electronic and Ionic Impacts.)* Moscow, IL, 1958.
2. Lamb, L. and S. Lin: Electrical conductivity of thermally ionized air in a shock tube. In: *Udarnyye trubyy. (Shock Tubes.)* Moscow, IL, 1962.
3. Ginzburg, V. L.: *Rasprostraneniye elektromagnitnykh voln v plazme. (Propagation of Electromagnetic Waves in a Plasma.)* Moscow, Gosizdat, 1960.
4. Zimin, E. P. and V. A. Popov: Determination of the mean cross section of electron collisions with neutral atoms of a weakly ionized gas mixture.

PMTF, No. 5, 1963.

5. Bazhenova, T. V. and Yu. S. Lobastov: Electron concentration and number of electron impacts with air molecules behind a shock wave. In: *Fizicheskaya gazodinamika i svoystva gazov pri vysokikh temperaturakh.* (Physical Gas Dynamics and Properties of Gases at High Temperatures.) Moscow, Izd-vo "Nauka", 1964.
6. Lobastov, Yu. S.: Improvement of the method of radio-wave sounding of a gas heated by a shock wave. In: *Fizicheskaya gazodinamika i svoystva gazov pri vysokikh temperaturakh.* (Physical Gas Dynamics and Properties of Gases at High Temperatures.) Moscow, Izd-vo "Nauka", 1964.
7. O'Malley, T.: Extrapolation of electron-rare gas atom cross sections to zero energy. *Phys. Rev.*, Vol. 130, 1963. /130
8. Predvoditelev, A. S., Ye. V. Stupochenko, A. S. Pleshanov, Ye. V. Samuylov and I. B. Rozhdestvenskiy: *Tablitsy termodinamicheskikh funktsiy vozdukha.* (Tables of Thermodynamic Functions of Air.) Izd-vo AN SSSR, 1962.
9. Bazhenova, T. V. and O. A. Predvoditeleva: Values of air parameters behind a normal shock wave and behind a reflected shock wave during equilibrium and frozen dissociation. In: *Fizicheskaya gazodinamika i teploobmen.* (Physical Gas Dynamics and Heat Exchange.) Izd-vo AN SSSR, 1961.
10. Lazarev, P. P.: *Trudy Fizicheskogo Instituta AN SSSR,* (Proceedings of the Physics Institute of the Soviet Academy of Sciences,) Vol. 30, 1964.
11. Logan, J.: Relaxation phenomena in hypersonic aerodynamics. *Mekhanika*, No. 1, 1959.
12. Chinitz, V., K. Eisen and R. Gross: Aerodynamic and electrical properties of some gaseous mixtures up to $M = 20$. *Voprosy Raketnoy Tekhniki*, No. 2, 1960.
13. Bazhenova, T. V. and S. G. Zaytsev: Parameters of carbon dioxide behind a reflected shock wave and a time estimate of the establishment of equilibrium dissociation at temperatures of 4,000–5,000°K. In: *Fizicheskaya gazodinamika.* (Physical Gas Dynamics.) Izd-vo AN SSSR, 1961.
14. Pleshanov, A. S. and S. G. Zaytsev: Composition, thermodynamic and gas-dynamic properties of carbon dioxide for temperatures from 1,000 to 12,000 °K and pressures from 10^{-2} to 10^3 atm. In: *Fizicheskaya gazodinamika.* (Physical Gas Dynamics.) Izd-vo AN SSSR, 1961.
15. Bazhenova, T. V. and Yu. S. Lobastov: The effect of impurity ionization on radio-wave absorption by a gas behind a shock in a shock tube. In: *Fizicheskaya gazodinamika.* (Physical Gas Dynamics.) Izd-vo AN SSSR, 1961.

SECONDARY PHENOMENA DURING THE REFLECTION OF SHOCK WAVES IN ARGON

T. V. Bazhenova and Yu. S. Lobastov

Some Results of an Experimental Investigation of the Reflection of Shock Waves in Argon in a Shock Tube

/131

The process of argon ionization behind shock waves is examined in [1, 2]. The argon ionization times are obtained by optical and probe methods, and it is noted that the ionization rate essentially depends on the initial state of argon and in particular, on the impurity concentration and the concentration of free electrons in front of the shock wave front as a consequence of photoionization.

In this study, we present some of the results of an investigation of ionization processes in argon behind a reflected shock wave, and we describe secondary effects; namely, nonstationary propagation of the reflected shock wave, and phenomena occurring during the interaction of the reflected shock wave in argon and the contact surface in the shock tube.

Experiments were carried out in a shock tube having a cross section of 72×72 mm at a distance of 4.7 and 6 m from the diaphragm. Töpler scannings of the reflection process were obtained and the absorption coefficients of radio waves with lengths of 1.6 and 0.8 cm behind the incident and reflected waves were measured [3, 4].

Figures 1 and 2 illustrate characteristic oscillograms of the absorption of radio waves with lengths of $\lambda = 1.6$ cm (a) and 0.8 cm (b) behind the incident shock wave at a distance of 36 cm from the end.

The first region of radio wave absorption is 450 μsec when $M_0 = 6.6$ and $p_0 = 15$ mm Hg; this corresponds to a distance of 90 cm from the shock wave front. The gas then remains radiotransparent for 40-50 μsec (9-10 cm). Further, at a distance of 20 cm, we observe a region of secondary radio wave absorption. Radio wave absorption in regions I and II occurs with a pressure decrease (see Figure 1). In the first region, the absorption amplitude increases as the shock wave M_0 number increases. In the second region, the radio wave absorption amplitude increases as the shock wave M_0 number decreases (see Figure 2). Figure 3 illustrates the dependence of free electron n_e concentration in the second region on the M_0 number calculated with respect to radio wave absorption on two wavelengths.

The absorption time in the first region corresponds to the absorption time of radio waves by hot argon behind the incident wave. A constant absorption coefficient value is not achieved within the gauge limits. A determination of the concentration of free electrons n_e behind the incident wave under the considered conditions was difficult since the signal with the 1.6 cm wavelength undergoes

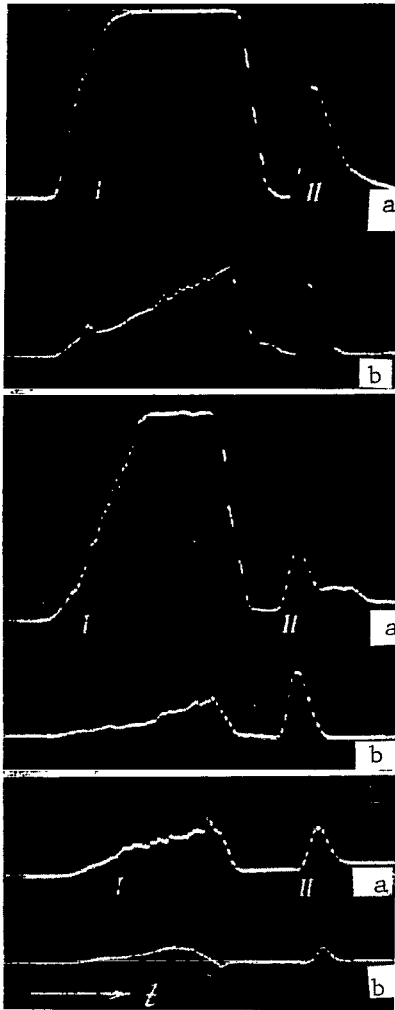


Figure 1. Absorption of Radio Waves of Two Frequencies Behind an Incident Shock Wave in Argon. $M_0 = 6.6$; $p_0 = 15$ (upper), 10 and 5 mm Hg; (1) 10 μ sec marker.



Figure 2. Absorption of Radio Waves of Two Frequencies Behind an Incident Shock Wave in Argon. $M_0 = 5.8$; at $p_0 = 10$ mm Hg; (1) 10 μ sec marker.

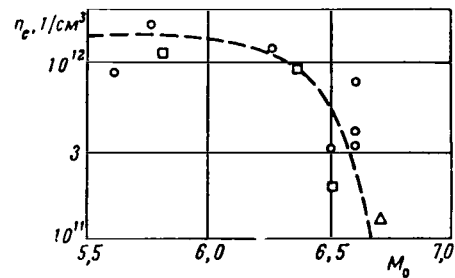


Figure 3. Dependence of n_e in the Second Region on the Shock Wave M_0 Number.

complete absorption, and it is not possible to independently determine n_e and the effective number of collisions.

Figure 4 illustrates an oscillogram of radio wave absorption by argon behind a reflected shock wave at the lowest M_0 numbers ($M_0 = 4.65$, $T_2 = 4,900^\circ\text{K}$, 132 $p_2 = 1.9$ atm). At 500-700 μ sec after shock wave reflection, a small concentration of free electrons ($n_e = 5.8 \cdot 10^{10}$ $1/\text{cm}^3$) arises and remains constant to 700 μ sec. An increase in conductivity then appears, which reaches $4 \cdot 10^8$ sec^{-1} ($n_e =$

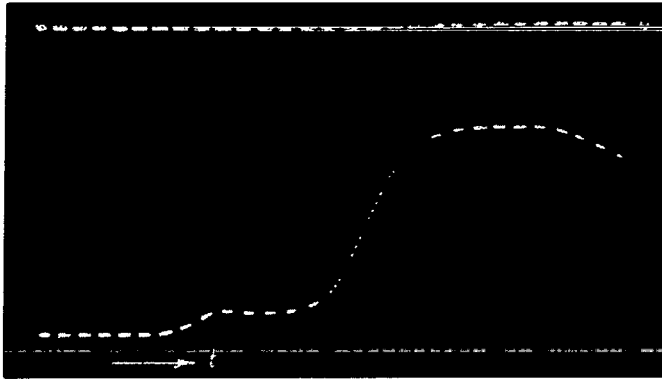


Figure 4. Radio Wave Absorption by Argon Behind a Reflected Shock Wave. $M_0 = 4.65$; $p_0 = 10$ mm Hg.

$0.9 \cdot 10^{12}$ $1/\text{cm}^3$) 1,000 μsec after shock wave reflection. The level of total absorption (0) is also noted on the oscillogram.

For an interpretation of the processes accompanying shock wave reflection, we took time photographs of the Töpler pattern of the reflection. Figure 5 illustrates a Töpler photograph of shock wave reflection in argon. Upon encountering the contact surface at point K , the reflected shock wave R is partially refracted and enters the cold propelling gas (hydrogen), and is partially reflected from the contact

region. This is accompanied by an increase in gas luminescence. The propagation of secondary reflected waves is observed especially well in photographs of reflection in air, where the flow structure is more clearly visible since strong emission is not present. (A detailed Töpler photograph is illustrated in Yu. S. Lobastov's article in this collection.)

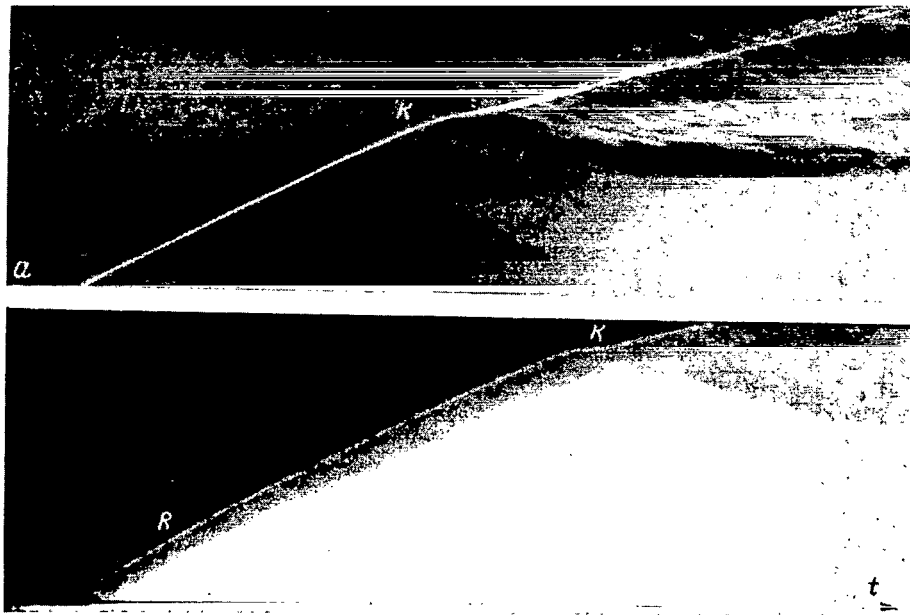


Figure 5. Töpler Scanning of Shock Wave Reflection in Argon. (a) $M_0 = 6.8$; $p_0 = 1$ mm Hg; (b) $M_0 = 7.4$; $p_0 = 5$ mm Hg.

The Effect of Nonequilibrium Ionization on the Propagation of a Reflected Shock Wave in Argon

As noted in earlier works [5], the observed velocity of a reflected shock wave in argon is less than the equilibrium values calculated. This is explained by energy losses during shock wave reflection from the tube end. During an examination of scannings of a Töpler reflection pattern in argon, it was found that the velocity of the reflected shock wave was not constant at certain M_0 and p_0 values (see Figure 5b). The shock wave decelerates from its velocity at the end, which exceeds equilibrium values, to lower velocities at the contact surface. Apparently, deceleration of the reflected wave is caused by a change of the boundary conditions at the end of the tube, where the gas state changes as equilibrium ionization is established. The state of the gas can change partially also as a result of losses.

To analyze the effect of nonequilibrium of the ionization process on the reflected wave velocity, we shall compare the observed change of the reflected wave velocity (Δu_R)_{exp} with the calculated change upon transition from a state with frozen ionization to an equilibrium state of argon behind the reflected wave. Calculation data for an initial pressure of 10 mm Hg are taken from [6], and data for initial pressures $p_0 = 5$ and $p_0 = 1$ mm Hg were integrated with data for $p_0 = 10$ and $p_0 = 0.8$ mm Hg. Tables 1 and 2 illustrate the results of calculating the parameters of argon behind incident and reflected shock waves at $p_0 = 0.8$ mm Hg.

TABLE 1. EQUILIBRIUM PARAMETERS OF ARGON BEHIND INCIDENT SHOCK WAVE AT $p_0 = 0.8$ mm Hg. $T_0 = 293^\circ\text{K}$.

M_0	7	8	8.5	9	9.5	18
u_0	2240	2540	2710	2840	3000	5720
$T_1, ^\circ\text{K}$	4800	6000	6700	7200	7900	12000
p_1, atm	0.065	0.085	0.095	0.108	0.12	0.50
$\rho_1, \text{g/cm}^3$	$6.5 \cdot 10^{-6}$	$6.8 \cdot 10^{-6}$	$6.8 \cdot 10^{-6}$	$7.2 \cdot 10^{-6}$	$7.3 \cdot 10^{-6}$	$17.4 \cdot 10^{-6}$
x_e	$0.16 \cdot 10^{-5}$	$0.76 \cdot 10^{-4}$	$0.55 \cdot 10^{-3}$	$0.4 \cdot 10^{-3}$	$0.35 \cdot 10^{-2}$	0.14
$n_e, 1/\text{cm}^3$	$1.6 \cdot 10^{10}$	$7.8 \cdot 10^{12}$	—	$1.5 \cdot 10^{14}$	$3.85 \cdot 10^{14}$	$4.3 \cdot 10^{16}$

TABLE 2. EQUILIBRIUM PARAMETERS OF ARGON BEHIND REFLECTED SHOCK WAVE AT $p_0 = 0.8$ mm Hg.

M_0	7	8	8.5	9	9.5	18
$T_2, ^\circ\text{K}$	9000	10 000	10 000	10 500	11 000	14 000
p_2, atm	0.32	0.47	0.53	0.61	0.75	5.0
$\rho_2, \text{g/cm}^3$	$17 \cdot 10^{-6}$	$22 \cdot 10^{-6}$	$24.8 \cdot 10^{-6}$	$27 \cdot 10^{-6}$	$31.0 \cdot 10^{-6}$	$146 \cdot 10^{-6}$
x_e	0.025	0.028	0.0282	0.046	0.065	0.158
$n_e, 1/\text{cm}^3$	$6.45 \cdot 10^{15}$	$0.91 \cdot 10^{16}$	—	$1.93 \cdot 10^{16}$	$3.2 \cdot 10^{16}$	$4.1 \cdot 10^{17}$
u_R/u_0	0.45	0.33	—	0.27	—	—

Table 3 illustrates the results of a comparison of the deceleration of the reflected wave observed in the experiments with the calculated values of deceleration from the frozen to the equilibrium value. The table also indicates deceleration time of the reflected wave from the values at the end to the values at the contact surface. It should be noted that the final values of the shock wave velocity were somewhat lower than the calculated equilibrium values.

TABLE 3. DECELERATION OF REFLECTED SHOCK WAVE IN ARGON

M_0	7,64	7,1	6,8
p_0 , mm Hg	5	10	1
u_{R0} , m/sec	1065	1065	875
$u_{R\infty}$, m/sec	880	985	740
Δu_R exp m/sec	185	80	135
Δu_R calc m/sec	220	160	120

The relationship between time of change of the reflected wave velocity and time of change of the boundary condition at the end of the shock tube is determined from an examination of the problem of gas flow between a piston and shock wave in a relaxing gas [7, 8].

Let us apply the relation obtained in [7] to determine the relationship between the relaxation time τ_0 and the onset time of the equilibrium velocity of the reflected shock wave τ_s . Table 4 illustrates the results of calculating the onset time of the equilibrium degree of ionization.

TABLE 4. RELATIONSHIP BETWEEN TIME OF CHANGE OF SHOCK WAVE VELOCITY τ_s AND IONIZATION TIME τ_0 BEHIND REFLECTED WAVE IN ARGON

M_0	7,4	7,1	6,8
T'_2 , °K	12 900	11 800	11 800
T_2 , °K	10 000	10 000	8800
p_2 , mm Hg	2000	3500	300
$M_s = uR/a_2$	0,60	0,59	0,50
τ_s/τ_0	1,9	1,6	1,8

From the data presented in Table 4, it follows that the change of the reflected shock wave velocity occurs in a time which is almost twice as long as the time of change of the degree of ionization. Nonstationary propagation of the reflected shock wave was observed under the conditions indicated along its

entire path, right up to the interaction with the contact surface, *i.e.*, for approximately 100–200 μsec . Therefore, it is possible to conclude that nonequilibrium ionization under these conditions exists for more than 50–100 μsec .

Measurements of the ionization rate behind an incident shock wave [1] established that the ionization time of argon at a temperature of 10^4K is 25 μsec in a laboratory coordinate system, when the pressure behind the shock wave is 7 atm. /136 The time, referred to 4.5 atm pressure and to a coordinate system connected to the gas, is 400 μsec . Thus, extrapolation of the data in [1] to the conditions behind the reflected shock wave indicates that for the time of observation of the reflection process until the reflected shock wave encounters the contact surface, the ionization of argon does not achieve equilibrium, and the reflected wave propagates with continuously changing boundary conditions at the end, which affects the change of the reflected shock wave velocity.

Interaction of Reflected Shock Wave and Contact Surface in Argon

Measurement of radio wave absorption behind the incident shock wave under certain conditions in argon at a distance of 36 cm from the end of the shock tube indicated that in the cold propelling gas (hydrogen and helium) noticeable ionization ($n_e \sim 10^{11}\text{--}10^{12}$) occurs after the contact surface passed by the microwave antennas. This phenomenon is not related to the presence of a layer of hot gas on the walls of the tube behind the contact surface, which was noted in the measurement of the heat flow to the wall with heat transducers, since it occurs after the gas has become radiotransparent over a period of 50–100 μsec (see Figure 1 and 2).

The appearance of radio wave absorption in hydrogen behind the contact surface was observed only during a study of shock waves in argon at comparatively high initial pressures ($p_0 = 5$ mm Hg and higher; $T = 11,000\text{K}$). If air, carbon dioxide, or nitrogen ($T_2 < 7,000\text{K}$) was in the expansion chamber, a similar phenomenon was not observed at the same flow velocities. Therefore, the detected radio wave absorption cannot be related to diffusion or absorption by molecular hydrogen or the metallic particles which form when the diaphragm is shattered. In addition, diffusion or absorption of microwaves by particles a fraction of a millimeter in size is not very probable.

Radio wave absorption by a gas behind the contact surface decreases with an increase of the Mach number of the shock wave (see Figure 3). Apparently, this is related to the fact that the contact surface at the lower M numbers of the shock wave is further from the shock wave front and is located closer to the measurement point of radio wave absorption after the shock wave is reflected from the end of the tube than at high M numbers.

A comparison of radio wave absorption oscillograms with a Töpler pattern of the reflection process indicates that the moment of appearance of free electrons in the cold hydrogen coincides with the moment of secondary reflection of the

shock wave from the contact surface (see Figure 5).

The appearance of a second reflected wave is also recorded during measurement of radio wave absorption at the end of the shock tube (see Figure 3) when a sharp increase of ionization is observed which coincides in time with the arrival of the second reflected wave.

Let us examine two possible causes of hydrogen ionization during the interaction of the reflected shock wave and the contact surface: propagation of the reflected wave in hydrogen and photoionization from argon emission.

After interaction of the reflected shock wave and the contact surface, a series of disturbances having a comparatively low velocity (~ 0.5 km/sec) is propagated upstream through the cold propelling gas. The velocity of these disturbances with respect to the stationary gas is 2.5–3 km/sec. The hydrogen behind the contact surface has a low temperature. If we consider that the process of expansion of the propelling gas is isentropic, the temperature drops 2.5 times in the expansion wave. The velocity of sound in hydrogen under these conditions is 865 m/sec. The Mach number of the refracted wave in hydrogen is 3–3.5 and the temperature behind the shock wave increases 3 to 3.5 times, *i.e.*, the temperature behind the refracted shock wave in hydrogen is not more than 400°K. /137

Thus, the heating of hydrogen and the impurities in it by the refracted shock wave cannot create a noticeable concentration of free electrons.

The existence of radiation with a wavelength of less than 800 \AA is necessary for photoionization of hydrogen at the contact surface at the moment of secondary reflection of the reflected shock wave from it, since the ionization potential of hydrogen is 12.4 eV [9]. If argon behind the reflected shock wave at $M_0 = 6.7$ has a temperature of up to 10,000°K (see Table 3), this temperature can increase 1.5 to 2 times during secondary reflection. To calculate the maximum possible radiation density, let us assume that argon radiates as an ideal black body with a temperature of 20,000°K. The number of photons having a frequency greater than $3 \cdot 10^{15}$ ($h\nu > 12.4$ eV) can be determined by Planck's equation. This number is equal to 10^{12} photons/cm²·sec. For 10^{-4} sec, during which an increase of electron concentration occurs in hydrogen, the argon behind the reflected wave emits 10^8 photons/cm³. These photons are practically entirely absorbed by the hydrogen behind the contact region since the hydrogen absorption coefficient of the vacuum ultraviolet is 10^2 cm^{-1} [9]. Near the contact surface, the concentration of free electrons in hydrogen appearing as a result of photoionization by emission during shock wave reflection in argon is 10^8 electrons/cm³. Electron density drops in proportion to the distance from the contact surface.

The electron density observed in the experiments in hydrogen behind the contact surface is 2 to 3 orders higher than the number of primary electrons which can arise as a result of photoionization by argon emission. Apparently, secondary ionization occurs in the gas by fast electrons which arise during photoionization by hard photons whose energy significantly increases the ionization potential of hydrogen. In addition, free electrons can penetrate hydrogen by

way of diffusion from argon behind the secondarily reflected shock wave, where electron concentration reaches 10^{18} - 10^{19} . The photoionization of alkali metal impurities having a low ionization potential in hydrogen can also lead to additional formation of free electrons.

Conclusions

1. Nonstationary propagation of a reflected shock wave in argon is observed under conditions wherein the degree of argon ionization behind the reflected shock wave is variable.

2. Secondary effects were found which accompanied the interaction of the reflected shock wave in argon and the contact surface: ionization in cold hydrogen and helium near the point of shock wave reflection from the contact region, and an increase of the degree of ionization at the shock tube end, which is related to the arrival of a second reflected wave.

REFERENCES

/138

1. Petschek, H. E. and S. Byron: An approach to equilibrium ionization behind a shock wave in argon. In: *Udarnyye truby. (Shock Tubes.)* Moscow, IL, 1962.
2. Biberman, L. I. and I. T. Yakubov: Establishing ionization equilibrium behind a shock wave front in an atomic gas. *Zhurnal Tekhnicheskoy Fiziki*, Vol. 33, No. 11, 1963.
3. Lobastov, Yu. S.: Improvement of the radio-wave method of sounding a gas heated by a shock wave. In: *Fizicheskaya gazodinamika i svoystva gazov pri vysokikh temperaturakh. (Physical Gas Dynamics and Properties of Gases at High Temperatures.)* Moscow, Izd-vo "Nauka", 1964.
4. Bazhenova, T. V. and Yu. S. Lobastov: Electron concentration and number of electron collisions with air molecules behind a shock wave. In: *Fizicheskaya gazodinamika i teploobmen. (Physical Gas Dynamics and Heat Exchange.)* Izd-vo AN SSSR, 1961.
5. Strelow, R. and A. Cohen: Limitations of the reflected shock wave technique in the study of rapid chemical reactions and its application for observing relaxation in nitrogen and oxygen. In: *Udarnyye Truby. (Shock Tubes.)* Moscow, IL, 1962.
6. Resler, E. L., S. C. Lin and A. Kantrowitz: The production of high-temperature gases in shock tubes. *J. Appl. Phys.*, Vol. 23, No. 12, p. 1,390, 1952.
7. Spence, D.: Nonstationary propagation of a shock wave in a relaxing gas. *Mekhanika*, No. 2, 1962.
8. Bazhenova, T. V.: An estimation of the relaxation time of carbon dioxide dissociation according to experiments in a shock tube. *Doklady AN SSSR*, Vol. 146, No. 3, 1962.
9. Wainan, N., W. Walker and G. Weissler: Photoionization efficiencies and cross sections in O_2 , N_2 , CO_2 , H_2O , H_2 and CH_4 . *Phys. Rev.*, Vol 99, 1955.

SOME GENERAL INEQUALITIES OF CHEMICAL THERMODYNAMICS FOR THE CASE OF PARTIAL EQUILIBRIUM

A. S. Pleshanov

The following general inequalities of chemical thermodynamics were proven /139 in [1] and [2]:

$$\begin{aligned} c_{p_0} > c_{p_\infty}, \quad c_{v_0} > c_{v_\infty}; \\ \left(\frac{\partial \ln \mu}{\partial \ln p} \right)_{T_0} > \left(\frac{\partial \ln \mu}{\partial \ln p} \right)_{T_\infty} = 0, \quad \left(\frac{\partial \ln \mu}{\partial \ln \rho} \right)_{T_0} > \left(\frac{\partial \ln \mu}{\partial \ln \rho} \right)_{T_\infty} = 0; \\ a_{T_0} < a_{T_\infty}, \quad a_{s_0} < a_{s_\infty}, \end{aligned} \quad (1)$$

where c_p and c_v are the molar heat capacities at constant pressure p or volume v ; T is the temperature; ρ is the density; μ is the molecular weight; and a_T and a_s are the isothermal and adiabatic velocities of sound, respectively. The subscripts 0 and ∞ refer to complete equilibrium and the complete absence of equilibrium of an arbitrary reacting gas system which is governed by the Clapeyron equation with respect to small disturbances.

The character of the change in the quantities from (1) as the reacting system "unfreezes", *i.e.*, upon transition from the complete absence of equilibrium through a state of partial equilibrium to complete equilibrium, is of interest. If r independent reactions transfer to a state of complete equilibrium in the reacting system, 2^r states of partial equilibrium are possible with respect to small disturbances; one of these states is completely nonequilibrium; $r - 1$ reactions in r states are completely nonequilibrium and one arbitrary reaction is completely equilibrium. $r - 2$ reactions in $r(r - 1)/2$ states are completely nonequilibrium and 2 arbitrary reactions are completely equilibrium, etc. We shall prove that the quantities from (1) vary monotonically in proportion to the monotonic "unfreezing" of the system. More precisely, we shall prove that

$$\begin{aligned} c_{p_{n+1}} > c_{p_n}, \quad c_{v_{n+1}} > c_{v_n}; \\ \left(\frac{\partial \ln \mu}{\partial \ln p} \right)_{T_{n+1}} > \left(\frac{\partial \ln \mu}{\partial \ln p} \right)_{T_n}, \quad \left(\frac{\partial \ln \mu}{\partial \ln \rho} \right)_{T_{n+1}} > \left(\frac{\partial \ln \mu}{\partial \ln \rho} \right)_{T_n}; \\ a_{T_{n+1}} < a_{T_n}, \quad a_{s_{n+1}} < a_{s_n}, \end{aligned} \quad (2)$$

where the subscript n designates that n reactions in the system are equilibrium with respect to small disturbances, and the subscript $n + 1$ denotes that the n previous reactions have one more additional new reaction.

The proof is based on the following fact [3]. Let the positive definite /140 quadratic form be given:

$$K_n = \sum_{i,j=1}^n a_{ij} x_{in} x_{jn} > 0 \quad (a_{ij} = a_{ji}), \quad (3)$$

where x_{in} is determined from the equation

$$\sum_{j=1}^n a_{ij} x_{jn} = b_i. \quad (4)$$

Then

$$K_{n+1} - K_n = \frac{\Delta_{n+1}}{\Delta_n} x_{n+1, n+1}^2 > 0, \quad (5)$$

where $\Delta_n > 0$ [1] is the determinant of system (4).

It is not difficult to verify that for the characteristics of (1) there are representations of type (3) with variable, definite systems similar to (4) [1, 2]. Thus, inequalities (2) follow from inequality (5).

The monotonic increase in the quantity $(\partial \ln \mu / \partial \ln p)_T - (\partial \ln \mu / \partial \ln \rho)_T$ as the system "unfreezes" follows from inequalities (2), as is easily demonstrated. With regard to the differences between other paired quantities, generally speaking, they vary monotonically only when the number of particles is constant during each equilibrium reaction.

REFERENCES

1. Pleshanov, A. S.: Some inequalities of chemical thermodynamics. *Doklady AN SSSR*, Vol. 140, No. 6, 1961.
2. Pleshanov, A. S.: Some inequalities of chemical thermodynamics. In: *Fizicheskaya gazodinamika, teploobmen i termodinamika gasov vysokikh temperatur.* (Physical Gas Dynamics, Heat Exchange and Thermodynamics of High-Temperature Gases.) Izd-vo AN SSSR, 1962.
3. Bokher, M.: *Vvedeniye v vysshuyu algebru.* (Introduction to Higher Algebra.) Moscow and Leningrad, GTTI, 1933.

NONISENTROPIC NONEQUILIBRIUM FLOW OF A GAS THROUGH A NOZZLE
WITH FRICTION AND HEAT EXCHANGE TAKEN INTO ACCOUNT

A. S. Pleshanov and P. A. Kon'kov

§1. Equations of Chemical Hydrodynamics

In the presence of diffusion processes and chemical reactions to known hydrodynamic equations

$$\frac{\partial \rho}{\partial t} + \operatorname{div} \rho \mathbf{v} = 0, \quad (1.1)$$

$$\rho \frac{d\mathbf{v}}{dt} = -\nabla p + \frac{\partial \sigma_{ik}}{\partial x_k}, \quad (1.2)$$

$$\frac{\partial}{\partial t} \left(\rho \varepsilon + \frac{\rho v^2}{2} \right) = -\operatorname{div} \left[\rho \mathbf{v} \left(w + \frac{v^2}{2} \right) - (\sigma' \mathbf{v}) + \mathbf{q} \right] \quad (1.3)$$

(designations according to [1]) K continuity equations should be added for each chemical component K_i ($i = 1, \dots, K$) which takes part in R direct reactions

$R_{s \rightarrow}$ ($s \rightarrow = 1, \dots, R$) and R inverse reactions $R_{s \leftarrow}$ ($s \leftarrow = R + 1, \dots, 2R$). We shall use the following form of these equations ($s = 1, \dots, 2R$):

$$\rho \frac{dc_i}{dt} = -\operatorname{div} \mathbf{i}_i - \sum_s m_i \nu_{is} \theta_s, \quad (1.4)$$

where c_i is the relative mass concentration of K_i ; \mathbf{i}_i is the diffusion flow of K_i ; θ_s is the velocity of R_s [mole/cm³ sec]; ν_{is} is the stoichiometric coefficient of K_i in R_s ; and m_i is the molecular weight of K_i [g/mole].

Let us turn our attention to the fact that the expression employed in this paper for the rate of change of K_i , $\rho dc_i / m_i dt \equiv V^{-1} dN_i / dt$ (V is the total volume of the system and N_i is the total number of K_i particles in the system), does not coincide with the expression $dn_i / dt \equiv d(N_i / V) / dt$, which is commonly used in chemical kinetics. Our determination is more accurate for variable V .

Let us also note that the diffusion flows \mathbf{i} are not independent. If we multiply (1.4) by the number of type m atoms in K_i , n_{m_i} , and sum (1.4) with respect to i , then owing to the constancy of the numbers of any type atoms, in

the course of each reaction we will have the obvious relationships $\sum_i n_i \frac{N_i}{m_i} = \text{const}$ and $\sum_i n_i v_{is} = 0$, as a result of using which the term on the left and the second term on the right in (1.4) become equal to zero, and the diffusion flows are related by α relationships (α is the number of various types of atoms) of the following form:

$$\text{div} \sum_i \frac{n_i \mathbf{i}_i}{m_i} = 0. \quad (1.5)$$

Besides (1.5), there is another relationship, which is obtained by summing (1.4) with respect to i : /142

$$\text{div} \sum_i \mathbf{i}_i = 0,$$

it is trivial, however, inasmuch as we have $\sum_i \mathbf{i}_i = 0$ on the basis of determining the diffusion flows [3].

We shall now prove that the adopted form of particular continuity equations ensures the determinacy of the sign of $\theta_{s \rightarrow}$ (analogous to $\theta_{s \leftarrow}$).

Using the Gibbs equation,

$$d\varepsilon = T ds - p dV + \sum_i \mu_i dc_i$$

(μ_i is the chemical potential of K_i), equation (1.3) can be written in the form of

$$\rho T \frac{ds}{dt} = \sigma'_{ik} \frac{\partial v_i}{\partial x_k} - \text{div} \left(\mathbf{q} - \sum_i \mu_i \mathbf{i}_i \right) - \sum_i (\mathbf{i}_i, \nabla) \mu_i + \sum_i \left(\sum_j v_{ij} m_j \mu_j \right) \theta_i. \quad (1.6)$$

The last term of (1.6), in view of $v_{is \rightarrow} = -v_{is \leftarrow}$, may be presented in the form

$$\sum_{s \rightarrow} \theta_{s \rightarrow} \left(\sum_i v_{is \rightarrow} \tilde{\mu}_i \right) (1 - \theta_{s \leftarrow} / \theta_{s \rightarrow}) (\tilde{\mu}_i = m_i \mu_i).$$

The ratio of reaction rates $\theta_{s \leftarrow} / \theta_{s \rightarrow}$ is equal to $\exp [-\sum_i v_{is \rightarrow} \tilde{\mu}_i / RT]$ when nonequilibrium is not too strong [2] since we have the following for the integral rate of change of entropy due to chemical processes:

$$\frac{\partial}{\partial t} \int \rho s dV = \sum_{s \rightarrow} \int R \theta_{s \rightarrow} \frac{\sum_i v_{is \rightarrow} \tilde{\mu}_i}{RT} \left\{ 1 - \exp \left[-\frac{\sum_i v_{is \rightarrow} \tilde{\mu}_i}{RT} \right] \right\} dV. \quad (1.7)$$

The sought result of $\theta_{s \rightarrow} > 0$ is hence obtained on the basis of the entropy increment principle (the elementary inequality $x(1 - e^{-x}) > 0$ ($x > 0$) is used).

Let us note here that the following expression for the heat flux [1] is used in this article:

$$\mathbf{q} = -\kappa \nabla T + \sum_i w_i \mathbf{i}_i, \quad (1.8)$$

where w_i is the enthalpy of K_i .

In addition, disregarding barodiffusion, thermodiffusion, and the correlation of diffusion flows, as usual, we shall limit ourselves in the expressions for diffusion flows to the diagonal terms with respect to concentration gradients. Then

$$\mathbf{i}_i = \rho D_i \nabla c_i, \quad (1.9)$$

where D_i is the diffusion coefficient of K_i .

§2. Equations of Gas Flow Through a Nozzle and Boundary Conditions

/143

The general hydrodynamic equations (1.1), (1.2) and (1.3), and the particular continuity equations (1.4) will be written for a stationary gas flow through an axially symmetric cylindrical nozzle. The flow is two-dimensional, and is determined by the axial coordinate $0 \leq z \leq z_0$ and the radius $0 \leq r \leq r_0$, where z_0 and r_0 is the nozzle length and radius, respectively. Since the distance at which a Poiseuille velocity profile of the gas flow develops [1] is $L \sim r_0 Re = r_0^2 \nu / v \gg z_0$ (if, for example, $r_0 \sim 10$ cm, $v \sim 500$ m/sec, $\nu \sim 0.1$ cm²/sec, and $z_0 \sim 1$ m), the velocity profile is uniform to a high degree. This makes it possible to consider the flow as consisting of two regions: the basic region, *i.e.*, the nucleus, where all characteristics are constant, and a small region, *i.e.*, the boundary layer, where all characteristics change sharply from their values in the nucleus to the values on the nozzle wall. Allowance for the change of characteristics in the boundary layer during derivation of averaged equations of gas flow through a nozzle is equivalent to an effective decrease in the cross-sectional area of the nozzle by the quantity $\Delta S/S \sim -2\delta/r_0$, where δ is the thickness of the boundary layer [4]. Such an allowance was made, for example, in [5] and is unfounded in view of the smallness of $\delta/r_0 \sim Re^{-1/2} \ll 1$.

However, as will be indicated below, allowance for friction and heat exchange provides terms which are also proportional to $Re^{-1/2}$ since the effective decrease in cross-sectional area of the nozzle should be taken into account. Nevertheless, for simplicity of analysis, this circumstance is not taken into

account. The necessary changes which should be introduced into our formulas are obvious from [5].

The Gauss-Ostrogradskiy formula is used to obtain averaged equations of gas flow through a nozzle from the general equations in §1; this formula, for an arbitrary vector \mathbf{w} , for which $\text{div } \mathbf{w} = 0$, upon integration for an infinitely small nozzle volume V (nozzle bounded by two cross sections with the distance between then dz and normal to the lateral surface \mathbf{n}), has the form

$$\int_V \text{div } \mathbf{w} dV = \oint_S (\mathbf{w}, d\mathbf{S}) = -\langle w_z \rangle S_1 + \langle w_z \rangle S_2 + \left(\langle (\mathbf{w}, \mathbf{n}) \rangle \frac{P}{\cos \theta} dz \right)_0 = 0,$$

hence

$$\frac{d \langle w_z \rangle S}{dz} + \langle (\mathbf{w}, \mathbf{n}) \rangle_0 \frac{P}{\cos \theta} = 0. \quad (2.1)$$

Here the sign $\langle f \rangle$ denotes averaging of f with respect to the nozzle cross section S , the perimeter of which P and the generatrix angle with axis z is equal to θ . The subscript 0 refers to the function at the nozzle wall.

In view of $(\mathbf{v}, \mathbf{n})_0 = 0$ (wall is impermeable), we obtain the following continuity equation from (1.1):

$$\langle \rho v_z \rangle S = \langle j \rangle S = \text{const}. \quad (2.2)$$

In view of $\mathbf{v}_0 = 0$ (attachment of gas to wall), we obtain the following energy equation from (1.3) and (2.1):

$$\frac{d}{dz} \left\langle j \left(w + \frac{v^2}{2} \right) - (j'v)_z + q_z \right\rangle S + \langle (\mathbf{q}, \mathbf{n}) \rangle \frac{P}{\cos \theta} = 0. \quad (2.3)$$

The motion equations of (1.2) will be written in tensor form [1]

$$\rho \frac{\partial v_i}{\partial t} = - \frac{\partial \Pi_{ik}}{\partial x_k},$$

where $\Pi_{ik} = p \delta_{ik} + \rho v_i v_k - \sigma_{ik}$ is the density tensor of the pulse flow*, and /144

$$\sigma_{ik} = \eta \left(\frac{\partial v_i}{\partial x_k} + \frac{\partial v_k}{\partial x_i} - \frac{2}{3} \delta_{ik} \frac{\partial v_l}{\partial x_l} \right) + \zeta \delta_{ik} \frac{\partial v_l}{\partial x_l} -$$

*The second viscosity coefficient ζ , which we use in Landau form is $2/3\eta$ greater than the hydrodynamic coefficient of the second viscosity.

is the "viscous" stress tensor (η and ζ are viscosity coefficients). Application of the Gauss-Ostrogradskiy formula to the motion with regard to axis z makes it possible to obtain the following averaged equation:

$$\frac{d(\langle \Pi_{zz} \rangle S)}{dz} + (\langle \Pi_{zi} \rangle n_i)_0 \frac{P}{\cos \theta} = 0$$

or, taking $(\mathbf{v}, \mathbf{n})_0 = 0$ in expanded form into account,

$$d/dz[(p + \rho v_z^2 - \sigma'_{zz})S] + (-p \tan \theta + \sigma'_{zz} \tan \theta - \sigma'_{zr})_0 P = 0. \quad (2.4)$$

Equations (2.2), (2.3) and (2.4) are accurate. We shall simplify them by using a high degree of uniformity of flow along the nozzle cross section, *i.e.*, we shall neglect $|v_r|$ everywhere in comparison with $|v_z|$ and all velocity gradients in the nucleus in comparison with $\partial v_z / \partial z$. In addition, we can disregard the axial velocity gradients in the boundary layer in comparison with the radial gradients, whereby only $\langle \partial v_z / \partial r \rangle_0$ should be taken into account, since the following ensues from the motion equation with respect to the radius under the condition of $\partial p / \partial r = 0$:

$$\left| \frac{\partial v_r}{\partial r} \right|_0 \sim \left| \frac{\partial v_z}{\partial z} \right| \text{ in nucleus, and } \left| \frac{\partial v_z}{\partial z} \right| \ll \left| \frac{\partial v_z}{\partial r} \right|_0.$$

Furthermore, with an accuracy to terms $\sim \delta / r_0$, the average values of all quantities with respect to the cross section are replaced by the values of these quantities in the nucleus. Finally, we shall disregard the dissipative process in the nucleus of the flow, since their contribution is proportional to Re^{-1} . Then the continuity equation has the form

$$\rho v S = j S = Q = \text{const}, \quad (2.5)$$

the motion equation*

$$\frac{1}{j} \frac{dp}{dz} + \frac{dv}{dz} + \tau_0 \frac{P}{Q} = 0, \quad (2.6)$$

and the energy equation

$$\frac{dw}{dz} + v \frac{dv}{dz} + q_0 \frac{P}{Q \cos \theta} = 0. \quad (2.7)$$

*Let us devote attention to the fact that the motion equation in the adopted approximation does not contain the second viscosity.

Here $v \equiv v_z$ and

$$\tau_0 = -\tau \left(\frac{\partial v}{\partial r} \right)_0 > 0, \quad q_0 = (q, n)_0 > 0. \quad (2.8)$$

We shall present the integral forms of the motion equation

$$\Delta v + \int_0^z \frac{dp}{j} = -\frac{1}{Q} \int_0^z \tau_0 P dz < 0 \quad (2.9)$$

and the energy equation

$$\Delta h \equiv \Delta \left(w + \frac{v^2}{2} \right) = -\frac{1}{Q} \int_0^F q_0 dF < 0, \quad (2.10)$$

where h is the total enthalpy of the flow, F is the lateral surface of the nozzle ($q_0 > 0$, since the nozzle is cooled), and also the equations of entropy change

$$Q \Delta s = - \int_0^F \frac{q_0}{T} dF + \int_0^z \frac{\tau_0}{T} v P dz.$$

Let us pay attention to the fact that the first term is negative in the last expression and the second term is positive, since, generally speaking, the situation is possible when $\Delta s = 0$, i.e., the process is isentropic but not adiabatic [6] (we do not consider the change in entropy due to nonequilibrium processes).

The particular continuity equations, as is not difficult to be convinced, have the form

$$\frac{dc_i}{dz} + \frac{1}{Q} \frac{d(I_i S)}{dz} + \frac{1}{j} \sum_i m_i v_{is} \theta_s + I_{i0} \frac{P}{Q \cos \theta} = 0. \quad (2.11)$$

Here the average values with respect to the cross section are replaced by the values in the nucleus, and

$$I_{i0} = (i_s, n)_0. \quad (2.12)$$

The integral form of these equations is as follows:

$$\Delta \left(c_i + \frac{I_i}{j} \right) = - \sum_i m_i v_{is} \int_0^z \frac{\theta_s}{j} dz - \frac{1}{Q} \int_0^F I_{i0} dF. \quad (2.13)$$

If the nozzle walls are impermeable and reactions do not occur in them, then $I_{z0} = 0$ and q_0 reduces to the term $-x(\partial T/\partial n)_0$. The value of the latter depends on the law of heat transfer from gas to wall. Newton's law is used most often:

$$-x\left(\frac{\partial T}{\partial n}\right)_0 = \alpha(T - T_0),$$

where α is the heat transfer coefficient. Experimental relationships of the Nusselt number, $Nu = \alpha r_0/x$, to the Reynolds number, $Re = r_0 v/\nu$, for the parameter of the Prandtl number, $Pr = \eta c_p/x = \nu/\chi$, are usually employed. Let us note that the validity of Newton's linear law is doubtful in the case of large temperature drops (convective, not radiant, heat exchange is taken into account).

Strictly speaking, the problem concerning heat exchange of a gas with a nozzle wall should be solved jointly with the determination of friction on the wall within the framework of boundary layer theory. If the compressibility of the gas, the presence of a longitudinal pressure gradient, and the transition of the laminar boundary layer to a turbulent one are taken into account, this type of problem will be too awkward. However, evaluations* of the contribution of viscosity to the equation of motion in the vicinity of the critical cross section (subscript * denotes the critical cross section)

$$\lambda_z = \frac{\tau_0}{p} \sim \frac{\tau_0/b}{p} \sim \tau \frac{\nu}{c_z} \sqrt{Re} \sim Re^{-1/2} \ll 1 \quad (2.14)$$

and the contribution of heat exchange to the energy equation

$$\lambda_q = \frac{q_0}{j c_p T} \sim \frac{x \Delta T/b}{c_p c_p T} \sim \left(\frac{\Delta T}{T}\right)_* Re^{-1/2} \ll 1 \quad (2.15)$$

indicate that the role of the dissipative processes is generally small. In this/146 case we can limit ourselves to considering them in the first and simplest approximation, *i.e.*, $Pr = 1$; the effective thicknesses of the dynamic and thermal boundary layers coincide, and the boundary layer is considered for an incompressible fluid in a laminar regime in the absence of a longitudinal pressure gradient. Then the effect of the dissipative processes can be evaluated with the aid of the simplest relationships of the type (2.14) and (2.15). It should be borne in mind that the boundary layer theory is not correct for small dimensions of streamlined bodies ($\tau_0 \rightarrow \infty$ when $z \rightarrow 0$). The difficulty is eliminated by using integral forms of (2.9) and (2.10).

If we assume the existence of local thermodynamic equilibrium, the system will be characterized by ordinary temperature and an equation of state which

*These evaluations are obtained naturally in §3.

is a Clapeyron equation with good accuracy (m is the molecular weight)

$$p = \rho \frac{R}{m} T. \quad (2.16)$$

Systems of equations I[(2.5), (2.6), (2.7), (2.11), (2.16)] or II[(2.5), (2.9), (2.10), (2.13), (2.16)], together with the condition of normalization of c_i ($\sum_i c_i = 1$), the condition of electroneutrality of the system on the whole (in the presence of ionization), the relationships of material balance, and the corresponding boundary-layer equations, are closed with respect to the sought variables p , T , ρ , v , c_i and the auxiliary terms τ_0 and q_0 .

§3. Investigation of Equations

We shall investigate system of equations I for an arbitrary reacting gas in complete or partial thermodynamic equilibrium.

We shall preliminarily present here some useful thermodynamic relationships. From the known expression [2] ($V = \rho^{-1}$ is the specific volume)

$$\left(\frac{\partial V}{\partial p}\right)_s = \left(\frac{\partial V}{\partial p}\right)_T + \frac{T}{c_p} \left(\frac{\partial V}{\partial T}\right)_p^2$$

we obtain

$$\left(\frac{\partial \ln V}{\partial \ln T}\right)_p = -\left(\frac{\partial \ln \rho}{\partial \ln T}\right)_p = 1 - \left(\frac{\partial \ln m}{\partial \ln T}\right)_p = \frac{\sqrt{(\gamma-1)} c_p T}{c} \geq 1. \quad (3.1)$$

The inequality sign is determined by the total heat effect of the reactions in the system when $p = \text{const}$. If the system absorbs heat with the increase of T when $p = \text{const}$, $(\partial \ln V / \partial \ln T)_p > 1$. Furthermore, in view of

$$\left(\frac{\partial w}{\partial p}\right)_T = V \left(\frac{\partial \ln m}{\partial \ln T}\right)_p$$

and using (3.1), we obtain

$$\left(\frac{\partial \ln T}{\partial \ln p}\right)_w = -\frac{p}{T} \frac{\left(\frac{\partial w}{\partial p}\right)_T}{\left(\frac{\partial w}{\partial T}\right)_p} = \left[\frac{\sqrt{(\gamma-1)} c_p T}{c} - 1 \right] \frac{R/m}{c_p} \geq 0. \quad (3.2)$$

The sign of this inequality coincides with the inequality sign in (3.1).

Introducing the designations $f = d \ln f / d \ln S$, we shall reduce system I /147
to the following form:

$$\bar{p} + \bar{v} = -1; \quad (3.3)$$

$$\bar{p} + \frac{\rho v^2}{p} \bar{v} = -\frac{\lambda_\tau}{\tan \theta}; \quad (3.4)$$

$$T - \left(\frac{\partial \ln T}{\partial \ln p} \right)_v \bar{p} + \frac{v^2}{c_p T} \bar{v} = -\frac{\lambda_q}{\sin \theta}; \quad (3.5)$$

$$\left(\frac{\partial \ln p}{\partial \ln T} \right)_p T + \left(\frac{\partial \ln p}{\partial \ln T} \right)_T \bar{p} - \bar{v} = 0. \quad (3.6)$$

Here λ_τ and λ_q are determined by (2.14) and (2.15). Hence, for \bar{v} , we obtain the following equation with the aid of (3.1) and (3.2):

$$\begin{aligned} (M^2 - 1) \bar{v} &= 1 - \frac{p/\rho}{c^2} \left(1 + c \sqrt{\frac{\gamma-1}{c_p T}} \right) \frac{\lambda_\tau}{\tan \theta} + \frac{\sqrt{(\gamma-1) c_p T}}{c} \frac{\lambda_q}{\sin \theta} = \\ &= 1 - \kappa_\tau \lambda_\tau / \tan \theta + \kappa_q \lambda_q / \sin \theta. \end{aligned} \quad (3.7)$$

The expressions for \bar{p} , \bar{T} and \bar{v} are obtained by substituting \bar{v} from (3.7) into the reduced form of system I.

We shall present another form of these equations:

$$\frac{d \ln p}{d \ln v} = -\frac{c^2}{p/\rho} M^2 - (\lambda_\tau / \tan \theta) / \bar{v} \quad (3.8)$$

$$\frac{d \ln T}{d \ln v} = -c \sqrt{\frac{\gamma-1}{c_p T}} M^2 - \left[\frac{R/m}{c_p} \left(\frac{\sqrt{(\gamma-1) c_p T}}{c} - 1 \right) \frac{\lambda_\tau}{\tan \theta} + \frac{\lambda_q}{\sin \theta} \right] \frac{1}{\bar{v}}. \quad (3.9)$$

For an ideal gas, (3.7), (3.8), and (3.9) have the form

$$\begin{aligned} (M^2 - 1) \bar{v} &= 1 - \lambda_\tau / \tan \theta + \lambda_q / \sin \theta; \\ \frac{d \ln p}{d \ln v} &= -\gamma M^2 - (\lambda_\tau / \tan \theta + \lambda_q / \sin \theta); \\ \frac{d \ln T}{d \ln v} &= -(\gamma - 1) M^2 + (\lambda_q / \sin \theta) / \bar{v}. \end{aligned}$$

The expression for the velocity gradient from (3.7) is the following ($dS = P \tan \theta dz$):

$$\frac{dv}{dz} = \frac{v}{S/P} \frac{\tan \theta - \kappa_\tau \lambda_\tau + \kappa_q \lambda_q / \cos \theta}{M^2 - 1}. \quad (3.10)$$

The singular point of all these equations is the point where $M = 1$. In an isentropic case, when $\lambda_\tau = \lambda_q = 0$, the singular point, as follows from (3.10), is situated in the critical cross section of the nozzle, where $\tan \theta = 0$. In a nonisentropic case, the singular point, generally speaking, does not coincide with the critical cross section: its coordinate is determined from the condition $\tan \theta - \alpha_\tau \lambda_\tau + \alpha_q \lambda_q / \cos \theta = 0$ or, in view of the smallness of λ_τ and λ_q , from the condition $\tan \theta \approx \alpha_\tau \lambda_\tau - \alpha_q \lambda_q$. Let us turn our attention to the graphic treatment of the point where $M = 1$, for an ideal gas with heat exchange disregarded: this point, where the relationship $p \sin \theta = \tau_0 \cos \theta$ occurs, *i.e.*, the point where the total effect of pressure and friction against the nozzle wall on the gas along axis z is equal to zero, whereby the total effect decelerates the gas before this point, and accelerates it after this point [6].

The nozzle profile near the critical cross section has the form ($k > 0$)

$$r_0/r_{0*} = 1 + \xi^{2k} + \dots,$$

where $\xi = (z - z_*)/l$ (l is a certain length scale). It is not difficult to be /148
convinced with the aid of (3.10) that in a nonisentropic case $M_* = v/c_*$ is then expressed in the following manner:

$$M_* = 1 + \alpha_* \xi^k + \dots,$$

where α_* is a certain coefficient. Since M_* increases monotonically upon transition to the critical cross section, $k = \frac{2i+1}{2j+1}$ (i and j are natural numbers).

We shall limit ourselves to the simplest case of $i = j = 0$, *i.e.*, $k = 1$. This means we are considering the nozzle profile in the vicinity of the critical cross section of a circular arc (if the radius of the circle is R_{0*} , then $l \approx \sqrt{2r_{0*}R_{0*}}$). Then the gradients of all quantities in the critical cross section are finite. In connection with this, we shall turn our attention to the errors made in [5], the author of which states that the gradients of all quantities in the critical cross section are infinite, regardless of nozzle profiling. The dissipative processes in the nucleus near the critical cross section are taken into account in [5] to eliminate this situation, which is unnecessary with the appropriate profiling of the nozzle, as we shall see. The analytical errors made in [5] are explained not only by not taking into account nozzle profiling, but also by making arbitrary assumptions (when taking dissipation in the nucleus near the critical cross section into account) with respect to the equality of d^2v/dz^2 and d^2T/dz^2 to zero in the critical cross section.

For the value of $dM_*/d\xi$ in the singular point when $k = 1$ and the small quantities $\alpha_\tau \lambda_\tau$ and $\alpha_q \lambda_q$ are constant, we obtain the following from (3.10):

$$\frac{dM_*}{d\xi} \approx \frac{2c}{V\sqrt{\gamma p_{rr}}} \left[1 + \frac{1}{2} x_q \lambda_q (x_\tau \lambda_\tau - x_q \lambda_q) \right]$$

or, neglecting terms of the second order of smallness,

$$\frac{dM_*}{d\xi} \approx \frac{2c}{V\sqrt{\gamma p_{rr}}} . \quad (3.11)$$

In view of this small divergence of the singular point and the critical cross section, all quantities in (3.11) are taken in the critical cross section, whereupon $P_{vv} \equiv (\partial^2 p / \partial V^2)_s > 0$, as it is traditionally assumed in gas dynamics [1], although the certainty of the sign on p_{vv} for arbitrary substances does not follow from thermodynamics.

An analysis indicates that the gradients of all the quantities are finite in the singular point of system I when $r/r_{0*} = 1 + \xi^2 + \dots$ since the transition through the singular point does not cause difficulties in the specific calculation.

§4. General Order of Calculation

The specific problem should be solved with successive complication of its statement. For the specific thermodynamic conditions at the nozzle inlet, p_+ , T_+ , etc., and the specific nozzle configuration, the isentropic flow of a corresponding ideal gas should be considered according to known formulas of the type [1]

$$M_* \left[\frac{\gamma+1}{2} - M_*^2 \frac{\gamma-1}{2} \right]^{\frac{1}{\gamma-1}} = \frac{1}{s} \equiv \frac{S_*}{S} \leq 1,$$

where $M_* = v/c_*$.

An isentropic, completely equilibrium flow of a specific reacting gas should be calculated. The calculation in this case amounts to finding the quantities in the critical cross section. It is convenient to use a $w - s$ diagram. At each point of the vertical $s = \text{const} = s_+$ below the initial point p_+ , T_+ we shall calculate the quantities $h = w + c^2/2$ and $i = \rho c$; we shall further calculate the values of velocity at the nozzle inlet by the two possible methods, i.e., $v_{+1} = \sqrt{2(h - w_+)}$, and $v_{+2} = i/\rho_+ c_+$; the point where $v_{+1} = v_{+2}$ is critical; the sought constants $h_* = w_* + c_*^2/2$ and $i_* = \rho_* c_* = j_*$ are determined in it; finally, since w and ρ are known at each point on the vertical $s = \text{const} = s_+$,

we shall calculate the finite quantities $v = \sqrt{2(\bar{h}_* - w)}$, $j = \rho v$ and $\sigma = j_*/j$. Thus, p and T , w and ρ , v and j are known for each σ (or z). Graphs of the quantities w , s , c and ρ as functions of T with the parameter p (or conversely) can be used instead of the $w - s$ diagram with equal success.

It is useful to compare both calculations.

The nonisentropic nature of the flow due to friction and heat exchange with even more complete thermodynamic equilibrium should be taken into account in the following stage. The calculation is performed from the critical cross section in both directions, by numerical integration of system I [(2.5), (2.6), (2.7), (2.11), (2.16)] (see, for example, [7]). The state in the critical cross section is adopted as that which was obtained in the isentropic flow of a reacting gas. Expressions of type (3.11) must be used directly in the vicinity of the critical cross section. It is natural that the values of p_+ , T_+ , etc. at the nozzle inlet which are obtained as a result of the calculation, will differ from the given values, although the difference, in view of the estimates (2.14) and (2.15), should not be great. A series of similar calculations for various values of p_+ and T_+ makes it possible to interpolate and find the sought distributions of all quantities along the nozzle length for the given values of p_+ and T_+ .

Allowance for chemical nonequilibrium of the flow in the presence of local thermodynamic equilibrium which we always assume, *i.e.*, the existence of local Maxwell distribution of particle velocity, is more important than allowance for friction and heat exchange, which makes it possible to use the conventional definitions of all thermodynamic quantities. At the nozzle inlet, all characteristics, including the chemical composition of the gas, are naturally equilibrium. In the convergent portion of the nozzle, in view of the low rate of gas flow, the deviations from chemical equilibrium are small, but they can be extremely essential in the divergent portion. Therefore, allowance for nonequilibrium, first disregarding friction and heat exchange, is best made in the order of successive complication of the statement of the problem in the following manner: the first two stages, *i.e.*, the completely "frozen" and completely equilibrium flow regimes, are considered; the flow regime that is completely equilibrium in the convergent portion (calculated) and completely "frozen" in the divergent portion should be considered in the second stage; finally, the flow regime that is equilibrium in the convergent portion and nonequilibrium in the divergent portion, whereby diffusion can be neglected, since we do not successively consider the dissipative processes in the nucleus of the flow; the deviations from chemical equilibrium in the convergent portion from the nozzle inlet to the vicinity of the critical cross section should be estimated at the concluding stage; if the deviation is not too small, the problem is extremely complicated, since satisfaction of the condition in the critical cross section, $v_* = c_*$, can then be achieved only by variation of v_+ (more exactly, see §5).

Finally, in the last stage of the calculation, it is necessary to consider friction and heat exchange on the nozzle walls in a nonequilibrium regime of flow by the method described above.

A comparison of the results of the various calculation stages graphically indicates the relative value of each of the considered factors.

§5. Statement of the Problem

/150

It is required, for example, to calculate the nonisentropic equilibrium flow of a lithium plasma through a nozzle with friction and heat exchange taken into account.

The consideration refers to the region of the p - T diagram in which: 1) there is no lithium vapor condensation; 2) dissociation recombination and double ionization of Li atoms and their negative ions can be neglected. Thus, the flow is accomplished in a homogeneous gaseous phase, where there is only Li (1), Li^+ (2), and electrons (3).

We shall provide the necessary thermodynamic information. From the normalization condition ($x_i = N_i/N$ are the molar fractions of K_i particles), $x_1 + x_2 + x_3 = 1$, the condition of electroneutrality, $x_2 = x_3$, and the law of effective mass (K_p is the equilibrium constant of single Li ionization), $x_2 x_3 / x_1 = K_p / p$, we obtain an expression for the degree of Li ionization as a function of p and T :

$$\beta = (1 + p/K_p)^{-1/2}, \quad (5.1)$$

whereby

$$x_1 = \frac{1-\beta}{1+\beta}, \quad x_2 = x_3 = \frac{\beta}{1+\beta}.$$

The molecular weight [g/mole] and the density [g/cm³] have the form

$$m = m_1 \frac{1}{1+\beta}, \quad \rho = \frac{pm}{RT} = 0,01219 \frac{pm}{T}, \quad (5.2)$$

where p is in atm and T in °K (all physical constants from [8]).

The expressions for enthalpy and internal energy (both in [cal/g]) are conventional:

$$w = \frac{1}{m} \sum_i H_i x_i, \quad \varepsilon = \frac{1}{m} \sum_i U_i x_i, \quad (5.3)$$

where H_i and U_i ($H_i - U_i = RT$) are the molar enthalpy and internal energy (both

in [cal/mole]).*

Entropy has the form

$$s = \frac{1}{m} \left(\sum_i S_i x_i - R \ln p - R \sum_i x_i \ln x_i \right), \quad (5.4)$$

where S_i [cal/mole·deg] is the molar entropy of K_i without nuclear spin taken into account [9].

The expression for heat capacity with correspondingly p or $V = \text{const}$ (both in [cal/g·deg]) have the following form:

$$\begin{aligned} c_p &= \frac{1}{m} \left(\sum_i C_{pi} x_i + \frac{Q_p^2}{RT^2} \frac{1}{\Phi} \right); \quad c_v = \frac{1}{m} \left(\sum_i C_{vi} x_i + \frac{Q_v^2}{RT^2} \frac{1}{F} \right); \\ (\Phi &= \frac{1}{x_1} + \frac{1}{x_2} + \frac{1}{x_3} - 1, \quad F = \Phi + 1); \\ (Q_p &= -H_1 + H_2 + H_3, \quad Q_v = Q_p - RT). \end{aligned} \quad (5.5)$$

where C_{pi} , C_{vi} , ($C_{pi} - C_{vi} = R$) and Q_p , Q_v are the molar heat capacities of K_i and the thermal effects of Li ionization, respectively, when p or $V = \text{const}$. The corresponding completely "frozen" heat capacities, c_{pf} and c_{vf} , are evidently equal (subscript f denotes "frozen"),

$$c_{pf} = \sum_i c_{pi} x_i / m, \quad c_{vf} = \sum_i c_{vi} x_i / m. \quad (5.6)$$

The velocity of sound is expressed by the formula

$$\begin{aligned} c &= \sqrt{\left(\frac{\partial p}{\partial \rho} \right)_S} = \sqrt{\gamma \left(\frac{\partial p}{\partial \rho} \right)_T} = \sqrt{\gamma \frac{RT}{m} \left[\left(\frac{\partial \ln p}{\partial \ln T} \right)_V / \left(\frac{\partial \ln V}{\partial \ln T} \right)_p \right]} = \\ &= 91,18 \left\{ \gamma \frac{T}{m} \left[\left(1 + \frac{Q_p}{RT} \frac{1}{F} \right) / \left(1 + \frac{Q_p}{RT} \frac{1}{\Phi} \right) \right] \right\}^{1/2}, \end{aligned} \quad (5.7)$$

where $\gamma = c_p / c_v$. The frozen velocity of sound is obviously equal to

* U_i is taken from a handbook similar to [9], whereby the ionization potential of Li, $I = 5.39 \text{ eV} = 124,300 \text{ cal/mole}$, should be added to H_2 and U_2 .

$$c_f = 91.18 \sqrt{\gamma_f \frac{T}{m}}, \quad (\gamma_f = c_{pf}/c_{vf}). \quad (5.8)$$

It is pertinent here to refine the concept introduced in §4 concerning the frozen state. We shall assume that at each point of the nozzle there exists equilibrium not only with respect to translational but also internal degrees of freedom (electronic excitation of Li and Li⁺ in this case); along the nozzle, however, particularly in the divergent portion, there may be deviations from chemical equilibrium, *i.e.*, the chemical composition in $z = z_2$, where $p = p_2$ and $T = T_2$, is indeed what it should be at equilibrium in $z = z_1 < z_2$, where $T = T_1 > T_2$ and $p = p_1 > p_2$ (see figure). Thus, the composition, as it were, lags behind the thermodynamic evolution of the flow, so that in calculations of frozen (in the sense of §4) flow regimes, the composition is fixed from the freezing point z_* in formulas (5.2), (5.3), (5.4), (5.6), and (5.8). If the equilibrium composition is substituted into (5.6) and (5.8), however, the values of the quantities that are completely frozen with regard to small disturbances are obtained. These quantities have no relationship to the calculation of flows that are frozen with regard to chemical composition.

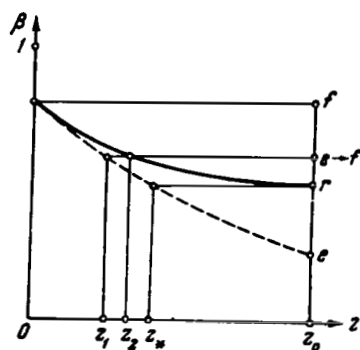


Diagram of Dependence of β on z .

The quantities in the nonequilibrium regime which include the derivatives of composition with regard to any thermodynamic parameter, when some other thermodynamic parameter (c_p , c_v , γ , α) is constant, are not determined. That is precisely why the treatment of the transition of a nonequilibrium gas through the critical cross section is fundamentally unclear. Such a treatment is given in §6.

The following equations should be used when calculating an equilibrium flow:

$$\rho v S = \text{const}; \quad (5.9)$$

$$\frac{dv}{dz} = \frac{v}{S/p} \frac{\tan \theta - \alpha_r \lambda_r + \alpha_g \lambda_g / \cos \theta}{M^2 - 1}; \quad (5.10)$$

$$\frac{dp}{dz} = -\rho v \frac{dv}{dz} - \lambda_r p \frac{1}{S/p}; \quad (5.11)$$

$$\frac{dT}{dz} = \left(\frac{\partial \ln T}{\partial \ln p} \right)_* \frac{T}{p} \frac{dp}{dz} - \frac{v}{c_p} \frac{dv}{dz} - \lambda_g T \frac{1}{(S/p) \cos \theta}; \quad (5.12) \quad /152$$

$$p = \rho \frac{R}{m} T. \quad (5.13)$$

This is a system of five equations with four unknowns (p, T, ρ, v). Any of the equations can be used for a check when calculating the other four. The value of $(\partial \ln T / \partial \ln p)_v$ is determined according to (3.2). The quantities τ_0 and q_0 in the simplest approximation (§4) are determined as follows [1]:

$$q_0 \sim \frac{c_p \tau_0}{v} (T - T_0). \quad (5.14)$$

$$\tau_0 \sim 0,3v \sqrt{\frac{\tau_{ff} v}{z}}; \quad (5.15)$$

The initial equations, (2.5), (2.6), (2.7) and (2.16), should be used when calculating a nonequilibrium flow, whereby the enthalpy in (2.7) is determined from (5.3) and has the form

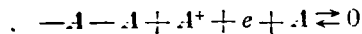
$$w = \frac{1}{m_1} (H_1 + Q_p \xi). \quad (5.16)$$

The particular continuity equations in the given case are reduced to one equation with respect to degree of ionization

$$v \frac{d\beta}{dz} = \alpha \frac{p}{kT} (1 - \beta) \left(\frac{K_p}{p} - \frac{\beta^2}{1 - \beta^2} \right) \leq 0, \quad (5.17)$$

where k is the Boltzmann constant; α [cm^3/sec] is the Li recombination coefficient according to the Thompson theory [10].

Expression (5.17) is obtained from (2.11) with diffusion, the use of the relationship for c_i and x_i ($c_i/m_i = x_i/m$), and the representation for a single considered reaction disregarded:



The expression for θ is in the following form:

$$-\theta = \theta_{\rightarrow} - \theta_{\leftarrow} = k_{\rightarrow} n_1^2 - k_{\leftarrow} n_1 n_2 n_3 = \alpha n n_1 \left(\frac{K_p}{p} - \frac{x_2 x_3}{x_1} \right) \leq 0$$

$$(\alpha = k_{\rightarrow} n_1, \quad K_p = kT (k_{\leftarrow}/k_{\rightarrow})).$$

56. Transition of a Nonequilibrium Gas Through the Critical Cross Section of a Nozzle

The equations of hydrodynamics are solved here in the first two approximations for small relaxation parameters, taking into account the relaxation

processes* for stationary flows of a nonequilibrium gas in the vicinity of the critical cross section of a nozzle and the following states: 1) close to equilibrium; 2) close to completely nonequilibrium (frozen).

The equations of the flow of a nonequilibrium gas, with ordinary viscosity and thermal conductivity disregarded, have a well-known form (designation according to [1]):

$$\frac{\partial \rho}{\partial t} + \operatorname{div} \rho \mathbf{v} = 0;$$

$$\rho \frac{d\mathbf{v}}{dt} + \nabla p = 0;$$

$$\frac{d\epsilon}{dt} + p \frac{dV}{dt} = 0.$$

By comparing the energy equation with the general thermodynamic expression /153

$$\frac{d\epsilon}{dt} = -p \frac{dV}{dt} + \sum_n \epsilon_n \frac{d\xi_n}{dt} + T \frac{ds}{dt},$$

where ξ_n are nonequilibrium parameters, we obtain the entropy balance equation:

$$T \frac{ds}{dt} = - \sum_n \epsilon_n \frac{d\xi_n}{dt}.$$

It may be assumed that the rates of change of the nonequilibrium parameters are determined only by "chemical" potentials, *i.e.*, the following "kinetic" equations are valid:

$$\frac{d\xi_n}{dt} = - \sum_m L_{nm} \epsilon_m - \sum_{m, l} L_{nml} \epsilon_m \epsilon_l - \dots,$$

where L_{nm} , L_{nml} , ... are kinetic coefficients. The condition of entropy increment over time imposes definite restrictions on the notated forms.

The given system of equations is closed by the expansion of the independent quantities (p , ϵ_n and T) with respect to the independent parameters (V , ξ_n and s) to the necessary orders of smallness.

Let us consider the stationary, quasi one-dimensional flow of a nonequilibrium gas through a nozzle in the vicinity of the critical cross section. In connection with the degeneration of the hydrodynamic equations in the critical cross section, the expansions of the dependent quantities should be taken with terms no less than of the third order of smallness. We shall limit ourselves to the simplest form of expansion and consider for simplicity only one nonequilibrium parameter; we then obtain

$$p' = p_V^{(1)} V' + p_\xi^{(2)} \xi' + \frac{1}{2} p_{VV}^{(2)} V'^2 + p_{V\xi}^{(3)} V' \xi' + \frac{1}{6} p_{VVV}^{(3)} V'^3 - T_V s', \quad (6.1)$$

$$\varepsilon_\xi = -p_\xi^{(3/2)} V' + \varepsilon_{\xi\xi}^{(3/2)} \xi' - \frac{1}{2} p_{V\xi}^{(3/2)} V'^2. \quad (6.2)$$

Here the prime refers to deviations from the state in the critical cross section, where all thermodynamic parameters are being calculated; the subscript letters denote differentiation; the numbers above the terms indicate their order of smallness*. The expansion for T' , in view of the smallness of s' , has the form of $T' = 0$.

The form of expansions (6.1) and (6.2) assumes that all derivatives are taken for a fixed composition, i.e., that they are frozen. The relationships between the equilibrium and frozen values of the thermodynamic parameters are obtained by substituting the equilibrium value of ξ' from the condition $\varepsilon_\xi = 0$ into (6.1), and they have the following form:

$$p_{V0} - p_{V\infty} = p_\xi^2 / \varepsilon_{\xi\xi} > 0, \quad p_{VV0} - p_{VV\infty} = 3p_\xi p_{V\xi} / \varepsilon_{\xi\xi}, \quad (6.3)$$

where the subscripts 0 and ∞ refer to the equilibrium and frozen states, respectively. The differences in the remaining derivatives can be disregarded in the cubic order of expansion adopted.

We shall introduce the following dimensionless variables:

/154

$$\eta = (z - z_*)/l; \quad \sigma = s/s_*; \quad \lambda = V/V_*; \quad \mu = v/v_*; \quad \nu = T_* s/p_* V_*; \quad \pi = p/p_*,$$

where l is a characteristic dimension. Then the investigated system of equations has the following form:

$$\frac{\mu}{\lambda} \sigma = 1; \quad (6.4)$$

$$\kappa \frac{d\mu}{d\eta} + \sigma \frac{d\pi}{d\eta} = 0; \quad (6.5)$$

$$\begin{aligned} \pi - 1 = & -x_{1\infty}(\lambda - 1) + \frac{1}{2} x_{2\infty}(\lambda - 1)^2 - \frac{1}{6} x_{3\infty}(\lambda - 1)^3 + \\ & + \delta \left[1 - \frac{1}{3} \frac{\Delta x_2}{\Delta x_1} (\lambda - 1) \right] + \vartheta_1 (\nu - 1); \end{aligned} \quad (6.6)$$

$$\vartheta_\mu \frac{d\delta}{d\eta} = -\delta + \Delta x_2 (\lambda - 1) - \frac{1}{6} \Delta x_2 (\lambda - 1)^2; \quad (6.7)$$

*As in [11], we shall assume that the order of smallness of p_ξ is equal to $1/2$. Then the order of ξ' is equal to $3/2$ and the order of s' is equal to 3.

$$\Delta x_1 \frac{dv}{d\eta} = \theta \mu \left(\frac{d\delta}{d\eta} \right)^2, \quad (6.8)$$

where the relaxation time $\tau = (L \epsilon_{\xi\xi})^{-1}$ or $\theta = v_* \tau / l$;

$$\begin{aligned} x &= v_*^2 / p_* V_*, \quad x_1 = -V_* p_v / p_*, \quad x_2 = V_*^2 p_{vv} / p_*, \quad x_3 = -V_*^3 p_{v^2} / p_*, \\ \Delta x_1 &= x_{1\infty} - x_{10}, \quad \Delta x_2 = x_{2\infty} - x_{20}, \quad \vartheta_1 = -V_* T_v / T_*, \quad \delta = p_\xi \xi' / p_*. \end{aligned}$$

The subscript $*$ refers to the critical cross section.

The combination of equations (6.4)-(6.8) makes it possible to obtain an equation for the velocity gradient. The singular point of this equation determines the "crisis" of nonequilibrium flow (see, for example, [6]). This question will be discussed below.

A small relaxation parameter may be θ or θ^{-1} . When $\theta \rightarrow 0$, the gas state is close to equilibrium; when $\theta^{-1} \rightarrow 0$, it is close to the frozen state. We shall seek the solution to system (6.4)-(6.8) in the form of

$$f = \sum_{i=0}^{\infty} f^{(i)} \omega^i,$$

where ω is a small relaxation parameter determined for each situation below. It is considered that the orders of smallness of the thermodynamic parameters Δx_1 and Δx_2 are equal to the order of smallness of θ (or θ^{-1}), i.e., 1.

For concreteness, we shall consider a nozzle whose profile in the vicinity of the critical cross section is approximated by a circular arc. Then

$$\sigma = 1 + 2\eta^2 + O(\eta^4), \quad l = \sqrt{2R_* r_*}, \quad (6.9)$$

where R_* and r_* are the radii of the circular arc and the critical cross section, respectively.

1. State Close to Equilibrium

From (6.7) and (6.8), in zero approximation ($\theta = 0$), we obtain

$$\delta^{(0)} = \Delta x_1 (\lambda^{(0)} - 1) - 1/6 \Delta x_2 (\lambda^{(0)} - 1)^2, \quad v^{(0)} = 1,$$

and (6.6) has the natural form

$$\pi^{(0)} = 1 - x_{10} (\lambda^{(0)} - 1) + 1/2 x_{20} (\lambda^{(0)} - 1)^2 - 1/6 x_3 (\lambda^{(0)} - 1)^3.$$

Using (6.9) and expanding the solution of the system with respect to η , we obtain in particular $x = x_{10}$, i.e., $v_* = c_0$ is the equilibrium "crisis" of the flow in the critical cross section of the nozzle. The solutions have the form

$$\lambda^{(0)} = 1 + 2\sqrt{\alpha}\eta + \frac{2}{3}\alpha(4 + \beta)\eta^2 + \dots, \quad (6.10)$$

$$\mu^{(0)} = 1 + 2\sqrt{\alpha}\eta + 2\left[\frac{1}{3}\alpha(4 + \beta) - 1\right]\eta^2 + \dots, \quad (6.11)$$

$$\pi^{(0)} = 1 - 2x_{10}\sqrt{\alpha}\eta - 2x_{10}\left[\frac{1}{3}\alpha(4 + \beta) - 1\right]\eta^2 + \dots, \quad (6.12)$$

where $\alpha = x_{10}/x_{20}$ and $\beta = x_3/x_{20}$ (as usual [1], we consider that $p_{vv} > 0$). These solutions assume that the values introduced above for all functions in the critical cross section (V_* , v_* , p_* , s_*) are equilibrium.

In the next approximation, (6.7) has the form

$$x_{10}\mu^{(0)}\left[1 - \frac{1}{3}\frac{\Delta x_2}{\Delta x_1}(\lambda^{(0)} - 1)\right]\frac{d\lambda^{(0)}}{d\eta} = -\delta^{(1)} + \Delta x_1\left[1 - \frac{1}{3}\frac{\Delta x_2}{\Delta x_1}(\lambda^{(0)} - 1)\right]\lambda^{(1)},$$

whereupon expansion is performed with respect to the natural parameter

$$\omega = \frac{\Delta x_1}{x_{10}}\theta = \frac{c_0\tau_0}{l} = \frac{c_0}{l}\frac{c_\infty^2 - c_0^2}{c_0^2}\tau = \frac{\zeta}{c_0\rho_*l} = \frac{1}{Re} \ll 1, \quad (6.13)$$

where c_0 and c_∞ are the equilibrium and frozen velocities of sound, respectively; $\zeta = \tau\rho_*(c_\infty^2 - c_0^2)$ is the second viscosity coefficient [1]; and Re is the corresponding Reynolds' number. The order of smallness of ω (or Re^{-1}) is equal to 2. Equation (6.8) has the form

$$\frac{dv^{(1)}}{d\eta} = x_{10}\mu^{(0)}\left[1 - \frac{1}{3}\frac{\Delta x_2}{\Delta x_1}(\lambda^{(0)} - 1)\right]^2\left(\frac{d\lambda^{(0)}}{d\eta}\right)^2.$$

The solutions (with respect to the first terms) are obtained as follows:

$$\lambda^{(1)} = \mu^{(1)} = \frac{2}{3}\alpha^{3/2}[7 + \beta - 3\theta_1 - 2\Delta x_2/\Delta x_1] - \dots = \frac{4}{3}\frac{5 - 3\gamma}{(\gamma + 1)^{3/2}} - \dots; \quad (6.14)$$

$$v^{(1)} = 4x_{10}\alpha\eta + \dots = \frac{4\gamma}{\gamma + 1}\eta + \dots; \quad (6.15)$$

$$\pi^{(1)} = -x_{10}(2\sqrt{\alpha} + \lambda^{(1)}) + \dots = -2/3 \cdot \frac{\gamma(13-3\gamma)}{(\gamma+1)^{3/2}} + \dots, \quad (6.16)$$

where the expressions with $\gamma = c_p/c_v$ are given for an ideal gas. It is essential when $\gamma < 5/3$ that allowance for nonequilibrium increases the specific volume and velocity and decreases the pressure in the critical cross section. The gradients of all quantities in this case should be less in absolute value than in the equilibrium state. For a monatomic gas ($\gamma = 5/3$) the second viscosity coefficient is equal to zero, and the characteristics of flow in the given consideration do not change. The same qualitative results are obtained also in a simpler, although inaccurate, quadratic isentropic approximation, whereby deviations from equilibrium are naturally large.

Without presenting the expressions for the rate of flow at the singular point of system (6.4)-(6.8), let us note that it is obtained by formal differentiation of (6.6) when $\xi = \text{const}$, i.e., at the "crisis" of the flow its velocity is equal to the frozen velocity of sound [12], whereby the value of ξ' is taken from the condition $\varepsilon_\xi = 0$. However, in distinction from [12], the crisis of 156 nonequilibrium flow occurs in first approximation not in the critical cross section, but at the point with the coordinate

$$\eta_{**} = \frac{z_{**} - z_*}{l} = 1/2 \frac{\lambda_{10}}{x_{10}} \sqrt{\alpha} = \frac{c_0}{2V_* \sqrt{V_* \rho_{fr}}} \frac{c_\infty^2 - c_0^2}{c_0^2} > 0, \quad (6.17)$$

i.e., in the divergent portion. It is interesting that the amount of displacement in the first approximation is purely a thermodynamic parameter which is not equal to zero even when $\Theta = 0$. The paradoxical nature of the situation for an equilibrium gas is typical for the derivations of relaxation hydrodynamics [13] and [14]. The amount of displacement has an order of smallness of 1.

It should be borne in mind that a description of the flow of a nonequilibrium gas through a nozzle by means of equations of ordinary hydrodynamics with only the bulk viscosity taken into account cannot be correct. This follows from the general fact that the very concept of the second viscosity coefficient is meaningful only for hydrodynamic equations in linear approximation [14], while the flow through a nozzle can be described only in the higher approximations. In particular, the result of (6.17) cannot generally be obtained within the framework of ordinary hydrodynamics. Actually, from the characteristics of the flow there can be constructed only two combinations which have the dimension of time (l/c and ζ/p), but none is related to the microscopic relaxation time. In other words, such a characteristic time scale τ_0 as

$$\lim_{\tau_0 \rightarrow 0} \zeta/\tau_0 \neq 0, p.$$

does not exist in ordinary hydrodynamics.

2. State Close to Frozen

From (6.7) and (6.8), in zero approximation ($\Theta^{-1} = 0$), we obtain $\delta^{(0)} = \text{const} = 0$ and $v^{(0)} = 1$, and equation (6.6) has the natural form

$$\pi^{(0)} = 1 - x_{1\infty}(\lambda^{(0)} - 1) + 1/2 x_{2\infty}(\lambda^{(0)} - 1)^2 - 1/6 x_{3\infty}(\lambda^{(0)} - 1)^3.$$

Using (6.9) and expanding the solution of the system with respect to η , we obtain, in particular, $x = x_{1\infty}$, i.e., $v_* = c_\infty$ is the "frozen crisis" of the flow in the critical cross section of the nozzle. The solutions have the form of (6.10)-(6.12) with the replacement of x_{10} and x_{20} by $x_{1\infty}$ and $x_{2\infty}$. The integration constant $\delta^{(0)} = 0$ was selected in order that not only the specific volume and velocity, but also the pressure, were frozen in the critical cross section.

In the next approximation, (6.7) has the form

$$\mu^{(0)} \frac{d\lambda^{(1)}}{d\eta} = x_{1\infty} \left[1 - 1/6 \frac{x_{2\infty}}{x_{1\infty}} (\lambda^{(0)} - 1) \right] (\lambda^{(0)} - 1),$$

whereby expansion is performed with respect to the natural parameter

$$\omega = \frac{x_{1\infty}}{x_{10}} \Theta^{-1} = \frac{v_\infty^{-1}}{c_\infty} = \frac{1}{c_\infty} \frac{c_\infty^2 - c_0^2}{c_\infty^2} \tau^{-1}, \quad (6.18)$$

the order of smallness of which is also equal to 2. It is not difficult to be convinced from (6.8) that the change in entropy has an order of smallness of 5, i.e., the state close to frozen is more isentropic than the state close to equilibrium. Moreover, to obtain even the gradients of the first approximation, it is generally sufficient to use the quadratic approximation for p' and ε_ξ instead 157 of the cubic approximation (6.1) and (6.2). The solutions have the form

$$\lambda^{(1)} = -1/2 a \eta + \dots; \quad (6.19)$$

$$\mu^{(1)} = -1/2 a \eta + \dots; \quad (6.20)$$

$$v^{(1)} = 1/3 x_{1\infty} a \eta^3 + \dots; \quad (6.21)$$

$$\pi^{(1)} = \pi^{(1)}(0) + 1/2 x_{1\infty} a \eta - \dots, \quad (6.22)$$

where $\pi^{(1)}(0) = \text{const} = 0$ (see below) is the integration constant. Thus, a small deviation from the frozen state does not change the values of the characteristics in the critical cross section. The gradients of all quantities are smaller in absolute value as compared to their frozen values.

From the total result of $v_{**} = c_{\infty**}$, in view of $v_* = c_\infty$, it follows that the crisis of the flow takes place in the critical cross section. For this reason, $\pi^{(1)}(0)$ must be equal to zero.

Let us note in conclusion that the results of this section are not difficult to generalize for the case of an arbitrary number of nonequilibrium parameters. In particular, instead of the second viscosity coefficient in the form of $\zeta = \tau_{\rho*} \times (c_\infty^2 - c_0^2)$, the following generalized quantity appears:

$$\zeta = \rho_* \sum_n \tau_n (c_{\infty n}^2 - c_0^2), \quad (6.23)$$

where τ_n is the relaxation time of parameter ξ_n and $c_{\infty n}$ is the equilibrium velocity of sound for the same frozen parameter.

Let us note that calculation of the nonequilibrium flow of a gas through a nozzle of arbitrary configuration beyond the critical cross section presents no difficulties if the state of the gas at the initial point of the nozzle (in the convergent or divergent portion) is given precisely.

REFERENCES

1. Landau, L. D. and Ye. M. Lifshits: *Mekhanika sploshnykh sred. (Mechanics of Continuous Media.)* Moscow, GITTL, 1953.
2. Landau, L. and Ye. M. Lifshits: *Statisticheskaya fizika. (Statistical Physics.)* Moscow, GITTL, 1951.
3. Chapman, S. and T. Cowling: *The Mathematical Theory of Non-Uniform Gases.* Cambridge University Press, 1939.
4. Abramovich, G. N.: *Prikladnaya gazovaya dinamika. (Applied Gas Dynamics.)* Moscow, GITTL, 1953.
5. Bolotina, K. S.: On the calculation of flows through a convergent-divergent nozzle with viscosity and heat exchange taken into account, concerning the transition through the velocity of sound. *Izv. AN SSSR, OTN*, No. 5, 1956.
6. Vulis, L. A.: *Termodinamika gazovykh potokov. (Thermodynamics of Gas Flows.)* Moscow and Leningrad, GEI, 1950.
7. Pirumov, U. G., V. A. Rubtsov and V. N. Suvorova: Calculation of axially symmetric nozzles with equilibrium physical and chemical transformations taken into account. In: *Chislennyye metody v gazovoy dinamike. (Numerical Methods in Gas Dynamics.)* Vol. II Izd. MGU, Moscow, 1963.
8. Stupochenko, Ye. V., I. P. Stakhanov, et al.: Thermodynamic properties of

air in the temperature interval from 1,000–12,000° K and the pressure interval from 0.001 to 1,000 atm. In: *Fizicheskaya gazodinamika*. (Physical Gas Dynamics.) Izd-vo AN SSSR, 1959.

9. *Termodinamicheskiye svoystva individual'nykh veshchestv*. (Thermodynamic Properties of Individual Substances.) Handbook edited by V.P. Glushko, Izd-vo AN SSSR, 1962.
10. Massey, G. and E. Barhop: *Elektronnyye i ionnyye stolknoveniya*. (Electron and Ion Collisions.) Moscow, IL, 1958.
11. D'yakov, S.P.: Shock waves in a relaxing medium. *Zhurnal Eksperimental'noy i Teoreticheskoy Fiziki*, Vol. 27, No. 6, 1954.
12. Vincenti, W.G.: Non-equilibrium flow over a wavy wall. *J. Fluid Mech.*, Vol. 6, No. 4, 1959.
13. Broer, L.J.F.; Characteristics of the equations of motion of a reacting gas. *J. Fluid Mech.*, Vol. 4, No. 3, 1958.
14. Stupochenko, Ye. V. and I.P. Stakhanov: Equations of relaxation hydrodynamics. *Doklady AN SSSR*, Vol. 134, No. 4, 1960.

AN EXPERIMENTAL INVESTIGATION OF THE ESCAPE OF DISSOCIATED GASES THROUGH SUPERSONIC NOZZLES

V. P. Ionov and G. N. Nikolayev

In a study [1] which we published earlier, it was shown that the region /158
behind the reflected shock wave in a shock tube where the gas is heated to a high temperature and is partially dissociated can be viewed as the reservoir from which a gas flows through a supersonic nozzle. This conclusion was based on data compiled from high-speed filming of Töpler disturbance patterns in a gas flow during shock wave reflection from a wall having a small aperture leading into a divergent channel, *i.e.*, a supersonic nozzle. A thorough analysis of the Töpler photographs indicated that a certain time interval exists in which a complex nonstationary flow is observed in the reservoir and nozzle and a quasi-stationary flow from the reservoir to the supersonic nozzle is established behind this flow.

In the present work, the flow of a thermally dissociated gas in a supersonic nozzle is investigated. For this, operating conditions of the shock tube were selected which ensured obtainment of a sufficiently high degree of gas dissociation behind the reflected shock wave. The parameters behind the reflected shock wave were calculated according to the laws of conservation, including high-temperature gas thermodynamics, based on the measured velocity of the incident shock wave and the initial pressure and temperature of the gas.

Two nozzle configurations were used in the experiments: (1) a flat, straight-walled nozzle; this nozzle has two parallel walls and two walls which form a convergent channel, a short portion with a constant cross section, and a divergent channel; the critical cross section has the shape of a slit (width, 1.9 mm); the walls of the divergent channel are straight and diverge at an angle of 20° ; (2) axisymmetric nozzles; in these, the radius distribution of the cross section is along the axis in the supersonic portion according to hyperbolic law; there is a full 20° angle between asymptotes; the critical cross sections are 10.44 and 5.67 mm, and the exit cross sections are 47.7 and 35.8 mm, respectively; the lengths from the critical to the exit cross sections are 135 and 105 mm.

The use of axisymmetric nozzles having such a profile permitted us to effect a smooth transition from the critical to the exit cross section of the nozzle. In addition, the nozzle's fabrication and installation in the operating portion of the setup were simplified.

The parameters of the flow and the state of the gas flowing from the nozzle at supersonic velocity were determined from an analysis of the pattern of flow around models of various shapes. For this purpose, we used the method described earlier [1]: *i.e.*, high-speed frame photography of disturbances visualized with the aid of a Töpler device. In most of the experiments, a wedge placed asymmetrically at 6° served as the model. One of its sides was set in the plane of symmetry of the flow at the nozzle cutoff. A weak disturbance appeared from the direction of this side. Its direction was identified with the direction of

the Mach line. Besides the wedge, in some experiments a hemisphere and a cylinder with the generatrix across the flow were installed at the nozzle cutoff. /159

The angles of inclination of the weak disturbance were measured either on photographic film (with an instrument microscope) or on impressions. The main error during angle measurement was caused by diffusion of the wave image on the wedge. The angles on each frame of a series of photographs taken in a separate experiment were measured three or four times. The average time-stabilized value (according to measurement on several frames) of the angle of inclination of the waves was a result of the experiment. Photographs on which drift distance of the shock wave was fixed in front of blunt models were processed in a completely similar fashion.

The supersonic exit of a dissociated gas through a nozzle placed at the end of a shock tube is very complex.

For an exact description of the flow pattern and calculation of the flow parameters in the nozzle, it is necessary to consider the nozzle configuration, the final velocity of dissociation and recombination of molecules, heat transfer and friction at the nozzle walls, and other processes.

The following simplified flow pattern was examined to analyze the qualitative flow picture and to compare the data obtained from determination of the M number of the flow at the nozzle cutoff with the calculated data.

Significant recombination of gas molecules occurs in the process of flow of the dissociated gas from the region behind the reflected shock wave through the nozzle. A redistribution of energy also occurs between the internal degrees of freedom. This leads to heat release in the gas volume.

From the number of possible processes of gas expansion, it is natural to examine the simplest (isentropic) flow. We shall assume, therefore, that the processes indicated (recombination and energy exchange between internal degrees of freedom) occur so quickly that local thermodynamic equilibrium is achieved. Thus, a shift of chemical equilibrium takes place in the process of gas outflow, and the gas enthalpy is determined so that it includes the heat of the chemical reaction.

For simplicity, a one-dimensional flow is examined.

Taking what has been said into account, the following system of equations is used for calculation of the flow parameters.

1. The isentropic equation is

$$S_0 = \frac{S}{\mu} = \frac{\sum_i S_i X_i}{\sum_i \mu_i X_i} = \frac{\sum_i (S_{i0} - R \ln p X_i) X_i}{\sum_i \mu_i X_i},$$

where S_0 is the entropy of a unit mass of gas; S is the entropy of one mole of

gas mixture; S_i is the entropy of one mole of the mixture component; X_i are molecular fractions of the mixture components; μ_i are molecular weights of the mixture components; p is the total pressure of the mixture.

Taking $S_0 = \text{const}$ into account and excluding p by the law of effective mass, the expression can be viewed as an isentropic equation for a dissociated gas in temperature variables T and degrees of dissociation α .

The isentropic equation appears as

$$f_1 \frac{2\alpha}{1+\alpha} + R \frac{2}{1+\alpha} \ln \frac{2\alpha}{1-\alpha} + f_2 = 0,$$

where

$$\begin{aligned} f_1 &= f_1(T) = (S_2 - S_1) + S_0(\mu_1 - \mu_2); \\ f_2 &= f_2(T) = S_1 - S_0\mu_1 - R \ln K_p. \end{aligned}$$

Here, $S_1(T)$ is the molar entropy of the molecular component; $S_2(T)$ is the 160 molar entropy of the atomic component of the gas; and K_p is the equilibrium constant of the dissociation reaction. K_p and the enthalpies H_1 and H_2 , which are necessary for the calculation of S_1 and S_2 , were taken from the tables in [2].

Assigning the temperature, we arrive at the coefficients f_1 and f_2 , and then we solve the transcendental isentropic equation with respect to α with the Newton-Raphson method.

2. For this temperature, we find the gas pressure with the law of effective mass

$$p = \frac{1-\alpha^2}{\alpha^2} \frac{K_p}{4}.$$

3. The gas density is determined from the equation of state of a dissociated gas

$$p = \rho(1+\alpha) \frac{R}{\mu_1} T.$$

4. The specific enthalpy of the mixture is calculated according to the values of molar enthalpy of the components for the given temperature and the degree of dissociation which has been found

$$h = \frac{1}{\mu_1} [H_1(1+\alpha) + 2\alpha H_2],$$

where H_1 is the molar enthalpy of the molecular component and H_2 is the molar enthalpy of the atomic component.

5. We use the energy equation $h_0 = h + u^2/2$. This permits us to calculate the velocity of the gas flow u according to the value of the specific enthalpy at a state of rest of the gas and with enthalpy corresponding to the selected temperature.

6. To transfer to the Mach number of the flow which is an experimentally determined value, it is necessary to calculate the velocity of sound for that particular local gas state. The velocity of sound was calculated on the supposition that translational and rotational degrees of molecular freedom are excited in the sound wave, and that vibration excitation and changes in the gas's chemical composition do not take place. Such a supposition corresponds to contemporary theoretical concepts concerning the propagation of disturbances in reacting media [3-6] and is confirmed in experimental studies [7-8].

In agreement with [4], we established in our experiments that a weak disturbance in the gas going from the peak of the wedge is determined by the frozen velocity of sound, which is calculated from the relationship

$$a = \sqrt{\Gamma \frac{p}{\rho}}.$$

Here, Γ is a coefficient whose value for the given degree of dissociation of the diatomic gas is determined in accordance with [9] with the formula

$$\Gamma = 1 + \frac{2Z}{\mu \sum_i (m_i D_i / M_i)},$$

where $Z = p/R\rho T$ is a coefficient in the equation of state which is determined by the gas state; μ is the molecular weight of the gas in the absence of dissociation; m_i is a molar fraction of the i -th component; D_i is the number of degrees of molecular freedom of the i -th component; and M_i is its molecular weight.

Knowing the velocity of sound and the velocity of flow, we determine the Mach number $M = u/a$.

Performing these operations for successive temperature values in the direction of a decrease from its original value in the reservoir, we arrive at the relationship between the Mach number, gas density and flow velocity. We determine the critical values of density ρ_{cr} and gas velocity u_{cr} from these relationships, using the conditions $M = M_{cr} = 1$. Further, we use the discontinuity equation $\rho_{cr} u_{cr}^F = \rho u^F$ to establish the dependence of the flow parameters

/161

determined earlier (particularly the Mach number $M = M(A)$) on the dimensionless area of the nozzle $A = F/F_{cr}$.

As a result of this calculation, all of the flow parameters (pressure, density, temperature, velocity, degree of dissociation, and specific enthalpy) proved to be related to the value of the nozzle's dimensionless area.

We calculated the isentropic expansion of oxygen in quasi one-dimensional approximation from the region behind the reflected shock wave in the shock tube by this method. These conditions were in turn calculated with the laws of conservation according to the initial values of temperature and gas pressure in the shock tube, and according to the shock wave velocity as measured by ionization transducers.

Similar results of calculation of the equilibrium expansion of nitrogen and carbon dioxide in nozzles are achieved by a somewhat different method, *i.e.*, by graphic integration of the motion equation:

$$u (du/dx) = - (1/\rho) (dp/dx),$$

which gives us the dependence of flow velocity on pressure

$$(1/2) u^2 = - \int_{p_0}^p (1/\rho) dp.$$

The relationship between density ρ and pressure p , which is necessary for integration, was arrived at in advance from thermodynamic parameter tables for the corresponding gases with constant entropy established by conditions in the reservoir. Data for nitrogen were taken from tables compiled in the ENIN laboratory for high-temperature gas dynamics and thermodynamics, and from [10] for carbon dioxide. The lower limit of integration was determined by the pressure in the reservoir; the upper limit is variable. The motion equation was integrated to a pressure in the exit section of the nozzle which was of practical interest. The relationship between the chemical composition of the gas and pressure was established by the same tables. Knowledge of the chemical composition is necessary to calculate the velocity of sound according to the above-indicated method. The dependence of the Mach number on pressure, and hence on gas density and flow velocity, was determined according to the flow velocity and the velocity of sound. Further, just as in the previous case, the critical values of gas density and velocity were determined, and the distribution of the Mach number as a function of the dimensionless area of the nozzle was found by applying the discontinuity equation.

Figures 1, 2 and 3 illustrate the dependence of M , the Mach number of the flow, on A , the dimensionless area of the nozzle for oxygen, carbon dioxide, and nitrogen. Experimental data are given on the measurement of the Mach number in the flow at the nozzle cutoff. They are shown above the calculated curve. To illustrate the results of calculating the isentropic expansion of a dissociated

gas, the variational behavior of the thermodynamic parameters of the gas (p , ρ , T), the flow velocity u , and the degree of dissociation α is shown in Figures 4 and 5 as a function of the dimensionless area.

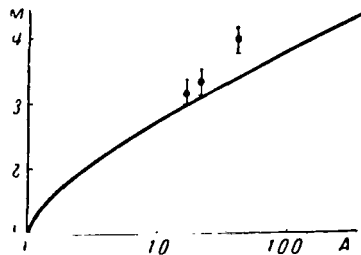


Figure 1. Dependence of M on A for Equilibrium Isentropic Expansion of Oxygen. $T_0 = 4,400^\circ\text{K}$; $p_0 = 10.3 \text{ atm}$; $\alpha = 43.6\%$.

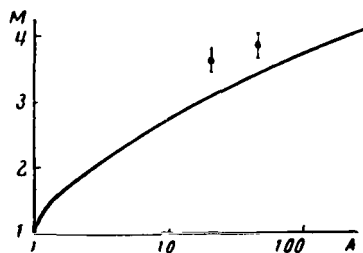


Figure 2. Dependence of M on A for Equilibrium Isentropic Expansion of Carbon Dioxide. $T_0 = 3,600^\circ\text{K}$; $p_0 = 32 \text{ atm}$; $\alpha \approx 50\%$.

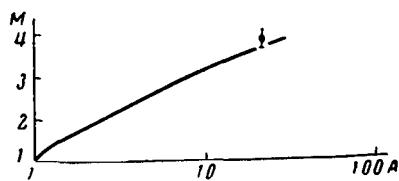


Figure 3. Dependence of M on A for Equilibrium Isentropic Expansion of Nitrogen. $T_0 = 6,100^\circ\text{K}$; $p_0 = 2.8 \text{ atm}$; $\alpha \approx 9\%$.

An interpretation of the results of an experimental determination of the M number of the flow and the magnitude of shock drift from a streamlined body is given below.

It is first necessary to estimate the possible calculation errors within the limits of the assumption which we made concerning the isentropic nature of the flow.

Errors are possible because of inaccuracy in determining the gas parameters in the reservoir, i.e., the state of the gas behind the reflected shock wave. Three sources of errors can be indicated.

1. Experiments with O_2 , N_2 , and CO_2 indicate that the velocity of the reflected wave with respect to a tube with a completely closed end is an average of 10% less than the calculated value by virtue of certain losses, including heat losses in the wall, which are a small fraction of the total losses, as experiments [11] have indicated.

2. Another source of error is the inaccuracy in determining the initial temperature and gas pressure in the expansion chamber, and mainly the velocity of the shock wave. This velocity could reach $\pm 5\%$ in the present experiments.

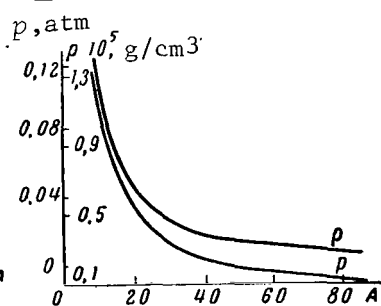


Figure 4. Dependence of ρ and p on A for Equilibrium Isentropic Expansion of Oxygen. Stagnation Parameters are Given in the Caption to Figure 1.

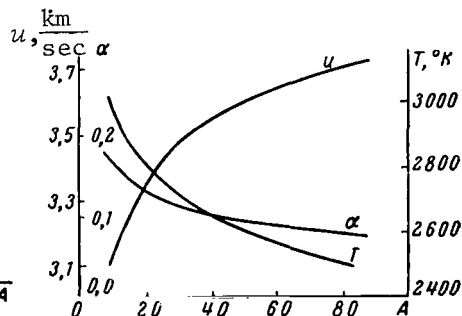


Figure 5. Dependence of T , α and u on A for Equilibrium Isentropic Expansion of Oxygen. Stagnation Parameters are Given in the Caption to Figure 1.

3. The third source of error is the inaccuracy in determining the parameters of the gas behind the shock wave when its flow through the nozzle is not taken into account as was done in the original calculations. Allowance for the gas flow rate through the nozzles used in the experiments should lead to a decrease in the reflected wave velocity of not more than 4% with respect to the wall.

We viewed the decrease in the reflected shock wave velocity as a decrease /163 in the shock wave intensity caused by losses and leakage of the gas through the nozzle; it must lead to a decrease in parameters, including the enthalpy and entropy of the gas behind the reflected shock wave.

The error in determining the shock wave velocity can be positive or negative. Therefore, the error in determining the enthalpy or entropy can also be either.

A computation of the change in entropy and enthalpy of the gas behind the reflected shock wave as a result of the causes indicated demonstrates that by virtue of a $\pm 5\%$ error in the determination of the shock wave velocity, an increase in entropy and enthalpy of approximately 10% is possible as compared to the adopted values of these magnitudes; and due to the three causes indicated, a decrease in these parameters by approximately 15% is possible.

A determination of the inaccuracy of measuring the parameters of the gas behind a reflected wave permitted us (assuming a one-dimensional isentropic flow) to estimate the variation of flow parameters and the M number at the nozzle exit. Calculations for oxygen indicated that the values of the M number of the flow can be 5-7% greater than the values cited above, and 1-2% less.

On the basis of the error estimates of the calculated values of the M number of the flow for oxygen, it should be mentioned that the experimental values for small area ratios lie approximately on the upper boundary of the calculated values, while the experimental value of M noticeably exceeds the calculated value for the maximum area ratio. It is advisable to estimate the errors in the calculated M number of the flow in dependence on ratio of areas related to a certain nonisentropic nature of flow caused by heat exchange and friction at the nozzle walls.

For the Reynolds numbers of the flows at the nozzle exit, $Re_d = 5 \cdot 10^3 - 10^4$, the flow has two regions: the main nucleus of the flow, where the parameters are uniform along the nozzle cross section, and a thin boundary layer at the nozzle walls, where dissipation processes take place. The presence of the boundary layer is equivalent to a slight decrease in the cross-sectional area of the nozzle.

A correction in the cross-sectional area of the nozzle, determined by the boundary layer, would lead to a shift of the experimental points relative to the calculated curves. The divergence with the results of the calculation, assuming an equilibrium character of expansion, increases somewhat. We also should indicate one more possible error in determining the M number of the flow at the nozzle exit, which is related to a serious assumption concerning the flow's

one-dimensional character, taking the above-indicated nozzle configuration into account.

Since the nozzle generatrices on a significant portion toward the nozzle exit had an angle of 20° , there was a nonuniform field of flow with respect to all parameters, including the direction and magnitude of the velocity of gas particles, at the nozzle exit where the peak of the wedge was located. In other words, a divergent gas flow flowed around the peak of the wedge. A weak disturbance occurring at the peak of the wedge propagated in the nonuniform field of flow. In proportion to its distance from the wedge, the disturbance propagated in a region of high flow velocities and large deflections of the streamlines from the axial line. These two factors changed the inclination of the line of propagation of the weak disturbance on opposite sides from the direction of the nozzle axis, and they compensated each other to a certain extent. Töpler photographs of the pattern of flow around the wedge indicated that both the line of weak disturbance along one side of the wedge and the line corresponding to the shock wave along the other side of the wedge hardly differed from the straight lines in the field of vision enveloping almost all of the flow's cross section. /164 Thus, the direction of the line of weak disturbance at the wedge peak was preserved. Furthermore, this made it possible for us to measure the angle between the wedge plane and the direction of the entire line of weak disturbance that we observed during measurement of the direction of the line of weak disturbance in relation to the center line of flow coincident with the direction of one of the wedge planes.

Henceforth, we shall bear in mind that stricter allowance for nonuniformity of the flow should be given.

Conclusion

1. Preliminary experiments concerned with the investigation of the flow of dissociated gases (O_2 , N_2 , CO_2) through supersonic nozzles in a shock tube having a nozzle were conducted.

2. Experimental values of the M number of the flow for various ratios of the areas of the exit section to the critical section were derived by a method of visualization of the flow around a half-wedge placed at the nozzle cutoff.

3. The M numbers of the flow from the experiment were compared with calculated values on the simplest hypothesis of equilibrium isentropic gas flow without taking into account the viscosity and heat conductivity of the gas and heat losses in the nozzle wall.

4. In the above-mentioned flow regimes, a noticeable deflection from the isentropic flow is observed for oxygen and carbon dioxide.

5. Approximate estimates of errors were made in calculating the isentropic flow by virtue of the inaccuracy in determining the gas parameters in the reservoir and deviations from the isentropic nature due to heat exchange and friction at the nozzle walls.

Taking the corrections for oxygen into account does not make it possible to coordinate the calculated and experimental values of the M number, which are much higher than the rated values. This qualitatively indicates the possibility of deviation of the flow from equilibrium at the nozzle exit.

REFERENCES

1. Ionov, V. P., G. N. Nikolayev, M. V. Gusev and O. I. Luneva: Use of the Töpler method and high-speed photography in a study of gas flows in a shock tube. In: *Fizicheskaya gazodinamika i svoystva gazov pri vysokikh temperaturakh*. (Physical Gas Dynamics and the Properties of Gases at High Temperatures.) Moscow, Izd-vo "Nauka", 1964.
2. Rozhdestvenskiy, I. B. and Ye. V. Samuylov: Thermodynamic functions of N_2 , O_2 , N , O , N_2^+ , O_2^+ , N^+ , and O^+ and equilibrium constants of dissociation and ionization reactions of oxygen and nitrogen (for temperatures from 300 to 6,000°K). In: *Fizicheskaya gazodinamika, teploobmen i termodinamika gazov vysokikh temperatur*. (Physical Gas Dynamics, Heat Exchange and Thermodynamics of High-Temperature Gases.) Izd-vo AN SSSR, 1962.
3. Spence, D. A.: Nonstationary propagation of a shock wave in a relaxing gas. *Mekhanika*, No. 6, 1962.
4. Stakhanov, I. P. and Ye. V. Stupochenko: The structure of Mach lines in relaxing media. *Doklady AN SSSR*, Vol. 134, No. 5, 1960.
5. Wood, V. V. and F. R. Parker: The structure of a centered rarefaction wave in a relaxing gas. *Mekhanika*, No. 6, 1962.
6. Moor, F. K. and W. E. Gibson: Propagation of weak disturbances in a gas subject to relaxation effects. *J. Aero/Space Sci.*, Vol. 27, No. 2, 1960.
7. Weigner, P. P.: Survey of studies on steady supersonic flow in a nozzle during reactions in a gas mixture. *Voprosy Raketnoy Tekhniki*, No. 4, 1963.
8. Wilson, J.: An experiment to measure the recombination rate of oxygen. *J. Fluid Mech.*, Vol. 15, No. 4, 1963.
9. Geiger, R.: On the frozen flow of dissociated gas. *J. Aero/Space Sci.*, Vol. 29, No. 12, 1962.
10. Zaytsev, S. G.: *Eksperimental'noye issledovaniye vosplamneniya gazovoy smesi v udarnoy trube*. (Experimental Study of Gas Mixture Combustion in a Shock Tube.) Candidate's Dissertation, MGU, 1959.
11. Bazhenova, T. V., O. A. Predvoditeleva and T. V. Nadezhina: Losses during reflection of shock waves from the end of a shock tube. In: *Fizicheskaya gazodinamika i svoystva gazov pri vysokikh temperaturakh*. (Physical Gas Dynamics and the Properties of Gases at High Temperatures.) Moscow, Izd-vo "Nauka", 1964.

CALCULATION OF THE RECOMBINATION RATE CONSTANTS OF
DIATOMIC GASES ACCORDING TO THE MACH NUMBER OF
THE FLOW AT THE EXIT OF A SUPERSONIC NOZZLE

G. N. Nikolayev

The intensive study of gas dynamics at high temperatures that has been going on recently has raised the question concerning the effect of finite dissociation rate and atomic recombination, vibrational excitation, ionization and other intramolecular processes on the properties of supersonic flows with particular acuity. The incompleteness of these processes leads to a gas state which is characterized by nonequilibrium values of its thermodynamic parameters and component concentrations. In particular, scale effects appear which are related to the correlation of streamlined body sizes and the extent of nonequilibrium flow regions.

An important part of the problems which arise in connection with this is an experimental determination of the recombination rate constants of diatomic gases in temperature and pressure ranges which are of practical importance. Most of the data concerning this problem is derived from experiments which make it possible to determine the dissociation rate constant k_D . The most widely used method of determining k_D is based on recording the density profile or concentration of the reacting component in the nonequilibrium zone behind the shock wave in a shock tube. The recombination constant k_R is calculated on the basis of these data with the thermodynamic equilibrium constant $K = k_D/k_R$, which depends on temperature [1].

In the study of recombination kinetics, the use of processes for this purpose in which recombination plays a predominating role is a qualitatively different approach. One of such processes is the expansion of a thermally dissociated gas in a supersonic nozzle. It follows from the experimental data of [2-5] that the expansion of a dissociated gas in supersonic nozzles experiences the effect of a finite recombination rate. It is of interest to analyze the possibility of calculating the recombination rate constants by measuring any parameter of the flow leaving the supersonic nozzle, *e.g.*, the Mach number.

To analyze dissociated gas flows in the nozzles, we used an approximate method of examining nonequilibrium flows (the method of "sudden freezing" of the chemical composition of the gas).

A number of theoretical works published [6-8] contain the foundation for the following assertion. Conditions arise in the nozzles during rapid expansion of the gas, wherein as a consequence of the finite chemical reaction recombination rate, the composition of the gas deviates from equilibrium. The degree of dissociation becomes excessive and does not correspond to the temperature and pressure in the flow. If the expansion process at a certain stage began to deviate noticeably from equilibrium, further change of the chemical composition

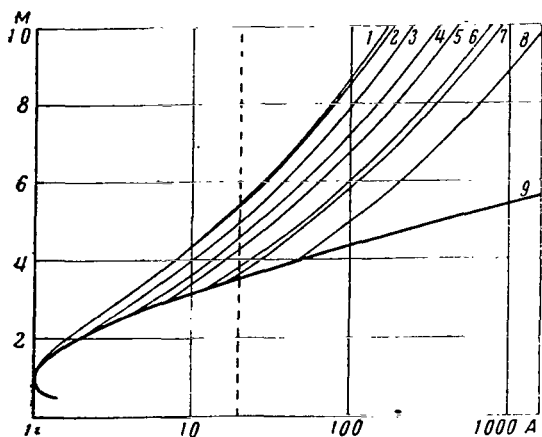


Figure 1. Dependence of M on A when $p_0 = 20$ atm; $T_0 = 8,500^\circ\text{K}$; $\alpha = 0.46$. Nitrogen. (1) $k_R = 0.0$; (2) $2.1 \cdot 10^{-14}$; (3) $2.2 \cdot 10^{15}$; (4) $2.2 \cdot 10^{16}$; (5) $1.4 \cdot 10^{17}$; (6) $3.8 \cdot 10^{18}$; (7) $1.5 \cdot 10^{19}$; (8) $1.3 \cdot 10^{20}$; (9) ∞ .

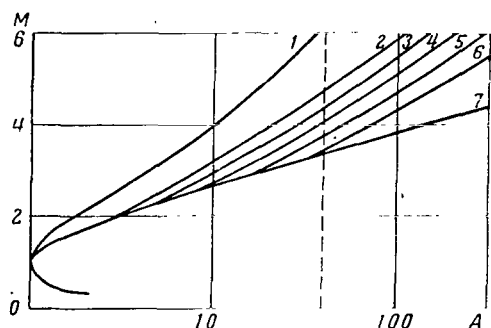


Figure 2. Dependence of M on A when $p_0 = 7$ atm; $T_0 = 4,200^\circ\text{K}$. Oxygen. (1) $k_R = 0.0$; (2) $4.7 \cdot 10^{15}$; (3) $2.7 \cdot 10^{16}$; (4) $7.6 \cdot 10^{16}$; (5) $2.4 \cdot 10^{17}$; (6) $2.0 \cdot 10^{18}$; (7) ∞ .

flow from thermodynamic equilibrium [6, 11]. We made a series of calculations on the change of the Mach number M as a function of the dimensionless area of the nozzle A (the ratio of the area of the given cross section to the area of the critical cross section). The calculations were performed in a one-dimensional approximation for the expansion of pure oxygen and nitrogen flowing from the reservoir, the selected gas parameters in which being attainable behind the

of the gas occurs so slowly that the degree of dissociation can be considered /166 as constant to whatever degree the flow might be expanded further. This result is reached by a numerical solution to a system of equations describing the flow of a gas in a quasi one-dimensional approximation, taking the finite recombination rate into account. An approximate method based on [6-8] is offered to calculate a nonequilibrium flow in which the flow is viewed as consisting of two sections, *i.e.*, the initial section, where chemical equilibrium is maintained completely, and the section adjoining it, where the gas composition does not change (is "frozen"). Calculation of the flow in the second section is simplified significantly since the chemical composition is constant. The position of the transition point from equilibrium to "frozen" flow can be calculated on the basis of the given recombination rate constant and, conversely, it is possible to calculate the rate constant by knowing

where the "freezing" occurred. A comparison of exact and approximate solutions in the quasi one-dimensional approximation for the nonequilibrium flow of dissociated gases (oxygen and hydrogen) cited in references [4, 9] revealed a very close similarity of results obtained by both methods. The regularity of this similarity is confirmed by the fact that the entropy change determined by the recombination nonequilibrium of the diatomic gas is extremely small [10]. What has been stated is the basis for using an approximate method to estimate the recombination rate constant of diatomic gases (oxygen and nitrogen) since existing experimental data concerning this constant differ significantly, and such data are very scarce for nitrogen.

The Mach number M is one of the parameters sensitive to the deviation of the

reflected shock wave in the shock tube. The one-dimensional approximation is widely used in gas-dynamic calculations. It is sufficiently accurate to describe the flow in conical nozzles with small (10-20°) aperture angles. The results of the calculations are illustrated by similar curve sets in Figures 1 and 2 for nitrogen and oxygen. The parameters of the gases in the reservoir are indicated in the captions to the figures. In Figures 1 and 2, the lower curves correspond to completely equilibrium gas expansion; curves 1 correspond to the unchanged chemical composition from the very beginning of expansion, *i.e.*, to a completely frozen flow. All of the remaining branches from the equilibrium curve were computed under the assumption that the degree of dissociation is constant, beginning from the branch point which corresponds to one cross section or another in which the sudden freezing of the chemical composition of the gas took place. The equilibrium flow curve was calculated for one-dimensional steady expansion under the supposition that the process was adiabatic with constant entropy. The equation of motion was graphically integrated; the dependence of density on pressure in the equation was taken from the thermodynamic property tables for oxygen and nitrogen* with constant entropy established by the gas state in the outflow reservoir. Distribution of the Mach number as a function of the dimensionless cross section of the nozzle was calculated according to the flow velocity derived from the equation of motion, and on the basis of the frozen velocity of sound with the aid of the discontinuity equation. The branches corresponding to frozen dissociation were calculated with an equation that relates the cross-sectional area of the flow to the Mach number for flows with a constant specific heat ratio γ . The latter was calculated assuming a constant composition of the atomic and molecular component mixture; the molecules were ascribed a full excited state of vibrational degrees of freedom. Each branch of the set corresponds to a determined value of the recombination rate constant k_R . The k_R values indicated in Figures 1 and 2 correspond to the hyperbolic law of distribution of the nozzle cross-sectional area (axisymmetric shape)

$$A' = A'_{cr} + K_N^2 x'^2,$$

where x' is the coordinate read off along the nozzle axis downstream from the critical cross section (values having physical nonuniformity denoted by primes); A'_{cr} is the area of the critical cross section and K_N is the constant.

If we selected a definite nozzle length, *i.e.*, fix a certain quantity for the cross section, then the Mach number (and correspondingly the Mach angle ϵ) in that section of flow is simply related to the value of the recombination rate constant. Figures 3 and 4 illustrate the results of an analysis of curve sets; Figures 1 and 2 are for nitrogen and oxygen. The circles on these figures designate calculated points whose scatter in relation to the corresponding curves is determined by error computations. It is possible to calculate other flow parameters similarly, *e.g.*, static pressure, and also to relate them to the recombination constant.

We conclude from the graphs in Figures 3 and 4 that the considered nozzles

*The thermodynamic tables used for oxygen were compiled at the ENIN Laboratory for High-Temperature Gas Dynamics and Thermodynamics.

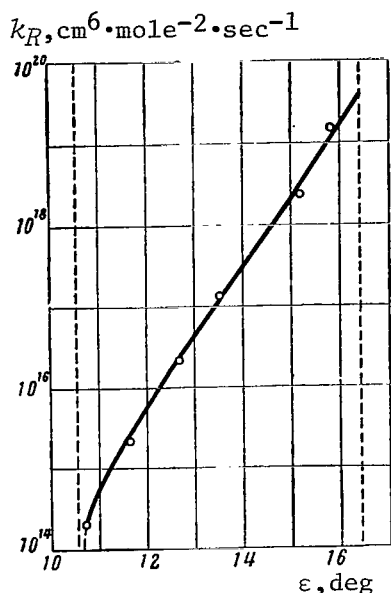


Figure 3. Relationship Between ϵ and k_R for Nitrogen when $A = 20$. Stagnation Parameters Indicated in the Caption to Figure 1.

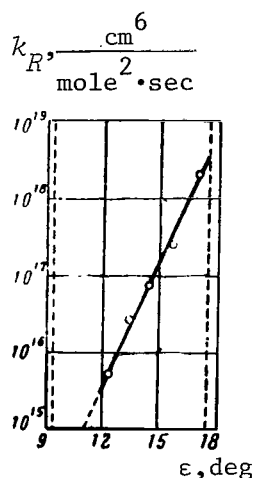


Figure 4. Relationship Between ϵ and k_R for Oxygen when $A = 40$. Stagnation Parameters Indicated in the Caption to Figure 2.

are suitable to determine the recombination rate constant within several (sufficiently wide) limits of its values. They correspond to the curve section at a distance from the maximal possible Mach number value for the given nozzle (which corresponds to a frozen flow). A comparison of similar curves for nozzles with various lengths indicates that the increase in the degree of expansion ensured by the nozzle expands the limits of the k_R values in which it is possible to determine these constants experimentally.

It should be noted that, in accordance with the supposition concerning the sudden freezing of the chemical composition of the gas in a definite nozzle cross section, the value of the recombination constant thus obtained refers to the static flow temperature in the frozen cross section.

Using nozzles with various angles between the hyperbolic asymptotes which determine the law of change of the cross-sectional area along the axis, it is possible to ensure dissociation freezing at different degrees of expansion, *i.e.*, at different temperatures [6]. Thus, by experimenting with various nozzles, it is possible to attempt to obtain information concerning the temperature dependence of the recombination rate constant. It should be noted that when processing the experimental data, it is necessary to take into account the displacement thickness of the boundary layer, which constricts the effective nozzle cross section.

All which has been stated has referred to one combination of gas parameters in the reservoir. Variation of the conditions in the reservoir expands the possibilities for an experimental determination of k_R .

Conclusion

A calculation based on the supposition concerning the sudden freezing of the chemical state of a gas was performed in a quasi-one-dimensional adiabatic approximation of the nonequilibrium expansion of partially dissociated oxygen and nitrogen in a supersonic nozzle.

The relationship between the recombination rate constant of the gas and the distribution of the Mach number along the nozzle length with a change of the nozzle cross-sectional area was analyzed using the hyperbolic law. The expediency of applying the given method of calculation was

demonstrated for determining the recombination rate constant of a dissociated diatomic gas with respect to the measured values of the Mach number of the flow leaving a supersonic nozzle. /169

REFERENCES

1. Rey, K. L.: Chemical kinetics of air at high temperature. In: *Issledovaniye giperzvukovykh techeniy*. (An Investigation of Hypersonic Flows.) Ed. by F. R. Riddel. [Trans. from Eng.] Moscow, Izd-vo "Mir", 1964.
2. Nagamatsu, G. T., J. Workman and R. E. Sheer: Hypersonic expansion of air in nozzles, accompanied by atomic recombination. *Voprosy Raketnoy Tekhniki*, No. 6, 1962.
3. Weigner, P. P.: A survey of investigations on steady supersonic flow in a nozzle during reactions in a gas mixture. *Voprosy Raketnoy Tekhniki*, No. 4, 1963.
4. Vidavskiy, A., R. Oswald and J. L. Harp: Experimental determination of the recombination rate of hydrogen. *Voprosy Raketnoy Tekhniki*, No. 12, 1962.
5. Ionov, V. P. and G. N. Nikolayev: Experimental investigation of dissociated gas outflow through supersonic nozzles. *Infra*, 1963.
6. Bray, K. N.: Atomic recombination in hypersonic wind tunnel nozzles. In: *Gazodinamika i teploobmen pri nalichii khimicheskikh reaktsiy*. (Gas Dynamics and Heat Exchange during Chemical Reactions.) Moscow, IL, 1961.
7. Bray, K. N.: Simplified method of "sudden freezing" in the investigation of a nonequilibrium flow in a nozzle. *Voprosy Raketnoy Tekhniki*, No. 6, 1961.
8. Hall, J. G. and A. L. Russo: Studies of chemical nonequilibrium in hypersonic nozzle flows. *Proc. First Conf. on Kinetics, Equilibria and Performance of High-temperature Systems*. London, Butterworths, 1960.
9. Lordi, J.: Comparison of exact and approximate solutions for nonequilibrium nozzle flows. *Voprosy Raketnoy Tekhniki*, No. 8, 1962.
10. Eshenreder, A. K.: Entropy changes in nonequilibrium flows. *Mekhanika*, No. 5, 1964.
11. Logan, J. G.: Relaxation phenomena in hypersonic aerodynamics. *Mekhanika*, No. 1, 1959.

MEASUREMENT OF CARBON DIOXIDE DENSITY IN THE FLOW BEHIND A SHOCK FRONT

S. G. Zaytsev and Ye. V. Lazareva

Experimental investigation of the flow parameters of carbon dioxide behind the shock front in a shock tube leads to varying data relative to the excitation time of an asymmetric valent vibration ν_3 of a CO_2 molecule. Density measurement by the interferometer method cited in [1] demonstrates that the vibration excitation time ν_3 of a CO_2 molecule at temperatures of 1,800-2,200° does not exceed 2-3 μsec . The authors of [2] arrive at a contrary conclusion. Using the same technique, they found that the time indicated exceeds 100 μsec . However, an analysis of the density measurement technique and a comparison of results cited in [1-3] and in the present study do not permit us to explain the data presented in [2].

In another group of studies, carbon dioxide behind the shock front was investigated by recording the gas-dynamic characteristics of the flow, *i.e.*, Mach line orientation [4] and speed of the reflected shock wave [5]. The authors compared the measured values with the calculated values obtained by relaxation gas dynamics methods under various assumptions relating to the thermodynamic parameters of the flow. The results of this group of studies led to the conclusion that ν_3 vibrations are not excited over a period of 100 μsec in the flow of carbon dioxide behind the shock front where $T \geq 2,000^\circ\text{K}$.

In the present work, we experimented with carbon dioxide containing an admixture of less than 0.6% (mainly oxygen and nitrogen). The results obtained were in the M_s range between 2 and 8. In the region of $M_s < 6$, the measured density values coincided with those obtained in the previous study [3]. The accuracy in determining density at the shock front is 2%. The error in determining the M_s number does not exceed 0.1.

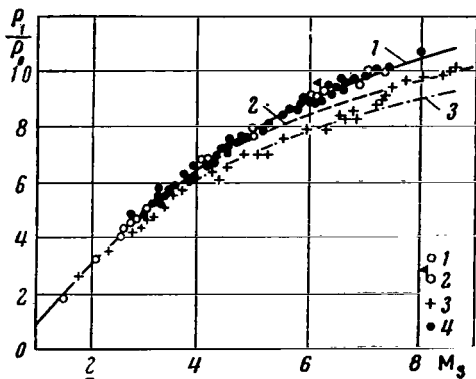


Figure 1. Density Behind Incident Shock Wave.

The density in the flow behind the shock front, which propagates from $M_s < 3$, increases and reaches a value corresponding to complete thermodynamic equilibrium. This process is caused by the excitation time lag of the deformed ν_2 vibrations of the CO_2 molecule. The measured values of excitation time correspond with those observed earlier (*e.g.*, see [6]). For shock waves from $M_s > 3$, the indicated increase in density was not observed within the limits of the procedure's resolving power

($\sim 2 \mu\text{sec}$). The measured density values directly behind the shock front (ρ_1^*) correspond to the average density value in the flow (ρ_1). The figure illustrates the values of ρ_1^*/ρ_0 derived in the present study and the previous one [3] (points 4), (ρ_0 is the density in front of the shock front). Curves 1, 2 and 3 correspond to density values calculated behind the shock front which were obtained when solving a system of conservation equations for the shock front under various assumptions relative to the thermodynamic state of the gas. Curve 1 /171 corresponds to complete thermodynamic equilibrium. Curve 3 assumes thermodynamic equilibrium between translational and rotational degrees of freedom and deformed v_2 vibrations of the CO_2 molecules. The v_1 and v_3 vibrations are assumed to be frozen. Curve 2 assumes thermodynamic equilibrium between translational and rotational degrees of freedom and the vibrational levels v_2 and v_1 . The v_3 vibrations are assumed to be frozen. Figure 1 also illustrates the density values behind the shock wave arrived at in references [1] (points 1 and 2) and [2] (points 3).

The comparison of measured and calculated density values permits us to conclude that directly behind the shock front, the density values (accurate to within 2-3%) correspond to the calculated values obtained under the assumption of complete thermodynamic equilibrium.

Interferograms of the flow indicate that density is subject to fluctuations relative to the average value of ρ_1 which will remain constant within an accuracy of 2-3% over the extent of the entire flow from the shock front to the contact surface. The amplitude of the density fluctuations in the flow increases with an increase of the shock front velocity (*cf. infra*).

M_s		3	4	5	6	7	8
$\Delta\rho/\rho_1, 0/0$	1	2	3	4	4	5	

Thus, taking into account the measurement errors and the density fluctuations, the gas density directly behind the shock front and in the flow is grouped around the calculation values which correspond to complete thermodynamic equilibrium. This permits us to conclude that for temperatures near $2,000^\circ\text{K}$, the excitation time of the vibrational level v_3 for a carbon dioxide molecule does not exceed 2-3 μsec .

REFERENCES

1. Zienkiewicz, H., N. Johannesen and J. Gerrard: Further results on the overall density ratios of shock waves in carbon dioxide. *J. Fluid Mech.*, Vol. 17, No. 2, 1963.
2. Griffith, W. C.: *Osnovnyye resul'taty eksperimentov na udarnykh trubakh.* (*Basic Results of Shock Tube Experiments.*) Ed. by A. Ferri. Moscow, Gosatomizdat, 1963.

3. Zaytsev, S. G., Ye. V. Lazareva and A. P. Shatilov: Investigation of normal shock wave reflection in a shock tube. *PMTF*, No. 4, 1964.
4. Bazhenova, T. V. and I. M. Naboko: The problem concerning the rate of physical and chemical transformations of CO₂ molecules behind a shock wave at 2,000-4,000°K. *Doklady AN SSSR*, Vol. 154, No. 1, 1964.
5. Soloukhin, R. I.: Some data on the nonequilibrium state of carbon dioxide behind the front of a shock wave. *PMTF*, No. 1, 1964.
6. Wittman, W.: Vibrational relaxation of carbon dioxide. *J. Chem. Phys.*, Vol. 37, No. 3, 1962.

AN INVESTIGATION OF THE STATE OF A GAS BEHIND A SHOCK WAVE
ON THE BASIS OF THE PATTERN OF FLOW AROUND AN OBSTACLE
PLACED IN A SHOCK TUBE

I. M. Naboko

The content of this article consists of a discussion of the prerequisites /172 and the conditions of experiments and calculations, on the basis of a comparison of the results of which conclusions can be drawn concerning the depth of excitation of gas molecules in the flow behind a shock wave according to the values of the gas-dynamic parameters of this flow. The basic results of the experiments which we conducted to determine the state of carbon dioxide behind a shock wave are given in [1].

Under the high-temperature conditions which are created behind strong shock waves, physical and chemical molecular changes must take place in the gas. In accordance with the achieved temperature, molecular rotation and vibrations should be excited, dissociation and ionization should occur, and the formation of molecules of new compounds may take place in parallel with the destruction of molecules of the original gas. These processes must affect the gas-dynamic parameters of the flow behind the shock wave. Measurement of the gas-dynamic parameters, therefore, can provide information on the degree of excitation of gas molecules. A determination of the degree of molecular excitation on the basis of measuring the gas-dynamic flow parameters obviously is most justified in the shock wave velocity range in which the temperature of the gas behind the wave is high enough for measurements by spectral methods, when the luminescence and absorption intensity are weak. For carbon dioxide, these are the velocities which correspond to Mach wave numbers $M_0 = 6-12$.

The temperatures behind the wave in this range are high enough to lead to noticeable physical and chemical changes in the CO_2 molecules but, at the same time, the molecular excitation occurs comparatively slowly at these temperatures, and it is possible to detect nonequilibrium gas states in the flow by measuring the gas-dynamic parameters of the flow. Several studies have been devoted to a determination of the relaxation time of CO_2 and air on the basis of the velocity of a shock wave reflected from the end of a tube [2,5]. The difficulties involved in measurements based on shock wave reflection are related to the boundary-layer effect in the flow behind the incident shock wave and, in any event, the tendency of this effect must be considered when interpreting the data. The velocity of a shock wave reflected from a model with a flat side placed at the open (divergent) end of a shock tube was determined in [6]; the author avoids the indicated complications by setting up the experiment in this manner.

The flow parameters behind an incident shock wave have also been investigated on the basis of observing the pattern of flow around an obstacle in a shock tube. The angle of inclination of the Mach line [1,7] and the angle of inclination of an oblique shock wave [8] were determined. Measurements of the angle of

inclination of the Mach line (see Figure 1) which separates the region of disturbed and undisturbed flows above a plate with a thin edge are suitable for determining the depth of molecular excitation and dissociation of CO_2 because the size of this angle, which is determined by the ratio of the flow velocity to the velocity of sound, has essentially varying values, depending on the depth of excitation of gas molecules in the flow.

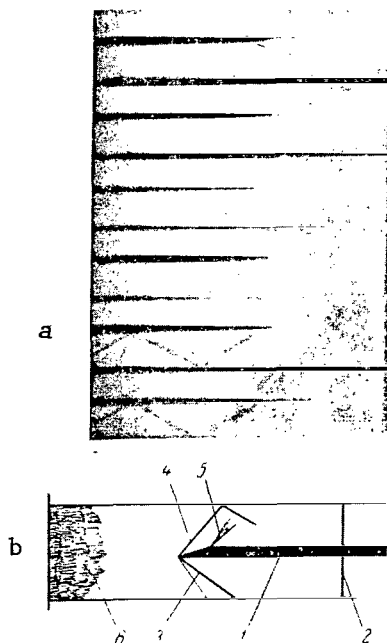


Figure 1. Gas Flow Around an Obstacle in a Shock Tube. (a) Series of consecutive frames of the pattern of flow around an obstacle in a shock tube. The wave moves through the tube from right to left. (b) Diagram of instantaneous pattern of flow: (1) obstacle (half-wedge); (2) shock wave propagating in tube; (3) Mach line; (4) attached shock; (5) rarefaction fan; (6) contact region boundary.

The velocity of the gas flow behind the shock wave (in the laboratory coordinate system) is maximum for a completely equilibrium state behind the wave and differs from the values which correspond to the frozen state by 3-10% for Mach wave numbers 6-11, respectively. We shall say that the state of the gas molecules is completely equilibrium if the excitation of internal degrees of freedom and the molecular dissociation correspond to the translational temperature of the molecules. The frozen state corresponds to equilibrium excitation of molecular rotation and to the absence of any excitation of molecular vibrations and molecular dissociation in the transition through the shock. For a triatomic linear CO_2 molecule, this transition will correspond to a change in the state from the initial temperature to the temperature behind the shock with the heat capacity $C_p = 7/2R$ ($\gamma = C_p/C_v = \text{const} = 1.4$). Partially frozen states are conceivable between these extreme cases for CO_2 molecules which correspond to: (a) the absence of dissociation and complete vibrational excitation; (b) the absence of dissociation and excitation of two vibrational modes which correspond to the vibrational numbers $\omega_1 = 672.2$ and $\omega_2 = 1351.2$; (c) the absence of dissociation and excitation of only one vibrational mode with $\omega_2 = 672.2$, *i.e.*, to a state with only deformation vibrations of CO_2 molecules excited.

The velocity of sound depends on the composition, temperature and state of excitation of internal degrees of freedom of the gas. When a gauge is placed behind the shock wave, the velocity of sound decreases with the approach to equilibrium. The equilibrium velocity of sound a_e , which corresponds to a completely equilibrium molecular state of the flow, differs from the frozen velo-

city of sound in a frozen flow by 15-35% for $M_0 = 6-11$, respectively.

For the velocity of a sound signal in a relaxing medium, it is presently sufficiently accurate to use two conventional values and terms, respectively, for the calculations: the equilibrium, or low-frequency, and the frozen, or high-frequency, velocity of sound. The first corresponds to the value at which sound is propagated at a frequency much less than the frequency of the relaxation processes in the medium; the second corresponds to the velocity of sound at a high frequency in comparison with the relaxation frequency.

In calculating the angle of inclination of the Mach line, the velocity of the flow may refer both to the equilibrium and the frozen velocity of sound, which corresponds to the proposed state in the flow. In accordance with this, the equilibrium and frozen M_1 number can be calculated for the given flow state.

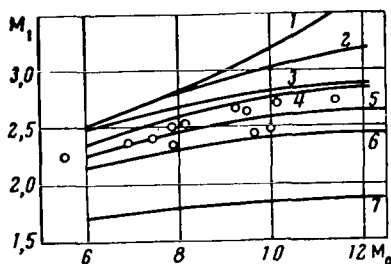


Figure 2. Dependence of M_1 Number on M_0 Under Various Assumptions Concerning the Degree of Excitation of CO_2 Molecules.

The graph in Figure 2 illustrates the possible calculated values of the Mach numbers of the flow. The difference between extreme versions of the calculated values of the Mach numbers amounts to 20-50% for $M_0 = 6-11$. The values of the Mach numbers which correspond to partially frozen states also differ considerably. The dots in Figure 2 denote the M_1 values obtained experimentally in a shock tube. It is obvious that conclusions concerning the state of the flow can be made quite simply only by answering the question of whether the equilibrium or frozen velocity of sound determines the inclination of the Mach line under experimental conditions. It is also obvious that a correct answer to this question requires data on the frequencies which determine the disturbance we observe by the

Schlieren method. Without having accurate data on the frequency spectrum of the originating impulse, we can nevertheless say that on the edge of the wedge there occurs an impulse with a rather deep front, to which there corresponds a wide frequency range. On the other hand, the intensity of this disturbance is not great, since the direction of flow does not change upon transition through the Mach line.

We shall estimate the attenuation of the sound signal with distance on the basis of data available in the literature, assuming, after the authors of [9,10], that the velocity of the disturbance front in the immediate proximity of the obstacle is determined by the high-frequency velocity of sound.

The classical relationship which characterizes the change in wave amplitude in connection with the dissipation of sound energy from heat conductivity and viscosity (according to Kirchhoff and Stokes) gives a value that coincides with the experiment for a low-frequency sound. In carbon dioxide, for frequencies of 60-500 kHz, absorption in the experiment is $1-3 \cdot 10^2$ times greater than can be obtained from calculation with the classical relationship [11]. In Knezer's

studies, the expression for absorption of high-frequency sound is derived with the depth of molecular excitation taken into account in the case of equilibrium displacement in the sound wave. On the basis of Knezer's relationships, the frequency can be obtained which corresponds to the absorption maximum for a gas with a known relaxation frequency of molecular excitation. The attenuation pattern of an ultrasonic signal in a relaxing gas can be thus described by the classical relationship in a region far from the frequencies which coincide with the relaxation frequencies and by Knezer's relationship in the relaxation region.

Relationships which reflect the influence of intramolecular processes on the absorption of sound signals and the analogous relationships of Knezer in this sense were recently obtained directly in reference to the question concerning the propagation of small disturbances and the motion of shock waves in a relaxing gas [9,10,12,13,14].

In order to estimate signal attenuation, which is determined by the inclination of the Mach line under the conditions of our experiment, we shall use the relationship given in [10]:

$$\frac{I}{I_0} = e^{\left(1 - \frac{a_f^2}{a_e^2}\right) \frac{t}{\tau}},$$

where I/I_0 is the signal intensity ratio; τ is the relaxation time; t is the time from the beginning of signal propagation; a_f and a_e are the frozen and /175
equilibrium velocities of sound, respectively. The quantities in this relationship which characterize the attenuation process are included in the ratio a_f^2/a_e^2 which contains, in concise form, the characteristics of the individual peculiarities of the medium and the physical and chemical transformations which take place in the molecules of the medium. The numerical difference between a_f and a_e indicates the intensity of the effect of possible molecular transformations on the thermodynamic parameters of the gas.

Attenuation depends considerably on the relaxation time of the process.

A calculation performed for a specific case for CO_2 indicated the following: with an 8% difference between a_e and a_f (which corresponds to $M_0 \sim 9$) the intensity of the signal decreases twice at a distance of 2 cm if $\tau = 5 \cdot 10^{-6}$ sec; when $\tau = 2 \cdot 10^{-6}$ sec, the signal attenuates five times at the same distance; and $I/I_0 = 0.371 \cdot 10^{-1}$ when $\tau = 1 \cdot 10^{-6}$ sec. The estimate given above bears a tentative character. The proposed relaxation times of the most rapidly excited vibrations of CO_2 correspond to $\sim 3 \cdot 10^{-6}$ sec [15]. Consequently, we may assume with a sufficient basis that at distances $l \leq 2$ cm, the leading edge of the Mach line

is determined by the frozen velocity of sound calculated from $\gamma = 1.4$ (curves 4, 5, and 6 in Figure 2).

The values which we measured experimentally coincide with the calculation performed under the assumption concerning the state in a flow with unexcited asymmetric valent vibrations of CO_2 molecules ($\omega_3 = 2396.4 \text{ cm}^{-1}$) and the frozen velocity of sound (curve 5 in Figure 2).

The time in which a stationary pattern of flow existed and the time in which the inclination of the Mach line corresponded to the calculated values of curve 5 in Figure 2 were determined on the basis of a series of photographs. This observation time Δt^* is converted to the time of existence of the observed state with the relationship

$$\Delta t = \Delta t^* \frac{v_0}{v_0 - u_1},$$

where v_0 is the wave velocity; u_1 is the flow velocity in a stationary (laboratory) coordinate system; Δt^* is the time of observance of the pattern from the beginning of flow; Δt is the time of existence of the corresponding gas layer in a heated state behind the shock wave. By multiplying Δt times the flow velocity in a coordinate system connected to the wave, we obtained the extent of the zone in which the indicated state exists, *i.e.*, the extent of the nonequilibrium zone. In our experiments, a state with unexcited vibrations was observed along the entire gauge, right up to the arrival of the contact surface.

The Mach numbers of the flow which determine the inclination of the Mach line are sensitive to the depth of molecular excitation, as was indicated above, but hardly change with the change of the wave velocity in the investigated M_0 range, which makes it somewhat convenient since it is guaranteed from errors which may be related to inaccuracy in measuring the velocity of the shock wave and the nonstationary character of wave motion in the shock tube.

Measurements of the angles of inclination of oblique shock waves which had occurred on wedges 10 and 16° (Figures 3 and 4) were less suitable for interpretation and evaluation of the flow state. Calculation of the angles of inclination of the oblique shock on a wedge for the same versions of the state of the incident flow and the changes of this state on an oblique shock, as well as in an evaluation of the results with respect to Mach lines, indicated that the values of the angles for a different degree of vibrational excitation differ by 1-2°, which is twice less than the scatter of the experimental values (see Figure 3). Therefore, it is not possible to draw a conclusion in favor of any of these states. The values of the angles of inclination of the oblique shock waves indicate only that dissociation of CO_2 molecules does not noticeably occur in the flow.

As a result of an analysis of the method applied for investigating the state of the flow in the shock tube, it was pointed out that the depth of

/176

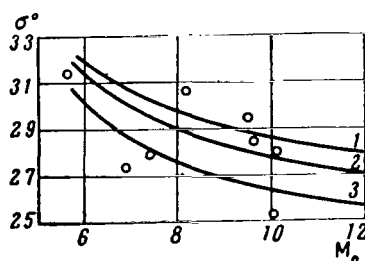


Figure 3. Calculated Dependence of σ on M_0 for Wedge Angle $\theta = 10^\circ$.

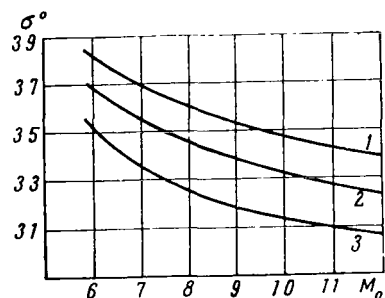


Figure 4. Calculated Dependence of σ on M_0 for Wedge Angle $\theta = 16^\circ$.

discontinuity equation, including the equation of state. On the basis of the known value of gas enthalpy, depending on the temperature, successive approximations can be employed to calculate all parameters of the flow behind the wave if the initial gas state is known. Enthalpy was calculated under the assumption that a CO_2 molecule, being linear, can be considered as a rigid rotator and a harmonic oscillator if excitation, rotation, and vibrations are taken into account [16].

Under this assumption:

$$H = \frac{5}{2}RT + RT \frac{TQ'_{rot}}{Q_{rot}}; \quad Q_{rot} = Q_{rr}Q_{h.o}; \quad Q_{rr} = \frac{1}{2} \frac{kT}{h^2 c B}; \quad Q_{h.o} = \prod_i Q_i.$$

$\prod_i Q_i = Q_1 Q_2^2 Q_3$ for a CO_2 molecule. The quantity Q_i is related to the frequencies of corresponding molecular vibrations by the expression

excitation of internal degrees of molecular freedom and dissociation can be determined by measuring the angles of inclination of the Mach lines on a plate in the flow. The experimental results obtained indicate that there is no dissociation in the flow at a distance to 15 cm behind the shock wave and asymmetric valent vibrations of CO_2 are not excited. The angle of inclination of the boundary which separates the region of disturbed and undisturbed flows is determined by the high-frequency velocity of sound calculated from $\gamma = 1.4$.

Supplement

Calculation of the flow parameters behind a shock wave with a varying degree of vibrational excitation of CO_2 molecules.

The flow parameters behind a shock wave were calculated for states with a varying degree of vibrational excitation of CO_2 molecules. The angles of inclination of the oblique shock for 10° and 16° flow deflection angles were also calculated.

The calculation procedure is described briefly below and the basic results are presented. The calculation was performed with the equations of the laws of conservation of momentum and energy, and the

$$Q_i = \frac{1}{1 + e^{-\frac{hc}{kT} \omega_i}}.$$

The structure of the notation of $\Pi_i Q_i$ for CO_2 is based on data concerning the vibrational modes of this molecule.

There exist deformation and valent molecular vibrations. Deformation vibrations lead to a change in the relative positions of the C and O atoms in the molecule without a change in the distance between them. Valent vibrations occur along the atomic bonds and include a change in the distance between them. There are two modes of deformation vibrations with an identical frequency $\nu_2 = 667.4 \text{ cm}^{-1}$. The portion of the static sum Q_2 which corresponds to them is squared; ν_1 corresponds to symmetric valent vibrations corresponding to $\nu_1 = 1388.15 \text{ cm}^{-1}$; Q_3 corresponds to asymmetric valent vibrations and $\nu_3 = 2349.16 \text{ cm}^{-1}$.

The vibrational constants for these frequencies are: $\omega_2 = 672.2$, $\omega_1 = 1351.2$, and $\omega_3 = 2396.4$; the characteristic temperatures are equal to $\theta_2 = 960.05$, $\theta_1 = 1930.19$, and $\theta_3 = 3379.95$, respectively. The final calculated relationship for gas enthalpy in a state with equilibrium-excited vibrations has the form

$$H = RT \left(\frac{7}{2} + \sum_i \frac{\frac{hc}{k} \frac{\omega_i}{T} e^{-\frac{hc}{k} \frac{\omega_i}{T}}}{1 - e^{-\frac{hc}{k} \frac{\omega_i}{T}}} \right).$$

The number of terms of the sum retained in the calculation determines the allowance for equilibrium excitation of the corresponding vibrational modes.

In the formula, R is the gas constant, T is the temperature, h is the Planck constant, c is the velocity of light, k is the Boltzmann constant, and ω_i is the vibrational constant.

Table 1 lists the values of enthalpy for a state with excitation of only deformation vibrations taken into account, H_2 , and a state with deformation and symmetric valent vibrations taken into account.

Tables 2-4 contain the values of the flow parameters behind shock waves for M_0 wave numbers in the 6-12 range, or wave velocity in the 1,500-3,500 m/sec range. Table 2 contains [wave velocity] calculated for a state, taking equilibrium excitation of only the deformation vibrations into account. Table 3 takes deformation and symmetric valent vibrations into account. Table 5 takes the equilibrium state of excitation of all vibrational modes into account. (The enthalpy values for the last state are taken from [16].) Table 5

TABLE 1.

T, °K	2000	2400	2800	3000	3400	3800	4000	4400	4800	5000	5400	5800
H_2	456,0	555,2	654,1	703,1	803,1	901,9	951,7	1049,4	1148,7	1148,7	1298,7	1397,7
$H_{1,2}$	508,0	625,4	741,3	799,4	917,0	1033,0	1091,5	1207,0	1324,7	1383,7	1502,9	1616,2

TABLE 1. (Conclusion)

T, °K	6000	6400	6600	6800	7000	7200	7400	7600	7800	8000	8400
H_2	1450,0	1548,0	-	1646,0	-	1747,0	—	1853,0	1906,0	-	-
$H_{1,2}$	1676,3	-	1852,1	-	1969,3	—	2086,5	—	—	2262,2	2379,7

lists the values of the parameters calculated under the assumption that $\gamma = \text{const} = 1.4$ upon transition through the shock. Tables 6 and 7 contain data on the values of the flow deflection angle in an oblique shock wave whose angle of inclination is given. It is assumed that this shock occurs in the flow behind /179 the shock wave with the Mach wave numbers M_0 given in the first line of each table. It was assumed when calculating the data in these tables that the state on the oblique shock varies in such a way that equilibrium excitation of those vibrational modes which were assumed to be excited in the flow behind the incident shock wave is established immediately behind the shock.

TABLE 2.

/178

M_0	5,55	6,48	7,40	9,25	11,10	12,95
T, °K	1425	1825	2270	3350	4660	6200
ρ_1/ρ_0	7,46	7,94	8,35	8,87	9,19	9,41
P_1/P_0	36,0	49,2	64,4	1000,8	145,3	198,0
$u_1, \text{m/sec}$	1390	1530	1760	2220	2675	3125

TABLE 3.

M_0	6	7	8	9	10	11
T, °K	1500	1890	2330	2840	3400	4030
ρ_1/ρ_0	8,5	9,0	9,8	9,9	10,5	10,7
P_1/P_0	43	58	77	96	120	146
$u_1, \text{m/sec}$	1430	1690	1940	2190	2440	2690

TABLE 4.

M_0	6	7	8	9	10	11	12
$T, ^\circ K$	1420	1780	2155	2590	3090	3650	4230
ρ_1/ρ_0	9,12	9,88	10,67	11,24	11,62	11,90	12,23
P_1/P_0	43,9	59,7	78,0	98,7	121,8	147,3	175,5
$u_1, m/sec$	1443	1700	1959	2215	2469	2722	2977

TABLE 5.

M_0	5,55	6,48	7,40	8,33	9,25	10,18	11,10	12,95
$T, ^\circ K$	1935	2530	3220	4000	4875	5840	6900	9290
ρ_1/ρ_0	5,10	5,31	5,46	5,56	5,64	5,70	7,75	5,81
P_1/P_0	33,5	45,7	59,8	75,7	93,5	113,2	134,7	183,5
$u_1, m/sec$	1260	1420	1630	1850	2060	2270	2480	2900

TABLE 6. VALUES θ

$M_0 \backslash \sigma$	45°	40°	35°	30°	25°
6	24°	19°20'	14°16'	8°07'	—
7	25°26'	20°54'	15°59'	10°20'	3°48'
8	26°26'	21°53'	16°52'	11°14'	4°30'
9	27°00'	22°30'	17°30'	11°52'	5°25'
10	27°25'	22°56'	17°56'	12°22'	6°10'
11	27°45'	23°20'	18°20'	12°50'	7°30'

TABLE 7. VALUES θ

$M_0 \backslash \sigma$	40°	35°	30°	25°
6	20°57'	15°48'	9°57'	3°35'
7	22°37'	17°30'	11°52'	5°36'
8	23°42'	18°48'	13°08'	6°50'
9	24°24'	19°30'	13°55'	7°36'
10	24°52'	19°54'	14°23'	8°11'
11	25°24'	20°22'	14°50'	8°38'
12	25°48'	20°47'	15°20'	9°12'

Curves 1 and 3 in Figures 3 and 4 were constructed on the basis of the values taken from Tables 6 and 7.

REFERENCES

1. Bazhenova, T. V. and I. M. Naboko: On the question regarding the rate of physical and chemical transformations of CO_2 molecules behind a shock wave at temperatures of 2,000-4,000°K. *Doklady AN SSSR*, Vol. 154, No. 2, 1964.
2. Bazhenova, T. V. and S. G. Zaytsev: The effect of dissociation on the parameters of reflected shock waves in carbon dioxide. *Tret'ye vsesoyuznoye soveshchaniye po teorii goreniya. (Third All-Union Conference on the Theory of Burning.)* Vol. 1, 1960.
3. Bazhenova, T. V. and O. A. Predvoditeleva: The value of air parameters behind a normal shock wave and behind a reflected shock wave in equilibrium and frozen dissociation. In: *Fizicheskaya gazodinamika i teploobmen. (Physical Gas Dynamics and Heat Exchange.)* Izd-vo AN SSSR, 1961.
4. Bazhenova, T. V. and S. G. Zaytsev: The parameters of carbon dioxide behind a reflected shock wave and an estimate of the onset time of equilibrium dissociation at temperatures of 4,000-6,000°K. In: *Fizicheskaya gazodinamika, teploobmen i termodinamika gazov vysokikh temperatur. (Physical Gas Dynamics, Heat Exchange and Thermodynamics of High-Temperature Gases.)* Izd-vo AN SSSR, 1962.
5. Bazhenova, T. V.: An estimate of the dissociation relaxation time of carbon dioxide on the basis of shock tube experiments. *Doklady AN SSSR*, Vol. 146, No. 3, 1962.
6. Soloukhin, R. I.: Some data on the nonequilibrium state of carbon dioxide behind the front of a shock wave. *Prikladnaya Mekhanika i Tekhnicheskaya Fizika*, No. 6, 1963.
7. Feldman, S.: An experimental study of the kinetics of chemical reactions in air at high temperatures. *Voprosy Raketnoy Tekhniki*, No. 1, p. 49, 1959.
8. Semenov, S. S.: A method for checking the equations of state of gases at high temperatures. *Doklady AN SSSR*, Vol. 114, No. 4, 1957.
9. Stakhanov, I. P. and Ye. V. Stupochenko: On the structure of Mach lines in relaxing media. *Doklady AN SSSR*, Vol. 134, No. 5, 1960.
10. Spence, D. A.: Nonstationary propagation of a shock wave in a relaxing gas. *Mekhanika*, No. 6, p. 76, 1962.
11. Bergman, M.: *Ul'trazvuk. (Ultrasound.)* Moscow, IL, 1957.
12. Broer, L. J. F.: Characteristics of the equations of motion of a reacting gas. *J. Fluid Mech.*, Vol. 4, 1958.
13. Ting, J. L.: Recent advances in nonequilibrium dissociating gas dynamics. *ARS Journal*, Vol. 31, No. 2, 1961.
14. Moore, F. K. and W. E. Gibson: Propagation of weak disturbances in a gas subject to relaxation effects. *J. Aero/Space Sci.*, Vol. 27, No. 2, 1960.
15. Leskov, A. and F. Savin: The relaxation of nonequilibrium gaseous systems. *Uspekhi Fizicheskikh Nauk*, Vol. 72, No. 12, 1960.
16. Gurevich, L. V., G. A. Khachkuruzov, et al.: *Termodinamicheskiye svoystva individual'nykh veshchestv. (Thermodynamic Properties of Individual Substances.)* Izd-vo AN SSSR, 1962.

CALCULATION OF THE ONSET TIME OF EQUILIBRIUM DISSOCIATION
ON THE BASIS OF EXPERIMENTAL DATA CONCERNING THE NON-
STATIONARY PROPAGATION OF A REFLECTED SHOCK WAVE

T. V. Bazhenova

As discovered in previous investigations [1], the velocity of a shock wave /180 in CO_2 reflected from the end of a shock tube, at M numbers of the shock wave $\sim 8-11$ and $p_0 = 12$ mm Hg, has values which correspond to frozen dissociation of molecules, and assume equilibrium values $7-30$ μsec after reflection. The dissociation relaxation times of carbon dioxide at $4,000-6,000^\circ\text{K}$ were estimated on the basis of these data [2]. The estimation was made on the assumption that the velocity of a reflected wave takes equilibrium values in a time interval τ_s equal to the sum of the dissociation relaxation time τ_0 and the time of signal propagation at the velocity of sound from the end of the tube to the front of the reflected wave. This process can be more precisely calculated on the basis of solving the problem concerning the nonstationary propagation of a shock wave in a relaxing gas.

The problem concerning the nonstationary propagation of a shock wave in front of a piston in a relaxing gas was solved in [3] by the method of linearized characteristics. The problem concerning the reflection of a shock wave from a flat wall differs from the problem concerning the propagation of a wave in front of a piston by the fact that the velocity of the piston is assumed to be equal to zero, while the initial flow encounters the reflected wave at a velocity equal to the velocity of the flow behind the incident shock wave. For the case of the reflection of a shock wave from a rigid wall, the M number of the flow behind the shock wave with respect to the shock wave should be considered to be equal to $M = U_0/a_0$, where U_0 is the velocity of the reflected shock wave in the absence of dissociation and a_0 is the frozen velocity of sound in the gas behind the reflected shock wave.

An expression was derived in [3] which relates the relaxation time τ_0 to the time of approach of the velocity of the shock wave to the equilibrium value of τ_s

$$\tau_s = \tau_0 \frac{2 \ln 2}{1 - M^2} \left(\frac{1 + \frac{3\gamma - 1}{3 - \gamma} M^2}{1 + 2 \frac{\gamma - 1}{3 - \gamma} M^2} \right). \quad (1)$$

here γ is the adiabatic exponent, which has different values before the front of the shock wave, on the front of the shock wave, and near the piston. Calculation with formula (1) indicates, however, that the ratio τ_s/τ_0 depends little on γ , if γ varies from 1.3 to 1.15 (see below).

Application of formula (1) to the results of our measurements of the onset time of the equilibrium velocity of a reflected shock wave in carbon dioxide indicates that the dissociation relaxation time τ_0 is 1.6 times less than the onset time of the equilibrium velocity of the shock wave τ_s .

/181

M_0	7.67	8.1	8.45	8.9	9.05	9.6
u_0 , m/sec	280	290	290	300	300	320
α_0 , m/sec	1,000	1,060	1,100	1,130	1,150	1,200
τ_s/τ_0 ($\gamma = 1.3$)	1.66	1.65	1.63	1.63	1.62	1.63
τ_s/τ_0 ($\gamma = 1.15$)	1.64	1.63	1.61	1.61	1.60	1.61
τ_s/τ_0 (from [2])	1.39	1.38	1.36	1.36	1.35	1.36

The ratio τ_s/τ_0 from formula (1) is only 15% greater than the ratio according to the formula ($\tau_s/\tau_0 = 1/1 - M$) which we obtained earlier from simple considerations concerning the propagation of elementary disturbances at the velocity of sound from the end to the shock wave [2]. The dependence of the onset time of equilibrium dissociation on the temperature of the gas behind a reflected shock wave is indicated below.

T' , °K	3,800	4,300	4,600	4,900	5,000	5,500
T , °K	2,700	2,900	3,000	3,200	3,200	3,300
p , atm	14	17	19	21	22	26
$\tau_0 p$, $\mu\text{sec} \cdot \text{atm}$	300	350	120	185	125	158

Here T' is the temperature on the front of the reflected shock wave under the assumption of frozen dissociation and excited rotational and vibrational degrees of molecular freedom; T is the equilibrium temperature behind the reflected shock wave; p is the pressure behind the reflected wave; $\tau_0 p$ is the dissociation relaxation time τ_0 referred to atmospheric pressure, converted from the experimental values of τ_s with formula (1). The relaxation time is obtained by an indirect method. It is of interest to compare the relaxation time obtained with certain results achieved by other methods. The temperature of carbon dioxide behind a reflected shock wave was measured in [4] under conditions which duplicate the conditions of our experiments. The gas temperature behind a reflected wave in CO_2 with the velocity of the incident wave 2,100 m/sec at a distance of 10 mm from the end of the tube, after passing the front of the reflected wave, was equal to 3,350°K, and dropped to 2,600°K in $13 \pm 5 \mu\text{sec}$. The first value corresponds to the temperature behind the reflected shock wave with excited vibrations and frozen dissociation; the second value corresponds to the equilibrium temperature calculated on the basis of the velocity of the incident

wave at the end. The time of arrival of the temperature at the equilibrium value, corrected to atmospheric pressure, amounts to 200 ± 70 μsec .

The onset time of the equilibrium temperature at $T' = 7,000^\circ\text{K}$ ($M_0 = 11$ and $p_0 = 12.7$ mm Hg), according to [4], is not more than 6 μsec (6 μsec is the time required to establish reliable readings of the equipment when measuring temperature in the given experiments). Corrected to atmospheric pressure, this time amounts to not more than 280 μsec .

Some information concerning dissociation relaxation time can be obtained from the results of measuring the CO_2 concentration and temperature behind an incident shock wave, which were determined on the basis of ultraviolet absorption in [5]. When $M_0 = 10.5$ ($T' = 3,320^\circ\text{K}$ and $p = 0.36$ atm) variation in composition and temperature was not recorded on the extent of the entire plug up to the contact surface ($t = 25$ μsec). When $M_0 = 12.5$, $p = 0.5$ atm and $T' = 4,050^\circ\text{K}$, a region was observed behind the front of the shock wave which corresponds to a drop in temperature and CO_2 concentration in 15 μsec laboratory time, and this time was reduced to 7 μsec at $M_0 = 14.8$. The times of existence of these non-uniform regions, corrected to atmospheric pressure in a coordinate system connected to the gas particles, amounts to 75 μsec at $T' = 4,050^\circ\text{K}$ and 21 μsec at $T' = 6,000^\circ\text{K}$. On the basis of the data which we obtained and the results of [4] and [5], the conclusion can be made that the dissociation relaxation time of carbon dioxide, corrected to atmospheric pressure at $3,000$ – $6,000^\circ\text{K}$, amounts to approximately $3 \cdot 10^{-4}$ sec. /182

The results refer to CO_2 dissociation with a 2% steam content. The relaxation time in moist CO_2 is of interest for gas-dynamic investigations, since this gas almost always flows in the presence of steam.

The data obtained, however, can also be used to calculate the dissociation kinetics of pure CO_2 , since [5] indicates that the rate of CO_2 dissociation has slightly differing values in the dry and moist gas.

Relaxation of dissociation and vibrations at high temperatures renders a significant effect on the flow of carbon dioxide and, in particular, on the state of the gas behind the shock wave which arises in the flow around bodies. The results of determining the dissociation relaxation time make it possible to determine the distance at which equilibrium parameters of carbon dioxide are established behind a normal shock wave. The results obtained for a normal shock give us an idea of the state of the gas behind the detached shock wave which arises in the flow around a blunt-nose body. At a pressure of 1 atm behind the shock and a 4 km/sec velocity of the incident flow, equilibrium is established behind the shock wave at a distance of 3 cm from the front of the shock wave, 10 cm at a velocity 3 km/sec, and equilibrium is not established at a distance of more than 15 cm with a velocity of 2.5 km/sec.

The gas temperature in the indicated region varies from the values on the front, T' , which correspond to frozen dissociation, to the equilibrium values. The difference between these temperatures amounts to several thousand degrees [6].

REFERENCES

1. Bazhenova, T. V. and S. G. Zaytsev: The effect of dissociation on the parameters of reflected shock waves in carbon dioxide. *Tret'ye Vsesoyuznoye soveshchaniye po teorii gorennya*. (Third All-Union Conference on the Theory of Burning.) Vol. 1, Izd-vo AN SSSR, Moscow, 1961.
2. Bazhenova, T. V.: An estimation of dissociation relaxation time of carbon dioxide on the basis of shock tube experiments. *Doklady AN SSSR*, Vol. 146, No. 3, 1962.
3. Spence, D. A.: Nonstationary propagation of a shock wave in relaxing gas. *Mekhanika*, No. 6, 1962.
4. Kudryavtsev, Y. M., L. I. Sobolev, F. S. Tunitskiy and F. S. Fayzullov: Pyrometric investigation of the state of a gas behind a reflected shock wave. *Issledovaniya plazmy. Tr. Fizicheskogo Instituta AN SSSR*. (Plasma Research. Transactions of the Physics Institute of the Soviet Academy of Sciences.) 1962.
5. Losev, S. A., N. I. Generalov and Z. A. Maksimenko: Investigation of the decay of carbon dioxide molecules at high temperatures. *Doklady AN SSSR*, Vol. 150, No. 4, 1963.
6. Bazhenova, T. V. and I. M. Naboko: On the question concerning the speed of physical and chemical transformations of CO_2 molecules behind a shock wave at temperatures of 2,000–4,000°K. *Doklady AN SSSR*, Vol. 154, No. 2, 1964.

PECULIARITIES OF MACH REFLECTION OF SHOCK WAVES MOVING IN
CARBON DIOXIDE AND NITROGEN AT VELOCITIES ON
THE ORDER OF 2,000 m/sec

L. G. Gvozdeva and O. A. Predvoditeleva

When a plane shock wave encounters a wedge, two processes occur simultaneously: reflection of the wave from the wedge surface and diffraction on its leading edge [1]. Let us assume that a shock wave SAM is moving along the surface of a wedge (Figure 1) with such a small α_0 that reflection occurs irregularly. The flow behind the shock wave is supersonic. The shock wave collides with the wedge at the moment $\tau = 0$. The disturbances which arise as a result of reflection of the shock wave are propagated upwards toward the flow, forming part of the reflected wave AR . Let us consider a coordinate system connected with the flow behind the wave in region 1. The leading edge of the body moves to the left with respect to the system, and the wave moves to the right. The leading edge of the wedge in the supersonic flow moves to the left more quickly than the disturbances which occur as a result of wave reflection. Consequently, region 5 will be disturbed only by the leading edge, and disturbances caused by the shock will not occur in it. Therefore, the angle formed by the wave OR with the wedge surface can be calculated with formulas for a stationary supersonic flow. Calculations of the Mach configuration near the triple point can be performed on the basis of the three-shock theory under the assumption of self-similarity of the configuration and for an angle of inclination of the line of motion of the triple point χ known from the experiment.

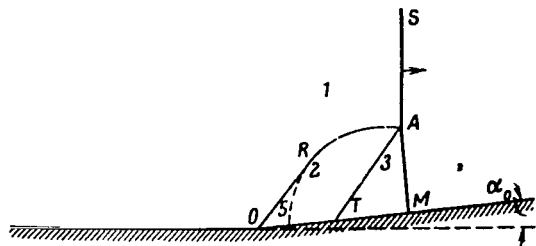


Figure 1. Diagram of Shock Wave Diffraction on a Wedge.

We investigated the peculiarities of Mach reflection of shock waves for Mach numbers $M_0 > 5$. The gas in this case must be considered to be imperfect and relaxation processes should be taken into account. The investigation was conducted in nitrogen and carbon dioxide on a UT-2 installation. A block diagram of the installation is shown in Figure 2, where 1 is the high-pressure chamber, 2,000 mm in length; 2 is the low-pressure chamber, 2,670 mm in length; and 3 is the experimental section. The

low-pressure chamber has a $40 \times 40 \text{ mm}^2$ square cross section.

Duralumin wedges were inserted into the experimental section which was equipped with windows. The gap between the wedge and the windows of this section did not exceed 4% of the shock tube cross section. The wedge vertex angles were $\alpha_0 = 24, 28, 32$ and 36° . The process of shock wave reflection was photographed with the aid of an IAB-451 Töpler device 4 and an SFR-L8 high-speed

camera. The adapter system for connecting these instruments consisted of MT0-500 and R0-2-12M objectives. Thirty frames of the process were obtained as a result of each experiment; the frame diameter was 10 mm, the exposure time of each frame was 0.5 μ sec, and the frame change time was 4 μ sec. The reduction factor was 10 [2]. RF-3 film with a sensitivity of 1,000 reverse roentgens was used. The light source was an IPS-500 pulse lamp 5. The power supply of the lamp is denoted by the number 6. The flash duration was 500 μ sec. The flash time of the lamp was synchronized with the moment of reflection of the incident wave by means of a synchronization unit 7. The velocity of the shock wave along the tube was measured with piezoelectric transducers built into sockets I-V, and on the basis of photographs of the process. The measured velocity distribution of the shock wave indicated that the wave is already completely formed at the moment of its arrival at the experimental section, and it passes the field of vision either at maximum velocity or at a velocity which attenuates by no more than 10%. The velocity of the shock waves fluctuated near the value of $u_0 = 2,000$ m/sec.

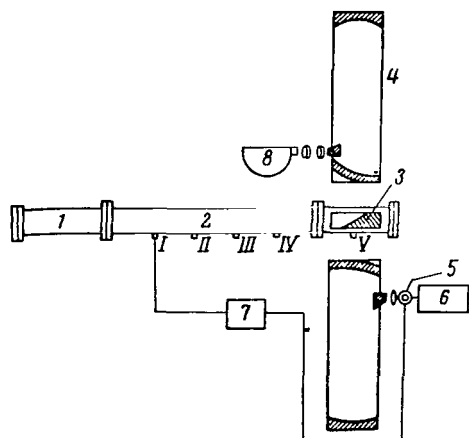


Figure 2. Block Diagram of UT-2 Installation.

is a time marker. The mount of the IAB-451 instrument was vertically positioned; therefore, the density gradients in the vertical direction are more difficult to distinguish than in the horizontal direction.

The following peculiarities which distinguish the obtained pictures from the pictures of reflection at low M numbers were noted.

First of all, a second triple point R appears during reflection. The reflected wave in carbon dioxide is situated below the trajectory of motion of the triple point, while the reflected wave in nitrogen is situated above this trajectory. It is interesting to note that marked deflections of the reflected wave are seen on the photographs of diffraction of shock waves on a cone obtained by Bryson and Gross [3], although the authors themselves do not indicate this. A break in the reflected wave during Mach reflection was observed also by White [4, 5], whereby this break, as the author indicates, becomes more expressed as

Figure 3 illustrates photographs of a shock wave in nitrogen, moving at a velocity of 2,100 m/sec, with reflection from a wedge with a vertex angle of $\alpha_0 = 24^\circ$. The initial gas pressure was $p_0 = 1.68 \cdot 10^4$ dynes/cm².

The first frame corresponds to a time of 10.5 μ sec from the beginning of flow around the wedge. Photographs of the propagation of a shock wave in CO₂ are shown in Figure 4. The conditions of the experiment were the same as those for nitrogen. The velocity of the wave was 1,900 m/sec. The first frame corresponds to a time of 23.3 μ sec from the beginning of flow around the wedge. The direction of propagation of the wave is from left to right: *SA* is the undisturbed portion of the incident wave; *AM* is the Mach stem; *ARNO* is the reflected wave; *AT* is the contact discontinuity; *L*

the strength of the shock wave increases.

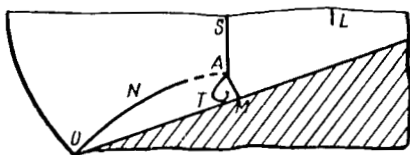
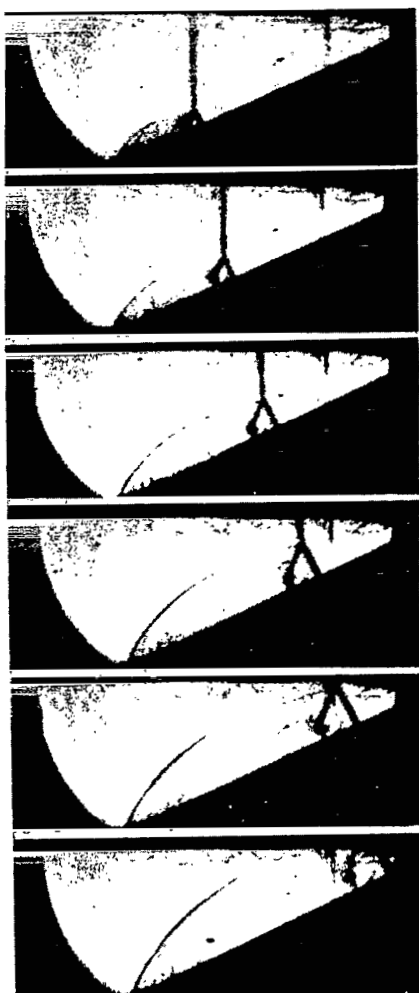


Figure 3. Irregular Reflection of a Shock Wave in Nitrogen.

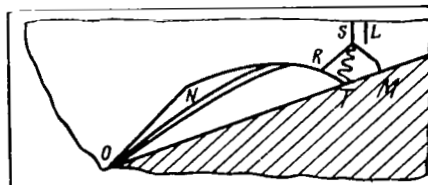
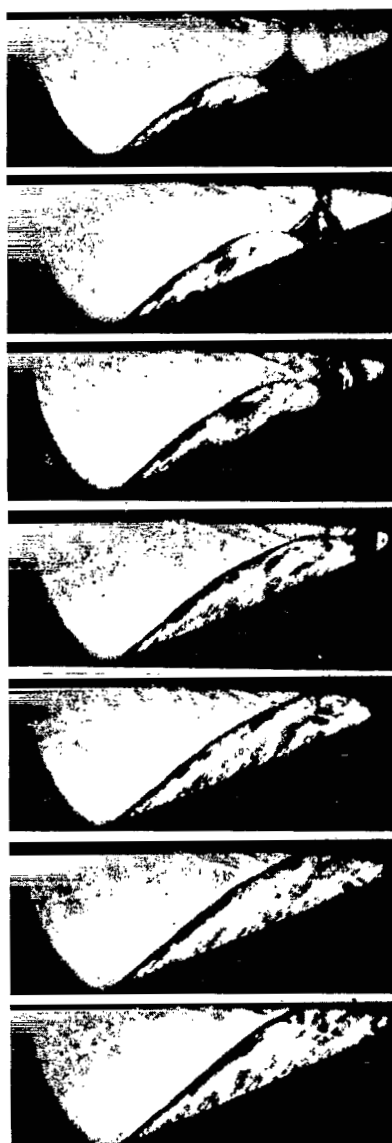


Figure 4. Irregular Reflection of a Shock Wave in Carbon Dioxide.

Secondly, instability of the contact discontinuity is sharply expressed. The contact discontinuity in nitrogen evolves into a vortex, which is especially well noted in the fifth and sixth frames of Figure 3. A similar type of instability was observed also in [3]. Sharp fluctuations of the contact discontinuity are visible in CO_2 at the vertex near the triple point.

Thirdly, if the Mach stem AM in N_2 is straight and perpendicular to the wall, the stem in CO_2 has a noticeable break. The Mach wave is perpendicular /186 to the wall near the wall and the inclination varies as the distance from the wall increases.

Interpretation of the experiments indicated that the triple point moves on a straight line inclined at a constant angle χ to the wedge surface. The self-similarity of motion of the configuration of the shock waves was checked. The distances r along the given rays from the vertex of the angle to the wave were determined on each frame. The measured distances r were plotted on the graph as a function of the time τ determined for each frame according to the position of the shock wave. The time of arrival of the wave on the forward edge of the wedge was adopted as the reference origin. If the points lie on a straight line for each ray in the coordinates r and τ , then, consequently, the entire picture changes only as a function of the ratio r/τ , i.e., the motion is self-similar. Figure 5 shows a graph which was obtained for N_2 in accordance with the photographs of Figure 3. The points which correspond to all rays except the seventh lie on straight lines with a 3% scatter. The region near the leading edge is not self-similar, and the corresponding points lie on curve 7.

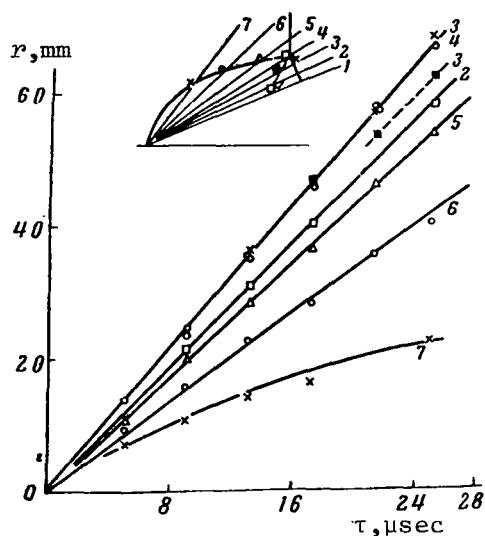


Figure 5. Dependence r of the Position of Individual Points of a Shock Wave on Time τ .

A diagram of shock wave reflection and the introduced designations of the angles are given in Figure 6.

The angles of inclination of the trajectory of motion of the triple point χ relative to the wedge side and the angles of inclination of the waves near the triple point ω_1 , ω_2 , ω_3 with respect to the line of motion of the triple point were determined on the photographs.

The value of the angles χ makes it possible to calculate the angles near the triple point according to the three-shock theory. The angles were calculated by the shock-polar method [6] in a coordinate system connected with the triple point. By knowing the state of the gas in front of the shock wave and the angle of influx into the wave φ_0 , it is possible to calculate the state of the gas behind the incident wave in region 1 and the angle of deflection of the flow θ_1 (Figure 6). Then,

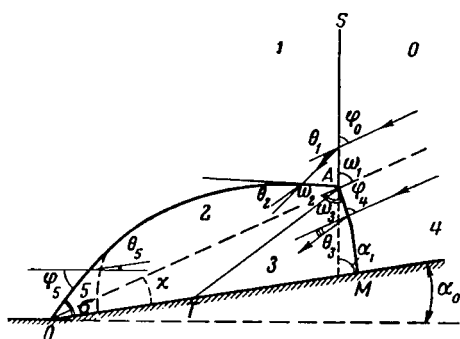


Figure 6. Diagram of Shock Wave Reflection.

having assigned various angles of influx of the gas into the reflected wave φ_1 , i.e., the velocity of the reflected wave, it is possible to calculate the shock adiabat for the state of the gas in region 2, which is written in the form of the dependence of the pressure drop in the reflected wave p_2/p_1 on the angle of deflection of the flow θ_2 . A similar shock polar can be constructed for the Mach wave AM . The following conditions of compatibility are satisfied at the point of intersection of the/187 polars: equality of pressures in regions 2 and 3 and parallelism of the flows in these regions, i.e., $p_2 = p_3$ and $\theta_3 = \theta_1 - \theta_2$. The parameters at this point provide the sought solution.

The shock polars were calculated by the method of successive approximations, which is discussed in detail in the article [7] for two assumptions concerning the state of the gas behind incident and reflected waves. In the first version of the calculation, which we have designated by letters without primes, it was assumed that the vibrations behind the incident and reflected waves were equilibrium-excited and dissociation had not occurred. This assumption was made on the basis of reference data [8], where it is pointed out that in processes up to 100-150 μsec in duration, under similar conditions, dissociation does not take place and the gas is in a nonequilibrium state. In the second version of the calculation, the gas was considered to be perfect with a specific heat ratio $\gamma = 1.4$. The corresponding parameters are denoted by letters with superscript primes. The enthalpy values were taken from the tables in [9]. The initial gas parameters were $p_0 = 1.68 \cdot 10^4$ dynes/cm² and $T_0 = 298^\circ\text{K}$. The calculation results and the experimental values for CO_2 and N_2 are listed in Table 1. The experimental values of the angles ω_2 were obtained for the times τ from 10 μsec to 22-30 μsec from the beginning of flow around the wedge.

Calculation of Three-Shock Configuration for CO_2 and N_2 .

The following designations were additionally employed in Table 1: u_m is Mach wave velocity; u_0 is the incident wave velocity; T is the temperature in $^\circ\text{K}$; and p is the pressure. The subscripts 0, 1, 2 and 3 refer to regions of undisturbed flow, flow behind the incident wave, behind the reflected wave, and behind the Mach wave, respectively. The designations of the angles are given in Figure 6.

The calculated dependence of the angle of reflection ω_2 on the angle incidence ω_1 is plotted on the graph in Figure 7 in the case of Mach reflection /188

TABLE 1.

	CO ₂				N ₂
α_0	24°00'	28°00'	31°50'	36°00'	24°00'
u_0 , m/sec	1900	2040	2070	2140	2100
χ_{exp}	9°30'	7°40'	6°00'	2°40'	9°40'
ω_2^{exp}	-12° ± 2°	-11° ± 5°	-12° ± 3°	-8°40' ± 1°40'	—
ω_2	-12°06'	-13°19'	-14°12'	-14°40'	4°49'
ω_2'	7°31'	8°04'	9°11'	—	10°47'
T_1 , °K	1780	1970	2020	2120	2150
p_1/p_0	58,7	67,9	69,9	74,7	42,8
ω_1	56°30'	54°20'	52°10'	51°20'	56°20'
T_2 , °K	1850	2090	2170	2270	—
p_2/p_1	1,43	1,50	1,68	1,64	1,43
T_3 , °K	2350	2725	3090	3190	2815
p_3/p_0	83,9	102,0	118,0	122,0	61,3
u_{sh} , m/sec	2270	2500	2700	2740	—
T_1' , °K	2900	3370	3470	—	2394
p_1'/p_0	53,4	61,3	63,0	—	41,6
T_2' , °K	3110	3775	4100	—	2590
$(p_2/p_1)'$	1,40	1,49	1,69	—	1,38
T_3' , °K	3940	4755	5490	—	3250
$(p_3/p_0)'$	76,4	92,4	106,0	—	58,5
u_{sh}' , m/sec	2245	2485	2680	—	2500

for the first version.

The gas was CO₂ and the shock wave velocity was $u_0 = 9.9$ km/sec. The values of ω_2 calculated for a velocity of 2.1 km/sec differ from the values for the velocity of 1.9 km/sec by no more than 1°, and a corresponding curve is not given in Figure 7. Experimental points are given for the incident wave velocity in the range of 1.9–2.07 km/sec.

It is evident from the table and Figure 7 that the calculations for CO₂ with vibration excitation taken into account provides a satisfactory agreement with the experiment. The values of the angles ω_2 , if vibrations are taken into account, are negative, *i.e.*, the reflected wave goes below from the triple point under the line of its motion. A qualitative matching is obtained for N₂ since the values of ω_2 in accordance with the experiment are positive. The poor visibility of the vertical gradients in N₂ did not make it possible to derive accurate values for ω_2 .

Negative values of angles ω_2 obtained for the calculation in CO₂ made it possible to clarify the distinction in the pattern of Mach reflection at high and low M numbers.

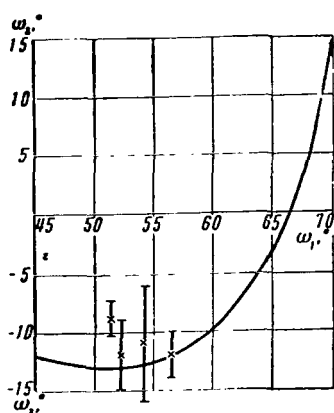


Figure 7. Dependence of ω_2 on ω_1 with Irregular Reflection of a Shock Wave in CO_2 .

after the beginning of flow, the wave occupies the position ABC ; a break appears in the wave, and the wave moves upward toward the flow. This phenomenon is caused by the effect of thickening of the boundary layer. In CO_2 , where the wave is attached, measurements were conducted to the times $\tau = 20 \mu\text{sec}$ according to the inclination of the wave ABC , after bending of the wave, *i.e.*, according to the inclination of section BC .

Since the boundary layer increases not only on the surface of the wedge, but also on the lateral walls of the tube, a shock on the wedge undergoes changes similar to those which occur in the reflection of a shock wave from an end plane [10], *i.e.*, a so-called "bifurcation" is obtained, only in a similar degree due to the decrease in intensity of the wave and the angle of its inclination. Actually, some stratification of the attached wave can be seen in Figure 4 (especially frame 5). The central line along which all measurements were made corresponds to the portion of the reflected wave situated in the nucleus of the flow.

The results of measurements of angle σ of the attached wave in CO_2 , depending on the time τ from the moment of the beginning of flow, are shown in Table 2 for the same experiments, the data from which are given in Table 1. The accuracy of measuring angle σ is $\pm 1^\circ$ (with the exception of individual measurements, whose errors are indicated in the table, the accuracy of determining τ is $\pm 0.4 \mu\text{sec}$). /189

In order to make conclusions concerning the state of the gas on the basis of the measurements, the gas parameters behind a shock wave formed in a supersonic flow around the forward edge of a wedge were calculated under various assumptions concerning the state of the gas behind an incident and reflected wave.

The calculation was performed with the shock-adiabat method in a coordinate

system connected with the vertex of the wedge, and values of the angle φ_5 between the direction of the incident flow and the wave on the wedge were selected (see Figure 6) for which the equality between the angle of the reflected flow and the wedge angle α_0 was satisfied.

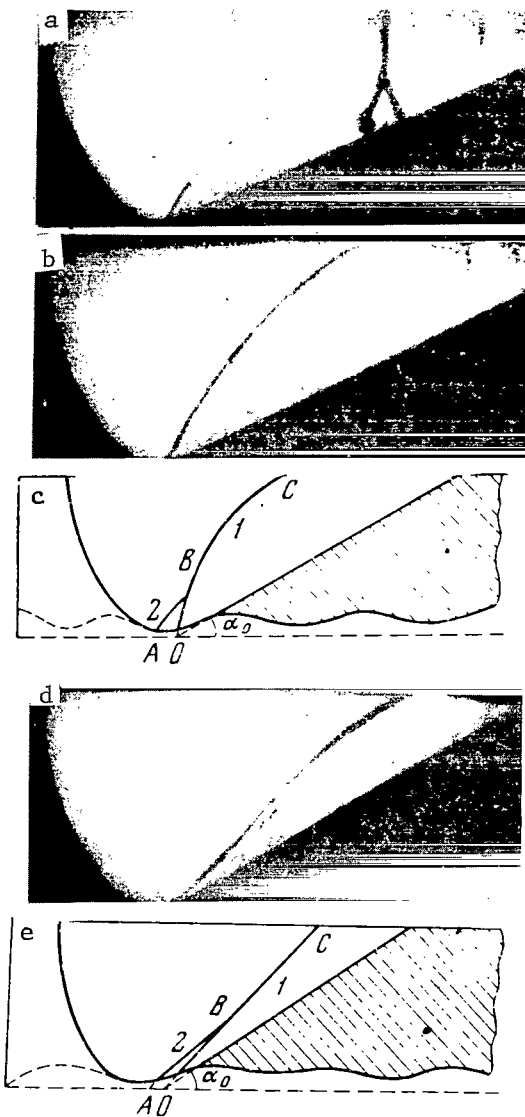


Figure 8. Flow Around a Wedge by a Gas Behind a Shock Wave at the Time τ_1 and τ_2 after Arrival of a Shock Wave at the Vertex of the Angle, $\tau_1 < \tau_2$. (a, b, c) N_2 gas; $\tau_1 = 22.5 \mu\text{sec}$ and $\tau_2 = 42.5 \mu\text{sec}$; (d, e) CO_2 gas; $\tau_2 = 38.5 \mu\text{sec}$.

210

The experimental and calculated values of the angles are shown in Figure 9. The calculation was performed for a velocity of 2,000 m/sec. Curve 1 was calculated under the assumption of equilibrium excitation of vibrations behind the incident and attached waves and the absence of dissociation; curve 3 was calculated under the assumption that $\gamma = 1.4$ both behind the incident wave and the attached wave.

A conclusion was made in [11, 12] concerning the fact that in the range of $M_0 = 6-11$ not only is there no dissociation behind the shock wave, but asymmetrical valent vibrations of CO_2 molecules are not excited in a time on the order of 100 μsec . Curve 2 is drawn in Figure 9, which was calculated under this assumption. The experimental points are located between curves 1 and 2, which indicates the correctness of the assumptions made in the calculations of Mach reflection.

Thus, it was established experimentally that Mach reflection at high shock wave velocities (on the order of 2 km/sec) has essential peculiarities in comparison with /190 the case of weaker waves in an ideal gas. The reflected wave in CO_2 has a break and its straight portion near the triple point is located closer to the wedge surface than the trajectory of motion of the triple point. The Mach stem has a break. Instability of the contact discontinuity is sharply expressed. Both in CO_2 and N_2 , the contact discontinuities are unstable. The self-similarity of motion and the applicability of the three-shock theory were checked in this region. The three-shock theory provides good agreement for CO_2 under the assumption concerning the excitation of vibrations of gas molecules.

TABLE 2. VARIATION OF ANGLE OF INCLINATION OF ATTACHED WAVE AT WEDGE VERTEX IN CO_2 AS A FUNCTION OF TIME τ .

$\alpha_0 = 24^\circ$		$\alpha_0 = 28^\circ$		$\alpha_0 = 31^\circ 50'$		$\alpha_0 = 36^\circ$	
$\tau, \mu\text{sec}$	σ	$\tau, \mu\text{sec}$	σ	$\tau, \mu\text{sec}$	σ	$\tau, \mu\text{sec}$	σ
—	—	5	—	6,5	18°	—	—
—	—	9	—	10,5	17°	9,3	$17^\circ \pm 2^\circ$
—	—	13	21°	14,5	$22^\circ 20' \pm 1^\circ 30'$	13,3	24°
—	—	17	21°	18,5	19°	17,3	18°
23,3	$18^\circ 30'$	21	18°	22,5	19°	21,3	20°
27,3	18°	25	$18^\circ 40'$	26,5	21°	25,3	—
31,3	—	29	$18^\circ 40'$	30,5	20°	29,3	—
35,3	19°	33	19°	34,5	21°	33,3	20°
39,3	$19^\circ 30'$	37	18°	38,5	21°	37,3	20°
43,3	19°	41	19°	—	—	—	—

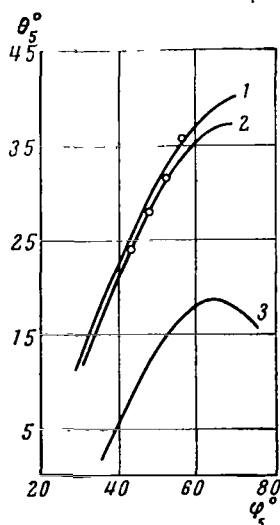


Figure 9. Dependence of θ_5 on $\theta_5 = \alpha_0$ in CO_2 .

The authors would like to express their sincere gratitude to their colleagues at the laboratory, T. V. Bazhenova and I. M. Naboko, for the interest they exhibited in the work, their discussion of the results, and for a number of valuable comments.

REFERENCES

/191

1. Ludloff, H. F.: Aerodynamics of explosion waves. In: *Problemy mekhaniki. (Problems of Mechanics.)* Edited by R. Mizes and P. Karman. Moscow, IL, 1955.
2. Gvozdeva, L. G.: The reflection of detonation wave in gaseous media. In: *Fizicheskaya gazodinamika i svoystva gazov pri vysokikh temperaturakh. (Physical Gas Dynamics and Properties of Gases at High Temperatures.)* Moscow, Izd-vo "Nauka", 1964.
3. Bryson, A. E. and R. W. F. Gross: Diffraction of strong shocks by cones, cylinders, and spheres. *J. Fluid Mech.*, Vol. 10, 1961.
4. White, B. R.: An experimental survey of the Mach reflection of shock waves. *Proc. of II Midwest Conf. on Fluid Mech.*, Vol. 21, No. 3, 1952.
5. Bleakney, V.: The Mach reflection of shock waves. *Proceedings of Symposium in Applied Mathematics*, Vol. 5, New York, 1954, p. 283.
6. Courant, R. and K. O. Friedrichs: *Supersonic Flow and Shock Waves*. New York, Interscience Publishers, 1948.
7. Bazhenova, T. V. and O. A. Predvoditeleva: Values of air parameters behind a normal shock wave and behind a reflected shock wave in the presence of equilibrium and frozen dissociation. In: *Fizicheskaya gazodinamika i*

teploobmen. (*Physical Gas Dynamics and Heat Exchange*). Izd-vo AN SSSR, 1961.

8. Bazhenova, T. V. and S. G. Zaytsev: Carbon dioxide parameters behind a reflected shock wave and an estimate of the onset time of equilibrium dissociation at temperatures of 4,000-5,000°K. In: *Fizicheskaya gazodinamika, teploobmen i termodinamika gazov pri vysokikh temperaturakh.* (*Physical Gas Dynamics, Heat Exchange, and Thermodynamics of Gases at High Temperatures.*) Izd-vo AN SSSR, 1962.
9. Gurvich, L. V. et al.: *Termodinamicheskiye svoystva individual'nykh veshchestv.* (*Thermodynamic Properties of Individual Substances.*) Vol. 2, Izd-vo AN SSSR, 1962.
10. Strelov, R. A. and A. Cohen: Limitations of reflected shock wave methodology. *Voprosy Raketnoy Tekhniki*, No. 9, 1959.
11. Bazhenova, T. V. and I. M. Naboko: On the question concerning the rate of physical and chemical transformations of CO₂ molecules behind a shock wave at temperatures of 2,000-4,000°K. *Doklady AN SSSR*, Vol. 152, No. 2, 1964.
12. Naboko, I. M.: Investigation of the state of a gas behind a shock wave according to the pattern of flow around an obstacle placed in a shock tube. In this collection.

NONSTATIONARY HEAT EXCHANGE IN THE REFLECTION OF A SHOCK WAVE

Yu. A. Polyakov

A shock tube makes it possible, under laboratory conditions, to reproduce /192 the following problem, which is important for the gas dynamics of flight vehicles: the reflection of a shock wave from a solid wall. The process of the formation of a shock wave in front of a body that is flying at supersonic velocity is, in principle, a nonstationary process, and it should be considered as a reflection process. In addition to the gas-dynamic parameters, the reflection process is also determined by the heat exchange between the solid and the layer of decelerated high-temperature gas which arises instantaneously after the reflection of the wave. In this case, after a certain length of time, the gas is stationary near the wall, and we have the nonstationary transfer of energy to the wall under the conditions of contact of two media with various initial temperature conditions. The energy losses related to the thermal conductivity of the mixture, diffusion (taken into account during recombination of atoms on the wall) and emission at high M affect the velocity of the reflected wave, the relaxation processes and, as a result, the process of the formation of a shock wave near the body. Determination of the heat flows during reflection makes it possible to estimate the losses and to trace their effect on the gas dynamics of the reacting gas.

Procedure for Measuring Heat Flows

The brevity of the processes in shock tubes imposes serious requirements on the recording equipment. To obtain reliable information on a process, a device is needed with a time resolution of up to 10^{-6} - 10^{-7} sec. An important value is acquired by questions of inertness and sensitivity of the heat-transfer meter when measuring heat effects under the conditions of rapid processes. In addition to thin-film resistance thermometers [1, 2], calorimetric transducers are employed in the study of heat exchange in a shock tube; these transducers directly measure the heat flows by integrating the nonstationary temperature profile along the thickness of the measuring plate (calorimeter) [3]. In this case the results of the experiments are quite accurate until heat losses begin to show up in the backing. An increase in the thickness of the transducer leads to a decrease in sensitivity of this method, an excessive decrease in thickness of the calorimeter decreases the "real" time of the experiment, or the losses in the backing increase in time, and the recording technique is not taken into account.

Consequently, when selecting the calorimeter thickness, the material of the transducer and the backing on which it is placed, it is necessary to analyze the technique from the viewpoint of heat losses through the contact surface: *i.e.*, plate (transducer) plus semibounded body (backing).

An expression was derived in [4] for the temperature field of the backing /193 when it makes contact with the plate, on the free surface of which a heat flow q_0 acts. Beginning with the period of time $\tau > \tau_0$, the temperature field of the backing is determined by the following expression:

$$t_i(x, \tau) = \frac{4q_0 \sqrt{a_i \tau} z}{\lambda_i (1+z)} \sum_{n=0}^{\infty} \left(\frac{1-z}{1+z} \right)^n \operatorname{ierfc} \left[\frac{(2n+1) \frac{l}{\sqrt{a_m}} + \frac{x}{\sqrt{a_i}}}{2\sqrt{\tau}} \right], \quad (1)$$

where $z = \frac{\lambda_i}{\lambda_m} \sqrt{\frac{a_m}{a_i}}$ [4]; α_i and λ_i are the thermal diffusivity and the heat conductivity of the backing, respectively; α_m and λ_m are the thermal diffusivity and the heat conductivity of the plate, respectively; l is the thickness of the transducer.

The problem consists of determining the heat flow to the backing, depending on the characteristic of the pair z and $Fo = \alpha_m \tau / l^2$. We shall differentiate expression (1) with respect to x

$$\frac{\partial t_i(x, \tau)}{\partial x} = \frac{2q_0 z}{\lambda_i (1+z)} \sum_{n=0}^{\infty} \left(\frac{1-z}{1+z} \right)^n \left\{ \operatorname{erf} \left[\frac{(2n+1) \frac{l}{\sqrt{a_m}} + \frac{x}{\sqrt{a_i}}}{2\sqrt{\tau}} \right] - 1 \right\}. \quad (2)$$

The heat flow to the backing is determined as follows:

$$q_n = -\lambda_i \frac{\partial t_i(x, \tau)}{\partial x} \Big|_{x=0} = \frac{2q_0 z}{1+z} \sum_{n=0}^{\infty} \left(\frac{1-z}{1+z} \right)^n \left[1 - \operatorname{erf} \left(\frac{2n+1}{2\sqrt{Fo}} \right) \right]. \quad (3)$$

The relative heat flow is determined from (3) in the following manner:

$$\frac{q_n}{q_0} = \frac{2z}{1+z} \sum_{n=0}^{\infty} \left(\frac{1-z}{1+z} \right)^n \left[1 - \operatorname{erf} \left(\frac{2n+1}{2\sqrt{Fo}} \right) \right]. \quad (4)$$

The calculation of q_n/q_0 as a function of Fo is performed with formula (4) for combinations of materials of the plate and the semibounded body which encompass practically all combinations of transducers and backings. In this case the thermophysical properties of the materials were considered to be independent of temperature (see table).

Figure 1 illustrates the results of the calculations. It can be seen from the graph that the thickness of the calorimetric transducer is related to the time of the experiment and the amount of given (and not considered in the experiment) losses across the contact to the backing. If we adopt 4% ($q_n/q_0 = 0.04$) as the permissible amount of losses, the corresponding Fo_{pr} can be determined

TABLE

Plate (transducer)	Semibounded body (backing)	z
copper	asbestos(sheet)	0.016
nickel	ebonite	0.020
platinum	asbestos(sheet)	0.046
nickel	quartz	0.186

for each pair of materials characterized by the quantity z . The thickness of the transducer is easily determined for the adopted α_m and experiment time

$$\tau \text{ as } l = \sqrt{\alpha_m \tau / Fo} \cdot pr.$$

Thus, in our case, for a nickel-foil transducer ($z = 0.02$) with a thickness of $l = 50$ microns, during an experiment of up to ~ 500 μ sec in duration, the heat flow across the contact to the backing cannot exceed $\sim 4.2\%$ of

the heat flow accumulated by the transducer. As will be indicated below, the selection of the transducer thickness l and the thickness of its material is closely related to the sensitivity of the calorimetric method of measurement.

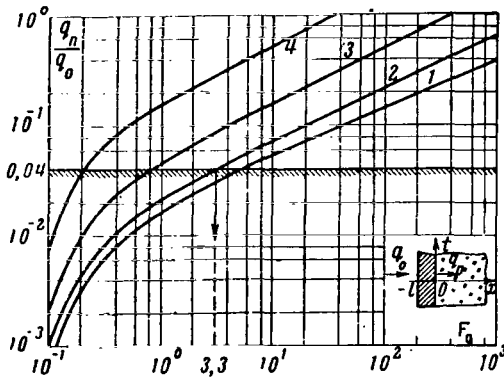


Figure 1. Dependence of q_n/q_0 on Fo ($Fo = \alpha_m \tau / l^2$). (1) $z = 0.016$; (2) $z = 0.020$; (3) $z = 0.046$; (4) $z = 0.186$.

To study the heat exchange behind a reflected wave, the calorimetric transducer was made from nickel foil 50 microns in thickness and 2.5×10 mm in area, and was glued to an ebonite backing made in the shape of a disk. BF-2 adhesive, due to its low heat conductivity, promotes a decrease in heat losses across the contact during the experiment. Silver leads were welded to the ends of the transducer.

Since the calorimetric transducer operates on the principle of a resistance thermocouple, it is easy to derive the relationship between the heat flow measured by the transducer and the voltage change in it when the initial current is flowing through the circuit.

It may be considered that the relationship $R_t = R_0[1 + \alpha(t - t_0)]$ is satisfied for the transducer material, where R_t is the resistance of the transducer at temperature t , R_0 is the resistance of the transducer at the initial temperature t_0 , and α is the temperature coefficient of the resistance of the transducer material.

It is important to note that $t = 1/l \int_{-l}^0 t(x, \tau) dx$ (see Figure 1), where $t(x, \tau)$ is the temperature profile along the transducer thickness. It is easy to see that $\frac{\partial R_t}{\partial \tau} = \frac{\alpha R_0}{l} \int_{-l}^0 \frac{\partial t(x, \tau)}{\partial \tau} dx$. Since $\frac{\partial t(x, \tau)}{\partial \tau} = \frac{1}{\gamma c} \frac{\partial}{\partial x} (\lambda \text{grad } t)$, however, we

have $\frac{dR_t}{d\tau} = \frac{\alpha R_0}{l\gamma c} \int_{-l}^0 \frac{\partial}{\partial x} (\lambda \text{grad } t) dx = \frac{\alpha R_0}{l\gamma c} (\lambda \text{grad } t) \Big|_{-l}^0$, where γ is the density of the substance and c is the specific heat. If we disregard the heat losses across the contact to the backing, $dR_t/d\tau = q_\tau \alpha R_0 / l\gamma c$, where $q_\tau = -\lambda \text{grad } t$ is the heat flow across the surface $x = -l$. If measuring current I_0 flows across the transducer,

$$\frac{dR_t}{d\tau} = \frac{du}{I_0 d\tau} = \frac{q_\tau \alpha R_0}{l\gamma c}$$

or $du/d\tau = \alpha I_0 R_0 q_\tau / l\gamma c$ is the time derivative of the signal (change in potential difference on the transducer). Consequently,

$$q_\tau = \frac{l\gamma c}{\alpha I_0 R_0} \frac{du}{d\tau}. \quad (5)$$

The sensitivity of the transducer is determined as $\Delta U = \frac{\alpha R_0 I_0}{l\gamma c} q_\tau \Delta \tau$.

To increase the sensitivity of the transducer, since $\Delta \tau$ is on the order of a microsecond, we try to select $\alpha R_0 I_0 / l\gamma c$ as large as possible. This means /195 that it is necessary to select a material for the transducer with the highest value of $\alpha \rho_0 / c\gamma$. In our experiments $\alpha \rho_0 / \gamma c = 3.6 \times 10^{-12}$ [ohms·mm²/kcal/m²].

The calorimetric method has a number of advantages over the film transducer for investigating heat exchange at high M_g :

1. The calorimeter transducer is durable and can withstand significant thermal shocks at high M_g (~ 20) without an essential change in its physical properties.

2. In view of the fact that the operating resistance of the calorimeter transducer is 100 times less than the resistance of the film transducer, the effect of the shunting resistance of the conducting medium on the transducer readings will show up at higher M_g than for the film transducer. Consequently, the range of action of the calorimeter transducer is somewhat wider. Calorimeters can be employed for media with a higher percentage of ionization.

3. The manufacturing technique of the calorimeter transducer is not complicated and does not require special equipment.

4. It can be seen from equation (5) that a calorimetric transducer in an experiment measures the quantity $du/d\tau$, which determines the amount and character of heat flow.

Thus, the character of energy losses during brief processes can be evaluated on the basis of pulse shape by a single value.

Application of a nickel transducer makes it possible to approximate the actual conditions with respect to the wall material of the shock tube, since

the heat flow to the glass backing in a nonstationary process for a film transducer and the heat flow to the steel wall of the shock tube are not equal to one another in principle. Special methodological experiments are necessary in order to evaluate the difference between them.

Shock Tube. Experiment

The experiments were conducted in a stainless-steel shock tube with an internal diameter of 50 mm. A single-diaphragm version of tube operation was employed with hydrogen as the propelling gas and air in the low-pressure chamber. A VN-461 fore pump with an oil trap was used to create a preliminary vacuum in the chambers; the vacuum was measured by a VT-2P thermovacuum meter. The layout of the experimental apparatus is shown in Figure 2. The length of the low-pressure chamber amounted to approximately 4 m. An ionization transducer was placed at a fixed distance from the end; this transducer triggered the scanning of an IO-4 oscillograph as a shock wave passed by it. The velocity of the incident shock wave was determined as the quotient from dividing the distance between the ionization transducer and the end of the shock tube by the time in which the wave traveled this distance.

The calorimetric transducer was placed flush against the end surface toward the front of the shock wave. The leads from the transducer were sealed with special vacuum cement.

After reflection, there appeared a new energy state in the gas volume at the end of the tube; this state can be calculated, in principle, under any assumption concerning the character of behavior of the physical and chemical processes in the gas. The experiments were conducted at an initial tube pressure of $p_1 = 10^{-3}$ atm in a shock wave velocity range from 2.5 to 4.5 km/sec. On the assumption of equilibrium dissociation behind the reflected shock wave, the gas

parameters from the velocity of the incident wave are given in Figure 3 [5].

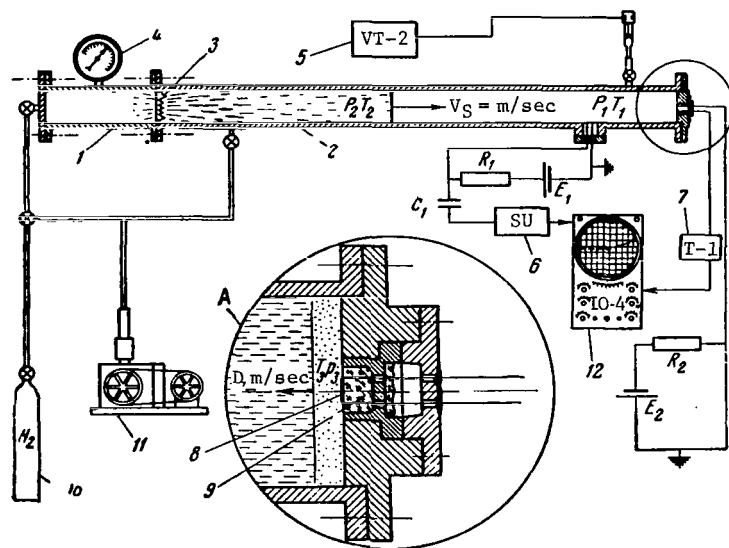


Figure 2. Schematic Diagram of Experimental Installation (Shock Tube and Measuring Circuit). (1) high-pressure chamber; (2) low-pressure chamber; (3) diaphragm; (4) manometer; (5) VT-2 vacuum gauge; (6) synchronization unit; (7) d-c amplifier; (8) calorimeter transducer; (9) backing (ebonite); (10) compressed hydrogen cylinder; (11) fore pump; (12) IO-4 pulse oscillograph.

The heat flows were measured in the experiment at $T_3 = 6,500^\circ\text{K}$ and $p \approx 2$ atm, when over 50% of the air molecules are in a dissociated state.

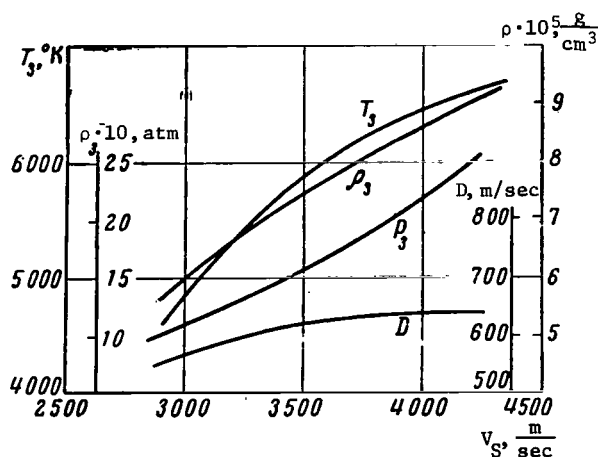


Figure 3. Dependence of Temperature T_3 , Density ρ_3 , Pressure p_3 , and Velocity of Reflected Wave D on Velocity of Incident Wave V_s (Equilibrium Dissociation).

Figure 4 shows a typical photographic oscillogram of a pulse from a calorimetric transducer. It can be seen from the experiment that $du/d\tau$ varies in proportion to $1/\sqrt{\tau}$. The arrival of the contact surface is clearly visible in the photograph. Consequently, the heat flow during the experiment varies $1/\sqrt{\tau}$. It is known from the theory of heat conductivity [6] that this law of variation of the heat flow in time is accomplished only in the case when the temperature on the boundary of a semibounded body remains constant during the heat exchange process after an instantaneous rise. /197

In other words, the contact temperature of two media remains constant during the reflection period, which confirms the theoretical conclusions of nonstationary contact heat exchange [7].

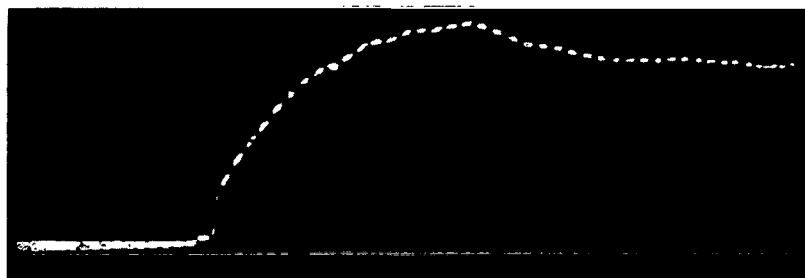


Figure 4. Typical Photographic Oscillogram of Heat Pulse From a Calorimetric Transducer After Reflection of a Shock Wave. $p_1 = 0.76$ mm Hg; $M_s = 8.0$; 10- μsec markers.

Actually, the film transducer, which was placed at the end, recorded a constant rise in surface temperature by Δt , which varied depending on the conditions.

Figure 5 illustrates the experimental values which correspond to the heat flows after a 30th of a microsecond from the beginning of the heat exchange process. The high absolute value of the heat flows, which reach $10^7 \text{ kcal/m}^2 \text{ hr}$,

should be noted.

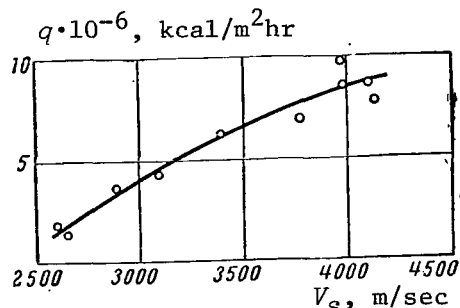


Figure 5. Dependence of Heat Flow q to the End of a Shock Tube After Reflection of a Wave on the Velocity of the Incident Wave V_s . $p_1 = 0.76$

mm Hg; $\tau_{cal} = 30 \mu\text{sec}$.

Discussion of Results of Experiments

In the reflection of a shock wave, a layer of reacting gas arises at the end wall with nonstationary temperature gradients and concentration of mixture components near the wall. Due to the short time in which the high-temperature gas remains at the wall (a tenth of a microsecond), natural convection can be disregarded, and the heat flow to the wall is determined by the sum of the amount of heat due to heat conductivity and the amount of heat transmitted to the body due to diffusion. The latter, however, is considered only for recombination of atoms on the wall.

The most detailed analysis of the problem of heat transfer for a binary mixture was conducted by Fay and Riddle [8], the qualitative aspect of which can be extended to 198 the problem of heat exchange behind a reflected shock wave.

It should be recalled, however, that there is no dynamic boundary layer during reflection and energy transfer is accomplished under conditions of nonstationary concentration and temperature boundary layers. In this case it is more correct to conduct the analysis by considering the change in enthalpy from the gas to the wall.

The conditions reproduced in the experiments ($p_1 \approx 10^{-3}$ atm), with respect to the parameters behind a reflected wave (see Figure 3), correspond approximately to flight altitudes at a supersonic velocity $H \sim 40$ km.

According to Cheng's calculations [9], this altitude corresponds to the zone of the equilibrium layer near the wall. We assumed that the reaction rates are high as compared to the diffusion rates of the atomic components of the mixture and that the rate of change of the temperature layer (enthalpy) near the wall does not destroy the local thermodynamic equilibrium. In this case the heat flow practically does not depend on the processes on the surface of the wall. If the wall temperature is relatively low ($< 1,000^\circ\text{K}$), the concentration of atoms will become equal to zero near the wall at a certain distance from the body. In other words, energy (if radiation is disregarded) is transmitted to the wall due to heat conductivity. In this case, undoubtedly, the diffusion flows distort the enthalpy curve and, as calculations of the kinetic transfer coefficients [10] at high temperatures have indicated, such coefficients as heat conductivity, heat capacity, and viscosity of the reacting mixture depend on temperature and concentration in a complicated manner.

Reflection of an ideal gas from a heat-conducting wall, under the assumption of $\lambda = \lambda_n T^n$, where λ is the heat conductivity of the gas, is considered by

Goldsworthy [11].

Approximation of the coefficient of heat conductivity of dissociated air by a linear function of temperature as $\lambda = \lambda_1 T$ is not well substantiated, but for pressures on the order of 1-10 atm, which was accomplished in the experiments in the zone behind the reflected wave, in the temperature range of 2,000-6,500°K, it can be taken as a first approximation [10].

This bold assumption makes it possible to solve Goldsworthy's heat conductivity equations (see [11] for designations)

$$\frac{\partial T}{\partial \tau} = \frac{\lambda_w}{\rho_w c_w} \frac{\partial^2 T}{\partial y^2} \quad (\text{for calorimeter}) \quad y > 0$$

and

$$\frac{\partial T}{\partial \tau} = \frac{\partial}{\partial \psi} \left(\frac{\lambda \rho_3 \partial T}{c_p R T \partial \psi} \right) \quad (\text{for gas}) \quad y < 0$$

under the condition

$$\left(\lambda \frac{\partial T}{\partial y} \right)_{y=0} = \left(\lambda_w \frac{\partial T}{\partial y} \right)_{y=0}$$

as

$$T - T_1 = A \left[1 - \operatorname{erf} \frac{y}{2\sqrt{a_w \tau}} \right] \quad (\text{when } y > 0) \quad (6)$$

and

$$T - T_3 = B \left[1 + \operatorname{erf} \frac{\psi}{2\sqrt{a_g \tau}} \right] \quad (\text{when } y < 0), \quad (7)$$

where $a_w = \frac{\lambda_w}{c_w \rho_w}$ is the thermal diffusivity of the calorimeter material, $a_g = \frac{\lambda_1 \rho_3}{c_p R}$ is the thermal diffusivity of the gas, $\psi = \int_{y=0}^y \rho dy$ is the integral variable, T_3 is the temperature of the gas behind the reflected wave, and T_1 is the temperature of the calorimeter prior to the arrival of the shock wave. Coefficients A and B are determined from the condition $y = 0$. /199

It was assumed in the evaluation of the heat flow from the gas aspect that there are no losses across the rear end of the calorimeter and the contact temperature of the calorimeter and the ebonite backing coincide with T_1 . Fo is approximately equal to 0.1 for a 30th of a microsecond and the contact temperature differs from T_1 by less than 5% [6].

To estimate the heat flow, it is necessary to differentiate equation (7) with respect to ψ and find the gradient for $y = 0$ ($\psi = 0$)

$$\frac{\partial T}{\partial \psi} = -\frac{T_3 - T_1}{1+m} \left(\operatorname{erf} \frac{\psi}{2\sqrt{a_g \tau}} \right)' = -\frac{T_3 - T_1}{1+m} \frac{2}{\sqrt{\pi}} e^{-\frac{\psi^2}{4a_g \tau}} \left(\frac{1}{2\sqrt{a_g \tau}} \right),$$

when $y = 0$ ($\psi = 0$)

$$\frac{\partial T}{\partial \psi} = -\frac{T_3 - T_1}{1+m} \frac{1}{\sqrt{\pi a_g \tau}}.$$

Since

$$\frac{\partial T}{\partial y} = \frac{\partial T}{\partial \psi} \rho(y),$$

then

$$\left. \frac{\partial T}{\partial y} \right|_{y=0} = \left. \frac{\partial T}{\partial \psi} \right|_{y=0} \cdot \rho|_{y=0}$$

and

$$q_\tau = -\lambda|_{\tau} \left(-\frac{T_3 - T_1}{1+m} \right) \left(\frac{1}{\sqrt{\pi a_g \tau}} \right) \rho|_{y=0}. \quad (8)$$

The quantity $m = \sqrt{\frac{\lambda_1 T_3 c_p \rho_3}{\lambda_0 c_w \tau}}$, where ρ_3 is the density of the gas behind the reflected wave, which was determined on the basis of our tables.

Calculations on the basis of formula (8) indicated that, in spite of the substantial assumptions, the heat flows due to heat conductivity lie in the zone of the experimental data. In the calculations, $m \ll 1$, which significantly simplifies calculation. A calculated curve was derived for (8) in Figure 5. It can be seen from the graph that the scatter of the experimental points becomes greater as the velocity increases.

One of the important questions concerns the conditions of retaining the initial statement of the problem regarding two semibounded bodies in contact (gas and calorimeter).

Calculations of the velocity of propagation of the temperature field with respect to a stationary gas indicated that after the time $\tau > 0.5 \mu\text{sec}$, the region of decelerated gas behind the reflected shock wave increases so quickly that the conditions of semibounded bodies are fully justified when considering the contact problem.

Having the laws of heat exchange on the end of the lateral wall after shock wave reflection at our disposal, we can compare the energy losses across the surface and the enthalpy of the gas mass behind the reflected wave. On the basis of the fact that $q \sim 1/\sqrt{\tau}$ for the end and for the lateral wall, and assuming that $D = \text{const}$, while $S_{\text{end}} = \pi d^2/4$, we can determine the form of the function which characterizes the ratio of energy losses to the enthalpy of the corresponding gas volume behind the reflected wave. As a result of an elementary calculation, the form of this function is presented as follows:

$$\varphi = \frac{Q}{U} = 8(q_{lat} D \tau + q_{end} \frac{d}{4}) / h_3 \rho_3 D d, \quad (9)$$

where h_3 is the enthalpy of the gas behind the reflected wave, d is the diameter/200 of the shock tube, D is the velocity of the reflected wave, τ is the time, q_{lat} is the heat flow to the lateral wall and q_{end} is the heat flow to the end of the tube.

For the given conditions, the losses change in time as

$$\varphi = \left(L_1 \sqrt{\tau} + \frac{L_2}{\sqrt{\tau}} \right),$$

where the first term determines the relative losses across the lateral wall of the tube and the second term determines them across the end.

Losses commensurate with the energy of the gas volume will take place when $\varphi \approx 1$, i.e., at the initial moment of reflection (formation of reflection after contact with front of wall). At this moment, when the losses from the lateral wall can be disregarded, an essential effect of heat exchange on reflection is established. The limiting time for the losses is determined by equation (9) for the corresponding φ .

The results of the calculation indicate that the assumption concerning thermodynamic equilibrium in the considered range of gas-dynamic parameters (T_3 , p_3 , ρ_3) apparently corresponds to actual conditions. It should not be forgotten, however, that a certain amount of arbitrariness in the selection of the transfer coefficient can render a substantial effect on the calculation of heat exchange in the region behind the reflected shock wave.

It should be noted in conclusion that the application of the calorimetric method for measuring heat flows is not restricted only to the considered problem. After ridding the film thermometer of its resistance with respect to sensitivity, however, it can be used successfully for investigating heat exchange in various models placed in a shock tube against a supersonic flow.

The author considers it his duty to thank A. S. Predvoditlev for his attention to the work and O. A. Predvoditeleva for her discussion of the results.

REFERENCES

1. Polyakov, Yu. A. and Ye. A. Mit'kina: Thin-film resistance thermometer. *Pribery i Tekhnika Eksperimenta*, No. 4, 1961.
2. Hartunian, R. A. and R. L. Varnig: On thin-film heat-transfer measurements in shock tubes and shock tunnels. *J. Phys. Fluids*, Vol. 5, No. 2, 1962.
3. Rose, P. H. and V. I. Stark: Measurements of heat exchange at a frontal point in dissociated air. *Problemy dvizheniya golovnoy chasti raket dal'nego deystviya*. (Motion Problems of Long-Range Missile Nose Cones.)

- Collection of translations. Moscow, IL, 1960.
4. Polyakov, Yu. A.: Application of film transducers for studying heat exchange in a dissociated gas flow. In: *Fizicheskaya gazodinamika, teploobmen i termodinamika gazov vysokikh temperatur.* (Physical Gas Dynamics, Heat Exchange, and Thermodynamics of High-Temperature Gases.) Izd-vo AN SSSR, 1962.
 5. Bazhenova, T. V. and O. A. Predvoditeleva: Values of air parameters behind a normal shock wave and behind a reflected shock wave in equilibrium and frozen dissociation. In: *Fizicheskaya gazodinamika i teploobmen.* (Physical Gas Dynamics and Heat Exchange.) Izd-vo AN SSSR, 1961.
 6. Lykov, A. V.: *Teoriya teploprovodnosti.* (Theory of Heat Conductivity.) Moscow, GITTL, 1952.
 7. Greber, G. and S. Erk: Fundamentals of the study of heat exchange. *ONTI NKTP, SSSR*, 1939.
 8. Fay, D. and F. Riddle: Theoretical analysis of heat exchange in a forward critical point enveloped by dissociated air. In: *Gazodinamika i teploobmen pri nalichii khimicheskikh reaktsiy.* (Gas Dynamics and Heat Exchange in the Presence of Chemical Reactions.) Collection of translations. Moscow, IL, 1962.
 9. Cheng, H. K.: Recent advances in hypersonic flow research. *AIAA Journal*, Vol. 1, No. 2, 1963.
 10. Stupochenko, Ye. V., B. B. Dotsenko, I. P. Stakhanov and Ye. V. Samuylov: Methods for calculating the kinetic coefficients of air at high temperatures. In: *Fizicheskaya gazodinamika.* (Physical Gas Dynamics.) Izd-vo AN SSSR, 1959.
 11. Goldsworthy, F. A.: The structure of a contact region with application to the reflection of a shock wave from a heat-conducting wall. *J. Fluid Mech.*, Vol. 5, No. 1, 1959.

HEAT LOSSES ASSOCIATED WITH THE REFLECTION OF A SHOCK WAVE FROM THE END OF A TUBE

O. A. Predvoditeleva

The amount of heat transmitted during the reflection of a shock wave to the lateral and end surfaces of a shock tube was estimated in [1]. The conditions of the experiment described in [1], however, did not make it possible to measure the heat flow to the end of the tube directly; therefore, an essential assumption was made that the heat flow from a reflected wave of heated gas to the end of a shock tube is equal to the heat flow to the lateral wall. This study was set up for the purpose of validating this assumption. /201

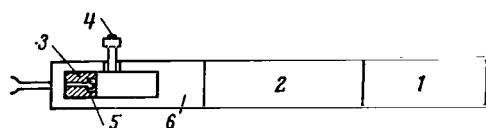


Figure 1. UT-2 Shock Tube.

The heat flow in [1] and in this article is determined by the surface temperature of the shock tube as measured by platinum resistance thermometers.

The velocity of the shock waves was determined by photographs of the Töpler pattern of flow.

A diagram of the shock tube is illustrated in Figure 1, where 1 is the high-pressure chamber, 2 m in length; 2 is the low-pressure chamber, 2.7 m in length; 3 is the duralumin end; 4 is the pressure pickup; 5 is the resistance thermometer; and 6 is the experimental section, 0.21 m in length.

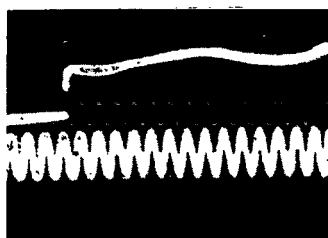


Figure 2. Oscillogram of Platinum Resistance Thermometer Readings. Oscillation Period of Sinusoidal Signal 10 μ sec.

The platinum resistance thermometer [2] was built into the shock tube in such a way that its surface was flush with the surface of the duralumin end of the shock tube. A typical oscillogram of the resistance thermometer readings is shown in Figure 2 (the oscillogram was recorded for an incident wave with $M = 7.2$, propagating in N_2 at an initial pressure $p_0 = 12.7$ mm Hg). The oscillograms were processed by /202 the method described in [1]. Characteristic curves of the change in temperature of the end surface and the change in the heat flow to the end converted with respect to it in time are illustrated in Figure 3.

The order of magnitude of the heat flow to the end of the shock tube can be obtained from the table for nitrogen and carbon dioxide for shock waves of different intensity. If we assume that the heat flow to the end of the shock tube is constant and equal to the maximum value of the flow \bar{q} (see Figure 3), then the amount of heat absorbed by the end in the time $t = 7 \mu$ sec (the time of 7 μ sec was adopted only for convenience of comparison

with [1]) can be calculated with the formula $Q_{end}^{exp} = qSt$, where S is the area of the end (16 cm^2) and q is the heat flow.

TABLE

Gas	N_2					CO_2		
$M_{inc. wave}$	7.2	8.3	8.3	6.6	8.3	8.5	7.8	8.4
q_{max} , cal/cm ² ·sec	250	300	300	138	375	213	160	358
D_{exp} , m/sec	600	648	627	520	none	375	365	370
p_0 , mm Hg	12.7	12.3	12.5	12.5	12.4	12.3	12.7	12.3
$Q_{end}^{exp} \cdot 10^2$, cal	27.9	3.35	3.35	1.55	4.20	2.38	1.78	4.0
ΔE , cal	0.71	0.35	1.11	0.67	none	-	-	-

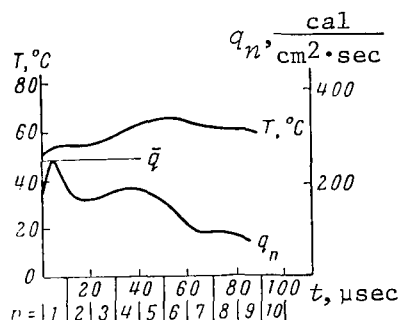


Figure 3. Variation of Temperature of End Surface and Heat Flow over Time.

The heat quantities thus estimated are shown in the table. They amount to $2-4.5 \cdot 10^{-2}$ cal in 7 μsec .

It should be noted that the accuracy in determining the heat flows with platinum resistance thermometers is rather low (in some cases the error amounts to 40-50%).

Nevertheless, the order of the obtained quantity Q_{end}^{exp} makes it possible to evaluate the role of heat losses in the process of reflection and subsequent propagation of a shock wave. The total energy of the gas behind a reflected wave, which is calculated on the basis of the velocity of the reflected shock wave D_{exp} , is less than the energy of the gas behind

the incident wave by $\Delta E \approx 0.5$ cal (see table), which determines the total amount of losses during reflection.

The following conclusion can be made on the basis of the tabular data: energy losses caused by the heat conductivity of the metallic end during shock wave reflection amount to approximately 2-10% of the total quantity of losses observed during reflection of the shock wave.

REFERENCES

1. Bazhenova, T. V., O. A. Predvoditeleva and T. V. Nadezhina: Losses during reflection of shock waves from an end in a shock tube. In: *Fizicheskaya gazodinamika i svoystva gazov pri vysokikh temperaturakh*. (Physical Gas

- Dynamics and Properties of Gases at High Temperatures.*) Moscow, Izd-vo "Nauka", 1964.
2. Polyakov, Yu. A. and Ye. Mit'kina: Thin-film resistance thermometer. *Pri-bory i Tekhnika Eksperimenta*, No. 4, 1961.

FORMATION OF A GAS FLOW BEFORE A FLAME FRONT

G. D. Salamandra

A series of studies [1-4] directed by A. S. Predvoditelev (Corresponding /203
Member of the Soviet Academy of Sciences) indicated that, according to the known law of flame propagation, the place of formation of the shock wave which forms before the flame front in the initial stage of flame development can be precalculated with a sufficient degree of accuracy. In these studies the state of the gas before the flame front was calculated by the characteristic curve method [5, 6]. It was assumed that the flame generates disturbances which set the gas into motion at a velocity equal to the flame velocity at the moment of sending the given disturbance. Only the place of formation of the shock wave was determined in all experiments. For lack of a technique, the velocity of the gas before the flame front was not measured. The question concerning the measurement of the velocity of a gas before a flame front is especially acute in the analysis of burning accompanied by the formation of a shock wave before the flame front. Usually, when analyzing this process, the state of the gas behind the shock wave is calculated on the basis of the velocity of the shock wave and the temperature and pressure of the gas in front of the wave. This calculation is based on the laws of conservation, the equation of state of the gas, and on the assumption concerning thermodynamic equilibrium of the gas behind the shock wave. The calculation makes it possible to estimate only the velocity of the gas directly behind the shock wave. The question with regard to the distribution of gas parameters between the shock wave and the flame front, which determines the further development of the combustion process, remains open. This study was set up for the purpose of filling this gap.

To visualize the flow of a gas before a flame front in a stationary medium prior to ignition of the mixture, several artificial optical inhomogeneities were created and then set into motion together with the ambient medium [7]. Experiments were conducted in circular and rectangular tubes. Both continuous recording and frame-by-frame photography of the process was accomplished at a rate of approximately 94,000 frames/sec. The process was photographed by the Töpler method.

Figure 1a illustrates a time scanning of the initial stage of the process of combustion of a stoichiometric hydrogen-oxygen mixture in a $36 \times 36 \text{ mm}^2$ square tube. Figure 1b gives a series of instantaneous photographs of the same process obtained with the aid of a UPR high-speed camera. The flame front is fixed on the Töpler photographs in the form of a dark zone. The artificially created optical inhomogeneities set into motion by the compression waves generated by the flame are clearly visible before the flame front. An analysis of the obtained photographs indicated that the velocity of the gas along each disturbance sent by this flame front remains constant.

In order to find the relationship between the velocity of the gas along each disturbance and the velocity of the flame at the moment of sending the dis-

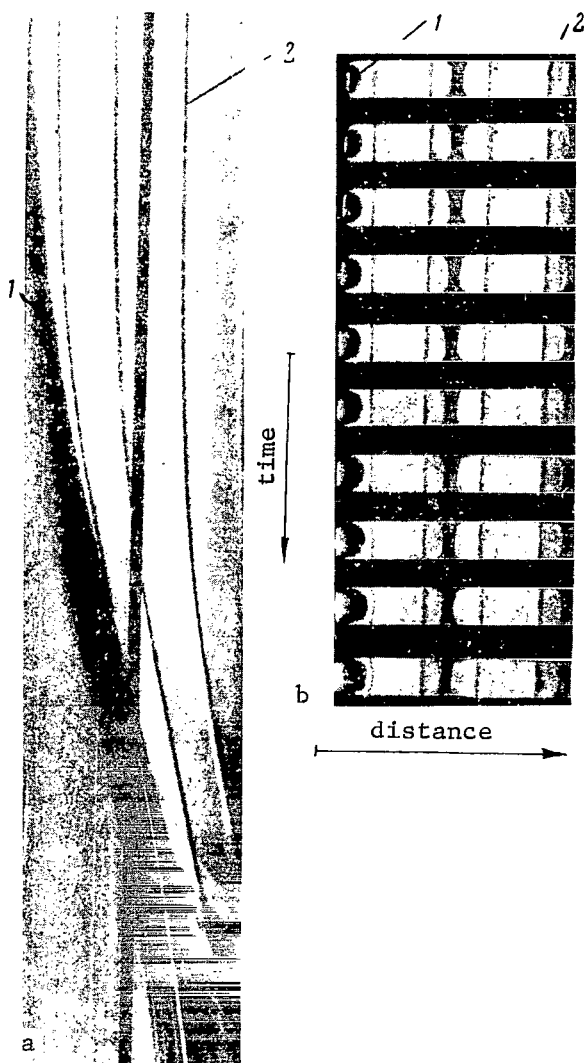


Figure 1. Initial Stage of Flame Propagation in Tube. (a) time scanning of process; (b) series of instantaneous photographs of process; (1) flame front; (2) artificially created inhomogeneity.

in the transition from slow burning to detonation.

Figure 4 schematically depicts a time scanning of the process of combustion of a stoichiometric hydrogen-oxygen mixture in a square tube. The distance from the ignition point is plotted on the abscissa axis in millimeters. The time is plotted on the ordinate axis. The numbers 1-7 denote the artificial optical inhomogeneities created at seven various points along the length of the tube.

turbance, we shall use the schematic representation of the time scanning of 204 the process as illustrated in Figure 2.

The numbers 1-4 denote the four artificially created optical inhomogeneities. The variation in flame velocity and the velocity of the inhomogeneities in time is shown in Figure 3. Having selected some fixed velocity in Figure 3, let us note in the x, t plane (see Figure 2) the moments in time in which each inhomogeneity achieves a given velocity. As can be seen from the graph, the points which correspond to equal gas velocities lie on one straight line.

The flame velocity at the moment of sending the disturbance can be found by continuing the straight lines until intersection with the flame. By knowing the velocity of the flame which sent the disturbance and the velocity of the gas set into motion by this disturbance, it is easy to find V_{gas}/V_{flame} .

An analysis of numerous time scanings of the process indicated that although 205 the flame does not overlap the entire cross section of the tube, the velocity of the gas before the flame front amounts to only a small fraction of the flame velocity, which increases to ≈ 0.8 of the flame velocity as the flame approaches the tube walls.

In order to explain how the gas flow is formed before the flame front and the nature of the relationship between the character of flame propagation and the distribution of the gas velocity before the flame front, the formation of a gas flow was studied both during so-called slow burning and

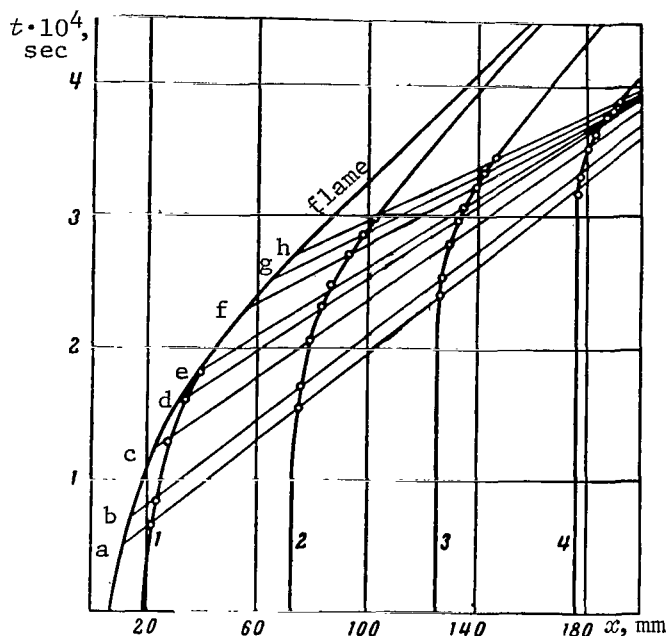


Figure 2. Schematic Representation of Time Scanning of Process. (a) 60 m/sec; (b) 80; (c) 140; (d) 200; (e) 240; (f) 300; (g) 340; (h) 360.

in time is shown in Figure 5. The distance from the spark that ignites the mixture is plotted on the abscissa axis in millimeters. The velocity is plotted on the ordinate axis in meters per second. The vertical line denotes the distance traveled by the flame. The horizontal line is drawn to the level which corresponds to the flame velocity at the time in which the plotting was made. The solid lines indicate the results of calculating the velocity of the gas before the flame front by the characteristic curve method. The dashed lines were constructed by extrapolation to the zero value

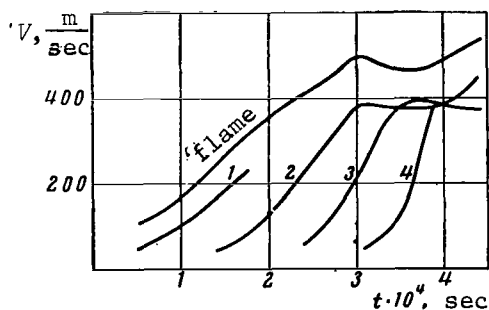


Figure 3. Dependence of Velocity of Flame Propagation and Four Artificially Created Inhomogeneities on t .

The thin solid lines indicate the disturbances fixed on a time scanning of the process. A shock wave is formed at the cumulation point of these disturbances. The dot-dash line indicates the disturbance which actuates the gas. /206

Table 1 lists the results of calculating the velocity of the gas before the flame front by the characteristic curve method [5, 6].

Some of the characteristic curves are illustrated in Figure 4 by the dashed lines. It is easily seen that the characteristic curves coincide quite accurately with the disturbances that are clearly visible in the time scanning of the process. Having plotted the characteristic curves in the x, t plane, a "velocity profile" of the gas before the flame front can be constructed for any moment of time. A corresponding plotting for five different moments

is shown in Figure 5. The distance from the spark that ignites the mixture is plotted on the abscissa axis in millimeters. The velocity is plotted on the ordinate axis in meters per second. The vertical line denotes the distance traveled by the flame. The horizontal line is drawn to the level which corresponds to the flame velocity at the time in which the plotting was made. The solid lines indicate the results of calculating the velocity of the gas before the flame front by the characteristic curve method. The dashed lines were constructed by extrapolation to the zero value of the velocity taken from the experiment. /207
The dots denote the values of the velocity of the gas before the flame front obtained from the experiment. It is easily noted that before the flame propagates with acceleration, the gas velocity reaches a maximum value near the flame front (see distribution of gas velocity before flame front at moments of time denoted by 1 and 2). A decrease in the flame velocity is accompanied by an increase in the distance between the region of maximum gas velocities and the flame. The boundary which separates the stationary gas from the gas set into motion becomes steeper and steeper as the compression waves build up. (Velocity distribution of gas before flame

TABLE 1

Time, 10^4 sec	1	1.5	2	2.5	3	3.5	4	4.5	5	5.5	6
V_{flame} , m/sec	175	260	320	380	490	510	452	450	450	456	482
V_{gas} , m/sec	140	208	256	304	392	408	362	360	360	365	386
$(2/\gamma - 1)a$, m/sec	2,815	2,883	2,931	2,979	3,067	3,083	3,037	3,035	3,035	3,040	3,061
a , m/sec	563	577	586	596	613	617	607	607	607	608	612
$V + a$, m/sec	703	785	842	900	1,005	1,025	969	967	967	973	998

TABLE 2

Time, 10^4 sec	1	1.2	1.5	1.7	2	2.2	2.5	2.7	3	3.2	3.5	3.78
V_{flame} , m/sec	300	317	357	396	465	514	590	638	706	745	785	818
V_{gas} , m/sec	240	254	286	317	372	411	472	510	565	597	627	655
$(2/\gamma - 1)a$, m/sec	2,915	2,929	2,961	2,992	3,047	3,086	3,147	3,185	3,240	3,272	3,312	3,330
a , m/sec	583	586	592	598	609	617	629	637	648	654	660	666
$V + a$, m/sec	823	840	878	915	981	1,028	1,101	1,147	1,213	1,251	1,287	1,321

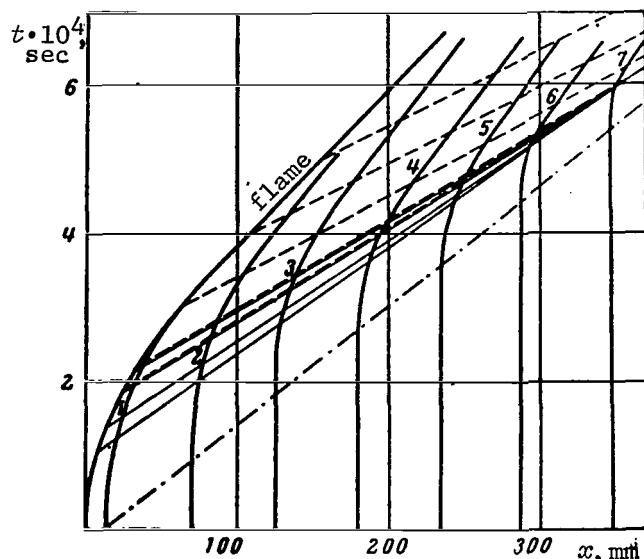


Figure 4. Development of the Combustion Process in a $36 \times 36 \text{ mm}^2$ Square Tube.

main channel before the flame front. A time scanning of the development of the process is shown in Figure 6. The shock wave, which leaves the narrow channel and enters the wide channel, is first decelerated and then gradually accelerated under the action of the compression waves which overtake it.

As can be seen from the photograph, this method of ignition provides for the continuous increase of flame velocity right up to the transition from slow burning to detonation.

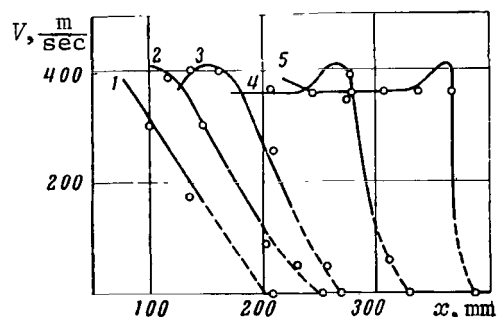


Figure 5. Distribution of V before Flame Front at Various Moments of Time. (1) $3 \cdot 10^{-4}$ sec; (2) $3.5 \cdot 10^{-4}$; (3) $4 \cdot 10^{-4}$; (4) $5 \cdot 10^{-4}$; (5) $6 \cdot 10^{-4}$.

front in subsequent moments of time.)

The formation of a gas flow before a flame front was examined above in the case when slow burning does not change into detonation. It is also of interest to study the gas flow before the flame front in the case of the transition from slow burning to detonation. In order to bring about the transition to detonation at a short distance from ignition, the mixture was ignited in a narrow channel with a diameter of 3 mm and a length of 45 mm and connected to a $36 \times 36 \text{ mm}^2$ square channel. The diameter and length of the narrow channel were selected in such a way that a shock wave was formed prior to entry into the

The results of calculating the state of the gas before the flame front are listed in Table 2.

The velocity distribution of the gas before the flame front for three various moments in time is shown in Figure 7. As the combustion process develops, there takes place a certain equalization of the gas velocity between the shock wave and the flame front, but the general tendency for the gas velocity to increase in a direction from the shock wave to the flame front is retained.

Since the gas parameters along each characteristic curve are maintained constant, the density and pressure distribution before the flame front can be found. Until the elementary compression waves build up into a shock wave, the following relationships can be used



Figure 6. Transition from Slow Burning to Detonation.

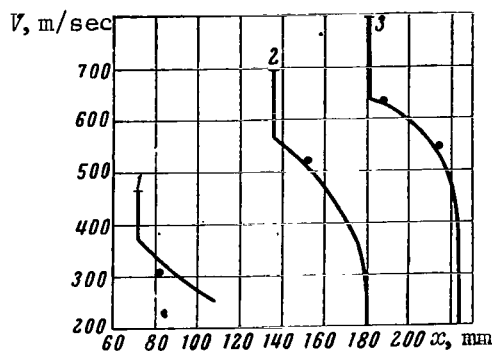


Figure 7. Distribution of V Before Flame Front at Various Moments of Time. (1) $2 \cdot 10^{-4}$ sec; (2) $3 \cdot 10^{-4}$; (3) $3.6 \cdot 10^{-4}$.

to calculate density ρ and pressure p :

$$\rho = \rho_0 \left(1 + \frac{\gamma - 1}{2} \frac{V^2}{a_0^2} \right)^{\frac{2}{\gamma - 1}};$$

$$p = p_0 \left(1 + \frac{\gamma - 1}{2} \frac{V^2}{a_0^2} \right)^{\frac{2\gamma}{\gamma - 1}},$$

where ρ_0 , p_0 and a are the density, pressure and velocity of the undisturbed gas, respectively; $\gamma = c_p/c_v$.

The density and pressure directly behind the shock wave are related to the gas velocity V by the equations

$$\frac{\rho}{\rho_0} = \frac{(\gamma + 1) M^2}{(\gamma - 1) M^2 + 2};$$

$$\frac{p}{p_0} = \frac{2\gamma}{\gamma + 1} M^2 - \frac{\gamma - 1}{\gamma + 1},$$

where M is the Mach number of the shock wave.

The calculation indicates that in the predetonation stage of development of the process, the gas pressure increases 4.5 times, the density increases by more than three times, and the gas velocity reaches 650 m/sec.

Thus, the transition to detonation explosion occurs in a preliminarily prepared medium.

In summary, the following conclusions can be made.

1. The state of a gas before a flame front can be calculated with sufficient accuracy by the characteristic curve method. It should be considered in the calculation that the velocity of

the gas before the flame front, which overlaps the entire tube section, amounts to ≈ 0.8 of the flame velocity.

2. An analysis of the state of a gas before a flame front at various moments of time, conducted for various conditions of the combustion process, indicated that while the flame front propagates with acceleration, the gas velocity, density, and pressure achieve a maximum value directly before the flame front and decrease as the distance from the flame front increases. A decrease in the velocity of flame propagation is accompanied by an increase in the distance from the region of maximum gas velocities, pressures, and densities to the flame front.

3. The transition from slow burning to detonation takes place in a medium that has been "prepared" by the compression waves generated by the flame front in the predetonation stage.

REFERENCES

1. Salamandra, G. D. and O. A. Tsukhanova: The formation of a shock discontinuity before a flame front. *Fizicheskaya gazodinamika. (Physical Gas Dynamics.)* Izd-vo AN SSSR, 1959.
2. Salamandra, G. D. and I. K. Sevast'yanova: *Vzaimodeystviye slabykh udarnykh voln s frontom plameni. (The Interaction of Weak Shock Waves with a Flame Front.)* Vol. 29, No. 11, 1959.
3. Salamandra, G. D., T. V. Bazhenova, S. G. Zaytsev, R. I. Soloukhin, I. M. Naboko and I. K. Sevast'yanova: *Nekotoryye metody issledovaniya bystro-protekayushchikh protsessov i ikh primeneniye k izucheniyu formirovaniya detonatsionnoy volny. (Some Methods of Investigating High-Speed Processes and Their Application to the Study of the Formation of a Detonation Wave.)* Izd-vo AN SSSR, 1960.
4. Salamandra, G. D., T. V. Bazhenova, and I. K. Sevast'yanova: The role of weak shock waves in the formation of a detonation. *Trudy Odesskoy Gosudarstvennoy Instituta, Seriya Fizicheskaya. (Transactions of the Odessa State Institute, Physics Series.)* Vol. 152, No. 8, 1962.
5. Hugoniot, H.: On the propagation of motion in bodies, and in perfect gases in particular. *J. École Polytechn.*, No. 57, 1887; No. 58, 1889.
6. Kochin, N. Ye., I. A. Kibel' and N. V. Roze: *Teoreticheskaya gidromekhanika (Theoretical Hydromechanics.)* Part II, Moscow, Gostekhizdat, 1948.
7. Salamandra, G. D. and I. K. Fedoseyeva: Measuring the velocity of a gas in an inflammable medium. *Inzhenerno-Fizicheskiy Zhurnal*, Vol. 7, No. 7, 1962.

PIEZOELECTRIC PRESSURE PICKUP

M. V. Gusev and O. I. Luneva

The piezoelectric method for measuring the pressure of gases and liquids /210 behind incident and reflected shock waves, and also for studying detonation phenomena, has been employed by many authors [1-12]. Plates made from natural crystals with piezoelectric properties (quartz, Rochelle salt, tourmaline, etc.) and artificial piezoelectric ceramic materials of various composition have been used as a sensing element. These artificial materials require preliminary polarization. Barium titanate ceramics are used most often.

If we examine the loading conditions of a cylindrical piezoelectric element (the direction of polarization coincides with the axis of the cylinder) in a shock tube, when one of the ends of the cylinder is part of the wall to which the shock wave is normally incident (Figure 1), and also when this end of the piezoelectric ceramic composes part of the lateral wall of the shock tube, along which the shock wave is propagated, it becomes clear that it is extremely difficult to find a mathematical relationship between the change in pressure $p_2(t)$

over time and the change in the charges on the faces of the piezoelectric ceramic $q(t)$, and extremely rough allowances for loading of the piezoelectric element are required even in the version depicted in Figure 1A. It is obvious also,

however, that no matter how complicated the deformation pattern was in the first and second cases, the charges on the ends of the piezoelectric ceramic will change during the entire period of time, while the deformation waves will propagate throughout the volume of the piezoelectric ceramic, and the relationship between $q(t)$ and $p_2(t)$ will have the following form:

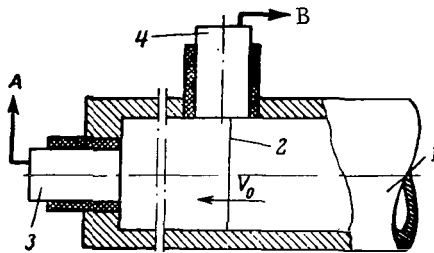


Figure 1. Arrangement of Piezoelectric Elements in Shock Tube. (1) shock tube housing; (2) shock wave front; (3) piezoelectric element at end of shock tube; (4) piezoelectric element in lateral wall of shock tube.

$$q(t) = K \int_{t_1}^{t_2} p_2(t) dt,$$

where K is a coefficient which takes into account the piezoelectric and elastic properties of the piezoelectric ceramic; $t_2 - t_1 = \Delta t$ is the pressure measurement time.

A more detailed examination of the relationship between $q(t)$ and $p_2(t)$ can be found in [8]. If the measurement time Δt of interest to the investigator is greater than the propagation time of an elastic deformation wave throughout the volume of the piezoelectric element, a signal of the wave reflected from the rear end of the piezoelectric element can appear. The appearance of a signal there is more

probable if we take into account that a gas-dynamic discontinuity acts upon the/211 piezoelectric element in the shock tube, where a pressure change occurs on several lengths of the free path of the molecule, and that the deformation wave caused by this pressure change will have a very steep front, at which dispersion of the wave due to radial vibrations in the ceramic with the appearance of higher harmonics should play an essential role in the process of ceramic deformations and the appearance of vibrations of the natural frequency of the ceramic (it could not be any higher). To remove the restrictions related to the appearance of the natural frequency of the ceramic, the piezoelectric element rests on a material whose acoustic resistance coincides with the acoustic resistance of the piezoelectric element being used [1]. Then the deformation waves enter the waveguide material without hindrance (if the connection between the piezoelectric element and the acoustic waveguide is good) without undergoing reflection on the boundary of connection with the ceramic.

A pressure pickup was developed in the laboratory with a piezoelectric element made from barium titanate in the shape of a cylindrical column which was connected by its supporting end to a zinc rod of the same diameter [4, 8].

Along with the many advantages of this pickup, it possesses a number of technical shortcomings. In the preparation of zinc waveguides, it is necessary to use homogeneous, finely crystalline zinc, the production technique of which is rather complicated under laboratory conditions. An attempt was made to grow single crystals from a zinc melt, but this did not simplify the technique very much. Moreover, zinc rods are excessively brittle, and therefore are difficult to process. An attempt to increase the resolution of the pickup by decreasing its linear dimensions (pickups with a barium titanate ceramic were fabricated to $d = 5$ mm) created additional difficulties in processing the zinc waveguides. In addition, a decrease in dimensions with a comparatively small piezoelectric modulus of the barium titanate ceramic led to searches for a more sensitive ceramic and a corresponding new ceramic for the waveguide material.

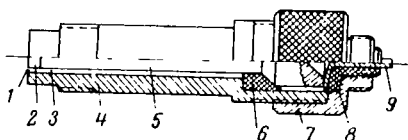


Figure 2. Design Diagram of Piezoelectric Pickup. (1) silver film; (2) piezoelectric element; (3) clearance between waveguide and pickup housing; (4) pickup housing; (5) waveguide; (6) teflon bushing; (7) clamp nut; (8) teflon insulator of internal current carrier; (9) internal current carrier.

A pickup was designed with the application of a sensing element made from a brand TsTS-19 ceramic in the shape of a cylindrical column 4 mm in diameter and 2 mm in height. This ceramic possesses greater sensitivity in comparison with the barium titanate ceramic.

The waveguide was fabricated from brand L-59 brass, the acoustic resistance of which is close to the acoustic resistance of the TsTS-19 piezoelectric ceramic.

A structural diagram of the pickup is shown in Figure 2. It does not differ from the design used earlier [4, 8, 11], except for the upper suspension of the waveguide rod, which made it possible to center the piezoelectric element well in the housing, when during pickup assembly the upper expanded part of the waveguide 5 is compressed between the teflon bushing 6 and the

positive current carrier 9, which is insulated and built into the clamp nut 7. In addition, as the experiments indicated, this expansion and conical depression in its end promotes a decrease in amplitude of the deformation waves which arrive at this expansion through the waveguide. The waveguide rod was manufactured with the same diameter as that of the ceramic. The space 3 between the housing 4 and the waveguide with soldered ceramic was filled with wax. The contact between the end of the piezoelectric ceramic which picks up the pressure and the pickup housing was made with silver foil, the thickness of which did not exceed 0.02 mm. The foil was cemented to the end of the pickup by No. 88 cement, followed by thorough pressing of the foil to the end of the pickup with a glass cylinder to remove the excess cement. The internal shape of the housing was varied in accordance with the conditions of attaching the pickup to the shock tube. The high curie point, which is approximately 305°C for the brand TsTS-19 piezoelectric ceramic, made it possible to solder it to the waveguide with an alloy having a melting point of approximately 105°C, for Schoop processing*, without any noticeable change in sensitivity of the piezoelectric element.

The resolution τ of the pickup with the piezoelectric element dimensions indicated above was in the interval from 0.2 to 0.4 μ sec. The resolution was estimated along the length of the leading edge of the signal from the pickup with various pressures on it (measurements were conducted for several analogous pickup designs). The pickups were arranged in the lateral wall of a square shock tube. The working gas was argon. The initial pressure and velocity of the shock wave were varied.

It is natural to consider that under the indicated loading conditions (see Figure 1B), τ is a function of both the dimensions of the piezoelectric element and the velocity of the shock wave.

A theoretical estimate of τ , performed under the frequently used assumption that longitudinal deformation waves are formed in a piezoelectric element despite the complexity of the loading conditions, gave the quantity $\tau_1 = 0.6 \cdot 10^{-6}$ sec.

This quantity was obtained for a longitudinal wave velocity C_0 with a wavelength $\lambda \rightarrow \infty$ [13, 14].

Other versions of estimates of τ_1 , which use the assumption that the velocity of propagation of the deformation wave front $C \leq C_0$ under any assumption concerning the orientation of this front, give values of pickup resolution which are much higher than the experimentally determined value of τ . This gives us a basis to assume that not longitudinal, but another form of deformation wave, originates in the piezoelectric element under the loading conditions which we set up.

The system for recording the change of the charge on the linings of the piezoelectric ceramic imposed its requirements on the design of the pickup and the recording instrument. An IO-4 electron-beam oscillograph with input resis-

*Translator's note: A method of metal spraying.

tance $R_{in} = 2 \text{ M}\Omega$ and input capacitance $C_{in} = 45 \text{ }\mu\text{F}$ was used as the recording instrument. It is obvious that the correspondence between the functions $q(t)$ and $U(t)$, where $U(t)$ is the voltage recorded as a function of time, will take place when charge leakage from the total capacitance R_{Σ} (the pickup of the power cable and the input capacitance of the oscillograph) across the total resistance of the same elements R_{Σ} is minimum. It is necessary in this case to satisfy the condition $R_{\Sigma cab} \gg R_c \gg R_{in}$, where $R_{\Sigma cab}$ is the total leakage resistance through the pickup and the power cable; R_c is the capacitive resistance of all elements before the control grid of the input amplifier of the oscillograph when measuring pulsating pressures. Then R_{in} will be decisive when calculating the time constant τ_{RC} of the system, which amounts to $\tau_{RC} = 3 \cdot 10^{-2}$ sec for our pickup and power cable. This provides a measuring time, $p_2(t)$, equal to $3 \cdot 10^{-4}$ sec without a noticeable drop in the signal.

For quantitative measurements of $p_2(t)$, the pickup was calibrated in a shock tube filled with argon. The pressure behind the incident wave in argon to Mach numbers of the shock wave $M = 9$ was calculated with the equation of conservation of pulse, mass and energy on the shock wave as for an ideal gas [15, 16].

The calibration curve for one of the pressure pickups placed in the lateral wall of the shock tube is shown in Figure 3

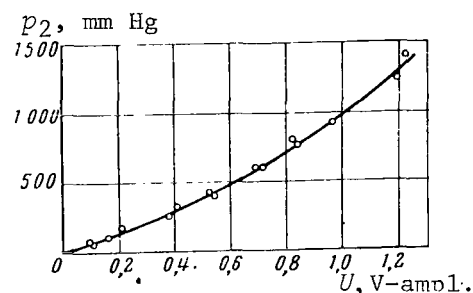


Figure 3. Typical Calibration Curve of Pressure Pickup.

(p_2 is the pressure behind the incident shock wave). The scatter of the experimentally obtained values of p_2 near the curve does not exceed $\pm 7.5\%$.

Typical oscillograms of the pressure behind the incident shock wave (pickup built into lateral wall of shock tube) and behind the reflected shock wave (pickup built into end of shock tube) are illustrated in Figure 4a and b. The oscillograph sweep is from left to right, and the time markers are at $10 \text{ }\mu\text{sec}$. The amplitude change of the oscillograph signal was recorded on film and was measured under an instrument microscope; then, in accordance with the calibration curve of the oscillograph, it was converted into amplitude volts. With a constant reduction factor of the natural dimensions of the screen on the photographic film, the expression for calculating the voltage amplitude on the input resistance of the oscillograph has the form

$$U = \frac{1}{k} aH.$$

In this expression, U is the voltage amplitude [V-ampl.], α is the sensitivity of the oscillograph with 1:1 amplification [V-ampl./mm (on film)], H is the oscillograph beam deflection measured on the film [mm], and k is the amplification factor of the oscillograph. In this case the maximum relative error is

$$\frac{\Delta U}{U} = \frac{\Delta \alpha}{\alpha} + \frac{\Delta H}{H} + \frac{\Delta k}{k} = \pm 4\%.$$

The calibration curve of the pickup, which expresses the relationship $p_2(U)$, was constructed in an independent calculation of $p_2(V_0)$ according to the known formula for the pressure ratio on a shock wave in an ideal gas

$$p_2 = \frac{2\gamma_0 M_s^2 - (\gamma_0 - 1)}{(\gamma_0 + 1)} p_0.$$

The maximum relative error for p_2 , calculated with the expression

$$\frac{\Delta p_2}{p_2} = \frac{4\gamma_0 M_s \Delta M_s}{2\gamma_0 M_s^2 - (\gamma_0 - 1)} + \frac{\Delta p_0}{p_0},$$

where M_s is the Mach number of the shock wave [$M_s = 3(+0.02) - 9(+0.23)$] and p_0 is the pressure in front of the shock wave [$p_0 = 1 - 25(+0.05)$ mm Hg], amounts to $\pm 10.1\%$.

When calibrating the pressure pickups under our conditions, when the initial pressures are low and the shock wave velocities have Mach numbers $M_s \leq 3$, the shock wave velocity was measured with a piezoelectric pickup.

The most extensively used method for determining shock wave velocity is the method which uses ionization pickups. For these pickups, however, it is necessary that the gas behind the shock wave possess sufficient conductivity. When setting up certain experimental problems in shock tubes, it is necessary to measure the velocity of relatively weak shock waves which do not cause noticeable ionization of the gas behind them, *e.g.*, when calibrating pressure pickups with weak shock waves. In addition, the ionization pickup method assumes that there is an electrical discharge in the region behind the shock wave, which introduces undesirable disturbances in a number of cases. The method which uses piezoelectric pickups with subsequent pulse shaping indicated good results under these conditions. This method was developed for measuring the velocity of shock waves in the shock tube whose diagram is shown in Figure 5. /214

The tube had a high-pressure chamber with a diameter of 100 mm and a length of 1.0 m; the length of the low-pressure chamber amounted to 5 m with a diameter of 60 mm. At a distance of 4 m from the diaphragm D , the circular section of the chamber gradually became square with a cross section of 60 \times 60 mm and a length of 260 mm. The square section had an area where the lateral walls of the

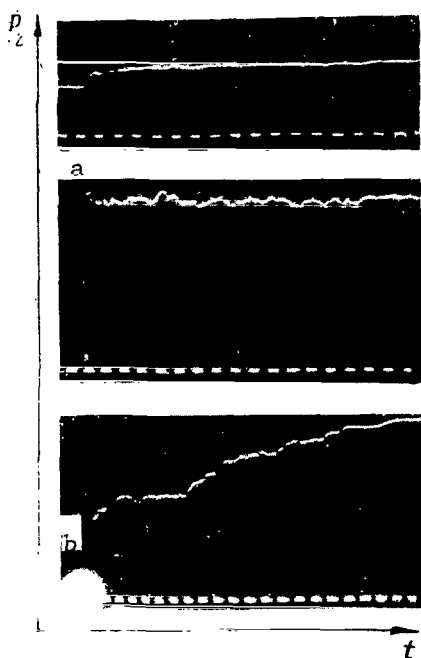


Figure 4. Pressure Oscillograms. (a) behind incident shock wave; (b) behind reflected shock wave with pickup placed in end of shock tube.

consists of two cascades. The first cascade is a 6Zh1P vacuum-tube amplifier (T_1), which has a positive voltage pulse of similar shape in the plate circuit due to the negative signal sent from the pickup to the control grid.

This positive pulse actuates the TG3-0.1/1.3 thyatron (T_2), across which capacitance C_3 is discharged. Single action (during one experiment) of the shaping unit is ensured due to the high resistance of R_5 . Resistance R_6 , capacitance C_4 and diode D provided for the obtainment of a narrow positive pulse at the output of the unit, which was then sent to the OK-17M oscillograph. Voltage was fed across diode D7Zh to the second input of the oscillograph from a GSS-6 generator.

The design of the shaping unit (see Figure 6) makes it possible to connect several units on one cable (up to nine units on one cable were used) without affecting each other.

As we mentioned above, a signal on the order of 10^{-2} V-ampl. can be obtained from the pickup at low pressures behind the shock wave. This imposes obligatory conditions on the amplifier cascade, which must amplify the obtained signal to a value higher than the firing level of the thyatron (thyratrons are

tube were made from optical glass. The installation is described in greater detail in [17].

Piezoelectric pickups were built into the walls of the low-pressure chamber and inserted into sockets 1-9 (Figure 5).

The design of the pickup is similar to the design of the pressure pickup illustrated in Figure 2.

When constructing the pickup, the ceramic was oriented in such a way that a negative charge appeared on the waveguide when the pickup was loaded, since this facilitates subsequent pulse shaping.

The pickup makes it possible to obtain a signal of 0.026 V-ampl. at an initial pressure of 1 mm Hg in the shock tube and with a shock wave velocity of approximately 1,000 m/sec in argon.

A signal was sent from this pickup to the electronic circuit shown in Figure 6; the circuit then generated a single positive pulse with a duration of 3-4 μ sec as the signal arrived at it. The leading edge of this pulse had a duration of 0.3-0.5 μ sec. The circuit

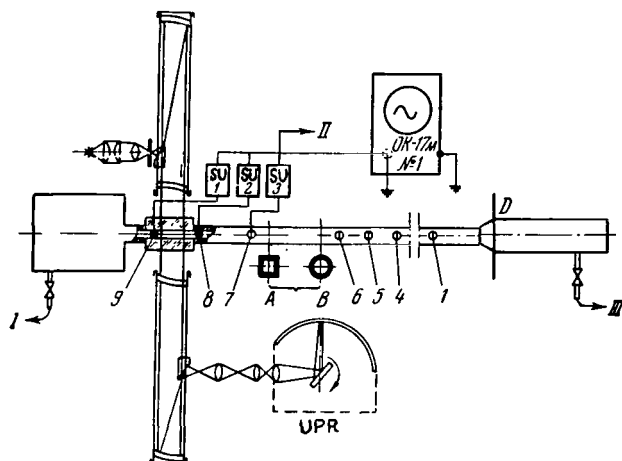


Figure 5. Diagram of Shock Tube and Arrangement of Measuring Equipment. (I) to vacuum system; (II) cable for starting OK-17M oscillograph; (III) to high-pressure system; (AB) transition section from circular internal cross section of tube to square cross section.

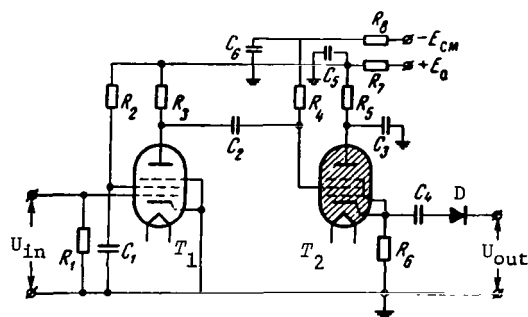


Figure 6. Schematic Diagram of Shaping Unit.

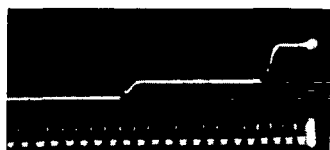


Figure 7. Oscillogram of Shock Wave Velocity.

selected with identical firing levels for all units).

The units operate without failure at the following values of the circuit elements: $R_1 = 1 \text{ M}\Omega$; $R_2 = 25 \text{ k}\Omega$; $R_3 = 4.5 \text{ k}\Omega$; $R_4 = 1.8 \text{ k}\Omega$; $R_5 = 100 \text{ M}\Omega$; $R_6 = 100 \text{ }\Omega$; $R_7 = 1.8 \text{ k}\Omega$; $R_8 = 1.8 \text{ k}\Omega$; $C_1 = 0.05 \text{ }\mu\text{F}$; $C_2 = 0.01 \text{ }\mu\text{F}$; $C_3 = 0.1 \text{ }\mu\text{F}$; $C_4 = 2,200 \text{ pF}$; $C_5 = 1 \text{ }\mu\text{F}$; $C_6 = 1 \text{ }\mu\text{F}$.

Signal delay in the circuit from the pickup to the shaper output does not exceed $1.5 \text{ }\mu\text{sec}$ with deviations of $\pm 0.25 \text{ }\mu\text{sec}$ from this value for various units.

The short duration of the leading edge of the signal obtained from the unit gives a concise discontinuity on the oscillograph sweep. Figure 7 illustrates a typical oscillogram of the shock wave velocity. The sweep is from left to right. The Mach wave number is equal to 2.9 (in argon). The time determined on the oscillogram makes it possible to calculate the average velocity on a fixed base between pickups. An analysis of the errors in measuring the velocity on a base to 200 mm indicated that they increase linearly from 0.7 to 2.6% as the shock wave velocity increases from 1,000 to 4,500 m/sec.

Measurement of shock wave velocity by the pickups was duplicated by measuring the same velocity by an optical method. The Töpler pattern of shock wave propagation along the tube was photographed on the section between pickups 8 and 9 through special windows of a UPR camera in a time-magnification mode [17].

As a result of the experiments, a velocity oscillogram and a series of photographs taken by the UPR ultrahigh-speed photorecorder were obtained in each experiment for various shock wave velocities in argon.

The known period between frames and the reduction scale of the natural

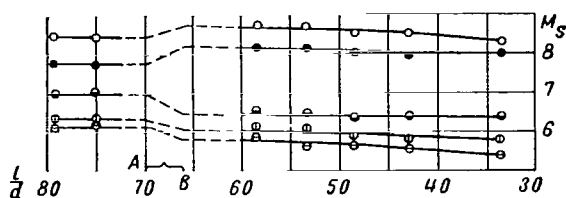


Figure 8. Variation of M_s of a Shock Wave in Argon as a Function of l/d .

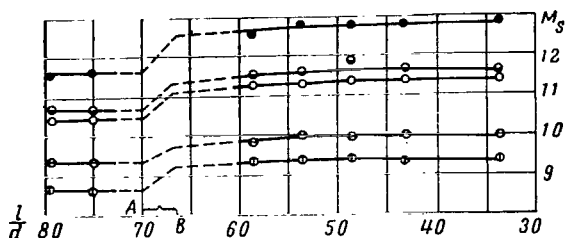


Figure 9. Variation of M_s of a Shock Wave in Carbon Dioxide as a Function of l/d .

dimensions on the film made it possible to obtain the shock wave velocity on the basis of UPR photographs.

A comparison of the shock wave velocities measured by the two independent methods indicated that the divergence of results lies within the error range of the roughest method (UPR) and amounts to no more than $\pm 4\%$.

As can be seen from Figure 5, the shock tube had a transition from the circular section to the square section with a 22% increase in size. By using the procedure described above for measuring shock wave velocities, the velocities were measured along the entire length of the tube. Velocity pickups ^{/217} were placed in nine sockets, beginning with the section at a distance of 31 tube diameters from the diaphragm (socket 1 in Figure 5). The results of the measurements are illustrated in Figures 8 and 9, where l/d is the ratio of the distance from the diaphragm

along the tube to the diameter of the internal cross section of the tube.

As can be seen from the graphs, the velocity of a shock wave in argon has the tendency to increase along the entire tube. In carbon dioxide, it can be considered to be steady at a distance of 31 calibers from the diaphragm and 40-50 calibers from the diaphragm to the section, after which there appears a tendency for the velocity to decrease.

The velocity was not measured on the transition section AB. The dashed curves indicate extrapolation of the experimentally measured behavior of the velocity before and after the transition section to the transition section. The effect of the transition section on the measurement of shock wave velocity is evident from the graphs.

The authors did not analyze the possible causes for the change in shock wave velocity on the transition section.

The measurement error for velocities measured before the transition section amounted to $\pm 7\%$, since the signals from all pickups that were placed in sockets from 1 through 7 (see Figure 5) were recorded on one oscillograph. After the transition section, judging by the measurements of the piezoelectric pickups in sockets 7-9 and by the UPR films, the shock wave velocity remains constant within the measurement error limits of $\pm 2.5\%$.

The measuring accuracy may be increased to $\pm 1.2\%$ if the shock wave velocity

is measured with two pickups on a base which does not exceed 200 mm, and if an IV-13M time meter is used.

REFERENCES

1. Turetric, W.: *Problem der Detonation. (The Problem of Detonation.)* Berlin, 1941.
2. Volchok, L. O.: *P'yezoelektricheskiye indikatory dlya dvigateley vnutrennego sgoraniya. (Piezoelectric Indicators for Internal-Combustion Engines.)* Moscow and Leningrad, Mashgiz, 1945.
3. Sinani, I. B.: Tourmaline indicators of shock waves in liquids. *Prib. i Tekh. Eksperim.*, No. 4, 1957.
4. Zaytsev, S. G.: The measurement of quickly changing pressures in a gaseous medium. *Prib. i Tekhn. Eksperim.*, No. 6, 1958.
5. Willmarth, W.: Miniature barium titanate pickups for aerodynamic and acoustic pressure measurements. In: *Udarnyye trubyy. (Shock Tubes.)* Moscow, IL, 1958.
6. Knight, G.: A piezoelectric pickup for shock waves in low-density gases. In: *Udarnyye trubyy. (Shock Tubes.)* Moscow, IL, 1958.
7. Gerrard, J.: Piezoelectric pressure gauges for use in a shock tube. *J. Acustica*, No. 9, 1959.
8. Salamandra, G. D., T. V. Bazhenova, S. G. Zaytsev, R. I. Soloukhin, I. M. Naboko and I. K. Sevast'yanova: *Nekotoryye metody issledovaniya bystroprotekayushchikh protsessov. (Some Methods for Investigating High-Speed Processes.)* Izd-vo AN SSSR, 1960.
9. Soloukhin, R. I.: A pulsed pressure pickup. *Prib. i Tekhn. Eksperim.*, No. 3, 1961.
10. A piezoelectric pressure-sensing element. In: *Ekspress-Informatsiya (VINITI), Seriya "Kontrol'no-Izmeritel'naya Tekhnika". (Express-Information (All-Union Institute of Scientific and Technical Information), "Measurement and Control Technology" Series.)* No. 23, 1961.
11. Topchiyan, M. Ye.: Experimental studies on spin detonation with pressure pickups. *Prikladnaya Mekhanika i Tekhnicheskaya Fizika*, No. 4, 1962.
12. Soloukhin, R. I.: *Udarnyye volny i detonatsiya v gazakh. (Shock Waves and Detonation in Gases.)* Moscow, Fizmatgiz, 1963.
13. Hudson, G. E.: Dispersion of elastic waves in solid circular cylinders. *J. Phys. Rev.*, No. 63, 1943.
14. Bergman, L.: *Ul'trazvuk i yego primeneniye v nauke i tekhnike. (Ultrasound and its Application in Science and Technology.)* Moscow, IL, 1956.
15. Resler, E. L., S. C. Lin and A. Kantrowitz: The production of high-temperature gases in shock tubes. *J. Appl. Phys.*, Vol. 23, No. 12, pp. 1390, 1952.
16. Fayzulov, F. S.: Pyrometric investigation of the state of air, nitrogen and argon behind a shock wave. In: *Trudy Fizicheskogo Instituta AN SSSR. (Transactions of the Physics Institute of the Soviet Academy of Sciences.)* Vol. 18, 1962.
17. Ionov, V. P., G. N. Nikolayev, M. V. Gusev and O. I. Luneva: A study of the gas flows in a shock tube with the aid of a Töpler pattern and high-speed frame photography. In: *Fizicheskaya gazodinamika i svoystva gazov pri vysokikh temperaturakh. (Physical Gas Dynamics and Properties of Gases at High Temperatures.)* Moscow, Izd-vo "Nauka", 1964.

18. Strong, D.: *Tekhnika fizicheskogo eksperimenta. (Techniques for Physics Experiments.)* Leningradskoye Knizhnoye Izdatel'stvo, 1948.

MUSHROOM-SHAPED TRANSDUCER FOR RECORD- ING PRESSURE IN A SHOCK TUBE

A. P. Shatilov

A technique for measuring pressure under the operating conditions of a shock tube has been developed over a number of years at the Laboratory for High-Temperature Gas Dynamics and Thermodynamics of the G. M. Krzhizhanovskiy Power Engineering Institute. One of the possible designs of a pressure transducer for this type of research is described below. /218

Piezoelectric transducers with a rod which damps the natural vibrations of the piezoelement are frequently used to record highly variable pressure as a shock wave passes a fixed cross section x of a shock tube [1]. Transducers of a similar design have been used in shock tubes (see, for example, [2, 3, 4]).

At the present time, the approximate theory of operation of this instrument is more or less clear. Nevertheless, the design of this sort of instrument encounters a number of difficulties caused by the specific nature of operation in shock tubes.

The accuracy of reproducing the pressure profile over time in a fixed cross section of a shock tube x depends on the space and time resolution of the transducer, which in turn depends on the configuration of the transducer and the frequency response of the intermediate channel (cathode follower, oscillograph, amplifier, etc.). The smaller the diameter of the transducer, the higher its space and time resolution. A limiting (in the sense of smallness) diameter, obviously, is restricted by the sensitivity of the electronic equipment, taking into account the value of limiting piezoelectric modulus of the applied crystal. It is natural that the input resistance R_{in} of the matching cathode follower should be correspondingly high.

During operation in a shock tube [5] it is necessary to record the velocity of the incident shock discontinuity and the pressure profile in time. To solve these problems, a pressure transducer was designed with an element that absorbs weak acoustic vibrations. The diameter of the surface which perceives the pressure changes amounted to 5 mm.

The designed pressure transducer possesses good acoustic insulation, mechanical strength, maintains a vacuum rather well, and is mounted flush with the inner wall of the shock tube.

Description of Design and Assembly Procedure of Mushroom-Shaped Pulse-Type Pressure Transducer (MPPT)

The transducer (Figure 1) was mounted in the mid-section of the viewing chamber of a Mach-Zehnder interferometer, which made it possible to record the variations in density and pressure simultaneously. A sensing element 2 made

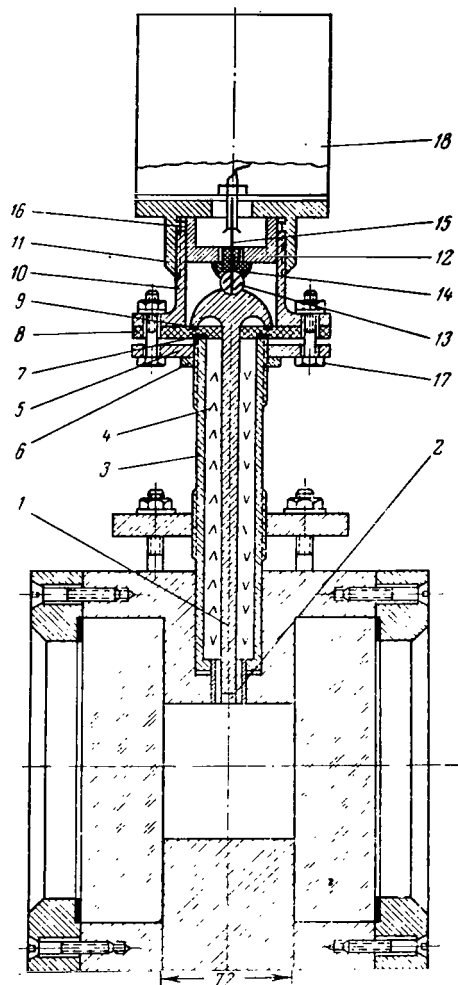


Figure 1. Overall View of Mushroom-Shaped Pulse-Type Pressure Transducer Together with Operating Section of Shock Tube.

parts 5, 8 and 10 are tightened by four bolts 17, by means of which, in addition, electrical contact is ensured between the transducer housing and parts 10 and 11, while part 11, which is screwed onto part 10, imparts translational motion to part 12, which presses on rubber ball 13 through part 14. The latter imparts translational motion to zinc rod 1. Part 11 is screwed onto part 10 until the lower side of sensing element 2 (BaTiO_3 crystal) is in the same plane with the lower (Figure 1) end of the transducer housing, *i.e.*, the so-called "nose" of /220

from BaTiO_3 piezoelectric ceramic ($h = 5$ mm, $d = 5$ mm) is ground into a zinc rod* 1 with a diameter of 5 mm and a length of 220 mm which /219 terminates in a shaped head. This element is cemented to the zinc rod with carbinal cement and dried for 1-2 days under a pressure of 30-50 kg. After drying, the lateral surface of the piezoelectric element, together with the zinc rods and the shaped head (except for the point of contact with the input cathode follower recess in the shaped head), is coated with shellac and then with ceresin before assembly to improve electrical insulation.

The zinc rod 1 with the sensing element 2 is placed inside a thin-walled steel cylinder 3 which serves as the transducer housing; the latter is closed by a plug 4. Flange 5 is secured by check nut 6. The sharp knife edge of the transducer housing cuts into rubber washer 7, thereby providing a vacuum seal between the housing and teflon part 8, which provides electrical insulation of the zinc rods from the transducer housing. Rubber washer 9, which comprises a second vacuum seal in the place of connection with the shaped head of the zinc rod, is placed into the circular recess of teflon part 8. Attention was given here to the fact that washer 9 did not come into contact with part 10; the latter, together with parts 11 and 12, and rubber ball 13, comprised the system of attachment and suspension of the shaped zinc element. The rubber ball rests on a special part 14 made from teflon. Copper rod 15, which serves as the contact which connects the current-conducting zinc rod to the input cathode follower, passes through the rubber ball and part 14. Cotter 16 prevents rotation of part 12 with respect to 10. During assembly,

*The rod with the shaped head was machined from billets which were kindly supplied to us by Yu. P. Yakovlev, and were cast according to a procedure proposed by him and described in his dissertation [6].

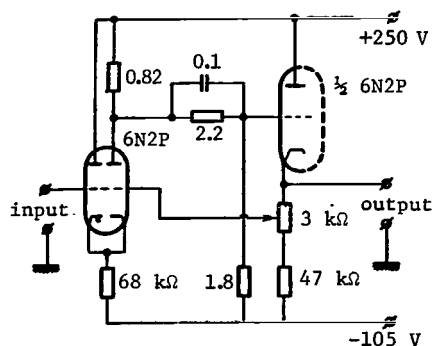


Figure 2. Schematic Diagram of Cathode Follower.

the transducer. Thin silver foil is cemented to the plane of the transducer nose with K-88 cement. A soft suspension (between washer 10 and the rubber ball) and also good acoustic insulation (plug filling) almost completely eliminates the effect of external factors on the sensing elements. The high insulation resistance (on the order of 10^{10} ohms) makes it possible for the transducer to record the pressure drops which follow one another in time intervals to several milliseconds, whereby the flat portion of the voltage pulse on the crystal linings drops with a time constant of ≈ 10 sec.

Reflection from the shaped head arrives at the BaTiO_3 crystal in ≈ 100 μsec , which is determined by the length of the zinc rod. This reflection, which is significantly reduced by the shaped head, is superimposed on the fundamental signal, which is caused by a change in pressure on the "lower plane of the crystal".

The accuracy of transducer operation depends essentially on the parameters of the matching electronic circuit-cathode follower, the location of which is indicated in Figure 1 by the number 18. The cathode follower must possess a high input resistance ($R_{in} \approx 10^{10}$ ohms) and a sufficient transmission band. A coated cathode follower without grid resistance was employed [7]. These circuits are called "floating-grid cascades" in the literature (Figure 2).

Having a high input and low output resistance, a sufficiently linear section, and a transmission band of several MHz, this cathode follower prevented a loss in amplitude on the input resistance and a signal drop in time. All of the same precautions (in the sense of leakage through the surface of the circuit elements) as those taken with regard to the transducer should be applied when assembling this cathode follower with regard to the grid circuits.

Calibration of Transducer

The design and the experimental conditions made it possible to conduct three types of calibrations.

1. Static calibration. In static calibration, the pressure transducer was loaded by a calibrated weight, and a signal from the transducer was recorded on an ENO-1 oscillograph.

2. Dynamic calibration. In this type of calibration, a weak shock wave of known intensity (only the initial pressure varied) was recorded by the transducer and, on the basis of the results of measurement, a calibration curve was constructed.

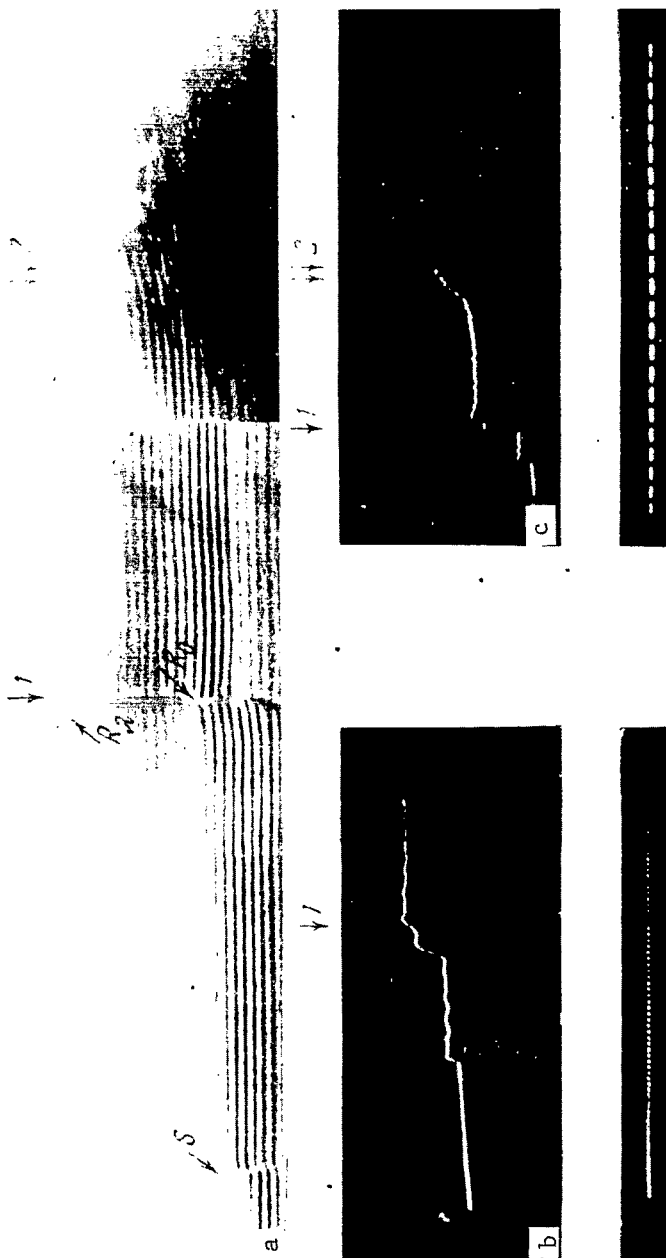


Figure 3. Simultaneous Recording of Gas Pressure and Density in a Fixed Cross Section of a Shock Tube.

boundary layer behind the incident discontinuity past the slit (of the pressure transducer); an increase in gas density (pressure) 2 behind the front of the reflected shock wave caused by turbulence of the boundary layer and the arrival of a disturbance from the contact surface; a decrease of pressure in the shock tube

3. Joint operation of transducer and interferometer. In this case, two parameters were recorded simultaneously.

Since static calibration, in the author's opinion, does not completely reflect the picture of operation of the instrument, it was used only to align the instrument. Dynamic calibration and joint operation of the transducer and interferometer more completely reflect the picture of the phenomenon, and therefore calibration was conducted by the dynamic method during joint operation of the transducer and interferometer.

Figure 3 illustrates an /222 interferogram of normal reflection of a shock discontinuity from the rigid end of a shock tube jointly with the recording of gas pressure behind the front of a shock wave on the lateral wall. The shock wave was excited in nitrogen at an initial pressure of 10 mm with a velocity of $M_1 = 3.15$. Pressure and density were recorded simultaneously at a distance of $x = 26$ mm upstream from the point of its reflection.

The interferogram was taken at a speed of recording the gas density behind the front of the shock wave equal to 0.117 mm/ μ sec; the duration of the time markers was 10 μ sec (b) and 100 μ sec (c). The following features are noted on the interferogram (oscillograms): a characteristic density (pressure) drop 1 caused by the passage of the front of the reflected wave distorted by the interaction with the increasing

is also observed immediately behind the front of the reflected shock wave. The gas pressure before the front of the reflected shock wave remains constant with an accuracy of $\pm 10\%$ right up to the arrival of the front in the section where the recording equipment was set up.

The experience derived in working with this type of pressure transducer makes it possible to draw the following conclusions.

1. The errors in pressure measurement for this type of transducer amount to 10-15% of the measured pressure.

2. The transducer correctly reflects the behavior of the processes at the wall of the shock tube and can be used for mutual monitoring of the two methods (measurement of $P(t)$ and $\rho(t)$) in a fixed cross section of the tube x .

3. The errors in measuring the absolute value of pressure are caused by reflection of elastic waves from the "shaped head" and the imperfection of the recording equipment.

4. The shock wave velocity can be determined with the aid of two transducers placed at a certain distance from each other (average velocity of shock wave on a certain portion of the shock tube) with an accuracy of 1.0-1.5%.

REFERENCES

1. Turetric, W.: *Problem der Detonation. (The Problem of Detonation.)* Berlin, 1941.
2. Soloukhin, R. I.: *Udarnyye volny i detonatsiya v gazakh. (Shock Waves and Detonation in Gases.)* Moscow, Gosudarstvennoye Izdatel'stvo Fizicheskoy i Matematicheskoy Literatury, 1963.
3. Zaytsev, S. G.: On the measurement of quickly changing pressures. *Prib. i Tekhn. Eksperim.*, No. 60, 1958.
4. Gusev, M. V. and O. I. Luneva: Piezoelectric pressure pickup. This collection.
5. Zaytsev, S. G., A. P. Shatilov, Ye. V. Lazareva, L. N. Trukhanova, L. A. Averina and M. K. Yaichkov: Methods for measuring the density of gas flows in a shock tube with an interferometer. In: *Fizicheskaya gazodinamika, teploobmen i termodinamika gazov vysokikh temperatur. (Physical Gas Dynamics, Heat Exchange and Thermodynamics of High-Temperature Gases.)* Moscow, Izd-vo AN SSSR, 1963.
6. Yakovlev, Yu. P.: *Issledovaniye protsessa lit'ya cherez vibriruyemye zalivochnyye ustroystva. (Investigation of the Process of Casting Through Vibrating Casting Devices.)* Candidate's Dissertation, Bauman Moscow Higher Technical School, 1964.
7. Griбанov, Yu. I.: *Izmereniya v vysokoomnykh tsepyakh. (Measurements in High-Resistance Circuits.)* Moscow and Leningrad, Gosenergoizdat, 1949.

FRANK C. FARNHAM COMPANY, INC.
133 South 36th Street
Philadelphia, Pennsylvania 19104
Translated by Gerald E. Bernfeld
NASw-1497

"The aeronautical and space activities of the United States shall be conducted so as to contribute . . . to the expansion of human knowledge of phenomena in the atmosphere and space. The Administration shall provide for the widest practicable and appropriate dissemination of information concerning its activities and the results thereof."

—NATIONAL AERONAUTICS AND SPACE ACT OF 1958

NASA SCIENTIFIC AND TECHNICAL PUBLICATIONS

TECHNICAL REPORTS: Scientific and technical information considered important, complete, and a lasting contribution to existing knowledge.

TECHNICAL NOTES: Information less broad in scope but nevertheless of importance as a contribution to existing knowledge.

TECHNICAL MEMORANDUMS: Information receiving limited distribution because of preliminary data, security classification, or other reasons.

CONTRACTOR REPORTS: Scientific and technical information generated under a NASA contract or grant and considered an important contribution to existing knowledge.

TECHNICAL TRANSLATIONS: Information published in a foreign language considered to merit NASA distribution in English.

SPECIAL PUBLICATIONS: Information derived from or of value to NASA activities. Publications include conference proceedings, monographs, data compilations, handbooks, sourcebooks, and special bibliographies.

TECHNOLOGY UTILIZATION PUBLICATIONS: Information on technology used by NASA that may be of particular interest in commercial and other non-aerospace applications. Publications include Tech Briefs, Technology Utilization Reports and Notes, and Technology Surveys.

Details on the availability of these publications may be obtained from:

SCIENTIFIC AND TECHNICAL INFORMATION DIVISION
NATIONAL AERONAUTICS AND SPACE ADMINISTRATION
Washington, D.C. 20546